



HAL
open science

Préparation et spéciation d'oxo-clusters de métaux du bloc p

Daniel Szczerba

► **To cite this version:**

Daniel Szczerba. Préparation et spéciation d'oxo-clusters de métaux du bloc p. Material chemistry. Université Bourgogne Franche-Comté, 2022. English. NNT : 2022UBFCK046 . tel-03948337

HAL Id: tel-03948337

<https://theses.hal.science/tel-03948337v1>

Submitted on 20 Jan 2023

HAL is a multi-disciplinary open access archive for the deposit and dissemination of scientific research documents, whether they are published or not. The documents may come from teaching and research institutions in France or abroad, or from public or private research centers.

L'archive ouverte pluridisciplinaire **HAL**, est destinée au dépôt et à la diffusion de documents scientifiques de niveau recherche, publiés ou non, émanant des établissements d'enseignement et de recherche français ou étrangers, des laboratoires publics ou privés.



THESE DE DOCTORAT DE L'ETABLISSEMENT UNIVERSITE BOURGOGNE FRANCHE-COMTE
Laboratoire Interdisciplinaire Carnot de Bourgogne, UMR CNRS 6303

Ecole doctorale n°533

Carnot-Pasteur

Doctorat de Chimie-Physique

Par

Daniel M. Szczerba

Preparation and speciation of p-block metal-oxo clusters

Thèse présentée et soutenue à Dijon, le 11.04.2022

Composition du Jury :

Mme. Millot, Nadine
Mme. Jensen, Kirsten M. Ø.
M. Olivier Soppera
M. Thomas Cottineau
M. Henry, Paul F.
M. Domenichini, Bruno
M. Kimber, Simon A. J.

Professor, Université de Bourgogne
Associate Professor, University of Copenhagen
Professor, Université de Haute Alsace
Professor, Université de Strasbourg
Senior scientist, ISIS Neutron and Muon Source
Professor, Université de Bourgogne
Associate Professor, Université de Bourgogne

Présidente
Rapporteur
Rapporteur
Examineur
Examineur
Directeur de thèse
Codirecteur de thèse

Titre : Préparation et spéciation d'oxo-clusters de métaux du bloc p

Mots clés : Diffusion des rayons X, analyse par fonction de distribution de paires (PDF), oxo-clusters de métaux

Résumé : Cette étude a été consacrée à l'utilisation de l'analyse par fonction de distribution de paires (PDF) pour la spéciation de phase durant la croissance de clusters de métaux. Les mécanismes de croissance de deux systèmes en solution ont été étudiés. Les précurseurs ont été synthétisés par voie mécano-chimique. Cette méthode a permis d'accéder à une large variété de systèmes.

La synthèse de principes actifs à base de bismuth a ainsi été étudiée. Les échantillons ont été analysés avec une large variété de techniques incluant la diffraction des rayons X sur poudre, l'analyse thermogravimétrique et la spectroscopie Raman. Par optimisation des paramètres de broyage, la synthèse du gallate de bismuth (III), du citrate de bismuth (III) ainsi que l'amélioration de la synthèse du bismuth (III) di- et trisalicylate ont été menées. Ce type de synthèse est réalisée en partant de Bi_2O_3 et des acides organiques correspondants. De façon remarquable, une transformation structurale, induite par l'eau, du citrate de bismuth (III) a été découverte conduisant à une nouvelle structure repliée de style origami qui se déplie sous effet de l'eau conduisant alors à une structure cubique fortement poreuse.

La première synthèse en solution d'un oxo-cluster de métal réalisée fut celle de $[\text{Bi}_{38}\text{O}_{44}]$, connu comme la molécule de taille magique de structure Keplerate de . Le di-salicylate de bismuth (III) a été utilisé comme précurseur pour cette réaction, résultant en la croissance de petits clusters de Bi_9O_7 . Cette croissance a été réalisée dans plusieurs solvants : l'acétone, la cyclohexanone, la pentanone, la méthyléthyl cétone ainsi que le diméthylformamide. La croissance est influencée par le type de solvant ainsi que par la quantité d'eau. Les observations par analyse PDF ont été confirmées par spectroscopie Raman ainsi que par diffusion dynamique de lumière (DLS).

Le deuxième système étudié est la formation du cluster $\varepsilon\text{-}[\text{Al}_{13}]$ à partir de la solution aqueuse de AlCl_3 . Deux mécanismes de croissance sont proposés pour ce système dans la littérature : un modèle de polymérisation progressive impliquant un ensemble d'oligomères intermédiaires et un modèle d'auto-assemblage spontané dans lequel la croissance se produit à partir de petites espèces $\text{Al}_1\text{-Al}_3$. La méthode PDF indique que le modèle d'auto-assemblage immédiat est exact. La diffusion des rayons X a été utilisée pour analyser la croissance du cluster $\varepsilon\text{-}[\text{Al}_{13}]$ en complément de l'approche calculatoire par la méthode l'analyse en composantes principales.

Title : Preparation and speciation of p-block metal-oxo clusters

Keywords : X-ray scattering, pair distribution function, metal-oxo clusters

Abstract : The main subject of this thesis is the use of Pair Distribution Function (PDF) analysis for solution phase speciation during metal-cluster growth. The PDF method allows the extraction of structural information from a sample in the form of an atom-atom distance distribution via Fourier transform of synchrotron X-ray scattering data. The growth mechanisms of two solution-based systems are analysed in this thesis. Precursor materials are synthesized through a mechanochemical method that was developed and shown to be able to access a wide range of related systems.

Mechanochemical routes of synthesizing bismuth Active Pharmaceutical Ingredients (APIs) were investigated and optimised. Samples were analysed using a range of techniques, including powder X-ray diffraction (PXRD), thermogravimetric analysis (TGA) and Raman spectroscopy. Various milling conditions were explored, resulting in optimised routes to bismuth (III) gallate and bismuth (III) citrate, as well as improving the literature syntheses of bismuth (III) di- and trisalicylate. All reactions used Bi_2O_3 and the corresponding organic acids. Significantly, a water dependent structural transformation of mechanochemically activated bismuth citrate was discovered, suggesting an origami-like folded structure that expands when filled with water to reveal a highly porous framework of the cubic crystal system.

The first solution-phase metal-oxo cluster studied was $[\text{Bi}_{38}\text{O}_{44}]$, a "magic-size" Keplerate-shaped molecule. Using bismuth (III) disalicylate as a precursor, it was found to grow in a multistep reaction with initial formation of the smaller $[\text{Bi}_9\text{O}_7]$ cluster. The growth occurs in multiple solvents, including acetone cyclohexanone, pentanone, methyl ethyl ketone and dimethylformamide. The growth mechanism is shown to be influenced by the solvent choice and water content. The PDF method observations were confirmed by spectroscopy and Dynamic Light Scattering (DLS).

The second system studied was the formation of the $\varepsilon\text{-}[\text{Al}_{13}]$ cluster from an aqueous AlCl_3 solution. Two mutually exclusive growth mechanisms are proposed for this system in the literature. A gradual polymerization model involving an array of intermediate oligomers and an immediate self-assembly model in which the growth occurs from small $\text{Al}_1\text{-Al}_3$ species. The PDF method indicated that the immediate self-assembly model is correct. Experimental X-ray scattering data was exclusively used to describe and analyse the $\varepsilon\text{-}[\text{Al}_{13}]$ cluster growth with the aid of computational methods such as Principle Component Analysis.

UNIVERSITÉ BOURGOGNE FRANCHE-COMTÉ

DOCTORAL THESIS

**Preparation and speciation of p-block metal-oxo
clusters**

Author:

Daniel M. SZCZERBA

Supervisor:

Dr. Simon A. J. KIMBER
Prof. Bruno DOMENICHINI

October 6, 2022

UNIVERSITÉ BOURGOGNE FRANCHE-COMTÉ

Abstract

Laboratoire Interdisciplinaire Carnot de Bourgogne

Preparation and speciation of p-block metal-oxo clusters

by Daniel M. SZCZERBA

The main subject of this thesis is the use of Pair Distribution Function (PDF) analysis for solution phase speciation during metal-cluster growth. The PDF method allows the extraction of structural information from a sample in the form of an atom-atom distance distribution via Fourier transform of synchrotron X-ray scattering data. The growth mechanisms of two solution-based systems are analyzed in this thesis. Precursor materials are synthesized through a mechanochemical method that was developed and shown to be able to access a wide range of related systems.

Mechanochemical routes of synthesizing bismuth Active Pharmaceutical Ingredients (APIs) were investigated and optimised. Samples were analyzed using a range of techniques, including powder X-ray diffraction (PXRD), thermogravimetric analysis (TGA) and Raman spectroscopy. Various milling conditions were explored, resulting in optimised routes to bismuth (III) gallate and bismuth (III) citrate, as well as improving the literature syntheses of bismuth (III) di- and trisalicylate. All reactions used Bi_2O_3 and the corresponding organic acids. Significantly, a water dependent structural transformation of mechanochemically activated bismuth citrate was discovered, suggesting an origami-like folded structure that expands when filled with water to reveal a highly porous framework of the cubic crystal system.

The first solution-phase metal-oxo cluster studied was $[\text{Bi}_{38}\text{O}_{44}]$, a "magic-size" Keplerate-shaped molecule. Using bismuth (III) disalicylate as a precursor, it was found to grow in a multistep reaction with initial formation of the smaller $[\text{Bi}_9\text{O}_7]$ cluster. The growth occurs in multiple solvents, including acetone cyclohexanone, pentanone, methyl ethyl ketone and dimethylformamide. The growth mechanism is shown to be influenced by the solvent choice and water content. The PDF method observations were confirmed by spectroscopy and Dynamic Light Scattering (DLS).

The second system studied was the formation of the ϵ - $[\text{Al}_{13}]$ cluster from an aqueous AlCl_3 solution. Two mutually exclusive growth mechanisms are proposed for this system in the literature. A gradual polymerization model involving an array of intermediate oligomers and an immediate self-assembly model in which the growth occurs from small Al_1 - Al_3 species. The PDF method indicated that the immediate self-assembly model is correct. Experimental X-ray scattering data was exclusively used to describe and analyse the ϵ - $[\text{Al}_{13}]$ cluster growth with the aid of computational methods such as Principal Component Analysis.

Contents

1	Introduction	1
1.1	Plan of the dissertation and defined goals	1
1.2	Thesis introduction	2
1.3	Metal-oxo cluster growth in solution phase	2
1.3.1	Metal-oxo cluster species	2
1.3.2	Metal-oxo cluster growth mechanisms	3
1.3.3	Nucleation theories	4
1.4	Speciation methods	6
1.4.1	Commonly used speciation methods	6
1.4.2	PDF method as a speciation tool	8
1.5	Chosen metal-oxo clusters systems	10
1.5.1	Keplerate-shaped bismuth oxo-cluster – [Bi ₃₈ O ₄₄]	10
1.5.2	Mechanochemical precursor for the [Bi ₃₈ O ₄₄] cluster growth	11
1.5.3	Keggin-shaped aluminium oxo-cluster – [Al ₁₃ O ₄₀]	11
2	Materials and methods	13
2.1	Mechanosynthesis	13
2.2	X-Ray Diffraction	15
2.2.1	Atomic form factor	16
2.2.2	Single crystal diffraction	17
2.2.3	Powder X-ray diffraction	19
2.2.4	Rietveld method	21
2.3	Pair Distribution Function (PDF) of total scattering data	23
2.3.1	Synchrotron radiation	23
2.3.2	Synchrotrons and beamlines	25
2.3.3	High energy X-ray beamlines	28
2.3.4	Total scattering and PDF	28
2.3.5	PDF extraction and analysis software	30
2.4	Spectroscopy	32
2.4.1	UV-Vis	32
2.4.2	Raman	34
2.5	Dynamic Light Scattering (DLS)	36
2.6	Electron microscopy	37
3	Mechanochemical synthesis of bismuth APIs	39
3.1	Introduction	40
3.1.1	Bismuth compounds as medicine	40
3.1.2	Mechanochemical synthesis of APIs	40
3.1.3	The main objectives	41
3.2	Experimental section	43
3.2.1	Chemical compounds	43
3.2.2	Mechanochemical synthesis process	43
3.2.3	PXRD	44

3.2.4	Raman spectroscopy	44
3.2.5	Thermogravimetric analysis (TGA)	44
3.3	Bismuth salicylates – BiSal ₂ and BiSal ₃	45
3.3.1	Reaction conditions	45
3.3.2	Results	45
3.3.3	Discussion of the results	51
3.4	Bismuth (III) gallate – BiGall	52
3.4.1	Reaction conditions	52
3.4.2	Results	52
3.4.3	Discussion of the results	57
3.5	Bismuth citrate – BiCit	57
3.5.1	Reaction conditions	57
3.5.2	Results	58
3.5.3	Discussion of the results	67
3.6	Conclusions	68
3.6.1	Remaining questions	69
3.6.2	Author contribution	70
4	Growth and stability of bismuth-oxo clusters – spectroscopic methods	71
4.1	Introduction	71
4.1.1	The main objectives	72
4.2	Experimental section	72
4.2.1	Synthesis and chemicals	72
4.2.2	BiSal ₂ dissolution in DMF and Acetone	73
4.2.3	Controlled water environment protocol	73
4.2.4	UV-Vis spectroscopy	73
4.2.5	Raman spectroscopy	73
4.2.6	Dynamic light scattering (DLS)	74
4.2.7	PXRD	75
4.2.8	Crystallization and single crystal diffraction	75
4.2.9	TEM	75
4.3	Results	75
4.3.1	Crystallization	75
4.3.2	UV-Vis Spectroscopy	76
4.3.3	Raman spectroscopy	81
4.3.4	DLS	82
4.3.5	TEM	82
4.4	Discussion of the results	84
4.4.1	Growth mechanism	84
4.4.2	Spectroscopic discussion	85
4.4.3	DLS	87
4.5	Conclusions	87
4.5.1	Remaining questions	88
4.5.2	Author contribution	88
5	Growth and stability of bismuth-oxo clusters – total scattering	91
5.1	Introduction	92
5.1.1	The main objectives	95
5.2	Experimental section	95
5.2.1	Synthesis and chemicals	95
5.2.2	Synchrotron experiments	95

5.2.3	Data integration and PDF extraction	96
5.3	Results	99
5.3.1	PDF fingerprints	99
5.3.2	Bismuth (III) disalicylate – solid state	99
5.3.3	Bismuth (III) disalicylate – solution	101
5.4	Discussion of the results	108
5.4.1	Bismuth (III) disalicylate – solid state color change	108
5.4.2	[Bi ₃₈ O ₄₄] oxo-cluster solution-based growth	110
5.5	Conclusions	111
5.5.1	Remaining questions	112
5.5.2	Author contribution	112
6	Speciation of the [Al₁₃] oxo-cluster precursor solution	113
6.1	Introduction	114
6.1.1	The use of aluminium in water solution	114
6.1.2	Aluminium oxo-clusters and their structure	115
6.1.3	Chemistry of AlCl ₃ solution	118
6.1.4	PDF data analysis	120
6.1.5	Speciation using NMR and ESI-MS methods – disadvantages	121
6.1.6	The main objectives	122
6.2	Experimental section	122
6.2.1	Data integration and PDF extraction	122
6.2.2	PDF fitting	122
6.2.3	Oxo-cluster modeling based on symmetry - in Igor PRO	123
6.2.4	Principal Component Analysis (PCA)	124
6.3	Results	125
6.3.1	Generated models and fingerprinting	125
6.3.2	Hydrolysis series	130
6.3.3	AlCl ₃ water solution	130
6.3.4	[Al ₁₃] synthesis - early time hydrolysis	130
6.3.5	[Al ₁₃] synthesis - late time hydrolysis	145
6.3.6	PCA - overview of components	147
6.4	Discussion of the results	153
6.4.1	Early stage hydrolysis	153
6.4.2	Late stage hydrolysis	155
6.4.3	Criticism of the fits	157
6.5	Conclusions	157
6.5.1	Remaining questions	159
6.5.2	Author contribution	159
7	General discussion and final conclusions	161
7.1	Results of the project	161
7.1.1	Mechanochemical synthesis of APIs	161
7.1.2	PDF method analysis of oxo-cluster growth	164
7.2	The intended impact	167
7.3	Acknowledgements	169
	Bibliography	171

Chapter 1

Introduction

1.1 Plan of the dissertation and defined goals

The dissertation is divided into seven chapters. Chapter 1 is the *Introduction*, which outlines the scope of the project and the questions of interest. It is followed by Chapter 2, *Materials and Methods*, where the basis of the methods used in the project are described. The following chapters are dedicated to three topics of the research done throughout the project and are collectively referred to as "topical chapters". The topics are:

- Mechanochemical synthesis of bismuth APIs,
- Growth and stability of bismuth-oxo clusters,
- Speciation of the $[Al_{13}]$ oxo-cluster precursor solution.

Chapter 3 describes the mechanochemical synthesis of bismuth-organic compounds, classified as Active Pharmaceutical Ingredients (APIs). The scope of this chapter grew from a process of perfecting synthesis of bismuth (III) disalicylate, a precursor in $[Bi_{38}O_{44}]$ cluster synthesis. This chapter is presenting new, mechanochemical routes of synthesizing bismuth (III) gallate and bismuth citrate, compounds similar to bismuth (III) disalicylate. It is also improving the reproducibility of the mechanochemical synthesis of bismuth (III) di- and trisalicylate. Additionally, it shows evidence of a water-dependent, structural change in the structure of bismuth citrate.

Chapters 4 and 5 are dedicated to the $[Bi_{38}O_{44}]$ cluster growth in organic solvent from a mechanochemical precursor. Chapter 4 describes laboratory experiments and their conclusions, whereas Chapter 5 describes synchrotron experiments and concludes the topic. These two topical chapters aim to establish the structural development of a Keplerate-shaped cluster, $[Bi_{38}O_{44}]$, from mechanosynthesized bismuth (III) disalicylate, dissolved in various solvents. The influence of water content, access to the atmosphere and choice of solvent on the growth mechanism are also analyzed.

The last topical chapter, Chapter 6, is also concerned with a growth mechanism of a metal-oxo cluster. The system presented in this chapter is the Keggin-shaped ϵ - $[Al_{13}O_{40}]$ cluster growth from an aqueous $AlCl_3$ solution. This system has a long history of ambiguous growth mechanism interpretation [25]. Consequently, the goal of this chapter is to establish which of the two models, gradual polymerization or immediate self-assembly, is supported with experimental PDF evidence.

Each of the topical chapters ends with its conclusions, which are then correlated into a general overview in Chapter 7. This chapter discusses the importance and potential of mechanochemical synthesis and the use of PDF methods for the speciation of solution-based systems. The latter is discussed based on its use in the Chapters 4, 5 and 6, and also its capabilities for analysing the structural evolution of other clusters.

1.2 Thesis introduction

Solution-phase reactions are a source of countless chemical compounds and materials, being arguably the most important types of chemical reactions on a planet covered in liquid. From biological processes to inorganic syntheses, solution-phase reactions are all around us, happening both spontaneously or deliberately, *i.e.* oxidation of submerged metal or industrial synthesis of pharmaceuticals respectively. The methods for analysing solution-phase reactions are also numerous and measure a variety of qualities in the process. Some of these qualities can be measured directly in solution as the reaction proceeds, such as pH or temperature. But some information can be more difficult to gather *in-situ*. One such piece of information is the molecular structure of the chemical species involved in a reaction.

The goal of the thesis is to incorporate X-ray total scattering data analysis with Pair Distribution Function (PDF) into the speciation of chosen metal-oxo cluster growth mechanisms. The metal-oxo clusters form in various solution-based systems and can achieve relatively large sizes, usually in the 1–100 nm range and consisting of up to hundreds of metal atoms in their framework. The molecular structures of metal-oxo clusters often form intriguing, highly symmetric shapes [238]. Despite the large symmetric structure of metal-oxo clusters being interesting, as well as their synthesis and potential use often being studied, the structural steps governing their formation often remain unidentified. Intermediate, metastable species can thus be easily overlooked when relying solely on methods focused on analysing the stable, metal-oxo cluster product. At the same time, methods enabling the *in-situ* monitoring of a solution often rely on qualities of the chemical species present that are not direct results of their structure. The PDF method is thus an ideal candidate for speciation of the metal-oxo clusters growth due to the capability of obtaining direct structural information from the reaction solution [62].

In addition to the main PDF part of the project, mechanochemical routes of obtaining four different bismuth-organic compounds were discovered and followed with experimentation. This part aims towards obtaining pure compounds and finding structures of those unknown ones.

This thesis is a finalization of a three-year project, supported by EIPHI Graduate School (contract ANR-17-EURE-0002), and the "Investissements d'Avenir" program of ISITE-BFC project (contract ANR-15-IDEX-0003).

1.3 Metal-oxo cluster growth in solution phase

Metal-oxo clusters are a class of nanomaterials that can form from a vast array of metal atoms. The precursors for these clusters are usually simple, metal-organic materials dissolved in solution. After formation, the stable metal-oxo clusters can usually be crystallized, enabling detailed analysis of their solid state structure through diffraction methods [238].

1.3.1 Metal-oxo cluster species

The term *metal-oxo clusters* (or *metal oxide clusters*) refers to a polynuclear class of molecules, which are composed of metal and oxygen atoms. Unlike metallic nanoparticles, the exact molecular structure of these clusters is defined. Therefore, each metal-oxo cluster species is represented by a molecule composed of two or more metal atoms [4, 136]. The main part of the structure of a metal-oxo cluster is composed of a metal-oxygen framework, referred to as a *core*. The core is surrounded by ligands. The ligands may vary, depending on the solvent in which the cluster are synthesized, as well as the precursor material. Some types of metal-oxo clusters are separated from the general group under a specific name *Polyoxometalates*, for example, are metal-oxo clusters composed of d-block transition metals [116, 224].

Metal-oxo clusters have broad uses dependent on their structures and formation processes. They can be useful for their catalytic [144, 216], optical [245], and physical [27, 250] properties [149]. If functionalized, the properties of specific metal-oxo clusters can be modified to suit other purposes or enhance their non-functionalized potential [113, 172]. The utility of metal-oxo clusters is not exhausted and new uses are being constantly proposed and explored [140].

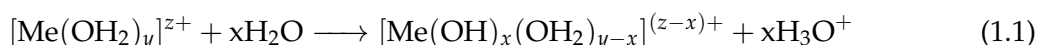
In this work, two p-block metal-oxo cluster systems are analyzed, bismuth-oxo cluster and aluminium-oxo cluster. The focus of the thesis, however, lies in analysing their growth mechanism rather than on their properties. As such, the potential uses of specific molecules are not as relevant for the purpose of this thesis as much as their molecular structures.

Collectively, metal-oxo clusters will be referred to as 'oxo-clusters' or simply 'clusters' in this dissertation.

1.3.2 Metal-oxo cluster growth mechanisms

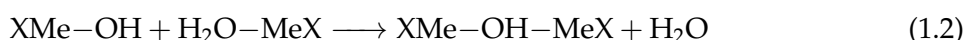
Chemical compounds containing metal atoms dissolved in solution can form metal-oxo clusters. The exact reactions are system specific and occur in the reaction environment. The general mechanisms, however, taking part in oxo-cluster growth can be described.

Hydrolysis is more often than not involved in metal-oxo cluster formation, especially in water environment [78, 138, 178]. It requires a water molecule to form an oxo-cluster precursor from the dissolving metal-bearing compound [86]. One of the processes that involves hydrolysis is deprotonation, a step important for creating precursors to metal-oxo clusters. The hydrolysis reaction can go as follows:



The x , y and z parameters express the amount of species and groups taking part in the reaction, and also their charges. Me is a metal atom coordinated with H_2O molecules. Through the hydrolysis reaction, it is deprotonated. This results in a more reactive form, that then can undergo other reactions.

In aqueous environments, metals can form coordination complexes after hydrolysis. This enables them to undergo condensation, a reaction where molecules are combined to form a larger product with expulsion of an additional smaller byproduct [86]. It can have a form of one of two mechanisms, first of them being the *olation* process [191]:



In this reaction Me is a metal atom and X is a non-reactive part of a monomer. The term monomer refers to the metal-bearing species that are condensed. The condensation reaction is in that regard similar to polymerization and can be referred to as such. In *olation*, the monomer is coordinated with a water molecule and OH group. The result is a dimer with a -OH- bridge connection in between the Me sites. An H_2O molecule is produced here as a byproduct. This reaction can be then repeated with a dimer and monomer, and so on, extending the polymer chain. Similarly to *olation*, an *oxolation* reaction may occur:



Oxolation results in a different type of bridge in the product. Here, monomers coordinated with OH groups produce an -O- oxygen bridge in between the metal atoms. It can be noticed, that for oxolation to occur, the monomers need to be more protonated than for *olation*. Oxygen bridges are typically found in metal-oxo cluster cores and form the central framework [86, 224].

1.3.3 Nucleation theories

As the focus of this dissertation is the growth mechanism of oxo-clusters, it is important to briefly discuss the theory behind nucleation. Although the term nucleation commonly refers to the beginning of the crystallization process, it is also used to describe the formation of nanoparticles and metal-oxo clusters in solution. This is appropriate when looking at nanoparticle and metal-oxo cluster growth as a formation of solid-state nanostructures dispersed in rather than molecules dissolved in a liquid. The beginnings of the theory behind nucleation, however, were concerned with crystallization. Crystallization can occur in cooling of melted systems, such as water decreasing its temperature below °C. It can also in a saturated solution, where crystals of the solute form.

Classical Nucleation Theory

In the core of understanding and studying crystallization lies the Classical Nucleation Theory, which had its beginnings in the first half of 20th century [17, 71, 214]. The formation of a new phase from a metastable system, such as crystallization, starts with a nucleation process. It can be understood as the formation of nucleation centers, that then expand in the crystal phase growth process. As a result, the stability of the entire system increases. The nucleation process, which is the assembly of a nucleus, changes the free energy of the system by ΔG . This value has two contributions:

$$\Delta G = G_S + G_V \quad (1.4)$$

where G_S represents the surface free energy, and G_V is the volume (bulk) free energy. The surface free energy has always a positive value and derives from the energy of the nucleus-liquid interface. For a spherical nucleus it can be described as:

$$G_S = 4\pi r^2 E_{int} \quad (1.5)$$

where E_{int} is the interfacial energy of a specific nucleus-liquid interface, and r is the radius of a nucleus. A similar equation describes the volume free energy:

$$G_V = \frac{4}{3}\pi r^3 \Delta G_V \quad (1.6)$$

where r once again is the radius of a nucleus. ΔG_V is a difference in between the free energies per unit volume of a solid and a liquid ($G_{solid} - G_{liquid}$), which is always a negative value.

The change in the total free energy of the system can be therefore described for a spherical nucleus as:

$$\Delta G = 4\pi r^2 G_{int} + \frac{4}{3}\pi r^3 \Delta G_V \quad (1.7)$$

This sum of surface (G_S) and volume (G_V) free energies of a nucleation system can be visualized in a form of an energy diagram (Fig. 1.1). This diagram reveals a new variable, energetic nucleation barrier (ΔG^*). It describes the energy that is required to grow the nuclei to its critical size (r^*). This nucleus size enables the growth of a crystallite. The surface and volume free energies are in equilibrium as long as ΔG has a positive value. The nucleus can both grow and dissolve in that state. However, once the nucleation barrier ΔG^* is reached, the energy of a system is free to decrease by increasing the nucleus size. When the ΔG reaches a negative value, the crystallization process starts and the volume free energy G_V decreases the total free energy of the system as the crystallites grow.

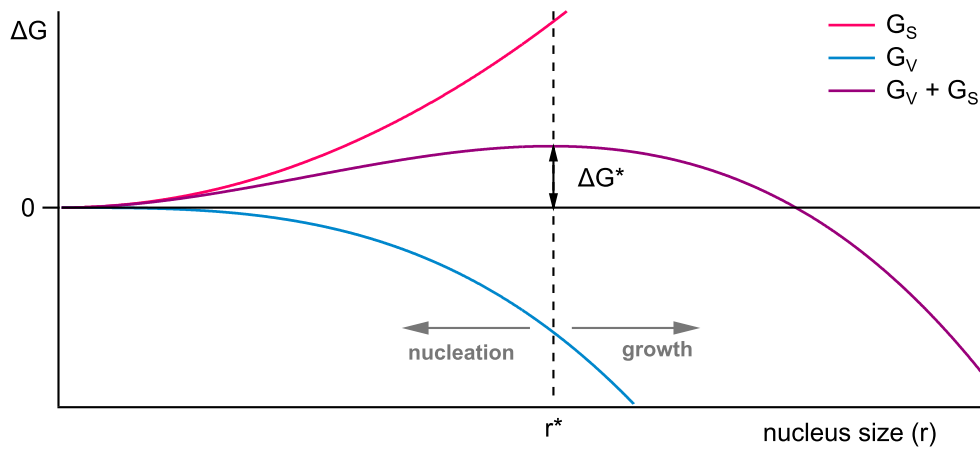


Figure 1.1: A Gibbs energy diagram of a nucleation process as a function of nucleus size. The diagram derives from the Classical Nucleation Theory. It shows how the total Gibbs energy, composed of surface free energy (G_S) and volume free energy (G_V) changes depending on the nucleus size. The ΔG^* is the nucleation barrier, an amount of energy that has to be provided to the system to start the growth process. The r^* is the minimum size of a nucleus that triggers the growth of a crystallite – which can be called a critical size of a nucleus [108].

The rate of the nucleation process differs accordingly to the crystallized species and other variables, in that the value of the nucleation barrier ΔG^* . From the Classical Nucleation Theory, a nucleation rate R can be given as:

$$R = N_S Z_j \exp \frac{-\Delta G^*}{k_B T} \quad (1.8)$$

where the nucleation barrier ΔG^* divided by the average thermal energy represented as the Boltzmann constant (k_B) times the absolute temperature (T). These values are enclosed in the exponential function. That function is further multiplied by the number of nucleation sites (N_S). This part of the equation expresses the probability of nucleation occurring in the system, which rises the nucleation rate when increased.

The other part of the equation is responsible for the probability of formed nuclei growing rather than dissolving. The variables here represent the rate of molecules attachment (j) and the Zeldovich factor Z , corresponding to the probability of a nucleus forming a new phase instead of reversing to the metastable state.

The Classical Nucleation Theory can help in understanding all nucleation processes when looking at achieving equilibrium in between the different energy contributions to the overall energy of the system. It does not, however, mathematically explain the nucleation of nanoparticles and metal-oxo clusters nor that of more complex crystallization processes [162]. The Classical Nucleation Theory does not account for factors like kinetics of chemical reactions, which is why modern nucleation theories are built and implemented.

Modern nucleation theories

Modern or non-classical nucleation theories are meant to describe mathematically complex nucleation systems. System-specific models are often built to account for the nuances of these systems. One of the most prominent elements is the addition of multiple nucleation stages,

which is not available in the Classical Nucleation Theory [108]. This addition helps for example to describe the intermediate, metastable stages of clusters growth [43, 119].

One modern approach to the theory behind nucleation is complementary to the Classical Nucleation Theory and expands on it. The Cahn-Hilliard theory describes the phase separation in a fluid. It is used to theoretically describe the assembly of nanoparticles and nucleation processes, with a distinction to the main phase, the separation layer and the second phase (crystallizing species). This particular theory proves phenomena observed in experiments, such as the decline of chemical species growth as a function of the power-law, to be connected to the concentration dependence [37, 177].

The modern approach to nucleation unveils how complex nucleation can be, though the Classical Nucleation Theory still can be used to predict in a reliable way nucleation of a simple system [108], such as crystallization from a melt in geological processes [107]. The modern approach broadens the possibility of modeling and predicting a process of nucleation for more complex cases [202] where nucleation takes multiple steps and depends on the kinetics of a condensation reaction. It also emphasises how cases like metal-oxo cluster growth can be difficult to understand fully without experimental analysis due to the dependence on factors like pH, metastable species concentration or the intermediate chemical reactions [43].

1.4 Speciation methods

The growth of large chemical species in solution phase, such as oxo-clusters, is likely not a single step reaction. It may contain an array of intermediate, metastable species that lead to the formation of a stable oxo-cluster. The term *speciation* in this dissertation refers to a process of elucidating structures of chemical species taking part in formation of a cluster [94].

1.4.1 Commonly used speciation methods

The unique aspect of the oxo-cluster growth in solution comes from the often unknown and presumably complex, intermediate stages. The structure of a final, stable oxo-cluster product is most often well-research and understood, in part, thanks to crystallization and diffraction methods such as single crystal diffraction. Crystallization is therefore one of the first speciation methods to reach for [94].

Crystallization

Attempts to crystallize new species of molecules are not infrequent among chemists and it is no different with oxo-clusters [10, 99, 145, 155, 219]. A starting point of analysing newly synthesized clusters is often crystallization from solution, targeted towards single-crystal diffraction. This method, if a good quality single-crystal can be obtained, results in a detailed, atomic structure of the crystallized species.

Apart from the advantage of directly obtaining a full structural model with one method, hard to overlook drawbacks exist for single crystal diffraction in the context of oxo-clusters growth. Good quality crystals can be difficult to obtain due to factors such as solubility or stability of a solution. Additionally, only the most stable species are likely to crystallize from solution, excluding the possibility of finding any metastable species unless the crystallization environment is tailored to stabilize these unknown metastable species [32, 127]. Moreover, the structure of a molecule in solid-state does not reflect its behavior and symmetry in solution, a quality important for understanding growth mechanisms.

Ultimately, diffraction methods are a wonderful source of structural information provided that the molecule of interest can be crystallized. This, however, may be challenging to do for some clusters and even impossible to do for metastable, intermediate species. As such, in order

to find and explain growth mechanisms for oxo-clusters, different speciation methods can be used [93].

Spectroscopic methods

Arguably, the most popular methods of characterizing species in solution phase are spectroscopic measurements [93, 132, 138, 150, 206]. The ability of a molecule to absorb energy of electromagnetic wave (UV–Vis, IR spectroscopy) [190, 233], or inelastically scatter it (Raman spectroscopy) [14, 92, 132, 167, 170] is a result of its atomic structure. Both absorption and emission spectroscopy are therefore used to analyse these effects in the context of molecular structures. In a similar fashion to techniques based on visible light radiation, X-ray absorption (XAS) [33, 133] and resonant inelastic X-ray Raman scattering (XRS) [112] utilize similar phenomena with the X-ray radiation.

Mass spectroscopy (MS) gives unique information about analyzed samples, by means of providing the mass-to-charge ratio (m/z) of charged particles. It can be useful in a vast array of speciation attempts [26, 50, 138, 141, 151, 209, 210, 246]. Analysis of a liquid sample is achieved by ionizing it, turning solvated molecules into ions in a gas phase. The m/z values are then assembled into mass spectra, presented in a function of intensity. The intensity corresponds to the amount of ions of a certain size detected by the method.

Nuclear magnetic resonance (NMR) spectroscopy can also be used for identification of chemical compounds, including oxo-clusters [1, 5, 6, 20, 40, 55, 67, 114, 138, 153]. This technique is sensitive to the magnetic field of atomic nuclei, which highly depend on how the atom is bound within the molecule. It is possible by measuring the response of a sample to a magnetic field, which results in NMR spectra. For some substances, such as organic molecules, the response of specific molecular structure is well-catalogued, providing a tool for the interpretation of unknown substances.

The obvious advantage of spectroscopic methods is their accessibility, both due to their relative popularity and the lack of required meaningful modification of solution-based samples. It is also an ever-developing and evolving field, offering more and more advanced methods. Spectroscopic techniques, however, are sensitive to very specific qualities, which are not always exhibited by the species (UV–Vis) or are obscured by the signal of the solvent (Raman). And lastly, some techniques do modify the sample – for example by ionizing it (MS). Regardless of what spectroscopic method is used and what specific disadvantage can be pointed out, the interpretation of results is an involved process. It requires putting together clues and forming hypotheses regarding an oxo-cluster growth mechanism rather than finding molecular structures of intermediate stages directly.

Electron microscopy

Electron microscopy is a fascinating tool, allowing users to take a look at chemical structures on subatomic and atomic scales in certain cases. Techniques such as scanning electron microscopy (SEM) and transmission electron microscopy (TEM) utilize the interaction of an electron beam with atoms. The images captured with them are most certainly providing structural information about the sample [7, 64, 128, 152].

It is, however, not a trivial task to prepare a microscopic sample, and the solution-based clusters are typically impossible to measure in solution. Electron microscopy requires conductive substrates under a sample or a layer of metal coating in order to prevent charging the sample itself during the data acquisition process. It is also essential for the electron beam to be contained under a vacuum. If an oxo-cluster sample is successfully deposited onto a substrate, the measurement is possible. Stability problems can arise, however, with molecules

being charged in the electron field, moving and even disintegrating. The resolution of microscopic images is largely dependent on the stability of given samples, the temperature and numerous instrumental factors [111].

Techniques not based on electrons, such as atomic force microscopy (AFM), use an electric field to scan the surface of a sample, resulting in its topographical map. They do not require conductive samples but their mode of scanning is most often dedicated to surfaces rather than deposited large molecules.

It is also important to point out that interpretation of microscopic results is not straightforward and artifacts are a common occurrence. Not only does microscopy require significant sample preparation but also is a very specialized method, requiring advanced equipment and expertise in the field. Similar to single-crystal diffraction, it does not provide direct insight into the molecular structures in the solution phase.

Other methods

There are also other methods, which can to a certain extent be used for speciation of oxo-clusters in solution. Potentiometric methods are used for characterising oxo-cluster solutions in terms of their charge [93, 208]. The Dynamic Light Scattering (DLS) is sensitive to the size of particles present in solution, but not necessarily to their atomic structure, which limits its use to an additional tool in discovering growth mechanisms [24]. The DLS is similar to more precise and demanding Small-Angle X-Ray scattering (SAXS), which although not sensitive to the intramolecular structure, provides intermolecular structural information in 1–100 nm range. SAXS is also utilized as a speciation method for oxo-clusters [150].

Computational methods are widely utilized for simulating theoretical particles in artificial environment, and compare their stability in order to establish the most likely theoretical model of a growth mechanism [16, 39, 161, 215]. However, computational power limitations make it impractical and even impossible to simulate large clusters in big box models, surrounded by solvent.

Assumptions forced by the classical speciation

Despite the number of accessible speciation methods, it is generally agreed that their use requires certain assumptions and educated guesses to either provide the necessary information to the computational system, or to interpret experimental data [93, 161]. Because of that, the mechanism of oxo-clusters growth in a solution is often rather theorized than understood. Solution-based systems are a dynamic environment. This results in that observing the intermediate species as they assemble a more stable product is often impossible *in-situ*.

It has to be stressed the use of indirect methods and chemical understanding of a system often allows to form a plausible growth mechanism, which can be further proved or disproved with unrelated methods. However, it is far from a straightforward process. Implementing a way of monitoring the growth with a method sensitive directly to the intramolecular atomic structure, can be a complementary step for any speciation process.

1.4.2 PDF method as a speciation tool

As already mentioned, the diffraction methods are reserved for long-range symmetry objects in the solid-state. They also provide direct information about the atomic structure. This type of information is unobtainable with traditional, speciation methods. Information about atomic structure of molecules in liquid can be, however, extracted from scattering measurements [94].

The *total scattering* information can be transformed from reciprocal space into the direct space with the Fourier transform. This procedure results in *Pair Distribution Function of total*

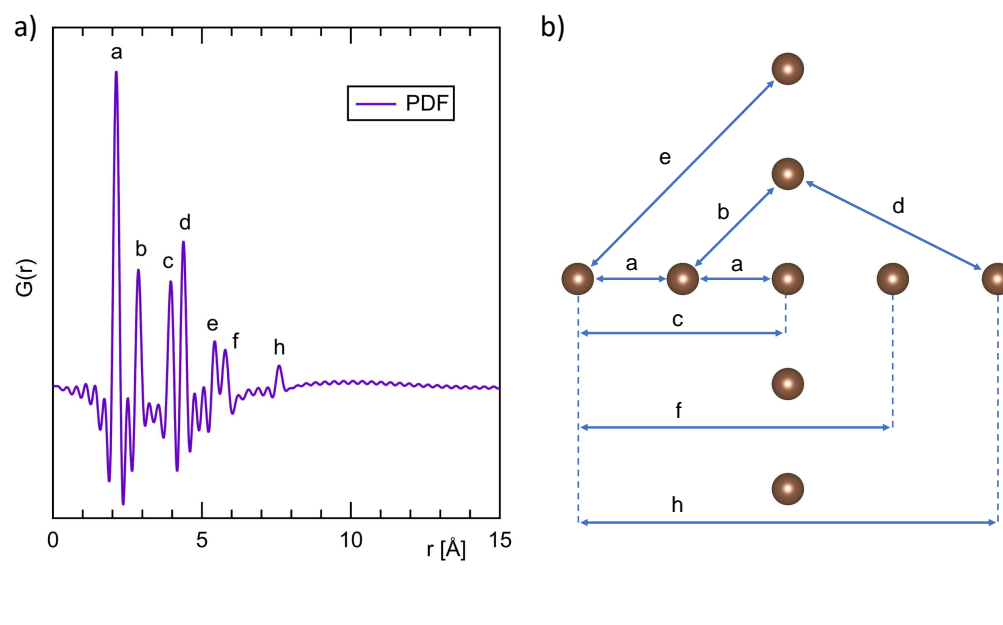


Figure 1.2: **a)** A PDF calculated for a grouping of nine objects in 2D space. Each peak (a-h) represents the object-object distance present in the grouping. The PDF was calculated as if the objects were carbon atoms and the PDF was based on X-ray scattering data. **b)** A visualisation of the nine objects grouping. All of the object-object distances (a-h) are described in the model. Even a relatively simple object grouping can have a multitude of varying lengths of the object-object distances.

scattering data – referred to as ‘PDF method’ or simply ‘PDF’ throughout this dissertation. This mathematical operation extracts intramolecular atom-atom distances, and to a lesser extent intermolecular correlation. It is therefore providing structural information about a sample, even if it is not crystalline. Thanks to that, the PDF method can be used even for analysis of a solution-phase system such as oxo-cluster growth [66, 97, 102].

The PDF can be calculated for any kind of object, described in space. As an example, PDF was calculated for a group of nine objects (Fig. 1.2). These objects were treated like carbon atoms, and the calculated PDF as if it was measured using X-ray scattering. The result of that is a function including peaks representing all of the object-object distances present in the grouping of the objects. Calculating a PDF of a free molecule can be performed in the same way. Calculating a PDF for a crystalline object is also possible, but has to be extended so that the symmetry of the crystal lattice is included. Calculating PDF based on total scattering data of a sample and comparing it to PDF of a model or refining a modelled structure against the data, are ways of using the PDF method for qualitative analysis of chemical samples.

PDF method use

The PDF method is not a novelty, since for the last 20 years it increased in popularity among a broader audience [97]. Moreover, the very first PDF was calculated from X-ray scattering data in 1930 [53], and was based on even earlier work [97]! And yet, when talking with scientists from outside of X-ray or neutron diffraction and scattering circle, it seems that the PDF method escapes notice of some. One historical reason is that the diffraction methods were enough to establish a structure of a compound, provided a crystalline sample was available. Another reason was the lack of computing power that is accessible today. And therefore, PDF was just used as an aid in the most difficult crystallographical cases [70].

Despite its historical lack of popularity, PDF is a powerful tool for analysing a vast range of materials, especially if they are "crystallographically challenged" [29, 62]. This umbrella term fits amorphous solids and non-crystalline powders, along with structures present in liquid phase. The latter includes nanoparticles and also metal-oxo clusters [97, 142]. Apart from the ability to deal with non-crystalline and liquid samples, a sought after trait is the direct (real) space character of PDF data [47]. The PDF method has gained significant traction in recent decades, starting from early 1990s [28] and only increasing with time [115, 130, 165]. This is due to the growing accessibility of large scale facilities, essential for efficient PDF dedicated measurements – synchrotron and neutron sources. It is also thanks to the common access to the computational power required for PDF calculations. This trend will most likely escalate, due to large facilities accommodating total scattering experiments better, while modernizing their beamlines and radiation sources [213].

The modern increase in interest in PDF method sees a variety of applications [94, 97], with experiments done both *in-situ* and statically. It is often used for materials chemistry purposes [45, 239]. Studies of processes like catalysis [48], structural studies of amorphous materials [201], and even studies of the structures formed by solvent surrounding nanoparticles [248] can be performed with PDF method.

1.5 Chosen metal-oxo clusters systems

In this project, two metal-oxo cluster growth mechanisms were analyzed – $[\text{Bi}_{38}\text{O}_{44}]$ and ϵ - $[\text{Al}_{13}]$. The first similarity is that the metal atoms of both species come from the p-block. Second shared quality is that both of them have a highly symmetric structure, formed from specific amounts of atoms, which makes them "magic-size" clusters.

Magic-size clusters

Nanoclusters stable enough to be crystallized are often found to be "magic-size". This term is associated with containing closed, geometric shells of atoms or valence electrons [79, 126, 148]. An interesting aspect of "magic-size" clusters is that although they are very stable molecules, they are labile enough to take part in further reactions and growth. One such example, presented in Chapter 6, is $[\text{Al}_{13}]$ Kegging-shaped molecule, which undergoes isomerization, and even forms a larger molecule, the $[\text{Al}_{30}]$ cluster. This quality of "magic-size" clusters is most likely related to their structure in solution and its dynamics.

The term "magic-size" is not exclusive to oxo-clusters, however. Experiments done on gold (Ag) [96] and cadmium sulphide (CdS) [229] "magic-size" nanoparticles show low energetic barriers of their re-organisation, such as isomerisation and polymorphisation.

1.5.1 Keplerate-shaped bismuth oxo-cluster – $[\text{Bi}_{38}\text{O}_{44}]$

The "magic-sized" Keplerate-shaped [41] $[\text{Bi}_{38}\text{O}_{44}]$ cluster is the first analyzed species. Synthesis of various sizes bismuth oxo-clusters is a well-researched, yet complex and still not fully understood process, leaving plenty of space for discoveries and improvement of the current understanding of the subject. It is also an opportunity for building a library of varying in size clusters from literature structures, which can be used as a fingerprinting tool for PDF analysis.

The analysis of this system is presented in Chapter 4 with spectroscopic tools, and in Chapter 5 continues with the PDF method. The goal is speciation of the $[\text{Bi}_{38}\text{O}_{44}]$ cluster growth mechanism. Additionally, analysing influence of factors such as choice of solvent and influence of water on the cluster growth.

1.5.2 Mechanochemical precursor for the $[\text{Bi}_{38}\text{O}_{44}]$ cluster growth

The precursor to the $[\text{Bi}_{38}\text{O}_{44}]$ cluster synthesis used in this work is mechanochemical bismuth (III) disalicylate [9]. This chemical compound is a part of a wider group of Active Pharmaceutical Ingredients (APIs), such as bismuth citrate and bismuth (III) gallate.

Bismuth (III) disalicylate was synthesized mechanochemically for the purpose of this work. Because this route of synthesizing a chemical compound rendered a fascinating and complex subject, the mechanochemical experiments were extended to other bismuth APIs. Thanks to that, mechanochemical routes of synthesizing bismuth citrate and bismuth (III) gallate alongside improvements to the bismuth (III) disalicylate and trisalicylate syntheses are described in Chapter 3.

Mechanosynthesis is thought to be a great and environmentally friendly way of synthesizing medical compounds [200]. Incorporating mechanosynthesis as a means of synthesizing the precursor is therefore following an interesting, developing method. Moreover, abandoning the use of bulk solvent and also the long-time heating and mixing processes, lowers the environmental impact of a synthesis process significantly in comparison to a bulk solvent reaction.

1.5.3 Keggin-shaped aluminium oxo-cluster – $[\text{Al}_{13}\text{O}_{40}]$

The Keggin-shaped $[\text{Al}_{13}\text{O}_{40}]$ cluster grows from AlCl_3 water solution. The growth mechanism of this cluster have been extensively studied with many methods, especially nuclear magnetic resonance NMR and mass spectroscopy MS [210, 211], but Raman spectroscopy [176] or ferron assay method [55, 158, 185]. Despite the extensive research [25], at the moment of writing this dissertation there are two competing growth mechanisms proposed for this system. This case is explored in Chapter 6, with the goal of confirming one of the growth mechanisms. The structural data provided by PDF analysis is an ideal candidate for adding information to the discussion about the growth mechanism of the $[\text{Al}_{13}\text{O}_{40}]$ cluster, due to the unique structural information it provides.

Chapter 2

Materials and methods

Various analytical methods and instruments were used in the work presented in the topical chapters of this dissertation. Below, the basis of these methods are described.

2.1 Mechanochemistry

The synthesis of metal-organic chemical compounds for the industrial purposes is predominately performed in a liquid state. The precursors are dissolved in their solvents to the ionic forms. Then the final product is formed in cycles of precipitation and repeated dissolution. However, there is an alternative to this complex, multi-step, solvent-based kind of reaction. The mechanochemical synthesis can result in the same product, in a solid-state reaction of a simple precursor mixture induced through grinding [57, 72, 218]. This, apart from saving time, eliminates the volume of contaminated solvents, making mechanochemistry additionally interesting as a 'green' solution for synthesis of chemical compounds [194].

Although many metal-organic compounds have been synthesized mechanochemically, the method is relatively novel and yet to be widely recognized for its potential in the chemical industry [34]. The potential lies also in the pharmaceutical industry, as it has been shown that clean mechanochemical synthesis of many Active Pharmaceutical Ingredients (APIs) is possible [200]. This term describes chemical compound that are used as active ingredients in medicine.

The mechanochemical process

The premise of mechanochemistry is quite simple. At the most basic, mechanochemistry is just grinding two chemical compounds expected to react together [222]. It is usually aimed to start with a stoichiometric ratio when trying to synthesize a known compound. This is a reasonable starting point aiming to reduce the amount of unreacted precursor material, therefore increasing the purity of the potential product. Sometimes the dry grinding is not enough. In those cases, more complex methods can be considered. The *Liquid-Assisted Grinding* method (LAG) involves the addition of a small volume of a liquid to the reaction mixture. The solubility of the reacting compounds is not required, as the liquid serves another purpose. It is meant to enhance the grinding process, increasing the contact surface in between the grains. Other theories suggest that it is a formation of a semi-liquidation state of the reaction mixture, similar to a slurry, that enables ions to form and react with each other when using the LAG method. Another type of synthesis adds catalyst into the LAG method. It is called the *Ion- Liquid-Assisted Grinding* method (ILAG). Apart from a liquid, it involves the use of a small amount of inorganic salt. Its addition is meant to increase the mobility of the reacting species, and therefore catalysing the reaction. The LAG and ILAG methods can increase the reaction rate, lower the required activation energy, or in some cases be essential for the reaction to occur at all [57, 72].

There are many types of grinding mills used for mechanochemistry, most of which require milling mediums such as steel balls. The milling medium is placed in a cylindrical vessel, along with the reaction mixture. The milling can be performed by rotating the cylinder around

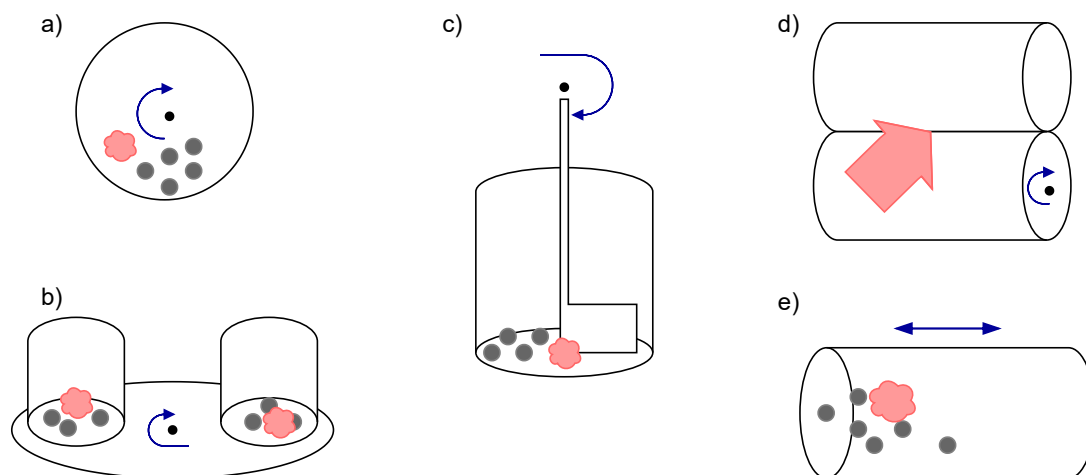


Figure 2.1: A diagram illustrating chosen types of the mills used in mechanochemistry. The blue arrows represent the direction of rotation around an axis (black dot), or the directions of vibration. The pink object represents a precursor mixture. Most types of mechanochemical milling use a grinding medium, such as grinding balls (grey circles). **a)** The ball mill is a horizontally placed cylinder, rotating around a centrally placed horizontal axis. **b)** A planetary mill is a vertically placed cylinder, placed on an edge of a rotating plate. **c)** The stirring ball mill is a cylinder equipped with a rotating stirrer. **d)** The rolling mill grinds by passing the precursor mixture through rotating rollers, which resemble a mangle. **e)** The vibrational mill is a horizontally placed cylinder, vibrating at a designated amplitude.

its center (ball milling) or spinning it on a horizontal, rotating plate (planetary mill). Other means are placing a stirring device inside the cylinder (stirring ball mill) or milling without balls, bypassing reaction mixture through rollers (rolling mill). The type of milling used in this project is based on vibrating a cylinder at a high frequency (vibrational mill) [15].

The vibrational milling process is performed in cylinders called *milling jars*, with the use of grinding balls. The balls can be chosen from different sizes and weights, and function as the grinding medium (Fig. 2.2). Depending on the qualities of reactants, jars and balls from various materials can be used – ceramics, metal and even transparent polymers like polymethyl methacrylate (PMMA). The last one allows for *in-situ* monitoring of a reaction with spectroscopic methods such as Raman spectroscopy [84, 104] or even X-ray diffraction [74, 106]. In this project, stainless steel jars with stainless steel balls were used. A mill for mechanochemical synthesis has the functions of controlling the frequency and time of grinding. The required milling time varies depending on a reaction, similarly to the frequency. It is even possible to obtain different reactions products depending on the time of grinding. The frequency is one of the means of controlling the kinetic energy of the system, which is one of the most influential parameters. The energy is also dependent on the number and mass of used balls, as well as the size of the milling jar. Some reactions occur only if a certain threshold of energy of the impact is achieved [57, 72].

Certain modifications can be made to all of the mechanochemical grinding processes in order to influence the reaction. One of them is heating the jars before a reaction or while the reaction is ongoing. This does increase the mobility of the species present in the system, increases the energy of molecules. Therefore, the heat decreases the energy required to break the bonds in the precursor, and facilitates formation of a new product [57, 72, 95].



Figure 2.2: A photograph of the milling jars and the stainless steel balls used in the project. During the synthesis, the reaction mixture is placed inside one half of the jar, and followed by the milling balls. Then, the jar is sealed with the other half and the rubber seal. The assembled jars are placed vertically in between the clamps of the mill, before the milling starts.

Instrument

The mechanochemical grinding was done using the *InSolido Technologies* vibration-type mill, number IST500, in stainless steel jars (10 and 25 ml) paired with stainless steel balls (7 and 10 mm).

2.2 X-Ray Diffraction

In the year 1912 Max von Laue discovered the diffraction of X-ray radiation on crystals. A year later, William Henry and William Lawrence Bragg successfully calculated the structures of diamond and other minerals. They did it using the law they mathematically described (2.1). Both achievements were awarded the Nobel prize in physics, respectably in the years 1913 and 1915. Although it has been over a century, the modern X-ray diffraction methods did not take off until the popularization of computer systems. Without them, calculating simple structures was a tedious task, attempted rarely and employing dozens of people running their calculations by hand, for months at a time. This was done only to achieve something, that computers today can do in a matters of minutes, sometimes seconds. Thanks to this advancement, crystallography moved from analysing simple structures of minerals to complex organic structures, such as crystalline proteins. The tremendous potential of X-ray diffraction is nowadays even used for entire biological structures, as found in living organisms [32, 127].

X-Ray diffraction methods are based on the interaction of electromagnetic wave in the X-ray range ($0.001 \text{ nm} < \lambda < 10 \text{ nm}$) with atoms and molecules. The radiation scatters when in contact with an electron cloud as a result of an electromagnetic interaction with the electron orbitals. If the scattering matter is crystalline, the scattering becomes diffraction. Most of the radiation scattered on a crystalline material interacts with itself, causing destructive interference. This

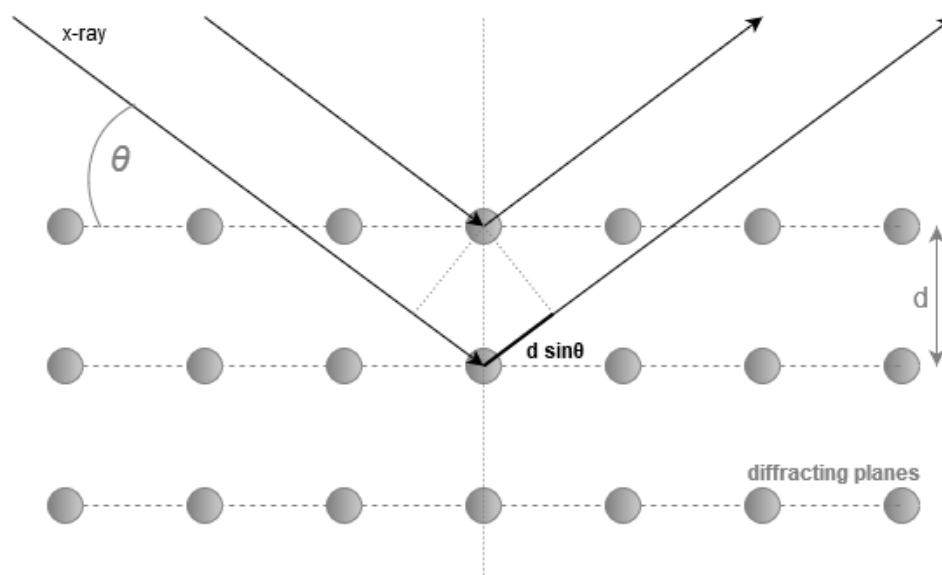


Figure 2.3: A schematic representation of Bragg's Law. The diffraction planes formed by the sites in a unit cell cause the X-ray radiation to scatter in specific directions. The distance in between diffraction planes is called d -spacing. The incident angle θ of a reflection is correlated with its value.

type of interference quenches the scattered radiation. However, constructive interference has an opposite effect. It is caused by scattering on the crystal planes, which adds up the scattered radiation and creates a reflection. The reflection occurs in specific directions, dictated by the symmetry and molecules packing in a single crystal. This phenomenon can be described with Bragg's Law:

$$2d \sin \theta = \lambda n \quad (2.1)$$

where d is the spacing between diffraction planes, θ stands for the incident angle, n is any whole number and λ the wavelength. The way it works can be presented on a scheme, where points represent a repeatable unit of a crystal lattice (Fig. 2.3).

The phenomenon of X-ray diffraction is used in many techniques, unified in the field of *X-ray crystallography*. It offers a variety of specialized techniques and equipment, allowing for very specific sample environments. High pressure measurements, temperature conditioned measurements, magnetism-related setups, etc. Together with neutron and electron diffraction methods, X-ray crystallography is one of the most important tools in structural chemistry research [59, 82, 222, 227].

2.2.1 Atomic form factor

The intensity of scattering on a specific elements depends on the *atomic form factor*. Its value depends on the type of scattered radiation – it is different for neutron, X-ray and electron diffraction. It is also dependent on the direction of scattering. The maximum intensity of scattering is reached at a small angle, and decreases as the angle rises. Generally, the atomic form factor is a Fourier transform of the spacial density distribution of a scattering object. In the case of the X-ray form factor, it is the electron cloud. The X-ray form factor can be calculated, and it is described with the assumption that the electron cloud surrounding the atom is spherical and homogeneous:

Table 2.1: Parameters a_i , b_i , and c of chosen atoms for $i = 4$. Atoms relevant to this project were picked for the table, and the values come from the International Tables for Crystallography, volume C [60].

	Al	Bi	O	C	H
a_1	6.4202	33.3689	3.0485	2.3100	0.489918
b_1	3.0387	0.7040	13.2771	20.8439	20.6593
a_2	1.9002	12.9510	2.2868	1.0200	0.262003
b_2	0.7426	2.9238	5.7011	10.2075	7.74039
a_3	1.5936	16.5877	1.5463	1.5886	0.196767
b_3	31.5472	8.7937	0.3239	0.5687	49.5519
a_4	1.9646	6.4692	0.8670	0.8650	0.049879
b_4	85.0886	48.0093	32.9089	51.6512	2.20159
c	1.1151	13.5782	0.2508	0.2156	0.001305

$$f(Q) = \int \rho(r) e^{iQr} d^3r \quad (2.2)$$

The $\rho(r)$ function is the electron density, and Q represents the momentum transfer. The r value is the distance from the center of an atom to the edge of the spatial density. For scattering of other than X-ray radiation, the $\rho(r)$ would be substituted as a spatial density distribution of the scattering object.

For the calculation of a X-ray form factor, a Gaussian approximation can be used. It is a sum of Gaussian functions, given as:

$$f(q) = \sum_{i=1}^4 a_i e^{-b_i(\sin\theta/\lambda)^2} + c \quad (2.3)$$

The θ is the incident angle of reflection, and λ represents the wavelength of X-ray radiation in Å. The a , b and c parameters are described for specific atoms in all of their electron states. The parameters of atoms relevant to this dissertation can be found in Tab. 2.1, for $i = 4$.

Because the X-ray radiation interacts with electrons, the X-ray form factor is proportional to the amount of electrons in an atom. It can be clearly illustrated on a graph, where the X-ray form factors are calculated in a function of $\sin(\theta)/\lambda$ (Fig. 2.4). This is important information, when looking at X-ray diffraction of molecules composed of a variety of atoms. The intensity of reflections associated with heavy atoms positions will be higher than for the light atoms. If the difference in mass of the atoms is significant, the heavy atom positions can even obscure the signal of the light atoms. Hydrogen positions are often difficult to find due to its low electron density, for example [32].

2.2.2 Single crystal diffraction

A type of diffraction method providing the most comprehensive structural information about a sample, is single crystal diffraction. The use of a single crystal has one, significant advantage. All of the reflections created by constructive interference of diffracted X-ray radiation are associated with a family of diffracting (lattice) planes. A family of planes is created by the same site, that is repeated in crystal lattice according to its symmetry. Because a single crystal is highly ordered, a single family of planes can only produce reflections at fixed angles. Because of that, rotating a crystal while exposing to the X-ray beam enables registering a three-dimensional map of reflections in reciprocal space. This map can then be used to find the direct (real) space structure of molecules present in a unit cell. This quality of single crystals popularised single crystal-diffraction method, which today is an essential tool for describing chemical structures.

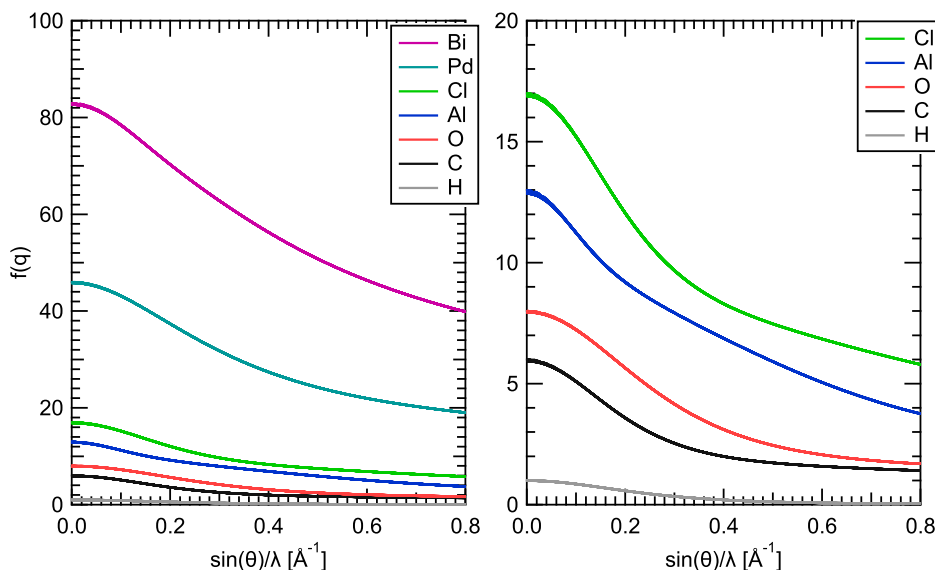


Figure 2.4: The calculated X-ray form factors of chosen elements, relevant to the project. The calculation was done using the variables in Table 2.1 and equation 2.3, for $\lambda = 1 \text{ \AA}$. The graph on the left clearly illustrates how much stronger bismuth scatters X-ray radiation, than elements like oxygen or carbon. The heavier the atom, and by default the larger its amount of electrons, the stronger it scatters the X-ray radiation. The graph on the right is expanded in order to clearly show the X-ray form factors of the weaker scattering elements.

A single crystal diffraction measurement is generally performed in a similar way, regardless of the type of a crystal. A monochromatic, coherent incident beam of X-ray radiation travelling through a single crystal, splits partially into mentioned before *reflections*. The crystal is rotating in the beam while reflections are gathered onto a 2D detector, and saved with their relation to the position of the crystal. This creates a three-dimensional map of reflections representing the *reciprocal space*. This connects the intensities of reflections with their positions described with *Miller indexes*: h ; k ; and l . The intensity $I(b)$ is in a direct relation with the electron density $\rho(b)$, and is the representation of a real-space electron density distribution, and by extension – the distribution of atom positions in a unit cell of a crystal. A connection bridge in between them is the structure factor F_{hkl} . The relation presents itself as follows:

$$I(b) \Rightarrow |F_{hkl}|^2 \leftarrow F_{hkl} \Rightarrow \rho(b) \quad (2.4)$$

This means that it is mathematically trivial to transform the electron density to structure factor, and then the square modulus of it ($|F_{hkl}|^2$) to the intensity. What is not trivial is going the opposite way, from the intensity to the electron density. This is the case for solving single crystal structures using the diffraction method. The step of transforming $|F_{hkl}|^2$ back into F_{hkl} faces the *phase problem*. The information about the phase is lost, therefore finding the atomic arrangement within the unit cell requires solving the phase problem. This is where the calculation power of computer systems comes in, allowing to step by step find the proper crystal system, point group and so on, using the characteristic for a specific symmetry intensity extinctions. It further allows for a map of electron density of a unit cell to be created. From that point, the electron density map can be matched to specific atoms and then molecules, typically using R-factors to assess the goodness of fit [32, 127].

Depending on the chemical species it consists of and the level of symmetry, a sample of

a certain quality is necessary to obtain good quality data. The presence of heavy atoms in molecules, high-level symmetry, and especially centrosymmetry, make the analysis and the calculations much easier. Difficulties obtaining a large enough crystal and significant amount of crystal lattice defects on the other hand, make the process harder and even impossible.

Single crystal diffraction measurement

A single crystal is placed on a glass rod with a help of a fixed medium. That can be either glue or grease. An important part is the size of a crystal, which should allow it to fit into the X-ray beam. The rod is then mounted on a goniometer, which allows the crystal to rotate during a measurement. Before the crystal is exposed to the beam, it has to be centered. Centring is usually done with a help of a CCD camera, by rotating the crystal in place so that in all the positions it is in the center of the beam.

A X-ray lamp is usually used as a source. The light passes through the monochromator and collimator to form a monochromatic beam. It further passes through a crystal and then most of it is caught by a beamstop. The part that is not absorbed by the crystal, but is instead diffracted, travels beyond the beamstop, where a 2D detector is placed.

Before an actual measurement starts, a couple of photos are usually taken to determine whether or not it is a monocrystal. If so, then a test measurement helps to establish a proper time for each picture, allowing to minimize the time of measurement and potential damage to the crystal while keeping the intensity of reflections high enough to obtain good quality data. As soon as that is established, a measurement can be started. The detector gathers information about reflections position and intensity, while the position of the goniometer adds information about the angle. This is then further analyzed by proper software.

2.2.3 Powder X-ray diffraction

The Powder X-Ray Diffraction (PXRD) is a method using the X-ray diffraction phenomenon, similar to single-crystal diffraction. It is widely used for the characterization of crystalline powders, as well as finding the structure of unknown, difficult to crystallize species. The major difference in regard to single crystal diffraction is the use of polycrystalline powders as the sample in the PXRD method [46].

A homogeneous powder material, consisting of a multitude of small single crystals is the most basic type of a PXRD sample. The size of crystallites typically should not be smaller than 1–10 μm . The reflections generated by a monocrystal appear on a diffractometer at fixed positions, dependent on the angle at which the crystal is illuminated. Each small monocrystal of the polycrystalline material is positioned in a different direction, and because of that all the possible reflections of a single crystal are generated in a polycrystalline material simultaneously. From Bragg's Law, each family of diffracting planes can only produce reflections at fixed angles. Because of that, the sum of all possible reflections in a family of planes produces results in the formation of the *diffraction cones* (Fig. 2.5). If a 2D detector is gathering the X-ray diffraction, the intensity forms *diffraction rings* [32, 127].

The PXRD data is usually presented as a graph of intensity in a function of angle, which from Bragg's law is expressed as 2θ (Fig. 2.6). It is commonly referred to as a *diffraction pattern*. In most laboratory diffractometers the detector for PXRD is one dimensional and moves as a function of angle, transforming the counts of photons right into the PXRD pattern directly. In synchrotrons the PXRD measurements are usually different, due to the use of 2D detectors. This results in a 2D image that then has to be transformed into a PXRD pattern with the help of dedicated software and callibrant with a well-known PXRD pattern.

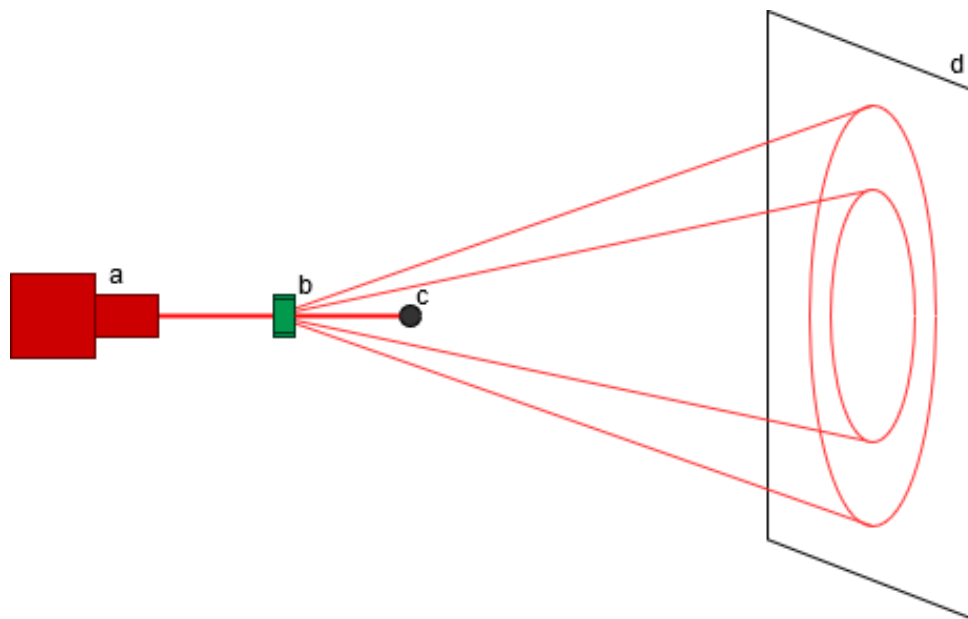


Figure 2.5: A schematic representation of diffraction cones generation. An initial X-ray beam is produced by the source (a) and directed through a polycrystalline sample (b), to then be caught by a beamstop (c). Some of the initial beam is diffracted in a form of the Debye-Scherrer diffraction cones. When gathered by a 2D detector, they form the diffraction rings that are associated with specific a family of diffracting planes.

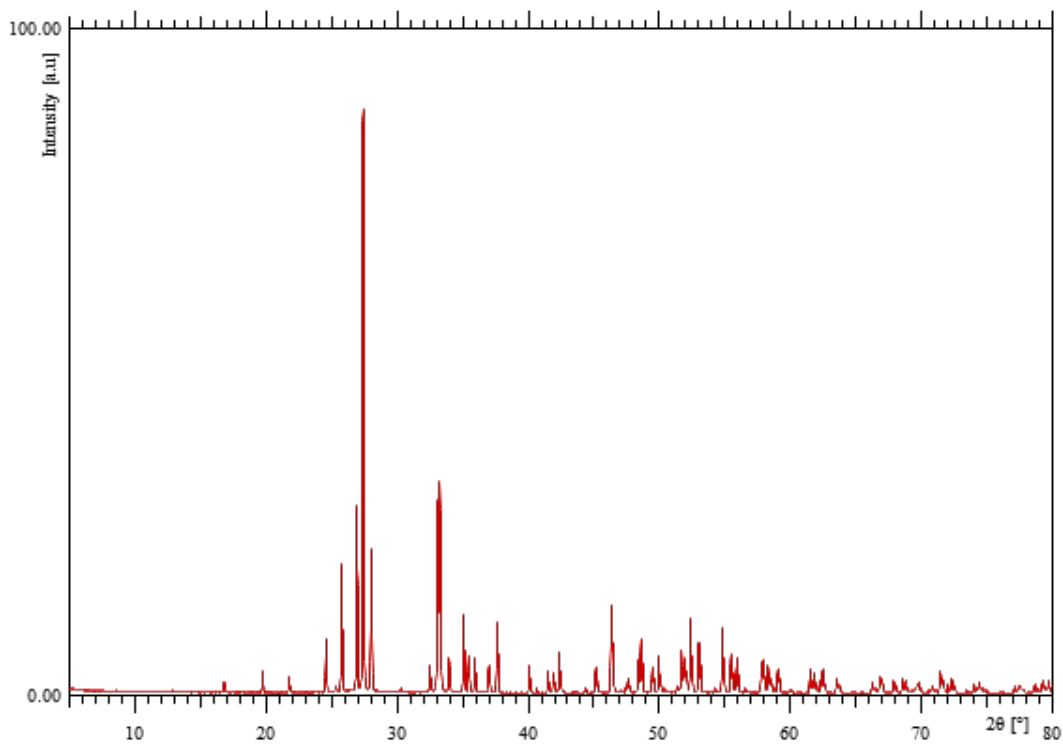


Figure 2.6: A PXRD pattern of Bi₂O₃. The diffraction pattern was gathered with a moving 1D detector, registering the intensity from smallest to largest 2θ value.

In terms of the sample preparation, the requirements are not as strict as with the single-crystal method. As mentioned before, the most classic example of a sample for PXRD measurement is polycrystalline material. However, an amorphous compound does hold structural information as well, provided the measurement is done in specific conditions, allowing to perform pair distribution function calculations (PDF). This process is described in the Pair Distribution Function section (2.3.4). A metal plate, a paste with crystalline content and other kinds of samples can also be measured using PXRD [32, 127].

The analysis of PXRD patterns can vary in the level of difficulty. Some samples can be simply compared with a database and checked for similar peak positions or even full matched. More advanced would be a Rietveld refinement method, which can be used on samples of unknown compounds. It allows to find the structure, provided that some initial information about the chemical compounds is provided – such as composition. This initial information can also be step by step discovered before the Rietveld refinement, using steps like peak fitting and indexing. As the PXRD and Rietveld refinement was extensively used in this work, it is described in detail in the next section.

2.2.4 Rietveld method

The Rietveld refinement method is one of the most popular techniques for PXRD data analysis [135]. At its core, it is based on fitting a model of a structure, or structures in the case of a multiple-phase system, to a previously measured powder diffraction data. The mathematical basis of that is the least-squares fit of a model to the dataset where the goal is minimizing quantity S_y represented as a sum of the data points:

$$S_y = \sum_i \frac{(y_i - y_{ei})^2}{y_i} \quad (2.5)$$

where y_i is the observed intensity and the y_{ei} is the calculated intensity at the i th step.

A PXRD pattern is a collection of reflection peaks, each with their position and shape, and an integrated area that is proportional to the intensity I_{hkl} , where h , k and l each represent the Miller index of a given Bragg's reflection. The I_{hkl} intensity is proportional to the square of the absolute value of structure factor, $|F_{hkl}|^2$. The value of intensity y_i chosen in a point i consists usually of the contributions from multiple Bragg peaks. The calculated intensity y_{ei} is based therefore on the structure factor values, calculated from the model of a structure by summation of neighbouring Bragg reflection contributions. It can be described as:

$$y_{ei} = s \sum_{hkl} L_{hkl} |F_{hkl}|^2 \phi(2\theta_i - 2\theta_{hkl}) P_{hkl} A + y_{bi} \quad (2.6)$$

where s is a scale factor, L_{hkl} represents contribution of the polarization, Lorentz and multiplicity factors, ϕ is reflection profile function, P_{hkl} is preferred orientation function, A is absorption factor (differing with the utilized instrument geometry) and y_{bi} is the background intensity at the i th step.

The following steps of a least-squares refinement are the use of *normal equations*, which involve derivatives of the previously calculated intensities, concerning the adjustable parameters. The solution is obtained by inversion of the *normal matrix*. Effectively the calculation of a model upon adjusting the parameters is falling better and better in line with the measured data [240].

The Rietveld model

Many parameters can and should be taken into consideration while performing a Rietveld refinement, depending on the software, the order of which may differ.

The background tends to be comparatively smooth, provided that the measured sample is highly crystalline. A higher amount of amorphous phase causes the background to rise significantly, revealing a polynomial function, used in a model as a calculated approximation. The high amorphous background contribution is often considered undesirable for the refinement of the crystalline phase, however, it not only provides important information about the sample but also in specific cases can be analyzed further, so that the relevant information about the amorphous phase structure can be mathematically extracted. This is of course a reference to the total scattering data Fourier transformation into pair distribution function (PDF) [240].

In an ideal case, where no crystal size effects, crystal lattice defects, and no beam dispersion is present, the peaks would be single points with intensities. In the reality, though physical phenomena, crystal lattice defects and amorphous phases result in that the *peak shapes* are typically based on a Gaussian function. However, multiple contributions result in the actual shape of a Bragg peak. Therefore, apart from the base function, other convolutions are implemented to capture the proper peak shape. The different shapes can be associated with the data acquisition process itself, from the technique itself to the geometry of an optical system and a detector. The X-ray diffraction pattern peaks for example tend to have longer tails than those of neutron diffraction origin but at the same time the second method results in notably more asymmetric peaks, which then require more complex functions to model properly. The totality of functions used to describe peak shapes is sometimes summarized as *PSF* – peak shape function. Regardless of the software used in Rietveld refinement it can be divided into three functions: the instrumental broadening function $\Omega(\theta)$, the wavelength broadening function $\Lambda(\theta)$ and the specimen function $\Psi(\theta)$. The first one takes into consideration the geometry and location of the beam source, monochromator and the sample itself. The second represents the distribution of wavelength in the source. The third one depends on the physical properties of the sample, such as crystallite size, and dynamic scattering. The last one, therefore, seems to be the most important in terms of sample analysis, since it does contain information about it. Although the purpose of the instrumental and wavelength broadening function is mostly just fitting the model, it is the goal of Rietveld refinement and should not be underestimated [240].

Rietveld refinement constraints

An important thing in Rietveld refinement is using proper constraints. With so many correlated variables and therefore possible outcomes, the least-squares refinement has to be guided by a user into the proper trajectory. Otherwise, the results may range from simply insufficient to physically impossible, even if the fit looks somewhat plausible with a naked eye.

Structural refinement of a diffraction pattern of crystalline material enforces the use of space group imposed constraints in the first place. The space group determines allowed peak positions, which once established properly are a key for starting a Rietveld fit. It is also a source of a constrained of positions and thermal displacement of atoms placed in special positions of a unit cell, which once shifted would change the space group. Thermal displacement parameters of other atoms in a unit cell are usually also left constrained for a good portion of a refinement, up until the very last steps. It is mostly due to the correlation with occupancy factors.

Apart from the structure-related constraints, the software offers the possibility of constraining other variables, that only refined one after another will result in a proper Rietveld refinement. Zero shift, polarization factor, peak shape-related constants, background function constants, instrumental constants, etc. All of those values should be carefully contained and refined in each calculation, taking into account the correlations in between them, that could unnecessarily increase their values without benefiting the overall fit [240].

Goodness of fit

The estimation of the uncertainty of an established model can be done using many different mathematical techniques. It has to be noted that none of the techniques gives actual information, whether or not the model is correct, nearly how statistically similar the calculated profile is to the dataset. That being said, some of those methods are widely used indicate whether or not a user gets closer to precise fit in the process of refinement [193, 240].

Rietveld software

Many software possibilities are available for refining PXRD patterns when using the Rietveld refinement method. In that, free of charge and paid options can be found. In this project only two programs were used.

One of the most popular, open-source programs is *GSAS-II*. Based on Python programming language and accessible on multiple computer systems, including Linux and Windows. As a general-purpose package, it supports structure solution, structure refinement and data reduction, for neutron (constant wavelength and time-of-flight) and both synchrotron and laboratory X-ray sources.

In this project, *GSAS-II* was often used for Rietveld refinement and peak fitting to determine quality and purity of synthesized samples, compare measured patterns to generated simulations and calculate phase fractions [207].

By far the most popular commercial option for Rietveld refinement is *TOPAS-Academic* software. It is a Windows-based computer program utilizing least-squares refinement algorithms. It allows users to use constraints and variables to fit X-ray and neutron data. It does also support structure solution, with peak extraction and indexing. In comparison to *GSAS-II* it is more advanced and at the same time more stable and convenient software, due to its algorithms being more optimized and less prone to errors. A command-based system allows for more flexibility and chances to influence and customize the process.

Diffraction meters

Two diffractometers were used for the laboratory PXRD measurements. The first one was Bruker D2 PHASER XE-T, Cu $K\alpha$ radiation, with zero background silicon sample holders. The second one was Bruker D8 DISCOVER, Cu $K\alpha$ radiation, zero background silicon sample holders.

2.3 Pair Distribution Function (PDF) of total scattering data

2.3.1 Synchrotron radiation

There many types of scientific facilities accessible equipped with instruments inaccessible for a regular laboratory environment. Often these facilities are government-funded, and offer free access to the scientists of the World, provided their research is considered of interest to the facility. Synchrotrons are one type of such facility, and give access to X-ray radiation with exceptional properties. A synchrotron generally consists of a storage ring that is surrounded by beamlines. Each beamline is connected to the storage ring with an insertion device that allows to source a small portion of accelerated electrons of the storage ring. These electrons are used to produce the synchrotron radiation.

The *synchrotron radiation* has many unique traits. One of the most characteristic is the extremely high brilliance of the beam. Brilliance means that the divergence of the beam is very small. Synchrotrons generate a white beam, with a wide range of wavelength (energy) of photons, allowing to choose energies suitable for specific uses when designing a beamline, and then

installing a monochromation system. Another important trait is the high flux of a synchrotron source, exceeding the photon counts of conventional X-ray sources greatly [91]. This results in a shorter time required for the experiment, which is a benefit of itself, and also less damage done to samples thanks to that. Moreover, an overall higher resolution of the measurements can be achieved due to the high energy of photons [62].

Generation of the radiation

The genesis of the synchrotron radiation discovery is quite interesting. Historically synchrotrons derive from particle acceleration facilities, where the humble beginnings of synchrotron radiation use for crystallographic purposes were undergoing parasitic experiments. This is reflected in how the synchrotron facilities operate using electron acceleration as a source of synchrotron radiation.

The process begins with generating a beam of electrons. One of the ways to do so is the so-called "electron gun" (used for example at DESY, Hamburg). A cathode used as a source expels electrons in pulses of which a part is transmitted through a chopper, guided by an anode and simultaneously accelerated, while focused with a collimator. Pulses of electrons enter then further acceleration system. Before entering the storage ring, electrons are meant to achieve their final speed, close to the speed of light, and then continue to follow the path in the storage ring, while maintaining high energy.

Redirecting the path of an electron beam of such velocity results in synchrotron radiation being ejected from it. An electron travelling at a velocity close to the velocity of light in a straight path travels with the electromagnetic field generated by it. When redirected, the electron changes the path rapidly, leaving behind the field, part of which is as a result torn off from the electron as a photon. All the photons generated this way collectively form synchrotron radiation. The synchrotron radiation wavelength is broad and covers the range from visible light to X-rays. This process is controlled with insertion devices, which are aligned with other devices, the direct desired range of radiation to beamlines [62].

Storage ring

The storage ring is a large, circular structure capable of storing high-speed electrons, are maintaining their energy. The inside of a storage ring is shielded with thick walls of concrete and other materials able to absorb a vast variety of particles generated by the stored electron beam. The electron beam runs inside a metal tube for many hours at a time, in which a high-quality vacuum has to be maintained for the stability of the electrons. The key components of the storage ring are bending magnets. They allow the electron beam to be bent, so that it circulates within the storage ring. The source of accelerated electrons is usually outside of the storage ring, and varies depending on a particular facility [62].

Insertion devices

For the radiation to be released to the beamlines, insertion devices are implemented around the storage ring. They consist of systems of magnets, which similarly to bending magnets of the storage ring, bend the electron beam (Fig. 2.7). However, the frequency of bending is much higher, and its goal is ejection of high energy photons from the beam – which is generating the synchrotron radiation. Depending on the needs of a beamline, the main two choices of an insertion device are a *wiggler* and an *undulator* [36, 156].

The focus of an undulator is brilliance. With a greater amount of closely packed magnets, each with a comparatively lower magnetic field, undulator forces the passing electron beam to bend with a smaller amplitude and higher frequency than wiggler. This causes synchrotron

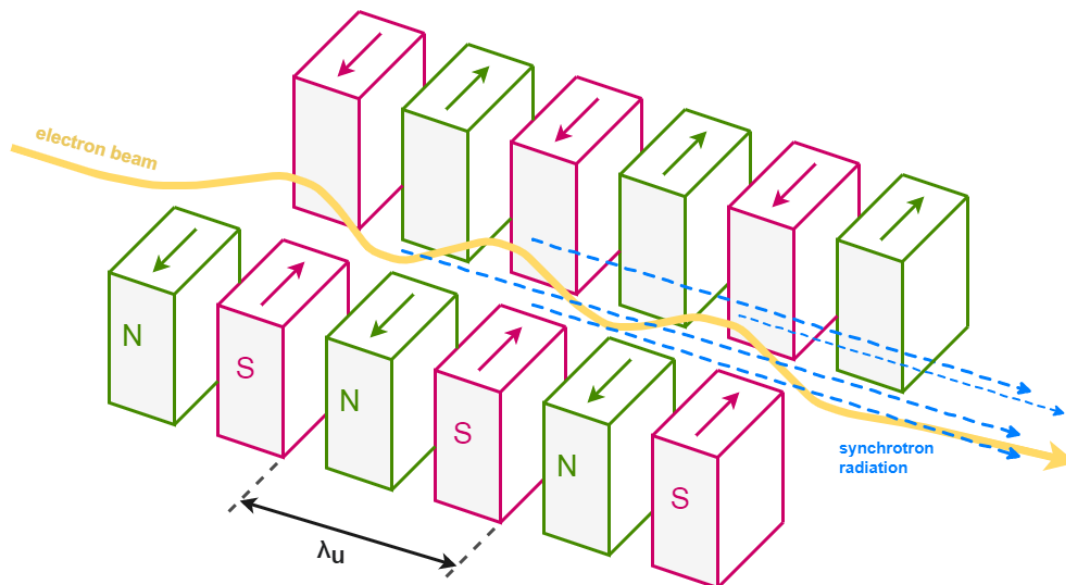


Figure 2.7: A schematic representation of an insertion device. Depending on the value of magnetic field and distances in between magnets (λ_u), as well as the amount of magnets used. The magnets face the opposite poles, and are placed alternately in their rows. A scheme can represent either a wiggler or an undulator.

radiation to be emitted at each bend. Due to a constructive interference effect, this increases the brightness of a generated synchrotron beam.

Generally speaking, the wiggler is characterized by a higher magnetic field used in a lower amount of magnets than in an undulator. Such system enables sourcing a continuous spectrum of a higher flux (amount of photons per second) in comparison with an undulator. Additionally, the radiation is reaching shorter wavelengths. The con of a wiggler is the loss in brilliance.

A distinguishing mathematical criteria between wiggler and undulator is the K -factor, given as:

$$K = \frac{eB\lambda_u}{2\pi m_e c} \quad (2.7)$$

where: e is the electron charge; B is a magnetic field; λ_u is a spatial period of the magnets; m_e is the resting mass of an electron and c is the speed of light. If $K \ll 1$ is true, the device works as an undulator. If $K \gg 1$ is true, it works as a wiggler [36, 226].

2.3.2 Synchrotrons and beamlines

Many synchrotron facilities are available to users around the world, more often than not accepting any scientific group as long as they submit experiment proposals that are considered interesting. For the purpose of a total scattering measurements of a liquid sample, high energy synchrotrons are required. Only the synchrotrons with highest energy beams are considered high energy, although there is no fixed lowest energy threshold. The highest energy synchrotron facilities are listed in Tab. 2.2.

Some of the most important parameters when comparing synchrotrons are their energy and brilliance. Some experiments specifically require high energy X-ray beam in order for the measurements to be quick and accurate. Similarly, for some of the experiments high brilliance is required. The brilliance is a term, which incorporates the amount of photons on an intersection

Table 2.2: A list of the highest energy synchrotrons, with chosen parameters. The energy, storage ring circumference (circ.), current and emittance. The beam emittance is one of parameters describing the brilliance of a light source. It describes the size of a beam.

Synchrotron	Country, City	Energy [GeV]	Circ. [m]	Current [mA]	Emittance [nmrad]
ALBA	Spain, Barcelona	3	268.8	200	4.33
APS	USA, Chicago	7	1104	100	3.0
ESRF-EBS	France, Grenoble	6	844	200	0.134*
DIAMOND	UK, Chilton	3	565.3	500	3.22
MAX-IV	Sweden, Lund	3	528	500	0.33
NLSL-II	USA, Upton	3	792	500	0.55
PETRA-III	Germany, Hamburg	6	2304	100	1.0
SOLEIL	France, Paris	2.75	354	500	3.68
Spring-8	Japan Sayo	8	1436	100	3.0
TPS	Taiwan, Hsinchu	3	518.1	500	1.6

*3.8 before 2020

of a beam. One way of describing brilliance is emittance, which is the size of the intersection. The smaller the beam intersection of a beam with unchanged count of photons, the higher the amount of photons per unit of area.

Two different synchrotrons were used for the experiments presented in this project, the PETRA-III and the ESRF.

PETRA-III

A 3rd generation radiation source based in Hamburg, Germany, and a part of the DESY. PETRA-III is one of the most brilliant light source in the world, with a storage ring circumference of 2.3 km. Currently 20 main beamlines are available for the users of different backgrounds (Fig 2.8). Materials science, structural chemistry, biochemistry and many other fields of studies benefit from the services of PETRA-III and its beam scientists, hosting around 3000 users every year according to their website [58].

European Synchrotron Radiation Facility – Extremely Brilliant Source (ESRF-EBS)

In 2020, the ESRF re-opened with a new source radiation, and added to its previous name "Extremely Brilliant Source" [223]. This change marked an opening of the first in the world, 4th generation synchrotron source. 50 specialized beamlines are available for the scientists of different fields, such as physics, medicine and chemistry. Due to the way the storage ring and facility are built, the beamlines surround the storage ring completely. Therefore, they outnumber these of PETRA-III despite the smaller storage circumference, reaching only 844 m. The experiments presented in this dissertation were performed at ESRF before the 2020 re-opening [168].

The synchrotron sources compete with each other in terms of improvements, and therefore the highest energy and brilliance titles are not fixed. The ESRF-EBS with its upgrade became the most brilliant source in the world, which was previously claimed by the PETRA-III. Regardless, both facilities are great places for research requiring high energy, brilliance and specialized beamlines with their scientific personnel.

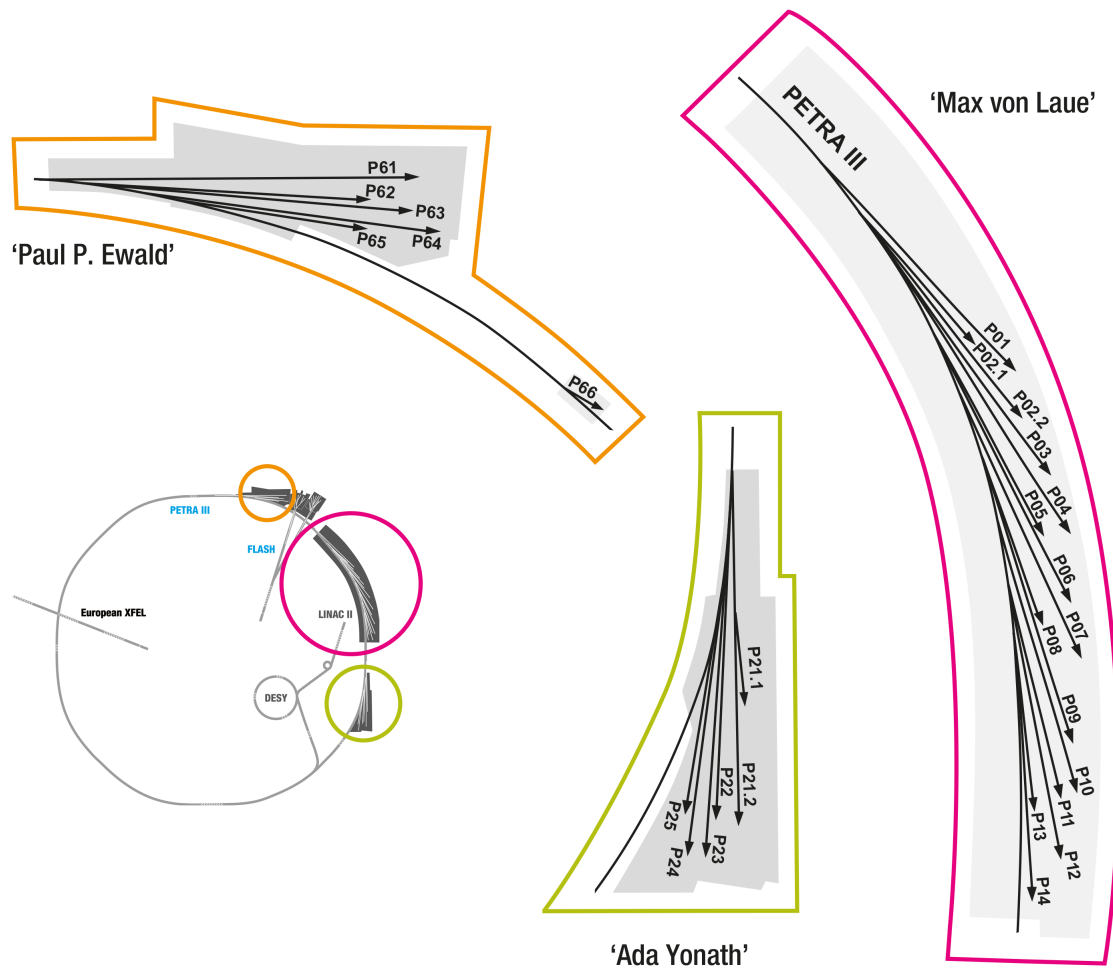


Figure 2.8: The PETRA-III facility with all 3 buildings and their beamlines. The plan is available at the official DESY website, www.photon-science.desy.de, alongside beamline descriptions and details.

2.3.3 High energy X-ray beamlines

The synchrotron radiation obtained in storage rings consists of a broad spectrum of energy. Most of that spectrum is cut away from the X-ray beam, as the beamlines are usually designed to use only precise wavelengths. While low energy X-rays are useful for number of applications, it is usually the high energy X-rays that are viable for experiments intended for PDF method.

Of course, each experiment is different. Because of that, the experimental environment should be planned individually, especially taking into account the possibility of measuring both solid and solution phase samples. In principle a good quality PDF could be calculated from a laboratory obtained data, using a X-ray diffractometer equipped in a Cu lamp. Provided that enough time is spent on the measurement and proper setup is used, and that the sample is a solid [63, 203, 204, 249]. In terms of samples in solution, the high energy is required for a reasonably quick measurement [62].

Generally speaking, high energy X-rays start from 80–100 keV. Their advantages include, but are not limited to:

- allowing for total scattering data acquisition due to increased Q-range, essential for PDF extraction,
- increased penetration of materials caused by reduced photo-absorption cross section,
- lower sample radiation damage,

Swedish Materials Science Beamline P21.1 at PETRA-III

Operating in a range of 40 to 150 keV this beamline is considered a high energy X-ray beamline of PETRA-III synchrotron. Consisting of two parallel branches, one specializing in WAXS and SAXS methods, second in broad band diffraction. The can second operates at three fixed energies thanks to a monochromation system – 50, 85 and 100 keV. This combined with detection system allows for total scattering measurements ideal for further PDF extraction [56].

ID-15 at ESRF-EBS

This beamline is operating in a 20–500 keV range, which makes it a high energy X-ray beamline. It is capable of many types of measurements, in that total scattering and PDF analysis. Small-Angle X-Ray Scattering (SAXS), Wide-Angle X-ray Scattering (WAXS), X-ray imaging and other methods can also be used at this beamline. The beamline specialized in materials chemistry and engineering use [213].

2.3.4 Total scattering and PDF

The Pair Distribution Function (PDF) of total scattering data is a still developing method, not as widely used as the PXRD or the single crystal diffraction. Although PDF has been becoming more popular for over 20 years now, its low accessibility due to a need of synchrotron radiation or neutron source¹ and difficult interpretation cause it to be still a considerably unpopular [28, 62].

The most basic premise of this technique is transforming the structural information in reciprocal space (intensity of scattered X-ray beam) to a direct (real) space function (atom-atom

¹Tools enabling the use of laboratory diffractometers for good quality total scattering data acquisition are being developed and used. So far it is an interesting option for powder samples measurement, yet due to the long time required to perform, not useful for *in-situ* PDF monitoring of any sorts and impractical for dynamic systems present in liquid samples [63, 203, 204, 249].

distance distribution). This is done with a Fourier transform. Reciprocal space (Q-space) and functions within it are described on wave vectors Q . Similarly, the real space uses vectors r . The intensity function $I(Q)$ is contained in a wider, total-scattering structure function $S(Q)$, given as:

$$S(Q) = \frac{I(Q) - \sum_{i=1}^n c_i |f_i(Q)|^2}{|c_i f_i(Q)|^2} \quad (2.8)$$

where c_i are atomic concentrations and f_i represent the form factors. This then is usually written as reduced structure function $F(Q)$:

$$F(Q) = \int \rho(r) \exp(iQ \cdot r) dr = Q[S(Q) - 1] \quad (2.9)$$

and then used in an equation for the reduced pair distribution function $G(r)$:

$$G(r) = \frac{1}{2\pi} \int_{Q_{min}}^{Q_{max}} F(Q) \sin(Qr) dQ \quad (2.10)$$

that in itself consists of atom-pair density function ($\rho(r)$), atomic number density (ρ_0) and naturally pair distribution function ($g(r)$), not reduced:

$$G(r) = 4\pi r[\rho(r) - \rho_0] = 4\pi r\rho_0[g(r) - 1] \quad (2.11)$$

which put in simple words contains the information about atom-atom distances [62]. This transformation can be useful for a variety of cases, one of which is a crystal of fullerene C_{60} . This chemical compound exhibits free rotation of molecules in the crystal lattice, breaking the translation symmetry. This causes the PXRD pattern to lack structural information. Similarly, an amorphous material like glasses can be challenging to analyse with PXRD due to lack of sharp peaks. However, Fourier transform to PDF can extract the subtle information about atom-atom distances hidden within the background. Whether it is an amorphous powder, glass or an even more unusual case, the PDF delivers information about the atom-atom distances. PDF can even go as far as being used for liquid samples [203, 248].

A point worth underlining over and over is the beauty of interpreting real space data [47]. Although the atom-atom distances distribution presented with PDF might be tricky to interpret at first due to a mixture of all the bond distances in the system added together, it is a pleasant departure from classic PXRD dataset to be just able to look at the graph and imagine exactly what the peaks represent in real space.

Total scattering X-ray measurement for PDF method

For a good quality PDF data to be acquired for a system, an array of measurement conditions has to be met. Unlike in the case of PXRD, the measurement is not focused on acquiring sharp and separated Bragg peaks. Those carry long-range structural information, a result of structural periodicity. It is the diffuse scattering that carries intramolecular structure information and atom-atom distances.

As mentioned before, synchrotron radiation is often essential for the total scattering data acquisition for the PDF method. Neutron sources can also be used for systems that are not suitable for X-rays, provided that longer data acquisition time is not against the goal of the experiment. This comes from the capability of achieving a range in Q-space broad enough for the Fourier transform to avoid truncation effects when using said radiation sources. This results in a comprehensive, sharp signal in real space. The more narrow Q_{max} , the less intense peaks in PDF signal will be visible. Needless to say, lots of information can be lost through calculating a PDF from dataset with narrow Q-space range – even to the point of the PDF signal containing virtually no structural information. The total scattering condition has to be

met when performing measurements for PDF method, which can be met thanks to the use of high energy X-ray beam. The size and resolution of a detector is also an important instrumental condition, enabling total scattering acquisition. Additionally, high flux of the beam is required for a reasonably fast data acquisition time. Moreover, the radiation has to have monochromatic character to increase the resolution. All of these requirements point out to a synchrotron source being an ideal candidate for X-ray total scattering measurements.

Not all beamlines will be sufficient for PDF purposes, neither will all synchrotrons. High energy and specific beamline setup for increased monochromatation and collimation of the beam is necessary. Therefore usually only synchrotrons with storage ring electrons of energies higher than 2.5 GeV are considered. Beamlines dedicated to PDF measurements do exist and are described as such by synchrotron facilities, so that finding them is not a problem, though at times more demanding systems require evaluation of the beamline capabilities while planning an experiment [62, 66].

Preparation and calibration

The samples are usually placed in glass or quartz tubes with thin walls. A measurement of an empty tube in case of a powder or tube with a pure solvent in terms of samples in solution is needed in order to subtract it from the sample signal. Although amorphous bodies usually can be neglected in PXRD or even single crystal diffraction, in PDF method their signal is too strong to overlook and can even fully cover the influence of researched compounds for samples in solution.

The synchrotron measurements require calibration due to the freedom of moving detector closer and further from the sample. For this CeO_2 , LaB_6 or other strongly scattering compounds of a well known structure and the Bragg peak distribution are utilized. Measuring a calibrant simply enables to add a proper Q-space scale to the detector image.

2.3.5 PDF extraction and analysis software

The synchrotron measurement is only a part of the experiment, and the data analysis is just as important. In the case of PDF method, the acquired data has to be calculated into pair distribution function. It is not a straight-forward process, since the Fourier transform of total scattering data can and should be adjusted for an individual case. Dedicated software is therefore required and described briefly below. All of the described programs are based in Python environment.

pyFAI

The first step is application of the calibration done during an experiment. The measurements performed in each detector-sample configuration should be paired with a measurement of a calibrant, and so in this step they should be matched with each other. The *pyFAI* software can be used in this step. The program enables couple of functions to the user. First, it enables forming a mask for the detector, allowing to omit all imperfections in the calculations, such as dead pixels or dead bands, the beamstop and others. Further it requests to load the calibrant data and point out characteristic rings (Fig. 2.9). Database allows to pick a calibrant, for example CeO_2 . This process allows not only to locate a proper Q-space scale for the detector images of the samples, but also provides help with detecting and correcting any detector flaws, such as potential tilt of the detector surface [13].

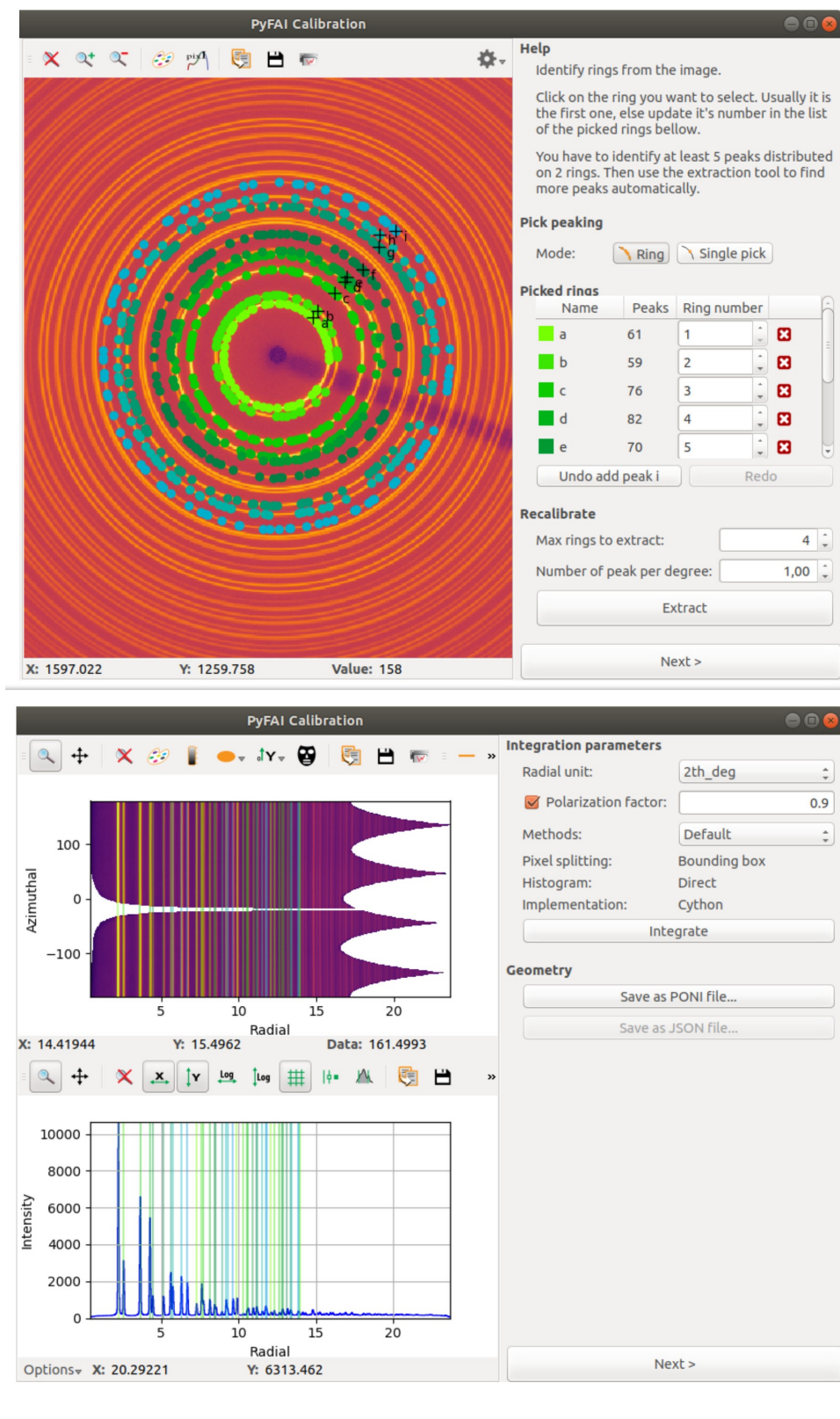


Figure 2.9: Steps of data integration using *pyFAI* software. After masking undesirable areas of the detector, such as dead pixels and breaks in detector panels, diffraction cones with their consecutive numbers for a calibrant (CeO_2) are chosen. This information is further processed and a detector image is transformed into total scattering data. Calibration and mask files are then used for integrating the images of the samples.

PDFgetX3

The next step is generating a PDF function from the sample measurements with the *PDFgetX* software. For that a file generated in *pyFAI* is used as a reference, and a background file is subtracted from the sample. An appropriate Q-range has to be picked. Due to the detector imperfections, the further the Q range, the bigger chance of them influencing the PDF signal. Moreover, a big range can cause signal fluctuations to appear. Yet as mentioned before, the smaller the range, the broader and less readable the peaks. A good balance can be found by trial and error. Adjusting the scale of the background is also an important step at this stage [101, 103].

PDFgui and DiffPy

The *DiffPy CMI* software is dedicated to analysis of obtained PDF signals. It is, similarly to Rietveld refinement software, based on creating a model of a structure and refining it against the data. It is based in Python programming language. There are two, main programs within the *DiffPy CMI* software, the first being *DiffPy*. This program is used in the command line of Python, where refining can be done through composed scripts. Both crystalline and non-crystalline models can be used within this program. It utilizes the Debye function method, which very accurately describes scattering of radiation on various structures, including nanoparticles and metal-oxo clusters. In this work, this model allowed for simulation of intramolecular atom-atom distances of species in solution [22, 52, 81].

An alternative for crystalline materials is *PDFgui*. It is equipped with an interface dedicated to the refinement of crystalline powders. It is a more restrictive, yet easier to use alternative to *DiffPy*. It uses small box approximation for modeling, which is suitable for crystalline materials. Thanks to the small box approach, the repeatable character of crystal lattice can be well simulated, and the intermolecular atom-atom distances are not lost [65, 164, 166].

2.4 Spectroscopy

2.4.1 UV-Vis

Ultraviolet-Visible light spectroscopy is a type of absorption, transmission and reflectance spectroscopy. In this work exclusively the light absorption technique was used. It consists of measuring a sample as a function of wavelength throughout the visible light range and adjacent regions. Depending on an available setup it ranges from 200 to 1200 nm, with the 400-850 nm visible range being the usual focus in analysis of metals or metal-organic compounds [222].

Transmittance and Absorbance

Total transmittance is used to describe the effectiveness of transmitting light through a medium, where the losses come from multiple physical and chemical phenomena, such as scattering, reflection and absorption. The internal transmittance takes only absorption into account as the value used in UV-Vis spectroscopy. It is given as:

$$T = \frac{I_T}{I_0} = \frac{I_0 - I_D}{I_0} \quad (2.12)$$

where I_0 is the incident beam intensity, I_T is the intensity of the absorbed light and I_D is the intensity of the light detected after passing through a sample, which can be used to describe I_T . In the practice of UV-Vis spectroscopy, the incident beam intensity is measured while measuring background, most often with a cell with a pure solvent. Therefore, the value

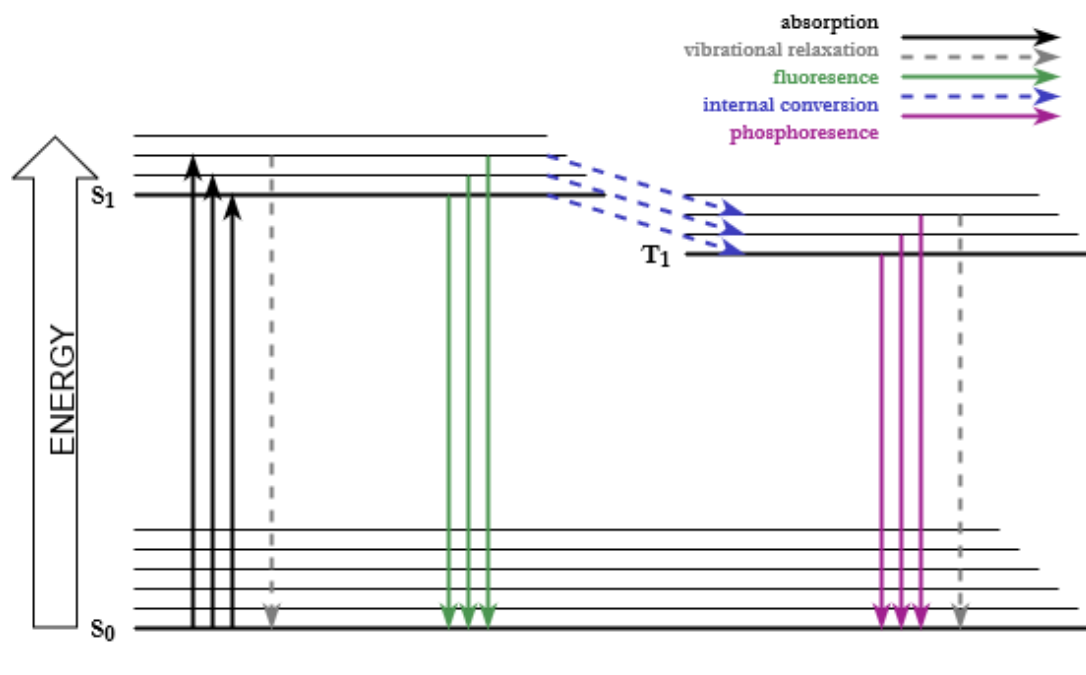


Figure 2.10: A Jablonski energy diagram. The scheme shows the energy state of an electron with a singlet ground state S_0 , a singlet excited state S_1 and a triplet excited state T_1 , with possible energy transmissions. Full lines represent radiant and dashed lines non-radiant energetic effects.

of I_0 is not *de facto* representing the incident beam in a realistic application. That allows to remove most of the effect of the total transmittance.

Absorbance is a value directly related to transmittance and usually the preferred way of expressing the level of absorption in UV-Vis spectroscopy. It is described as [222]:

$$A = -\log_{10} T \quad (2.13)$$

Energy absorption by electrons

The technique is based on light absorption by chemical species. Molecules consist of atoms bonded together, therefore bonding electron pairs are present in molecules, often with non-bonding pairs on some of the atoms. Those electrons are in a ground state, unless they absorb a portion of energy equal to the energetic difference in between their ground and excited state (Fig. 2.10). Although UV-Vis spectroscopy is focused on the process of energy absorption, the excited electron can release absorbed energy in interesting ways, some of them utilized in different kinds of spectroscopy. Energy can be lowered in a non-radiant way by vibrational relaxation, causing the electron to once again achieve the ground state or undergo lateral conversion from a singlet to a triplet state. Other ways are radiant and involve fluorescence, provided the conversion from an excited singlet state to a singlet ground state, or phosphorescence in the case of conversion from an excited triplet state to a singlet ground state. The energy can be provided by a photon and described as:

$$E = \frac{hc}{\lambda} \quad (2.14)$$

where h is the Planck's constant, c is the speed of light and λ represents a wavelength. For this reason the name UV-Vis spectroscopy is interchangeably used with electron spectroscopy.

The different levels of energy of electrons present in molecules able to be excited by UV–Vis radiation results in a characteristic UV–Vis spectrum, which is directly linked to the energy absorbed by a sample, since particular wavelength is associated with particular energy. The shape of a characteristic differs from chemical species to species, but often peaks are observed, especially in case of metal and metal-organic ions and complex molecules.

The energy of excitation differs for different types of electrons. The σ electrons require the highest level of energy. Because of their stability and low energy of ground state. The π electrons usually have much higher energies of ground state, making them easier to excite by UV–Vis range of energy. Similarly the non-bonding electrons tend to be excited by ultraviolet and visible light range, since their ground state energy is even higher than in the case of π electrons. Knowing that, most of the UV–Vis absorption is due to the π and non-bonding electrons, with σ electrons providing very rare excitation states in lower ultraviolet range, not accessible with most optical setups [222].

Lambert-Beer law

The absorbance is directly related to a concentration of a known species with Lambert-Beer law:

$$A = C\epsilon l \quad (2.15)$$

where l is the length of the light path in a sample, ϵ is the absorptivity of a molecule, and C represents concentration of the compound. Depending on the concentration unit, the ϵ may be represented with different units, with l usually in centimeters [222].

Spectrophotometers

The UV–Vis measurements were performed with a Mettler-Toledo Spectrophotometer, model UV5 Nano.

2.4.2 Raman

A spectroscopic technique based on the phenomenon of inelastic scattering of light, referred to as Raman scattering. Using a monochromatic light source, usually a laser in ultraviolet to near infrared energy range, a sample is illuminated. The detector is placed away from the direct beam, gathering the scattered photons and reading their energy at an angle after cutting off elastic scattering with monochromator system. This signal further forms Raman spectrum, as the intensity in a function of energy. It is used as a fingerprinting tool in chemistry, enabling to recognize certain cataloged chemical compounds [222].

Inelastic scattering

The most common instances of light scattering on molecules is the elastic scattering (Fig. 2.11). It occurs when a molecule takes the energy of an incident photon, stores it in a virtual energy state as a kinetic energy, then emits back a photon of the same energy, reverting this way to the ground state from before the incident photon impact. This phenomenon occurs often in nature and is a cause of most of the light scattering observed with a naked eye. Less common than elastic scattering is the phenomenon of inelastic scattering. In some instances the energy of a photon absorbed by a molecule differs from the energy of photon emitted afterwards. Vibrations of molecules which are the method of storing photon energy may loose or increase that energy, causing the difference. Collecting the inelastically scattered light and plotting it in

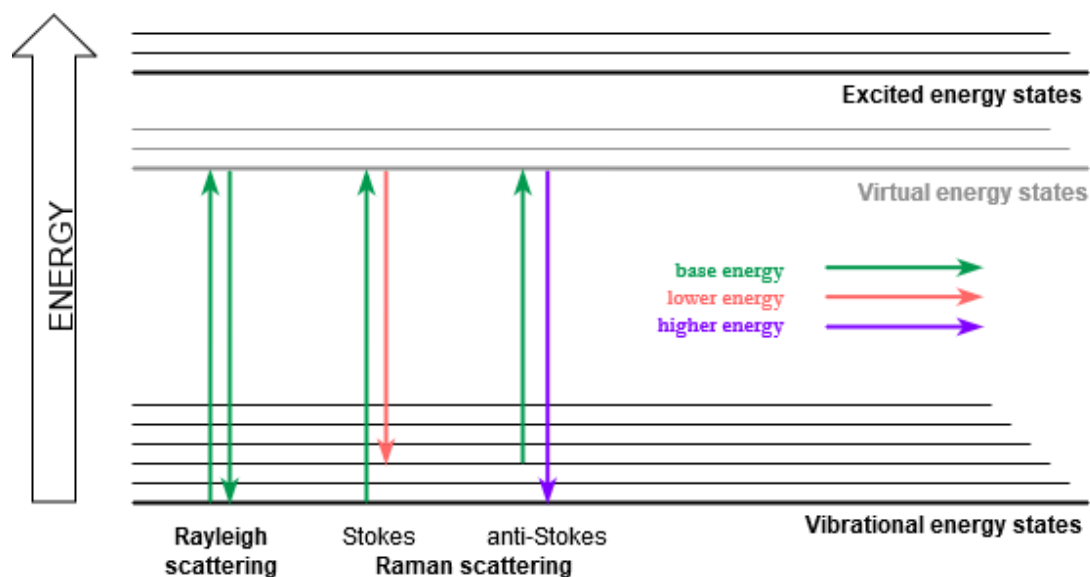


Figure 2.11: An energy diagram of light scattering. A scheme showing energy state of an electron that temporarily stores energy of a photon in a virtual energy state, to later emit a photon and lower its energy back to the ground state. Colors of the arrows symbolize energies of the absorbed photon. The first instance is Rayleigh scattering, where incident photon and emitted photon have the same energy. Raman scattering occurs when the energy of emitted photon is different. Stokes scattering emits a photon of lower energy and anti-Stokes one of higher energy.

a function of frequency (cm^{-1}) results in a Raman spectra. It represents vibrational states of the molecules present in the system [222].

Possible energy changes are dependent on the atoms and bonds building a molecule, and also its polarizability. Moreover, unlike FTIR Spectroscopy (Fourier-Transform Infrared Spectroscopy), Raman scattering is sensitive to different kinds of bond in between heterogeneous atoms, such as a different C-C bond. This results in Raman spectroscopy being an excellent tool of differentiating in between chemical species similar structurally, but with different types of bonds. An example being alkanes and alkenes with the same amount of carbon atoms [222].

Another important advantage of Raman spectroscopy over the complementary FTIR and the UV-Vis methods is no requirements in terms of sample preparation. Because Raman spectroscopy is not an absorption method, it is fairly easy to measure both solids and liquids in the same setup – the sample has to be illuminated with a laser, and the scattered spectrum gathered with a detector. Thanks to addition of a microscopic lens, Raman setup allows to focus the laser on small objects as well as scan large areas. However, potential artifacts can be found in a Raman spectra measurement. Reflectance of a sample or a sample holder, absorption, luminescence effects, all of these can minimize the share of inelastic scattering in the scattered light. Additionally, luminescence can cause a significant rise in the background, since the emitted in this process light will be lower energy than absorbed. This can be mistaken for inelastic scattering [132].

Raman spectrometer

In the experiments a Renishaw inVia spectrometer was used, equipped with a green (532 nm), red (633 nm) and ultraviolet (785 nm) laser wavelengths.

2.5 Dynamic Light Scattering (DLS)

Dynamic Light Scattering (DLS) method of particle size distribution determination incorporates the correlation of a particle size and its Brownian motion in a solution. At the most basic, a smaller particle moves faster, whereas random movements of bigger ones (such as polymers [124]) occurs at a slower pace [160]. It can be described using Stokes-Einstein equation:

$$d(H) = \frac{kT}{3D\pi\eta} \quad (2.16)$$

where $d(H)$ describes the hydrodynamic diameter of a particle, D is the transitional diffusion coefficient, T the absolute temperature and η is the viscosity of a solvent, with k representing the Boltzmann's constant. Therefore, a DLS measurement requires known viscosity of a solution and a stable temperature of a measured sample. Any temperature swing will cause non-random movements. Moreover, the size of a particle detected with DLS being calculated with the hydrodynamic diameter parameter, is in fact the size of an orb that has the same D , which is also influence by molecules and ions surrounding the actual particle.

The measured intensity of light diffused on a sample is measured in this technique. The Brownian motions cause the diffusion to form a pattern, which if imagined as a 2D screen surrounding measured optical cell, would be reminiscent of a white noise on a television screen. This speckle pattern changes with the size of particles in solution, increasing and decreasing the size of speckles and their intensity, along with the time it takes for the pattern to shift into new one in its entirety. This phenomenon is utilized by placing a detector reading only a very small part of the signal, creating intensity fluctuation graph in a function of time. This function then is transformed into a correlation function, enabling software to calculate a predicted size distribution of the particles in a solution. Although it is not impossible to skip that step, the correlation function does unify information of the random intensity fluctuation. It is presenting a degree of similarity of a signal in a function of time as a correlation graph. It does it by measuring the dispersed light intensity in a point, in small, fixed gaps of time, where the actual time from the start of a measurement is given as: $t + n\tau$ (t = the time, n = a number of measurement, τ = the correlator time delay) [83].

The correlation function $[G]$ of the correlator time delay is represented as:

$$G(\tau) = A[1 + Be^{-2\Gamma\tau}] \quad (2.17)$$

The constant A is a baseline, whereas B is the intercept of the correlation function. The variable A graph being a product of correlation analysis has direct information on the time of correlation decay. Multiple steps presented on such graph usually inform of multiple species being present in a sample. A rapid drop of the correlation coefficient without steps indicates a single, coherently sized species in a sample.

The computer calculations do not end here, a correlation function is further used to calculate a size distribution. Many different ways are used in DLS software, the basic is using modeling a correlation function with suitable sizes of particles to obtain a good fit to the measured one. The final result is a size distribution function.

The optical configuration consists of a laser of specific wavelength as a light source, a cell and a detector, where usually one of which has adjustable position. The detector is usually positioned in a way allowing to measure back scattering. An important note is that for measuring small particles, a smaller wavelength is needed. A specific intensity must reach the detector, otherwise the detected signal is saturated or insufficient. An attenuator is usually connected to the laser for the purpose of manipulating its intensity and preventing mentioned instances from occurring. The wavelength of a laser is important since in principle the lower the wavelength (the higher the energy), the smaller species can be observed [100, 109].

What is worth noting is that a DLS measurement is susceptible to artifacts generated at many levels, from sample preparation up until the measurement itself. Speckles of dust in a solution can influence signal enough to cover the presence of nano-sized species. Large aggregates of otherwise small clusters may have similar effect. And finally calculation errors and choosing an incorrect calculation model is an easy mistake, resulting in inadequate results [222].

DLS Instrument

The DLS measurements were performed with a Malvern Zetasizer instrument.

2.6 Electron microscopy

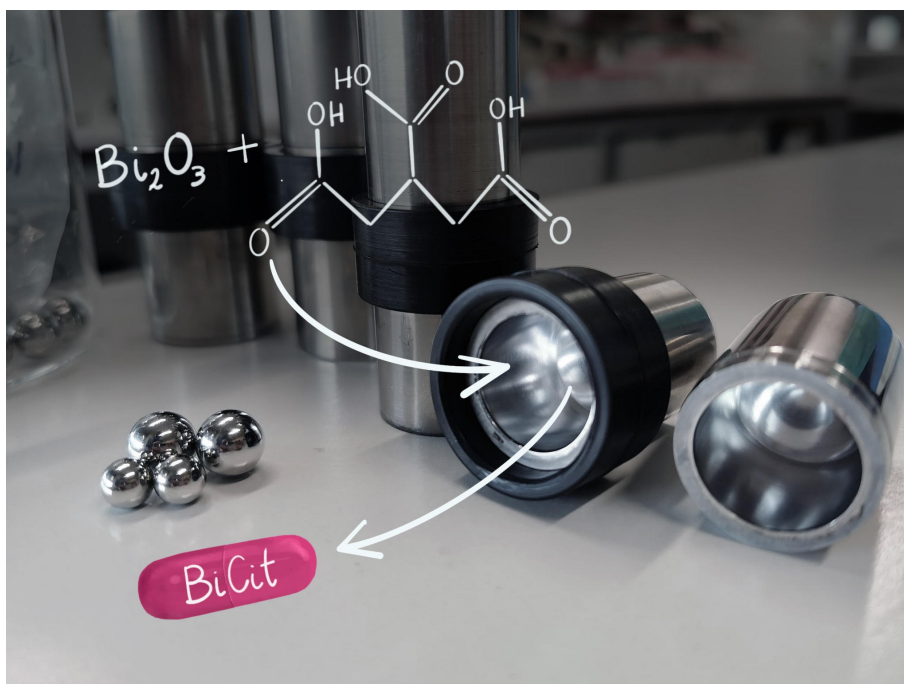
A type of microscopy using electrons as a means of imagining. Depending on the type, electrons can be either reflected (Scanning Electron Microscopy – SEM) or transmitted (Transmission Electron Microscopy – TEM), which directly forces each type to be only topographic or compositional. This type of microscopy is suitable for measuring all types of samples, since electrons interact with all matter, however, preparations are required.

Transmission Electron Microscopy (TEM)

TEM is a technique allowing to observe compositional images of samples. It requires very thin sample material, usually not reaching above 100 nm. The sample is placed on a flat grid made of a conductor material, for example copper, that is then exposed to a focused electron beam. The beam is directed perpendicularly onto the flat sample. After scanning the sample the remaining electrons land on a detector, which depending on a setup can simultaneously show the image on a monitor. Unlike in the case of SEM, the sample does not have to be a conductor itself, nor to be coated in a conducting layer. The resolution depends on a setup and the sample environment, and can reach atomic level. It makes TEM a desirable tool for virtually any type of structural chemistry, including nanoclusters and metal-oxo clusters [228].

Chapter 3

Mechanochemical synthesis of bismuth APIs



3.1 Introduction

This chapter is dedicated to the mechanochemical synthesis of Active Pharmaceutical Ingredients (APIs)¹ containing bismuth. Bismuth (III) disalicylate (BiSal₂) is a precursor material used in the chapters 4 and 5 for the growth of the [Bi₃₈O₄₄] metal-oxo cluster. It also belongs to a group of bismuth salicylate compounds used in medicine. Its mechanochemical synthesis to be a precursor evolved to a separate chapter, due to the discovery of similar synthesis routes for other bismuth APIs. Bismuth (III) gallate (BiGall), bismuth citrate (BiCit), bismuth (III) trisalicylate (BiSal₃) and the mentioned BiSal₂ were obtained mechanochemically, and their respective syntheses environments analyzed and adjusted to establish the most favourable conditions for the full conversion to the desired product.

3.1.1 Bismuth compounds as medicine

Bismuth-organic compounds have been incorporated into various treatments since the 16th century, especially aimed to aid in various digestive issues [129], although some metallodrugs have been used even before that [11, 143]. In the modern day medicine, compounds such as bismuth subsalicylate (Pepto-Bismol[®]) and bismuth (III) gallate (Devrom[®]) are still in use (Fig. 3.1). It proves an ongoing medical interest in bismuth APIs, that could even increase if other uses are developed and implemented [35, 171]. Bismuth APIs show antibacterial and antiviral properties [118, 196]. Namely, bismuth APIs were successfully used in the fight against *Helicobacter Pylori* [134], which is an extraordinary asset due to the evolving antibiotics resistance in common bacterial species. Bismuth metallodrugs were even shown to inhibit the activity of SARS coronavirus [235], and even more recently, ranitidine bismuth citrate has been shown to suppress replication of virus responsible for the COVID-19 pandemic in animals [241]. This indicates clearly that public interest in bismuth APIs is not declining, but rather increasing.

3.1.2 Mechanochemical synthesis of APIs

Mechanochemical synthesis of BiSal₂ and BiSal₃ [9] inspired exploring possibility of using similar means for other bismuth APIs synthesis. That is why BiGall and BiCit mechanochemical synthesis was attempted (Fig. 3.2). The initial goal was improving the recipe for BiSal₂ synthesis, in order to utilize it as precursors for metal-oxo formation, namely the [Bi₃₈O₄₄] cluster. The reaction conditions recommended in the literature for BiSal₂ [9] yielded initially exclusively BiSal₃, hence the need to improve on the understanding of both bismuth salicylates synthesis.

Mechanosynthesis as a means of synthesizing APIs is a still developing method [12], extensively reviewed by many [57, 72, 80, 87, 95, 173, 218]. It is thought to be an environmentally friendly alternative for solvent-based syntheses [225]. Mechanochemical synthesis of APIs [9, 200] is the only one of the branches of mechanochemistry, next to synthesizing materials like MOFs (metal-organic frameworks) [73] and ZIFs (zeolitic imidazolate frameworks) [19].

Benefits of mechanochemical synthesis

Using large amounts of solvent is a norm for synthesizing APIs for the pharmaceutical industry, which is also the case for bismuth APIs. Methods popularly used for synthesizing bismuth salicylate [205], BiGall [242], BiCit and other bismuth APIs, are based on heavy use of nitric acid and large amounts of water. For example, precipitation from bismuth nitrate solution [243]. The water after synthesis becomes a polluted waste. Heating the water during the process, and

¹Metal-organic compounds being considered APIs, are also referred to as metallodrugs [143] and metallopharmaceuticals [85].



Figure 3.1: Examples of medicine, containing bismuth APIs as the active ingredient. Devrom[®] contains bismuth gallate (a), Pepto-Bismol[®] bismuth subsalicylate (b), and PYLOTAC[®] bismuth citrate (c).

maintaining the required temperature for an extended time of synthesis, adds to the waste in a form of used energy. Apart from the waste, these essentials generate additional costs.

The main benefit of mechanochemical over solution-based syntheses of APIs are minimizing the amount of waste. Additionally, the potential of reducing the cost of a process. Mechanochemical reactions can often be performed at room temperature [19, 51], which eliminates the cost of upholding reaction temperature. Minimizing the time of a reaction is possible thanks to limiting the number of reaction steps to just one with mechanochemistry. The time of mechanochemical reactions is also generally shorter than solution-based processes, like precipitation from a solution. Moreover, the limited amount of precursor compounds and intermediate reactions decreases the number of potential side-products. This limits the amount of adverse impurities, undesirable in medicine production. In terms of bismuth APIs mechanochemical synthesis routes presented in this work, Bi_2O_3 and organic acid are used as precursors for each of the compounds. This stands in contrast to more elaborate, and potentially expensive metal-organic precursors, and the use of additional acids [205, 206, 242, 243].

3.1.3 The main objectives

The main goal of this chapter is finding the best conditions for mechanochemical synthesis of BiSal_2 , BiSal_3 , BiGall and BiCit . A variety of conditions were implemented, and the produced samples were investigated with PXRD in order to meet the goal.

Crystallization of BiSal_3 and BiCit was also attempted, as these species have an unknown solid-state structure. Additionally, crystallization of BiGall was also tried, in order to confirm its already known structure [221]. During these attempts, an interesting, water-dependent change in the BiCit was discovered and investigated with Raman spectroscopy and thermogravimetric analysis (TGA).

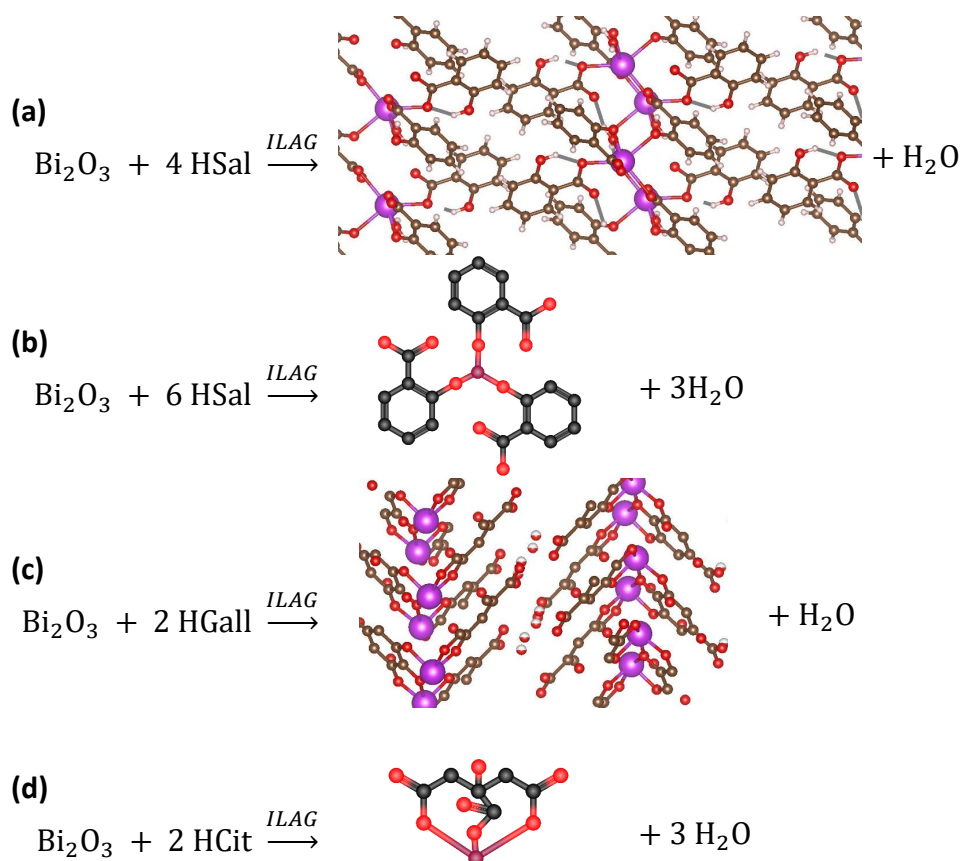


Figure 3.2: Reaction schemes for synthesized bismuth APIs. (a), The synthesis of bismuth (III) disalicylate with ILAG, showing structural model of the compound [9]. (b), The synthesis of bismuth (III) trisalicylate, showing a theoretical model of its molecule. (c), The synthesis of bismuth (III) gallate with a structural model [221]. (d), The synthesis of bismuth citrate, showing a stoichiometrically correct, unrealistic model of a molecule.

One more puzzling observation was made, when mechanochemically synthesized BiSal₂ was found to change its color from white to pink, after being exposed to the atmosphere. BiSal₂ being a precursor to the [Bi₃₈O₄₄] oxo-cluster formation is especially important to this work, and therefore investigating this color change became one of the goals. This is done with PXRD and Raman spectrum techniques.

3.2 Experimental section

3.2.1 Chemical compounds

All chemical ingredients used were purchased from Sigma-Aldrich if not stated otherwise (Tab. 3.1). Bi₂O₃ (99,999%) was used in all of the synthesis experiments. Salicylic acid (HSal, ≥99.0%), gallic acid (HGall, ≥98.0%, Merck KGaA), citric acid (HCit, ≥99.5%) and acetylsalicylic acid (≥99.0%) were used as the second reaction ingredient, along KNO₃ (≥99.0%) and NH₄NO₃ (≥99.5%) as an ionic salt catalysts in the following experiments. For some synthesis citric acid monohydrate (HCit monohydrate, ≥99.0%) was used instead of anhydrous HCit, and for some experiments, commercial bismuth citrate (BiCit, 99.999%) was used.

Table 3.1: Chemical compounds used in the experiments of synthesizing bismuth APIs.

Compound	Purity [%]	Code	Supplier
Bi ₂ O ₃	99,999	202827-10G	Sigma-Aldrich
salicylic acid	≥99.0	105910-500G	Sigma-Aldrich
gallic acid	≥98.0	8.42649.0025	Merck KGaA
citric acid (anhydrous)	≥99.5	791725-100G	Sigma-Aldrich
citric acid monohydrate	≥99.0	C1909-500G	Sigma-Aldrich
bismuth citrate	99.999	480746-100G	Sigma-Aldrich
acetylsalicylic acid	≥99.0	A5376-100G	Sigma-Aldrich
KNO ₃	≥99.0	1050630500	Merck KGaA
NH ₄ NO ₃	≥99.5	A7455-500G	Sigma-Aldrich
Acetone	≥99.5	179124-1L	Sigma-Aldrich
DMF	≥99.8	227056-1L	Sigma-Aldrich
ethanol	99.5	-	-
ethylene glycol	99.5	-	-
propanol	≥99.7	279544-1L	Sigma-Aldrich

3.2.2 Mechanochemical synthesis process

The mechanochemical grinding was done using InSolido Technologies vibration-type mill, IST500, in stainless steel jars (10 and 25 ml), paired with stainless steel balls (7 and 10 mm). Three methods of mechanochemical synthesis were used, described in detail in Chapter 2. Mechanochemical grinding (dry grinding), liquid assisted grinding (LAG) [72, 75, 76] and ion- and liquid-assisted grinding (ILAG) [72, 105]. Distilled water was used as the default liquid in the latter two methods.

Preparation of samples for each experiment started with weighing appropriate amounts of ingredients, on a balance with 0.1 mg precision. 200 to 1000 mg of the reaction mixture was prepared for each sample by mixing the ingredients before placing them in the milling jars. Liquid (for LAG and ILAG methods) was added each time after the milling balls were placed inside the milling jars.

Some of the experiments included heating the jars. This was done both with and without the reaction mixture. An insulated drier, typically set to 85 °C, stationed next to the mill was

used for that task. The jars were placed inside and closed for the appropriate time, usually 30 minutes.

Two jars at a time were mounted onto the mill. Heated jars were mounted rapidly, to reduce the heat loss. Each set of two samples was milled for the same amount of time, with the same frequency, and the same set of milling balls. This was done in order to prevent weight imbalance, as recommended by the mill producer. After milling, samples were extracted from the jars and placed in labelled containers for further analysis. Depending on the expected time sensitivity, measurements on the samples were performed right after synthesis, or after gathering a larger amount of samples.

3.2.3 PXRD

The PXRD measurements were done with two diffractometers, Bruker D2 PHASER XE-T and Bruker D8 DISCOVER. Both use Cu K α radiation, and zero background Si sample holders.

The powdered samples were measured on the diffractometers in order to analyse their composition. Measurements were done typically on two to ten different samples, synthesized on the same day. A limited amount of the reaction conditions were changed for a thorough analysis and comparison. Over 200 samples were prepared and measured with PXRD in the process. The range of the measurements was typically set from 5°, which allowed to capturing the first peaks of the compounds of interest. The upper limit was set in a range of 50 to 100° and was adjusted depending on the intended use of the measurement. For visual peak comparison, the typically smaller range was chosen for a quicker measurement time. For Rietveld refinement purposes, a larger range was measured to ensure a correct fit.

3.2.4 Raman spectroscopy

Raman spectrum measurements were obtained with Renishaw inVia spectrometer, using a green (532 nm), red (633 nm) and ultraviolet (785 nm) laser wavelengths. The samples were placed on glass holders, and the background was removed from the measured data.

Raman spectra of synthesized BiCit, aged and mechanochemical, and similarly commercial BiCit, were measured at different stages of drying, and different times from synthesis. Samples in a dry powder form were placed on a glass sample holder for the time of measurement. Similarly, wet and suspended in water samples were placed on a metal, low background sample holder. Then measured while wet, and at different stages of drying, mimicking the environment of PXRD measurements.

3.2.5 Thermogravimetric analysis (TGA)

For the TGA measurements, a TA Instruments TGA Discovery with high-temperature Pt sample holders was used. Samples of synthesized and commercial BiCit were measured in similar conditions, from room temperature or 100 °C up to 600 °C. The measurement was done in a steady flow of 1:3 O₂ and N₂ mixture, mimicking air. The rise of temperature was set to 3-5 °C/min. An internal weighing system was implemented in weighing the sample in the process. Different samples were measured at different stages of wetness. In order to ensure similar accuracy, approximately 1 mg of dry material was placed on a sample holder for each measurement.

3.3 Bismuth salicylates – BiSal₂ and BiSal₃

3.3.1 Reaction conditions

The reaction environment was modified with a series of variables for bismuth (III) disalicylate (BiSal₂) and bismuth (III) trisalicylate (BiSal₃) in order to achieve repeatably full conversion into the desired compound.

The tested ratios of Bi₂O₃ to salicylic acid (HSal) were 1:2, 1:4 and 1:6. The amounts of reaction mixture varied from 200 to 300 mg for a 10 ml jar, and from 400 to 1000 mg for a 25 ml jar. The amounts were weighed on an analytical balance with 0.1 mg precision. The amount of ionic salt (KNO₃ or NH₄NO₃) used in ILAG method varied from 1 to 10 weight %, in order to increase mobility. The volume of water added to the reaction varied from 0 to 150 μl per 200 mg of the reaction mixture. Stainless steel balls were used for the grinding, with both 7 and 10 mm sizes tested as single balls, and 7 + 7 and 10 + 10 pairs.

Heating of the reaction mixture to 85 °C for 30 min before the grinding was tested as a means of enabling the BiSal₂ synthesis. While heating, the mixture was kept inside the jars, with the water in case of LAG and ILAG experiments. Alternatively, the mixture was heated in a holder, before being transported into jars and added to water. In the first case, the hot jars were rapidly mounted into the mill, in the second the mixture was packed into the jars and water was added rapidly, in order to start the synthesis as soon as possible. The cooling fan of the mill was set on the highest flow, and turned off, in order to test the influence of cooling of the sample and enable the heating to persist longer. The time of grinding varied from 15 to 60 min. The frequency of milling was at all times set to 30 Hz.

The samples were synthesized in batches of two at the same time, in two different jars. After synthesis, each sample was transferred into a separate container, for later PXRD pattern measurement.

3.3.2 Results

Mechanochemical synthesis of pure BiSal₂ (Fig. 3.3) proved to be a complex process, influenced significantly not only by controlled experimental conditions but also by the external environment, especially the temperature of a room. This became apparent after dozens of prepared samples contained nothing but BiSal₃ and Bi₂O₃. And even after obtaining BiSal₂, the conversion was far from complete. Luckily, the clear differences in PXRD patterns of BiSal₂, BiSal₃ and Bi₂O₃ enabled quick peak-position analysis of measured samples (Fig. 3.4). The leftover HSal was not typically detected next to the unreacted Bi₂O₃, which is expected as a soft, organic crystal becomes amorphous during the grinding. Unsuccessful attempts to recreate synthesis based on literature [9] were consulted with the Friščić group at McGill University in Montréal, and resolved after meticulous analysis of extensive parameter adjustments, improving the reproducibility of the BiSal₂ mechanochemical synthesis.

The use of ion- and liquid-assisted grinding (ILAG) method with the addition of 1-2 mass % of ionic salt (NH₄NO₃ or KNO₃) to improve mobility in the system is not to be overlooked. Water as the liquid is also essential, with no other solvent enabling the reaction. 75 μl per 200 mg of reaction mixture provides the best results. The use of two 7 mm steel balls yields exclusively BiSal₃, regardless of the Bi₂O₃:HSal ratio. Exchanging those to two 10 mm balls, and therefore increasing the force of impact in the grinding process, proves to be essential for successful BiSal₂ synthesis. Another step, ensuring successful synthesis, is heating of the jars with the starting 1:4 (Bi₂O₃:HSal) reaction mixture and water, to 85 °C for 30 min, before milling. 30–45 min of milling is enough to ensure full conversion. Exceeding the amount of reaction mixture over 500 mg for 25 ml milling jars can lead to not full conversion, therefore the reaction might require further adjustments for larger-scale synthesis. However, below 500 mg

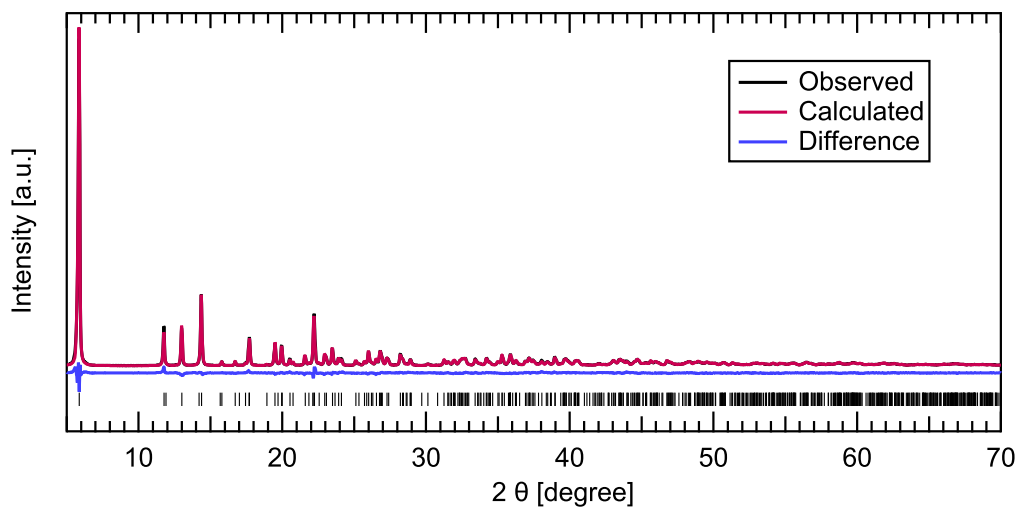


Figure 3.3: Observed, calculated and difference profiles of PXRD data, fitted with the Rietveld method. The PXRD data for BiSal_2 sample at 300 K was refined using the Rietveld method and GSAS-II software [207]. The tick marks represent Bragg peak positions. The fit shows full conversion achieved with mechanochemical synthesis of BiSal_2 . Fitting of the literature structure of BiSal_2 was performed [9].

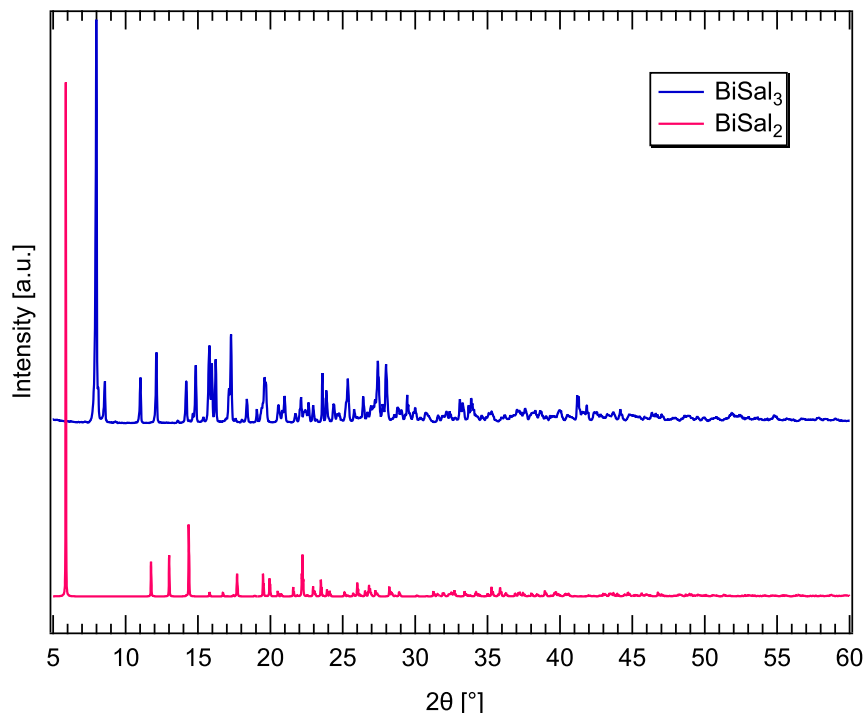


Figure 3.4: A PXRD pattern of BiSal_2 and BiSal_3 , showing characteristic differences. First peak at around 6° and almost evenly spaced, three peaks at 11.75° , 13.0° , and 14.35° help distinguish BiSal_2 from BiSal_3 . The latter shows first, intense peak at 8° , which can be used as a marker of BiSal_3 impurity in BiSal_2 sample.

the reaction can be reproduced with the same conditions, provided the volume of water is proportionally adjusted.

Interestingly enough, some commercially available Bi₂O₃ batches do not convert into BiSal₂ under any circumstances, yielding the BiSal₃ product every time. It took many attempts at synthesis in varying conditions, to notice this peculiarity (Fig. 3.5). We also discovered, that once such batch of Bi₂O₃ is kept in 600 °C overnight, the synthesis of BiSal₂ becomes possible. The heating of such a batch is without any mass loss. There is no apparent difference between batches, according to the labels, including crystalline size.

For the intended synthesis of BiSal₃, apart from using 7 mm balls and 1:6 (Bi₂O₃:HSal) ratio, no heating can be applied to the jars before milling, as a high temperature of reaction mixture favours BiSal₂. High room temperature, exceeding 20 °C, may also cause the partial conversion to BiSal₂, therefore the use of a cooling fan is recommended. The ratio of Bi₂O₃ to HSal should be stoichiometric for the full conversion. The volume of water, amount of ionic salt and other parameters may be used for the BiSal₂.

BiSal₂ amorphous content analysis

Apart from routine BiSal₂ PXRD measurements, amorphous phase control measurements were performed. The goal was to determine whether the BiSal₂ samples become pink due to being a mixed-phase with another, amorphous compound. Pure BiSal₂ samples were spiked with 0, 5 and 10 mass % of lanthanum hexaboride (LaB₆).

The spiked BiSal₂ was analyzed with the Rietveld refinement method (Fig. 3.6). Two-phase model was used, with the first phase being BiSal₂ [9], and the second LaB₆. The unit cell size and atomic displacement parameters for LaB₆ and Bi, O and C atoms in BiSal₂ were refined. Isotropic domain size was also refined for both phases, due to a difference in peak widths likely deriving from a different crystallite size. Additionally, instrument-dependent parameters were also refined, such as peak shape and zero shift.

The fit does not leave any traces of possible, amorphous content, indicating that only the disalicylate and LaB₆ are present in a sample. This is further confirmed by the weight fractions, which show 10.5% for LaB₆ and the remaining 89.5% for BiSal₂.

There is a good agreement between the data and structures, with the $R_w = 15.365\%$. When looking at the fit, it becomes clear that the reason for this value not being lower is the not fully fit peak intensities. The not ideal peak shape fit is true for both of the phases, which enables their direct comparison.

Raman spectroscopy

Raman spectra of the precursors and products of mechanochemical bismuth (III) disalicylate synthesis were measured (Fig. 3.7). The differences between salicylic acid and disalicylate are not strongly pronounced, but visible enough to be able to serve as phase presence indicators.

In order to analyse the possible formation of the [Bi₃₈O₄₄] metal-oxo cluster on the surface of BiSal₂, a comparison of Raman spectra was performed (Fig. 3.8). The [Bi₃₈O₄₄] was crystallized from a BiSal₂ solution, and part of it ground before the measurement. The comparison shows clear similarities between both samples, such as the sharp 1030 cm⁻¹ peaks present in both samples. These similarities are to be expected, due to both structured having Bi-O bonds and incorporated into their structure HSal. However, some features that are relatively intense in the [Bi₃₈O₄₄] cluster data, are not present at all in the BiSal₂ dataset. The 805 cm⁻¹ peak is especially intense, and yet no traces of it can be found in the BiSal₂ data. 1385 and 1483 cm⁻¹ features are other examples of this.

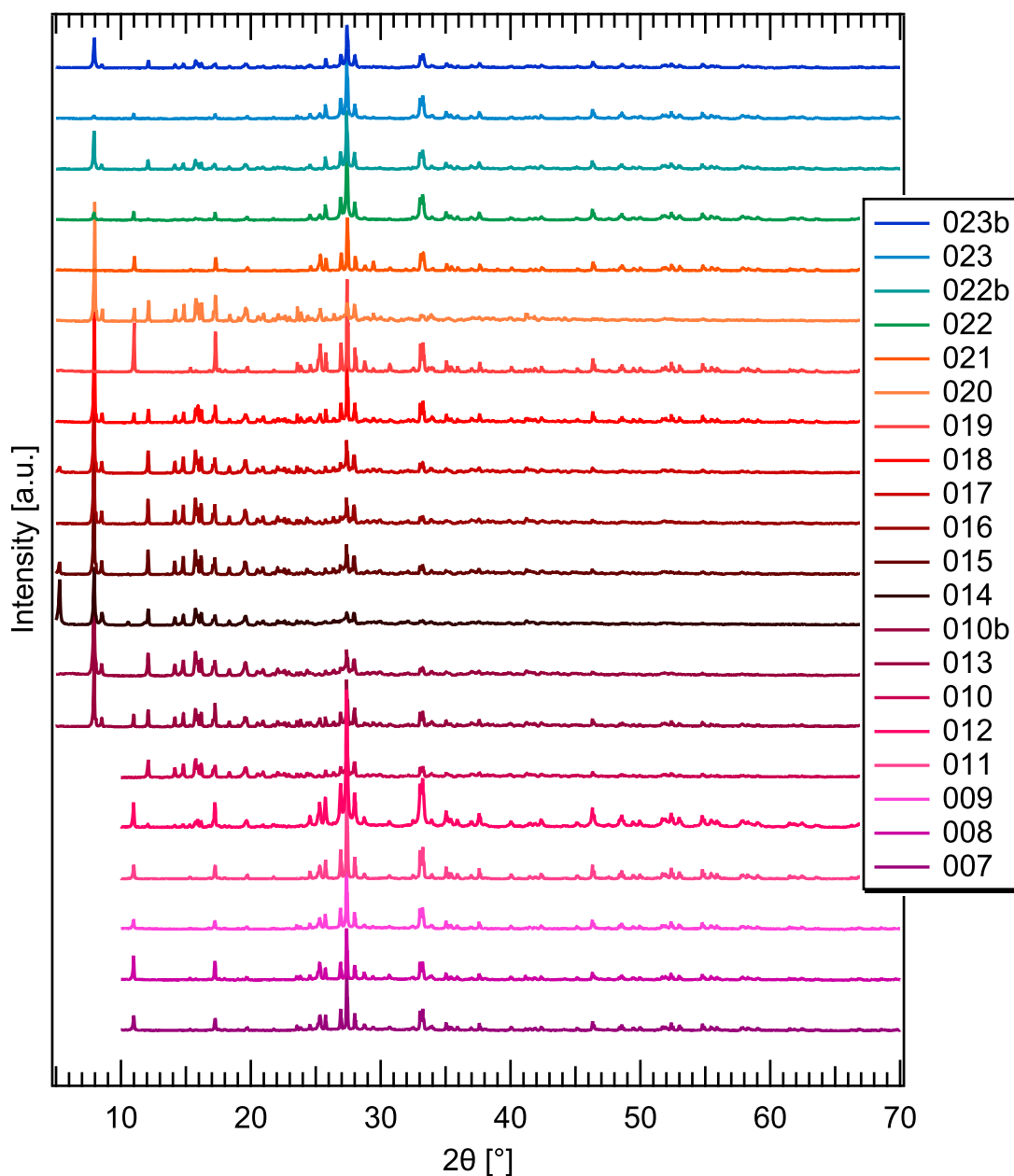


Figure 3.5: PXRD patterns of some of the first samples, synthesized as a means of obtaining BiSal_2 . All of the samples from 007 to 023b were synthesised by modifying the reaction environment of the literature recipe for BiSal_2 , as the original did not yield the expected result [9]. No traces of the desired BiSal_2 could be found, however. Only the BiSal_3 was obtained, and apart from it the HSal and Bi_2O_3 structures can be distinguished in the patterns. Dozens of experiments were performed in that way, before discovering the Bi_2O_3 batch used for the synthesis was unable to react to BiSal_2 , and dozens more before the synthesis of BiSal_2 was perfected.

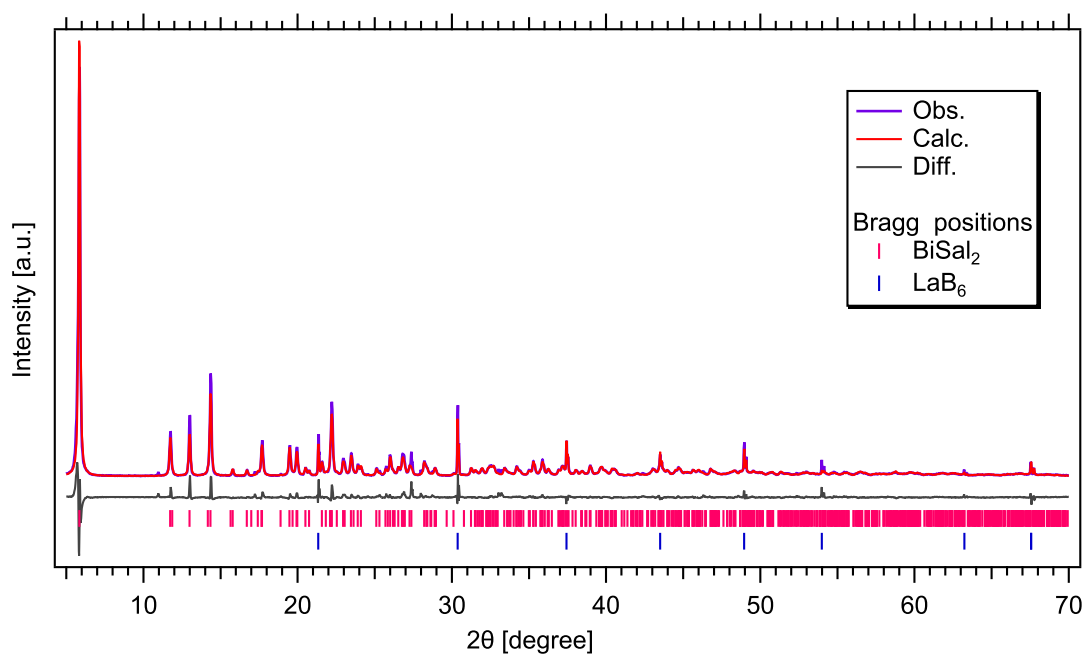


Figure 3.6: Characterisation of BiSal_2 . PXRD dataset, collected for a fresh BiSal_2 sample mixed with 10 mass % of LaB_6 . The goal of this measurement was to find possible amorphous content. The model at 300 K was refined using Rietveld method and GSAS-II software [207]. Observed (obs.), calculated (calc.) and difference (diff.) profiles of the Rietveld fit to the data are shown. The possible Bragg positions are shown for each phase as tick marks. No evidence of an amorphous phase was detected, as the weight fractions of the calculated two-phase model represent the samples well. 10.5% is the calculated weight fraction of LaB_6 in the model. The R_w value of the fit is 15.365%.

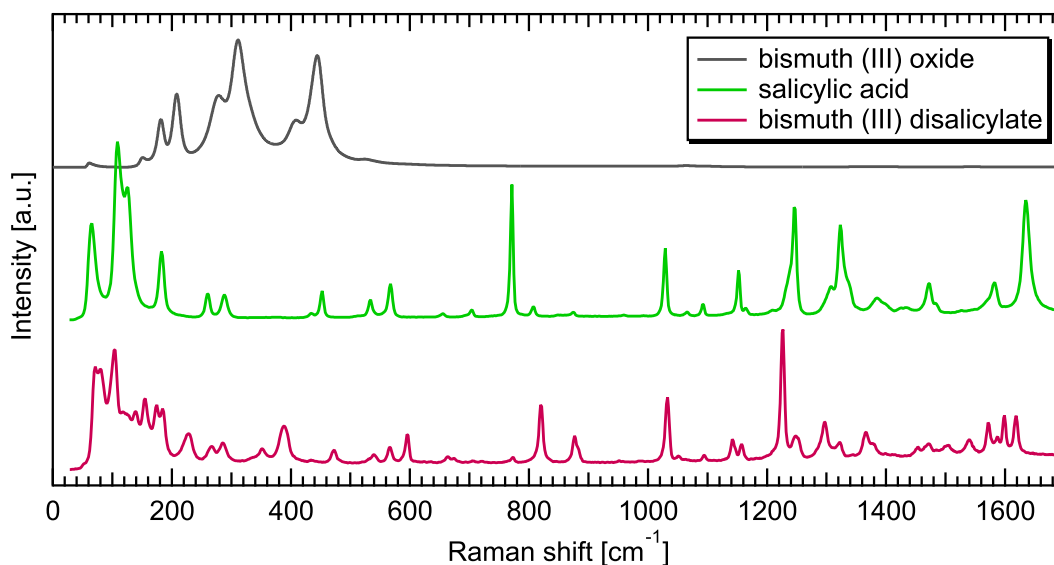


Figure 3.7: A comparison of Bi_2O_3 , HSal and BiSal_2 Raman spectra. The mid-range molecular Raman spectra of BiSal_2 and HSal are similar. Both signals, however, are different enough to enable differentiation between species with Raman spectroscopy. This information could be valuable for example for mechanochemical reaction monitoring with the Raman spectroscopy.

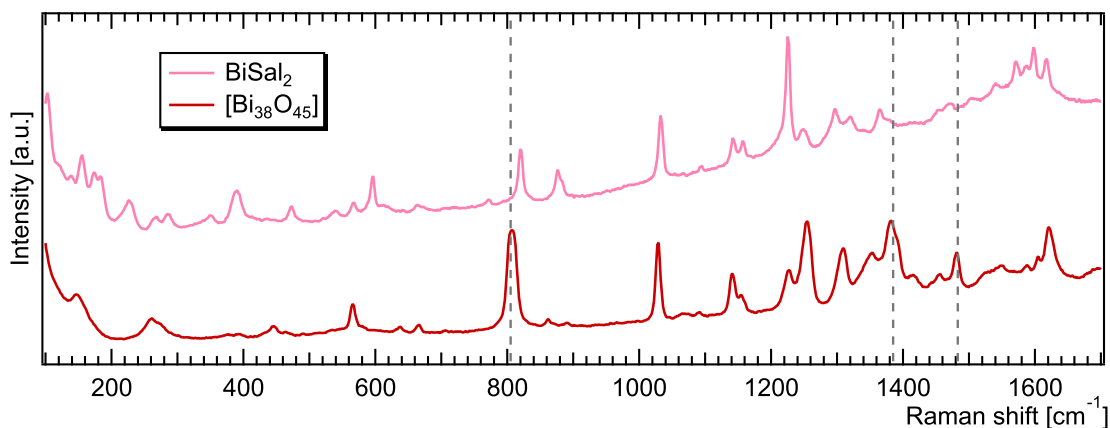


Figure 3.8: A comparison of BiSal_2 and the $[\text{Bi}_{38}\text{O}_{44}]$ metal-oxo cluster Raman spectra. Both species share some of the modes, which is not surprising since both contain Bi-O bonds, as well as salicylate groups. However, some peaks present in the cluster spectra are clearly missing from the BiSal_2 signal. The 805, 1385 and 1483 cm^{-1} are examples of such peaks, marked with the broken, grey lines. If the measured BiSal_2 was mixed with $[\text{Bi}_{38}\text{O}_{44}]$ metal-oxo cluster, all of these peaks would be visible in the BiSal_2 dataset. $[\text{Bi}_{38}\text{O}_{44}]$ data was gathered for a sample of a ground crystal, in order to eliminate peaks associated with a crystalline structure.

BiSal₃ crystallization

Attempts to crystallize BiSal₃ were performed in acetone and DMF, as this compound has an unknown structure. Although it is soluble in both of these solvents, and its solution exhibits an interesting change in color appearing in time, no crystals were obtained. The samples were dissolved and left open to the atmosphere, sealed, and also partially sealed with perforated parafilm, in order to achieve a varying speed of evaporation. Solutions were left for crystallization both unfiltered and filtered, to no apparent change.

The solution of BiSal₃ in DMF was investigated and is described in Chapter 4.

3.3.3 Discussion of the results

Synthesis of BiSal₂ and BiSal₃ was improved in their reproducibility. The reaction conditions were better understood especially for the BiSal₂ synthesis. Heating the reaction mixture before grinding, and maintaining high temperature by limiting the cooling of the jars are some of the most important conditions for obtaining the BiSal₂. Others are the use of two 10 mm balls rather than 7 mm, and the use of ionic salt. These conditions are crucial for successful BiSal₂ synthesis. On the other hand, synthesizing pure BiSal₃ can be achieved at low temperature (without heating of the jars) and use of 7 mm balls. This ensures that no BiSal₂ is present in the desired BiSal₃ product. Differentiating the conditions favourable for BiSal₂ and BiSal₃ syntheses in this way enables targeting which compound should be the result, and can open the doors for targeted large scale production.

When reproducing BiSal₂ synthesis according to the instructions presented in literature failed, the ineffectiveness of certain Bi₂O₃ batches was discovered. This led to finding a solution in heating the particular batch of Bi₂O₃, which in return enables the BiSal₂ synthesis. The phenomenon of some Bi₂O₃ batches not yielding BiSal₂ until processed with heat remains unsolved. However, there are some ideas that were excluded as a possible solution to this question. There is no difference between effective and ineffective batches according to their labels, including crystalline size. There is also no mass loss registered after placing ineffective batch in over 24 hours in 600 °C, even though in this process the ineffective Bi₂O₃ batch activates, and BiSal₂ synthesis becomes possible. The lack of mass loss suggests that the activation of the ineffective batch is most likely not connected to reversing any chemical change. It is also not connected to water adsorption. The heat could, however, influence the structure of crystallites or cause other, physical changes to the Bi₂O₃ powder.

BiSal₂ color change

The color change of initially white BiSal₂ powder to pink can be observed with a naked eye. As mentioned previously, BiSal₂ is a precursor to the [Bi₃₈O₄₄] cluster formation. Worth noting is that this cluster in a crystal form is vividly red, and its matrix solution varies in hue from pink to salmon. This arises a suspicion, that perhaps the BiSal₂ color change is related to some oxo-cluster formation.

The method of spiking BiSal₂ with a known mass % of LaB₆ confirms that no significant amounts of an unknown species can be found in the sample. This includes the amorphous phase and therefore excludes the possibility of the white BiSal₂ powder turning pink being related to the development of a significant amount of a new, chemical compound. It does not exclude undetectable with PXRD traces of a new compound.

The evidence speaking against the theory of BiSal₂ color change relation to the [Bi₃₈O₄₄] cluster formation on the grain surface, is the Raman spectroscopy. Both molecules exhibit a vastly different spectrum, and the solid-state BiSal₂ spectra do not contain traces of the cluster. The Raman spectrum method does not penetrate the sample significantly but rather scans the surface. This method is penetrating only 3 μm for a 633 nm laser, which was used in this

measurement. Because of that, the changes on the crystallite surface should be detectable with that method. Therefore, it is unlikely that the $[\text{Bi}_{38}\text{O}_{44}]$ cluster is responsible for the change of color in solid BiSal_2 . This implies that if the $[\text{Bi}_{38}\text{O}_{44}]$ cluster forms on the surface of the grains, its Raman signal would be detectable when scanning solid-state BiSal_2 . All of the measured BiSal_2 samples were synthesized mechanochemically, and there is no comparison to an unambiguously pure BiSal_2 . Because of that, the shown BiSal_2 spectra could contain traces of an unknown oxo-cluster, or another type of molecule.

Because the color change of the powder is unambiguous and occurs when after it is exposed to the environment, this theory is not unreasonable. An undetectable amount of an unknown compound could cause a visible change in the white powder appearance.

3.4 Bismuth (III) gallate – BiGall

3.4.1 Reaction conditions

The synthesis of bismuth (III) gallate (BiGall) was performed similarly to the salicylates, with changing the reaction environment.

The 1:2 and 1:4 ratios of Bi_2O_3 to gallic acid (HGall) were tested. 200 mg of the reaction mixture was used with a 10 ml jar and two 10 mm balls. An addition of 1-2 weight % of NH_4NO_3 was used for ILAG synthesis. For LAG and ILAG methods, apart from water, acetone, DMF, ethanol, and propanol were tested as the liquid, with 50 μl per 200 mg of the reaction mixture. Water and propanol were used also at different volumes, from 30 to 150 μl per 200 mg of the reaction mixture, pure and as water-propanol mixtures.

Heating of the reaction mixture inside of the jars for 30 min to 85 °C was implemented for chosen samples. The time of grinding varied from 30 to 45 min. The cooling fan of the mill was turned off, and the frequency of grinding was set to 30 Hz. After each synthesis, both batches were transferred into separate containers, for later PXRD pattern measurements.

3.4.2 Results

The products of BiGall synthesis were measured after each mechanosynthesis using X-ray diffraction. The patterns were analyzed, looking for the purest product. The intensity of highest Bi_2O_3 peak (27.5°) remaining in the majority of samples was compared to the BiGall peak next to it (26.9°) for a visual clue of given sample purity, that was later additionally analyzed with Rietveld refinements. This then was directly used to establish the best possible result of manipulating the reaction environment.

Mechanochemical synthesis of both molar ratios of 1:2 and 1:4 (Bi_2O_3 :HGall) results in a pea-green powder, determined with PXRD to be BiGall (Fig. 3.9). The stoichiometric 1:2 ratio yields fewer leftover precursors (Fig. 3.10).

The type of mechanosynthesis was chosen based on a comparison of dry grinding, LAG and ILAG results. The product of dry grinding contains mainly unreacted Bi_2O_3 (Fig. 3.11, DG), both with and without heating of the jars. Besides the oxide, only broad peaks of BiGall are visible in PXRD. LAG method improves the reaction significantly, and its product shows mostly BiGall peaks. ILAG with 1-2% of NH_4NO_3 further minimizes the amount of leftover Bi_2O_3 , and improves achieving repeatably good results, however, it is not a necessary step for obtaining BiGall yield. The heating of the jars with the reaction mixture also improves the reproducibility of the reaction. Moreover, 45 min of grinding yields better conversion over the 30 min experiments.

In terms of the best solvents for mechanosynthesis, both water and propanol in LAG yield BiGall (Fig. 3.12). Acetone and ethanol work as well, however, the product conversion to BiGall and its crystallinity are worse. The use of DMF results in a different, unidentified product.

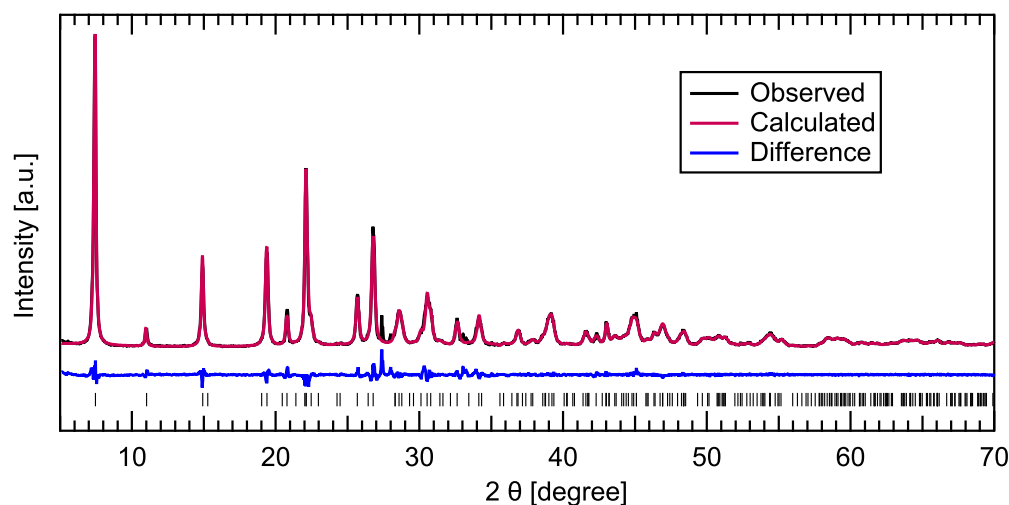


Figure 3.9: Observed, calculated and difference profiles of PXRD data, fitted with the Rietveld method. The PXRD data for BiGall sample at 300 K was refined using the Rietveld method and GSAS-II software [207]. The tick marks represent Bragg peak positions. The fit shows nearly full conversion achieved with mechanochemical synthesis for BiGall. The Literature model of BiGall was used for the refinement [221].

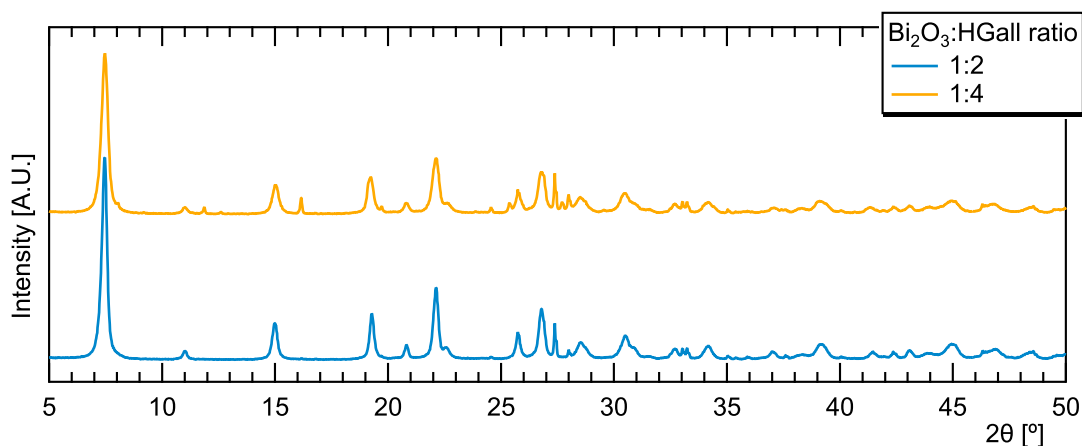


Figure 3.10: PXRD diffraction patterns of two ILAG samples, synthesized with water. The 1:2 (Bi_2O_3 :HGall) ratio is superior due to the fact that the Bi_2O_3 leftover is less pronounced. The 1:4 ratio results in a clearly visible HGall signal, at 12° and 16.1° , apart from more pronounced Bi_2O_3 peak at 27.5° . This result matches the stoichiometry of BiGall.

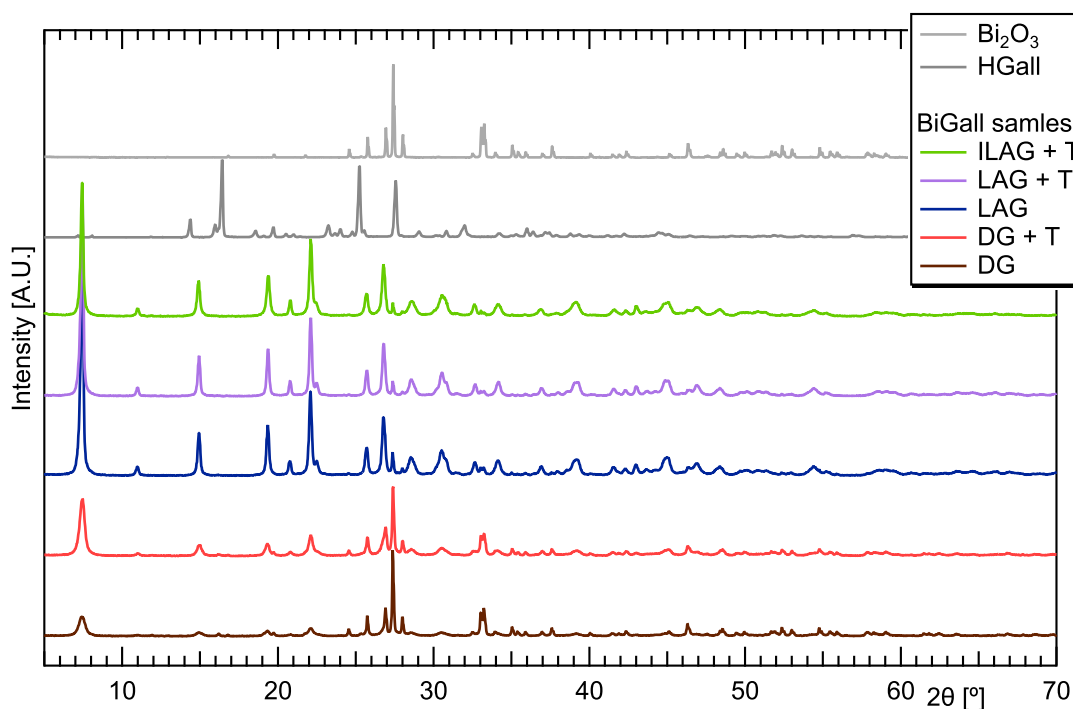


Figure 3.11: PXRD patterns showing the differences between dry grinding (DG), LAG and ILAG samples, in comparison to pure precursors. Dry grinding results in an insignificant conversion to BiGall, consisting mostly of unreacted Bi₂O₃. However, implementing heating of the jars for 30 min to 85 °C before synthesis does improve dry grinding. LAG reaction is a significant improvement, leading close to a full conversion. Heating improves LAG slightly, similarly to using ionic salt (ILAG). Using LAG method with heating is enough to obtain BiGall, however, using ILAG does improve the process in terms of reproducibility.

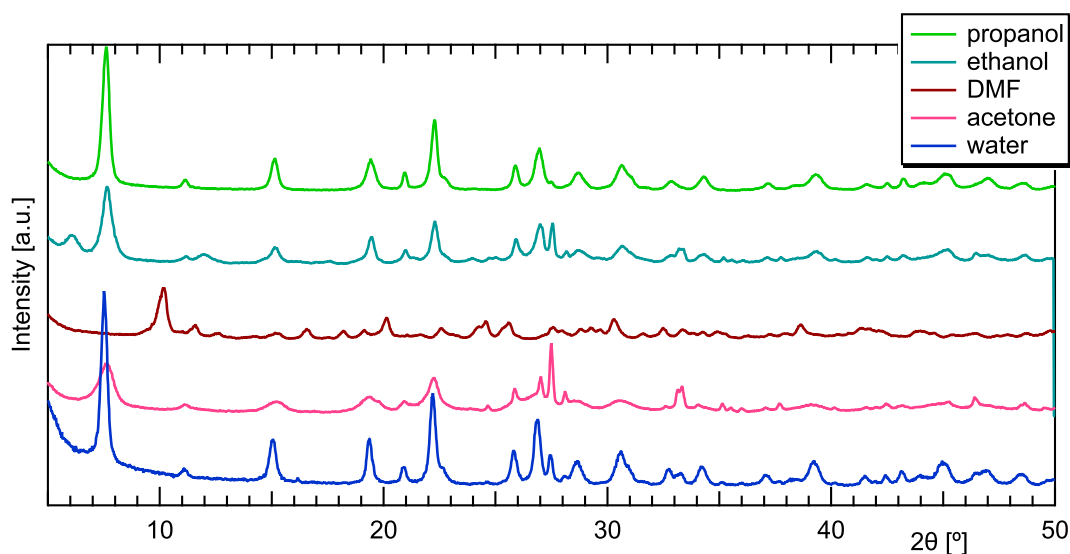


Figure 3.12: PXRD patterns of BiGall samples synthesized with LAG method, using different liquids. Propanol, water, ethanol and acetone all show BiGall peaks. The acetone sample shows a high content of leftover Bi_2O_3 , which we suspect to be caused by evaporation, resulting in dry grinding. Ethanol apart from poorly crystalline BiGall, shows a very small amount of other an unknown phase, and higher Bi_2O_3 amount than water and propanol. DMF yields an unknown product. Water and propanol are superior for the LAG synthesis of BiGall.

Because water and propanol showed the best result, their mixtures were implemented in a search for full conversion to BiGall (Fig. 3.13). However, it did not improve the reaction and therefore water was chosen as the best liquid to use for this reaction.

BiGall crystallizes as a hydrate, therefore the amount of water is important in order to obtain a well-crystalline sample. Adjusting the amount shows that $100 \mu\text{l}$ per 200 mg of reaction mixture yields the best results (Fig. 3.14). According to its structure, a minimum of $26.8 \mu\text{l}$ of water for 200 mg of BiGall is necessary for obtaining a fully crystalline sample, which is exceeded with the volume best suited for LAG method. It is expected that too low volume results in a reaction close to dry grinding, and too high volume causes the reaction mixture to flow with the liquid around the grinding balls.

Crystallization

Crystallization from mechanochemically synthesized BiGall partially dissolved in DMF solution was attempted as a means of confirming its structure. Other solvents, such as water, acetone and ethanol were also tried, but with worse levels of dissolution and no crystalline yield. BiGall is not well soluble in any of these solvents, but DMF becomes green after couple of days, and therefore some amount of the powder was visibly dissolved. The solution in DMF was filtered multiple times, before being left for a slow crystallization. Green sediment precipitated from the solution, next to transparent crystals. Single crystal diffraction revealed the crystals to be gallic acid.

A solution in water was also made and left for crystallization afterwards. This attempt gave no single crystals whatsoever. Similarly to DMF, green sediment precipitated.

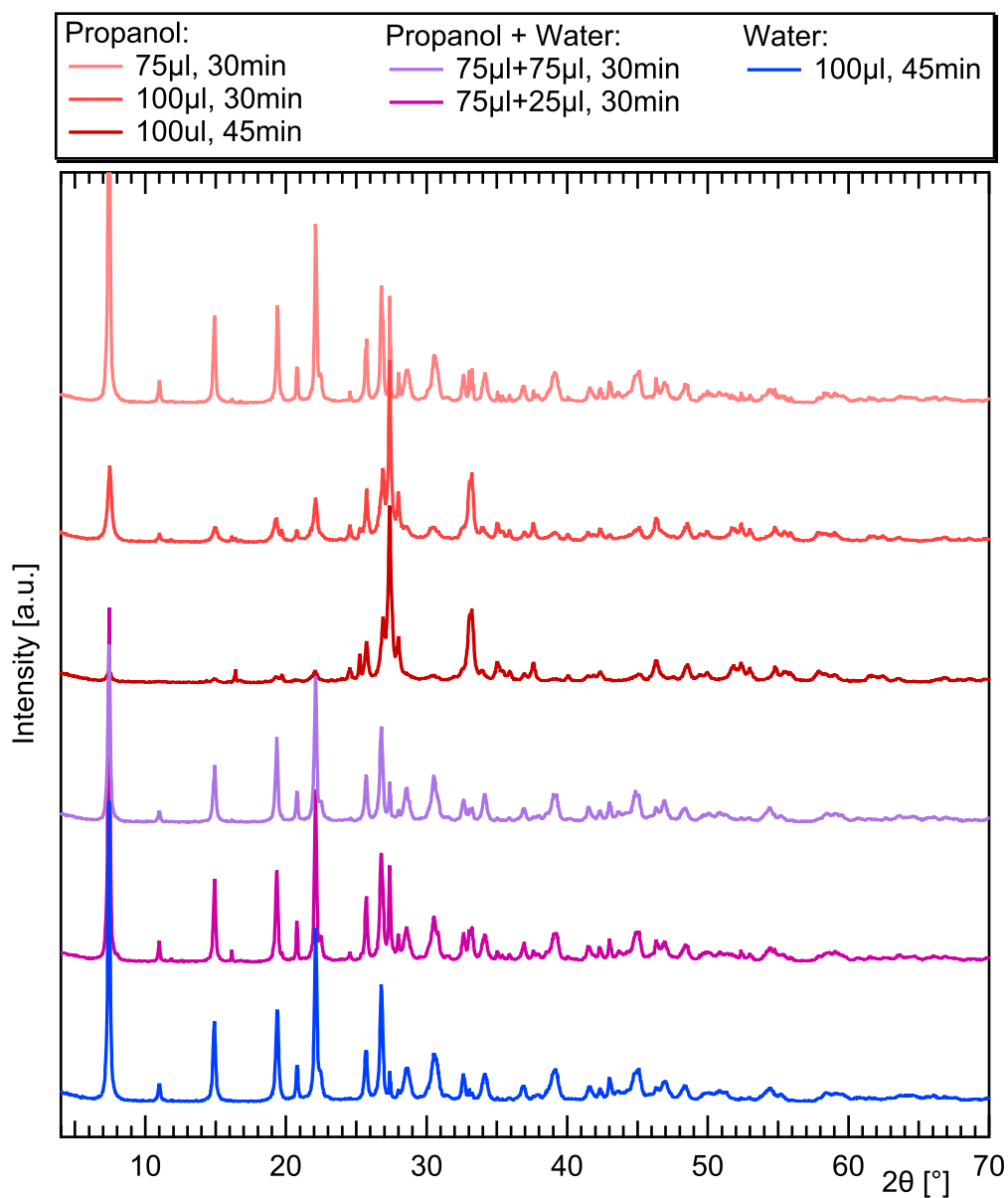


Figure 3.13: PXRD of BiGall samples exploring the use of water-propanol mixture, and its impact on LAG synthesis results. Using pure water provides consistently higher conversion to the BiGall product, than pure propanol and the mixtures of both propanol and water. This can be seen when looking at the 27.5° Bi_2O_3 peak, which is relatively the lowest in a pure water sample.

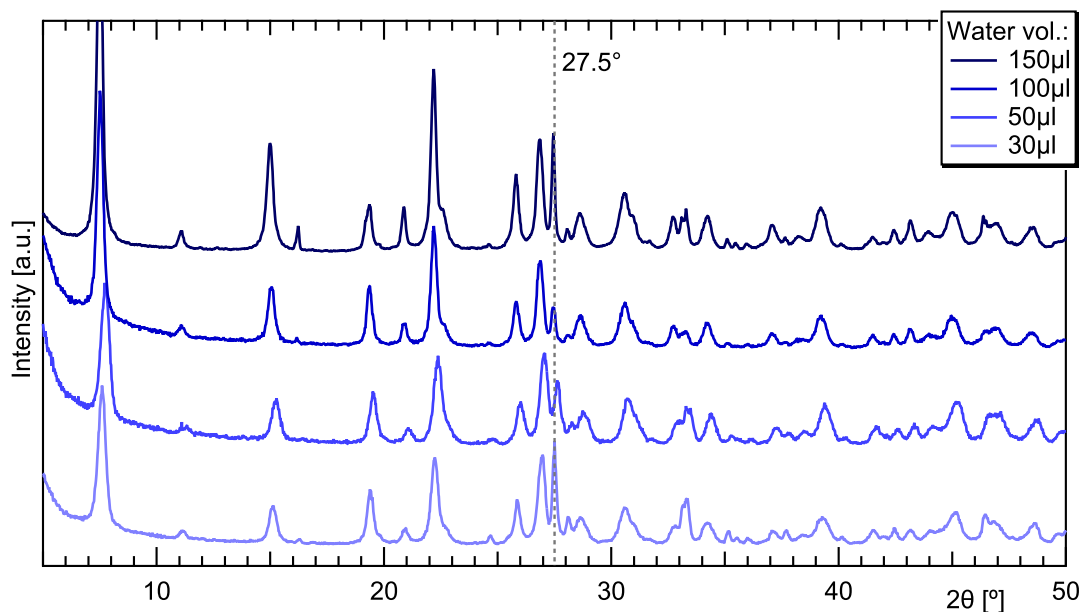


Figure 3.14: PXRD patterns of ILAG samples, where the influence of the used water volume can be seen. The use of 100 μl per 200 mg of reaction mixture results in the highest conversion of precursors to BiGall, indicated by the lowest 27.5° peak. This peak is indicative of the leftover Bi_2O_3 presence in the sample.

3.4.3 Discussion of the results

Based on PXRD evidence, mechanochemical synthesis of BiGall was achieved with high purity. Although crystallization of BiGall dissolved in water, ethanol, acetone and DMF was unsuccessful, due to its low solubility, the powder diffraction evidence is satisfactory for claiming the reaction produce as BiGall. It is based on the literature structure BiGall [221].

Full conversion to BiGall, without Bi_2O_3 27.5° leftover peak, was not achieved. The amount of unreacted mixture was ultimately minimized for the best result. The established, best conditions are reliable in producing BiGall synthesis. It is most likely possible to obtain full conversion when mechanochemically synthesizing BiGall, if a new condition is introduced. Change of one of the precursors, alternative ionic salt, or alternative liquid could be such conditions. However, due to the seemingly endless possibilities, the resulting reliable mechanochemical synthesis of BiGall is a satisfactory achievement.

3.5 Bismuth citrate – BiCit

3.5.1 Reaction conditions

For the synthesis of bismuth citrate (BiCit), two synthesis methods were implemented. Mechanochemical grinding methods and synthesis by aging, in a humid environment.

Multiple ratios of Bi_2O_3 to citric acid (HCit) were tested mechanochemically and by aging, 2:1, 1:1, 3:4, 1:2, 1:3 and 1:4. Only a 1:2 stoichiometric ratio was used for synthesis with HCit monohydrate.

The aging was performed inside a desiccator, filled with distilled water. The reaction mixture, without additives, was placed in a dish (Fig. 3.15). The desiccator with the reaction mixtures was then insulated, preventing water from escaping the system, and placed in a drier

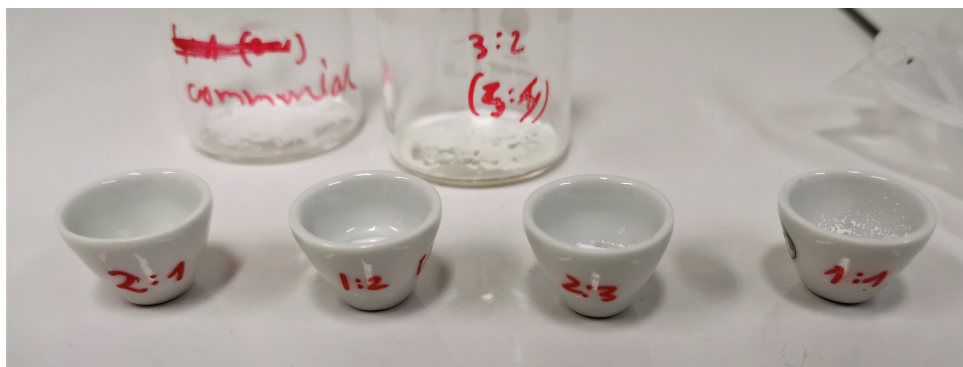


Figure 3.15: Containers used for the synthesis of BiCit by aging. The process was performed in small crucibles, beakers, and Petri dishes, placed for the time of synthesis in a desiccator.

set to 50–60 °C for 7 days. After that time, each batch of samples was retrieved, dried, ground, and its PXRD pattern measured.

For the mechanochemical synthesis, 300 mg of the reaction mixture and 10 ml jars were used. An addition of 2-5 weight % of NH_4NO_3 or KNO_3 was used for ILAG synthesis. Acetone, DMF, ethylene glycol, ethanol, methanol and water were used as the liquid in LAG and ILAG, kept at 75 μl per 300 mg of the reaction mixture. For the water, volumes from 75 to 100 μl were tested.

Heating of the reaction mixture inside of the jars for 30 min to 85 °C was implemented for most samples. The time of grinding varied from 4 to 50 min. The cooling fan of the mill was at turned off, and the frequency of grinding was set to 30 Hz.

Commercial BiCit was ground with LAG method, using water as a liquid, and aged in described above conditions for testing.

The PXRD measurements of BiCit were done for samples at different steps of drying. Some of the samples were intentionally mixed with water to create a suspension, which was then slowly dried, while PXRD pattern was repeatedly measured.

3.5.2 Results

In the case of BiCit, the synthesis proves to be less straightforward. However, using Raman and TGA characterization aided in the understanding of the PXRD data, and the synthesis process.

PXRD

The mechanosynthesis attempts for BiCit at first resulted in an amorphous product, hard to classify. Therefore, the aging of Bi_2O_3 with HCit was tested. Afterwards, dried and ground aging product was measured, revealing that a partial reaction occurred, resulting in PXRD matching commercially available BiCit (Fig. 3.16, a, structure 2a). aging in a stoichiometric 1:2 (Bi_2O_3 :HCit) ratio, in a small surface container, results in nearly full conversion.

Dry grinding experiments yield only an amorphous product. The use of water in experiments allows a well crystalline product to develop. No other than H_2O liquid yields successful BiCit synthesis. The assistance of ionic salt proves not to be necessary for improving the reaction. Therefore, LAG process is recommended, using 75 μl of water for 200 mg of the reaction mixture. The heating of the reaction mixture in jars is on the other hand a necessary step for the reaction to occur.

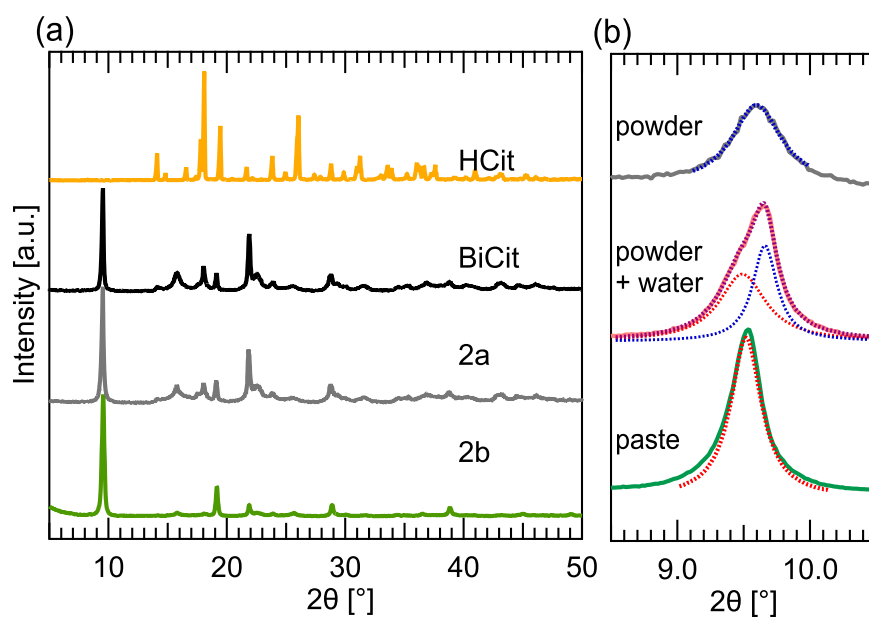


Figure 3.16: PXRD patterns for BiCit synthesis. **(a)**, Simulation of HCit PXRD pattern, compared to measured PXRD patterns of commercial BiCit, synthesized **2a** and synthesized **2b** BiCit structures. The **2a** and **2b** measurements come from the same sample, synthesized by aging 1:1 (Bi_2O_3 :HCit) reaction mixture. **2a** was measured as a dry powder, and **2b** as a wet paste. **(b)**, PXRD patterns showing transformation of mechanochemically synthesized BiCit, from **2a** to **2b** structure, from dry powder to wet paste, formed by drying suspension. The graph is focused on the first peak of both structures, showing the change in its position when transforming from **2a** to **2b**. The peaks were fitted with Lorentzian functions, highlighting two-peak contribution in the intermediate state.

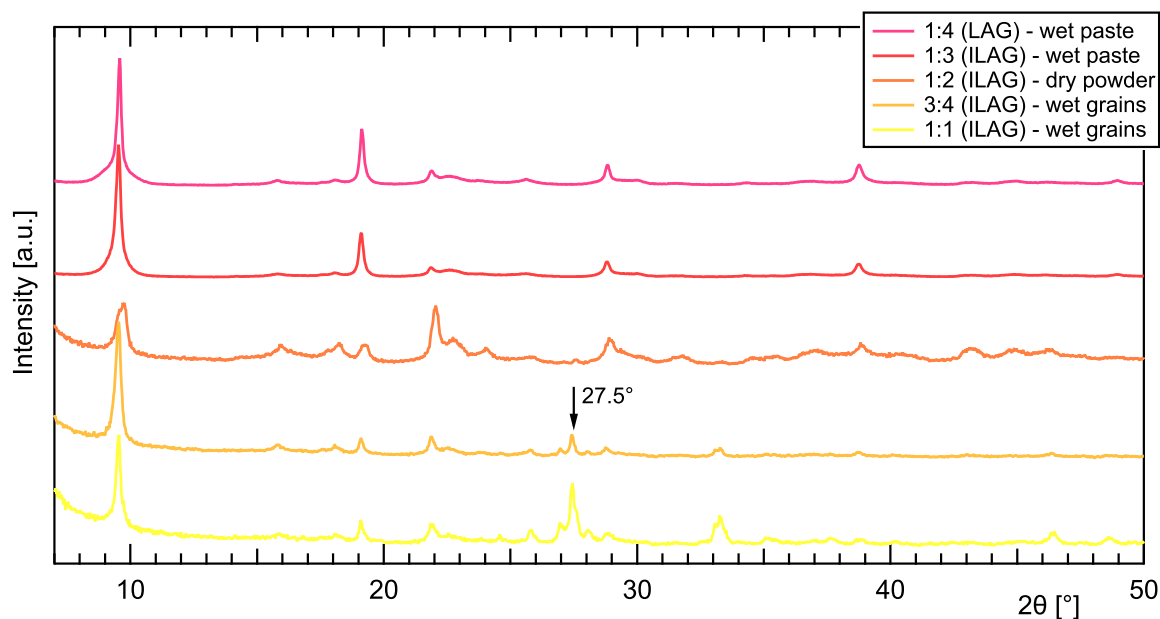


Figure 3.17: PXRD of mechanochemically synthesized samples with different Bi_2O_3 to HCit ratios, measured right after synthesis. The conditions for each sample were the same, apart from the use of LAG method for the 1:4 ratio sample. Although each sample used $75 \mu\text{l}$ of water, the resulting consistency was not the same in all cases due to evaporation while heating was implemented before each grinding. Not all containers were well sealed while heating, and for these samples, water was added to the reaction mixture before not after the heating. Varying ratios of precursor mixture also contribute to the varying amount of water required for achieving the same consistency. However, these results clearly show an excess of Bi_2O_3 for 3:4 and 1:1 samples and the 27.5° peak. Additionally, these measurements show that the amount of water in the system influences not only the structure but also the synthesis itself. For the sample with a 1:2 ratio, the water evaporated significantly in the furnace, resulting in drier LAG. It, therefore, shows a poorly crystalline sample, with **2a** structure visible in the pattern. Samples with more water (1:4 and 1:3) show the **2b** structure.

The presented aging process is not as reliable as mechanochemical grinding. However, implementing mixing and a container that allows for better contact between the reaction mixture grains, increases the chemical reaction yield, and even allows for a full conversion. This was proved with two samples, prepared with reaction mixtures in stoichiometric ratios, made using aging. One of them was prepared in a small, porcelain crucible, with curved bottom. The second one is in a standard size Petri dish. Both were filled with 1000 mg of the reaction mixture. The first one resulted in a nearly full conversion, whereas the second did not, due to the reaction mixture being more scattered on the surface of the dish.

PXRD of a mechanochemical product revealed in some cases an unknown structure (**2b**) next the structure of commercial BiCit (**2a**) (Fig. 3.16, a). All of the PXRD data contained the peaks associated with **2a**, which indicated that the conversion to **2b** occurring in some samples was not full. Adjusting the time of grinding and Bi_2O_3 :HCit ratio did not yield "pure" **2b** (Fig. 3.17). However, it was clear that any ratio of Bi_2O_3 to HCit higher than 1:2 yields excess of Bi_2O_3 , which can be seen in PXRD as the 27.5° peak. No synthesis resulted in obtaining only the new, **2b** peaks. However, full conversion of reaction mixture to **2a** was achieved at 30 min of grinding, with 1:2 (Bi_2O_3 :HCit) stoichiometric molar ratio.

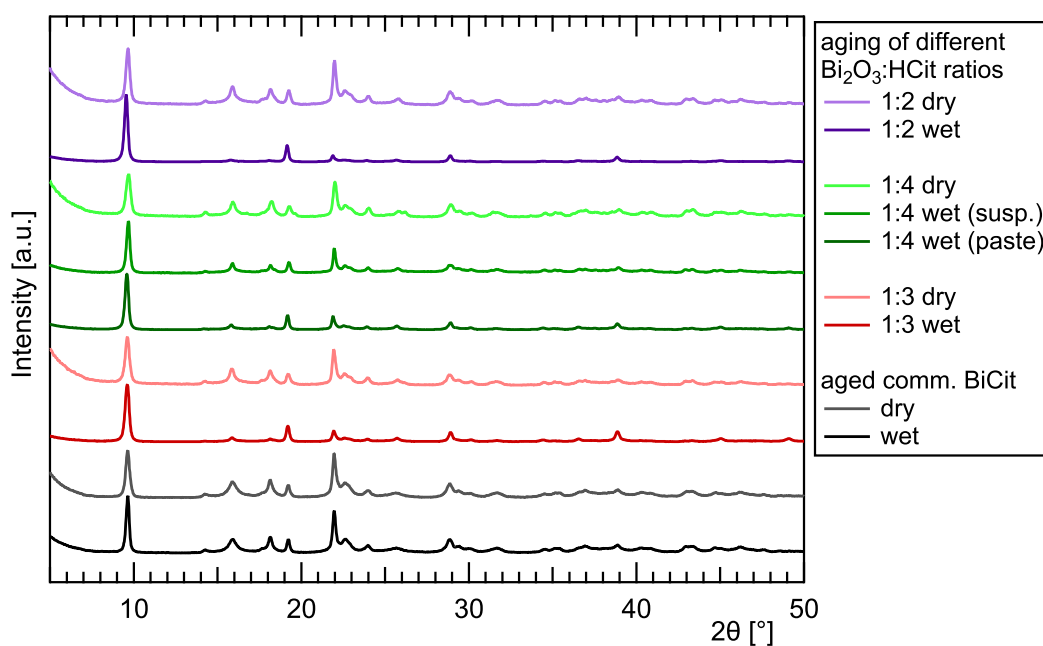


Figure 3.18: PXRD patterns of aged samples, in different Bi_2O_3 to HCit ratios. The reaction mixtures, each in a separate vessel, were placed in a desiccator, filled at the bottom with water. The sealed desiccator was then placed in a drier set to 60°C , for 7 days. The samples were then retrieved and let dry. The measurements were done for dry samples and then repeated after they were mixed with a small amount of water. All synthesized samples are showing the change from **2a** to **2b** structure, regardless of the Bi_2O_3 to HCit ratio. The commercial BiCit sample shows no structural change after aging. The measurement was normalized for the first peak ca. 9.5°

Ratios with a higher contribution of HCit than 1:2 (Bi_2O_3 :HCit) were also analyzed to find one, that would result in full stability of the **2b** structure [3.18](#). Although seemingly all of the ratios showed the **2b** structure when wet, none retained it after drying. Because all of the ratios reverted to the **2a** structure, the 1:2 stoichiometric ratio of commercial BiCit is the most reliable to look at the **2b** structure.

Yellow precursor mixture, from a dry powder, turns into a white paste after grinding. It was discovered that **2b** is present in the product measured right after the reaction, while the consistency of the sample resembles a wet paste (Fig. [3.16](#), b). After the sample is completely dry, however, only **2a** structure can be seen. In an attempt to rehydrate an already dry sample, it was mixed with water, forming a suspension or a paste, depending on the amount of water. While drying, right after the glistening disappears, leaving matt, yet still wet paste, the structure of **2b** emerges in PXRD. After fully drying, the PXRD patterns contain exclusively **2a** structure. Transforming the samples from **2a** back to **2b** by mixing with water, and the other way when drying proves the change in structure to be reversible.

The same process does not work in the case of commercial BiCit, its structure remains as **2a** even when exposed to excess water (Fig. [3.19](#), a). However, grinding 200 mg of commercial BiCit with the addition of $75\ \mu\text{l}$ of water "activates" the compound (Fig. [3.19](#), b). After that, its structure changes from **2a** to **2b** when exposed to excess moisture, and back when drying. aging commercial BiCit does not activate it in the same way (Fig. [3.18](#), commercial BiCit).

No difference was detected between results with HCit monohydrate and anhydrous HCit. Samples of BiCit were synthesized with HCit monohydrate using the best reaction conditions,

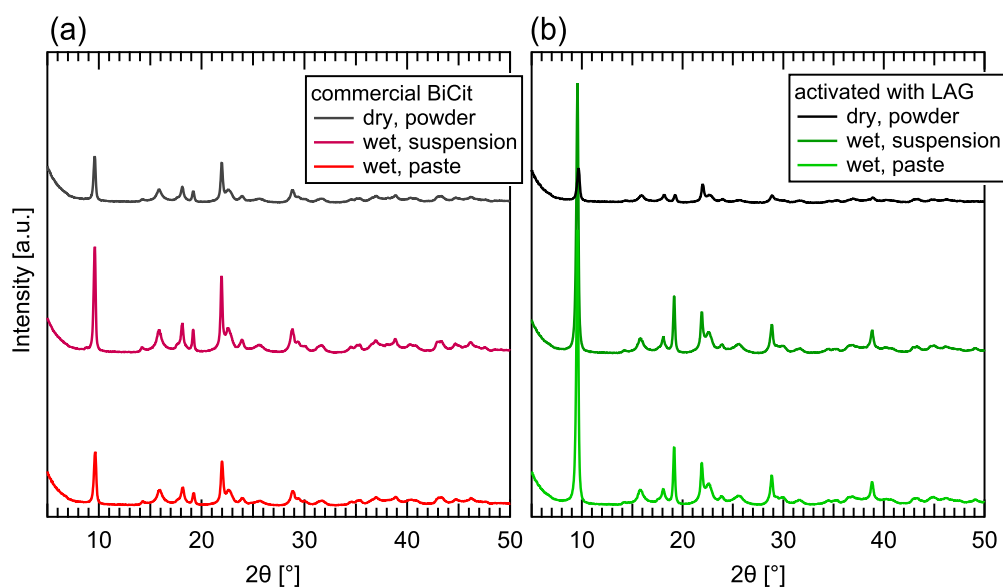


Figure 3.19: PXRD patterns of commercial BiCit. **a)** A sample was first measured dry, then mixed with water and measured while drying, and changing from suspension to a paste. The experiment showed that the **2a** structure of commercial BiCit does not change into **2b**, unlike synthesized BiCit. **b)** Sample of commercial BiCit activated by LAG. The grinding was implemented for 300 mg of commercial BiCit, in 10 ml stainless steel jars, with two 10 mm stainless steel balls. 75 μ l of water were added to the LAG process. The jars with reaction mixture were placed and heated to 85 $^{\circ}$ C for 30 min, before grinding for 30 min in 30 Hz frequency. The result was activating the commercial BiCit – the structure changes from **2a** to **2b** after the powder is mixed with water, and allowed to slowly start drying to form a paste.

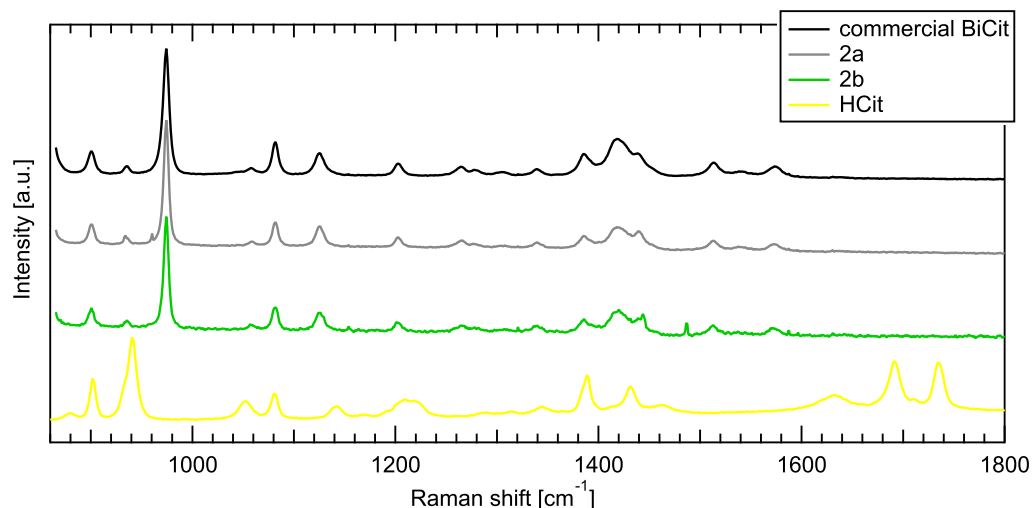


Figure 3.20: Raman spectrum of commercial BiCit and synthesized **2a** and **2b** structures in compare to HCit. The synthesized samples and commercial BiCit measurements show no difference. The Raman spectrum of the synthesized **2a** and **2b** structures also does not differ. There are no traces of HCit in either BiCit measurement, synthesized or commercial. This indicates that the synthesized compounds are just as pure as the commercial one, and additionally **2a** and **2b** are not chemically different from each other. Sharp spikes in the **2b** spectrum, not matching peaks from **2a** and BiCit measurements, come from the detector background and are visible due to a longer signal gathering time, required for the wet sample.

resulting in a full conversion to BiCit. The **2a** and **2b** structures are both present in the samples made with HCit monohydrate, with the **2b** being present only in the wet samples.

Raman spectroscopy

Raman spectra of synthesized aged and mechanochemical BiCit, and the commercial BiCit were measured along with HCit. The spectra were gathered for dry powders, rehydrated paste and drying suspensions, to directly correspond with the PXRD data (Fig. 3.20).

Comparing the results, it is clear that the synthesized samples have a spectrum identical to commercial BiCit. At the same time, no peaks associated with citric acid are found in the samples, supporting the claim of full conversion. The bands in 1600–1800 cm⁻¹ region, associated with [-COOH] group, is present only in the pure citric acid, due to the [-OH] part of that group releasing proton to bond with bismuth in the BiCit. This is further proving the success of aging and mechanochemical synthesis routes. However, the most interesting detail is that the dry and wet measurements do not differ in terms of peak positions, or intensities. This stands in contrast with PXRD, where two structures were detected – **2a** for dry powder and **2b** for wet paste.

TGA

The TGA measurements allowed for additional comparison of the synthesized BiCit samples with commercial BiCit (Fig. 3.21). It was established that the excess of water in each measurement evaporates below 100 °C, and therefore normalizing of the TGA data to 100% of mass at 100 °C was used for easier comparison of the samples (3.21).

The decomposition of post-reaction BiCit mixtures can be divided into three steps, the first being combustion of citric acid (200 °C):

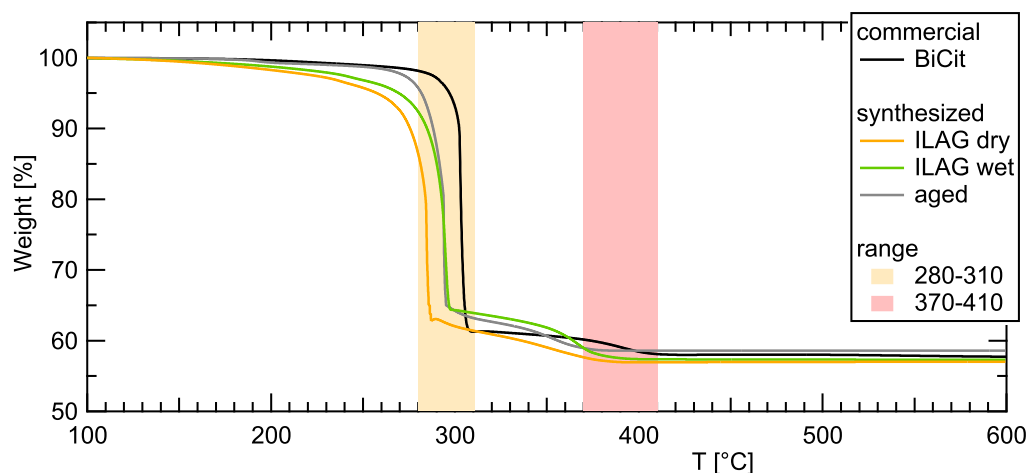
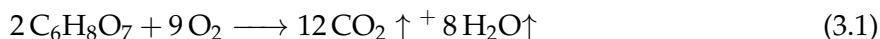
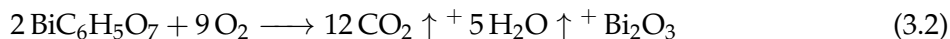


Figure 3.21: TGA measurements of commercial and synthesized BiCit, with two decomposition stages. Temperature ranges for two decomposition stages are highlighted in orange and red. The first one (orange) is associated with the combustion of the majority of BiCit to Bi_2O_3 , and partially to species such as bismuth (III) carbonate. The latter (red) is the further reaction of partially decomposed BiCit to Bi_2O_3 . No significant traces of leftover citric acid, which would decompose at 200 °C, can be detected in the curves presented for synthesized BiCit. The offsets in temperature, resulting in temperature ranges rather than a single decomposition temperature for each sample, are due to particle size differences. The measurements were normalized to 100% of mass at 100 °C to erase water content bias.



This step is unsurprisingly pronounced in samples synthesized in a non-stoichiometric ratio, with an excess of HCit. It can be also detected in some samples synthesized by aging (Fig. 3.22, e), where conversion was not full. Attributing this decomposition step to HCit combustion is confirmed by TGA of pure HCit (Fig. 3.22, a). A certain amount of mass is left in pure HCit decomposition, most likely due to incomplete combustion, leaving carbon as a product. When the temperature increases further, carbon oxidizes to differentiation, leaving no mass behind. This observation is consistent with TGA measurements found in literature [186]. The contribution of incomplete combustion can be increased due to high temperature increase rate, and crystallite size, and is the reason a third decomposition step is isolated.

The second step in decomposition of BiCit samples is BiCit combustion (280–310 °C):



This step is the most prevalent in the synthesized samples with correct ratio, after adjusting for water loss below 100 °C. It can be distinguished both in commercial (Fig. 3.22, b), and synthesized (Fig. 3.22, c-f) BiCit samples.

The third step is a result of not fully decomposed BiCit, decomposing further into Bi_2O_3 (270–410 °C). This process most likely involves BiCit combusting to bismuth (III) carbonate ($\text{Bi}_2(\text{CO}_3)_3$), then bismuth (III) subcarbonate ($\text{Bi}_2\text{O}_2(\text{CO}_3)$), to then finally yield Bi_2O_3 , which is supported by literature data [98, 157]. The proposed mechanism of the third step of BiCit samples decomposition, therefore, consists of three stages:



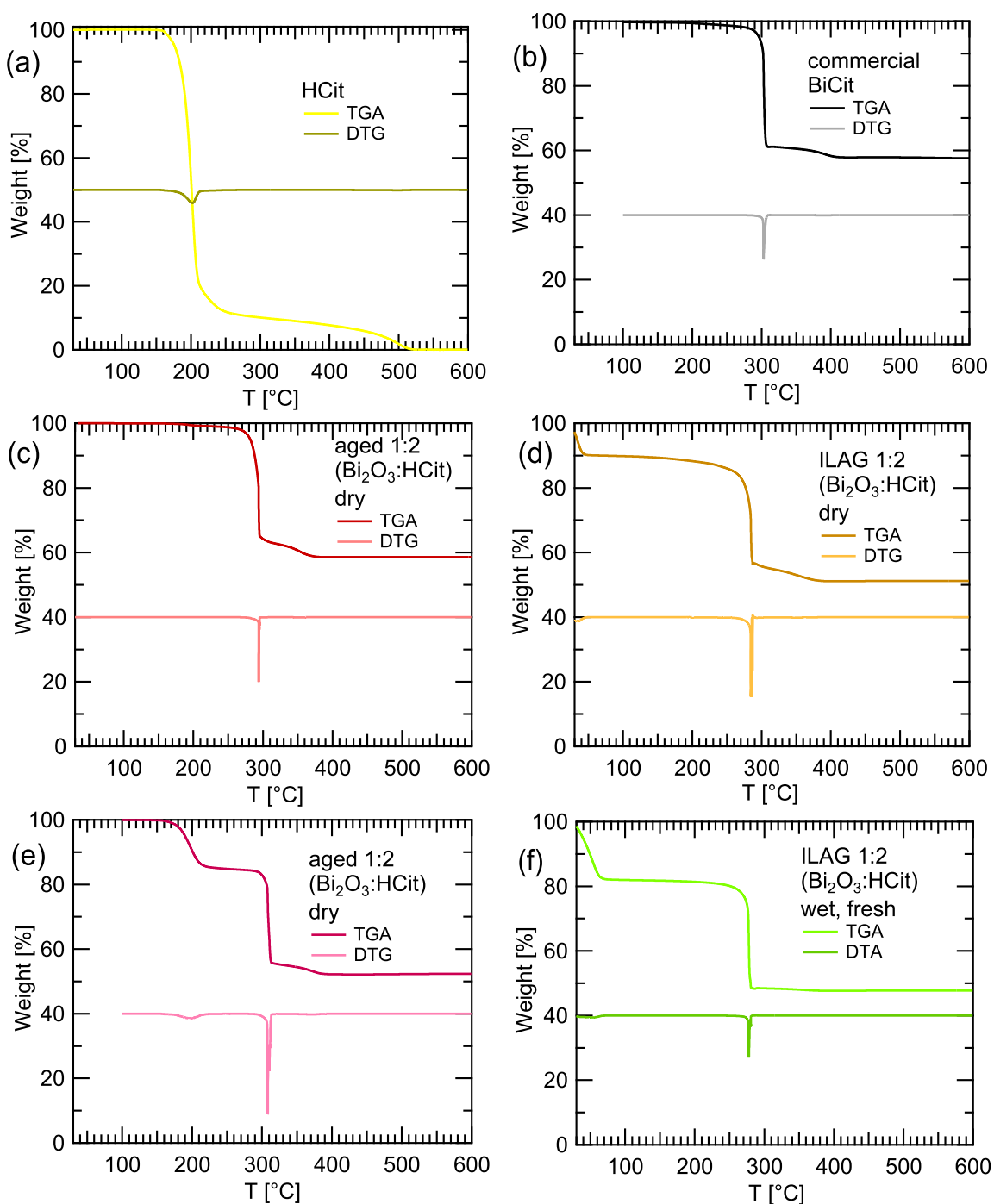
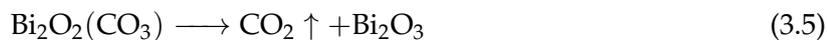
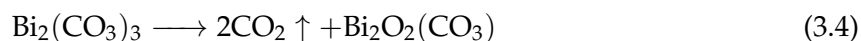


Figure 3.22: TGA and DTG curves for various samples. The measurements were performed as a temperature ramp, increasing by 3-5 °C/min, from the room temperature up until 600 °C, with some, mentioned exceptions. Detailed description can be found on the following page.

Figure 3.22 consists of six graphs of TGA measurements, each representing a different sample:

- (a) Commercial citric acid. The measurements show the majority of a sample decomposes at 200 °C. The 10% of mass left are most likely carbon, a product of incomplete combustion, oxidized in higher temperatures to CO₂.
- (b) Commercial BiCit. The measurement started after the sample was exposed to 100 °C for 10 min. The TGA curve is similar to those of pure, synthesized BiCit, with no notable differences.
- (c) BiCit synthesized by aging 1:2 mixture of Bi₂O₃ and HCit. The sample characterizes nearly full conversion to the BiCit. The stage attributed to the decomposition of pure citric acid right below 200 °C is only slightly visible. The reaction mixture was aged in a packed crucible, allowing for a good contact between grains and full conversion to BiCit by aging.
- (d) BiCit synthesized by ILAG of 1:2 mixture of Bi₂O₃ and HCit. The sample characterizes full conversion to BiCit. The stage attributed to the decomposition of pure citric acid right below 200 °C is not visible. Although the sample was visibly dry, 10% of the initial mass was lost below 100 °C, and can be attributed to excess water content.
- (e) BiCit synthesized by aging 1:2 mixture of Bi₂O₃ and HCit. The measurement started after the sample was exposed to 100 °C for 10 min. The sample characterizes only partial conversion to the BiCit, due to the not ideal environment for aging reaction. The reaction mixture was aged on a Petri dish, which allowed grains to scatter around a bigger surface, reducing the contact between them. The stage attributed to the decomposition of pure HCit is equal to the loss of 15% of the total mass, and the measurements present an example of not a full conversion from precursor to BiCit product.
- (f) BiCit synthesized by ILAG of 1:2 mixture of Bi₂O₃ and HCit. The sample characterizes full conversion to BiCit. The stage attributed to the decomposition of pure citric acid right below 200 °C is not visible. The sample was measured right after synthesis, as a homogeneous paste in order to measure the **2b** structure. 18% of the initial mass was water, as seen in the loss occurring below 100 °C. The following stages match exactly those of a dry sample, revealing no information about **2b** structure.



The contribution of the third step is varied among samples, which is a result of the consistency and crystallite size varying among the samples, due to different preparation methods. However, the measurements consistently show a comparable mass loss, from 41.4 to 43.0%, for both commercial and synthesized BiCit samples (Fig. 3.21, 3.22). This leaves pure bismuth (III) oxide (Bi_2O_3) above 420 °C.

Analysis of the difference between **2a** and **2b** structures using TGA is not a straightforward process, due to the **2b** structure being water dependent. Measurements comparing a paste-wet sample and the same sample as the dry powder was taken, revealing that both behave similarly, apart from the water evaporation process taking place below 100 °C. Measurements of mechanochemical sample freshly made and rehydrated after drying were also unsuccessfully in capturing any difference.

Crystallization

Attempts of dissolving BiCit in available solutions were unsuccessful. No crystals were obtained from filtered solutions of water, DMF and acetone. Because of that, no single-crystal diffraction could be used for attempting to solve the BiCit structure.

3.5.3 Discussion of the results

Similarly to BiGall, BiCit is not soluble in water, ethanol, acetone, or DMF. Therefore, the goal of crystallizing BiCit after synthesizing it mechanochemically was not reached. Due to the structure of BiCit remaining unknown, other than the Rietveld method means of analyzing the samples were implemented. Raman spectra analysis and TGA experimental data, unambiguously confirm the synthesized BiCit is the same compound as the commercially available BiCit. Comparison of PXRD data for synthesized and commercial BiCit agrees with that assessment. Moreover, there is no traces of Bi_2O_3 , nor HCit in the synthesized samples, according to all three methods. Therefore, full conversion was achieved in mechanochemical synthesis of BiCit. Additionally, aging Bi_2O_3 and HCit in a moist environment was discovered to be another route of BiCit synthesis.

The structural change in BiCit from **2a** to **2b** is both water dependent and reversible, based on the PXRD data. Establishing water dependence is a big step in understanding the system. The **2b**, widespread peaks indicate high symmetry, most likely of a cubic unit cell due to their regular spacing. It fits well with a 16.1 Å unit cell of the cubic system. This adds a possible, large unit-cell as another, interesting trait of this structure. Attempts of finding a solvent that would allow the **2b** to be fully stable were made. Different solvents were used in the LAG process, such as acetone, DMF, methanol, ethylene glycol (EG) and ethanol (Fig. 3.23). These attempts to obtain full conversion to BiCit were, however, unsuccessful. This proves water to be the preferred liquid for this reaction, as its use ensures consistently full conversion to BiCit. However, the **2b** structure seems to only be stable with an excess of water present. It should not be overlooked that some of the alternative solvents also produced BiCit, though poorly crystalline (Fig. 3.23, DMF, methanol and EG).

No change in the Raman spectra, together with changing PXRD pattern, makes it clear that the change in the BiCit structure from **2a** to **2b** does not occur due to any chemical reaction. The only new chemical compound would enable new Raman peaks to appear in the spectrum. The most probable explanation of the change in structure is then physical. The **2a** to **2b** structural

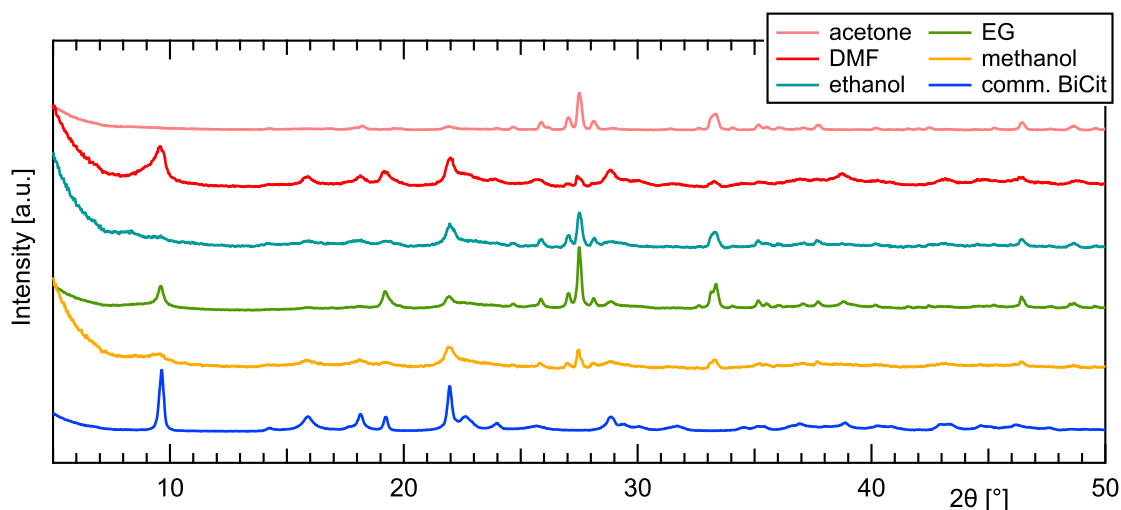


Figure 3.23: PXRD patterns of samples synthesized with LAG method, using solvents alternative to H_2O . The samples are compared with commercial BiCit PXRD. The Bi_2O_3 leftover can be seen in all of the samples, even though the correct 1:2 Bi_2O_3 :HCit ratio was used. DMF and methanol show poorly crystalline, BiCit structures. Ethylene glycol (EG) shows the BiCit structure as well, however, it is significantly less intense than the Bi_2O_3 signal. Ethanol shows a single peak at 22° that is also present in BiCit structure, however, no other BiCit peak is to be found in that measurement. Acetone produced no BiCit.

change is most likely prompted by inflating compacted, origami-like **2a** structure with water, resulting in water-filled, highly porous and regular **2b** structure.

3.6 Conclusions

Detailed recipes for synthesizing bismuth (III) gallate, bismuth citrate, and an improved bismuth di- and trisalicylate can be found in Tab. 3.2. Due to the benefits of mechanochemical synthesis route, such as lower environmental impact, these reactions could be implemented in pharmaceutical and chemical industries for efficient production of bismuth APIs from simple ingredients. The synthesized product was shown to be of high purity for the BiGall, and fully converted for BiSal_2 and BiSal_3 . The BiCit synthesis is by far the easiest to perform for full conversion, with no traces of leftover Bi_2O_3 . These conclusions are based on Rietveld refinements for BiSal_2 and BiGall (Fig. 3.3 and 3.9), PXRD comparisons for BiSal_3 and PXRD, TGA and Raman spectroscopy data analysis for bismuth citrate (Fig. 3.20 and 3.21).

BiCit water-dependent structure

An interesting, water-dependent, structural effect was found in BiCit. This effect implies folding, origami-like structure for **2a**, which then is filled with water, to reveal high symmetry, porous **2b** structure (Fig. 3.16, (a), **2a** and **2b**). The large size of water-filled **2b** unit cell is the indicator of high porosity of the material, which paired with low solubility of BiCit in water, could be a property of interest for purposes such as adsorption.

Table 3.2: Best parameters for mechanochemical synthesis of BiSal₂, BiSal₃, BiGall and BiCit. They are described for 200 mg of the reaction mixture, synthesized in 10 ml jars in a vibrational mill set to a frequency of 30 Hz.

API	precursor		ratio [A:B]	H ₂ O [μ l]	salt [%]	heating [°C]/[min]	balls d[mm]	time [min]
	A	B						
BiSal ₂	Bi ₂ O ₃	HSal	1:4	75*	1-2*	85/30*	2x 10*	30–45
BiSal ₃		HSal	1:6	75*	1-2	-*	2x 7*	30
BiGall		HGall	1:2	100*	1-2	85/30	2x 10	45
BiCit		HCit	1:2	75*	-	85/30*	2x 10	30

*parameters crucial for reaction occurring

BiSal₂ amorphous content

Although no traces of the [Bi₃₈O₄₄] clusters were found in the solid-state BiSal₂ with Raman spectroscopy, it does not disprove the theory that some new species forms on the surface of BiSal₂ grains. Additionally, this species could be similar in structure to the BiSal₂, and therefore share most of its Raman modes with it.

There is, however, evidence that no, a quantitatively significant amount of an additional species is present in mechanochemically synthesized BiSal₂, based on the laboratory PXRD evidence. Especially the spiking with a known mass % of LaB₆ confirms that no additional phase, amorphous or otherwise, can be found in the bismuth (III) disalicylate with diffraction methods.

Synchrotron measurements of solid state BiSal₂ are described in Chapter 5, as a means of further analysing the meaning behind the color change of mechanochemically synthesized BiSal₂.

3.6.1 Remaining questions

Despite insightful conclusions and discoveries, some aspects of this chapter are still waiting to be answered.

Full conversion in BiGall mechanochemical synthesis was not achieved in the end. Although the use of ILAG and other parameters were found to optimize the repeatability of a good result, it is not perfect, and leftover Bi₂O₃ can be found in each synthesized sample.

The structure of BiCit (**2a**) remains unknown, due to its low solubility, and therefore difficult to crystallize. It also proved to be unfeasible to solve this structure from PXRD using Rietveld refinement, due to the lack of information on its symmetry. Because of that, the water-dependent change in a structure of mechanochemically synthesized or activated BiCit, although certainly fully reversible and not associated with a chemical reaction, also remains unknown. Solving this structure with PXRD was too difficult due to its high symmetry allowing only for a limited amount of peaks. Moreover, even the best wet BiCit (**2b**) dataset contained peaks that may, or may not be a part of the dry structure (**2a**), further complicating the already mysterious data. A solution to that problem would be finding the structure of a dry BiCit (**2a**), which is suspected to be harmonic-like and folded. Then, theorizing on how the structure expands with the addition of water could be feasible.

One more question that comes to mind, and reaches beyond the scope of this project is the viability of the bismuth APIs mechanosynthesis for industrial use. Research on the presented APIs large scale synthesis would have to be the first step of implementing it in any industry. The reactions have been shown to vary in result significantly, with only small changes – this could pose a challenge in a large scale synthesis batch. The economical aspects would have to

be considered afterwards, and then, in the case of the pharmaceutical industry, the safety of mechanochemically synthesized APIs for medical use.

3.6.2 Author contribution

Experimentation, including mechanochemical syntheses and performing analytical measurements, such as PXRD, TGA and UV–Vis spectroscopy, was done by the thesis author.

Raman spectra measurements and their analysis was done by the thesis author with the help of Prof. María del Carmen Marco de Lucas.

Chapter 4

Growth and stability of bismuth-oxo clusters – spectroscopic methods

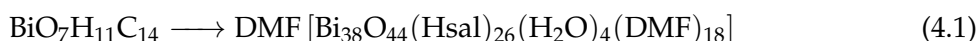
4.1 Introduction

The tendency of bismuth compounds to form various oxo-clusters has been observed in multiple systems [9, 10, 131, 138, 182]. An example of such a system is the growth of the $[\text{Bi}_{38}\text{O}_{44}]$ oxo-cluster from a mechanochemically synthesized precursor, bismuth (III) disalicylate, dissolved in acetone and DMF solutions [9]. As described below, however, the growth mechanism of this reaction is currently unknown. Speciation of this system using spectroscopic methods and DLS are investigated in this chapter.

Some of the work presented in this chapter was published in Journal of the American Chemical Society [199].

Bismuth (III) disalicylate as a precursor

Bismuth (III) disalicylate, a mechanochemically synthesized compound with a known structure, produces rectangular red crystals when dissolved in DMF. This reaction can be written as [9]:



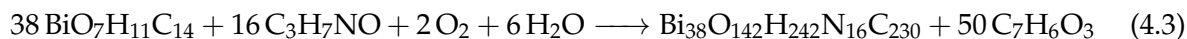
The product of this reaction is the $[\text{Bi}_{38}\text{O}_{44}(\text{Hsal})_{26}(\text{H}_2\text{O})_4(\text{DMF})_{18}]$ oxo-cluster. It is functionalized with salicylate groups and the solvent, DMF. The analogous reaction can be performed also in acetone, with a crystalline product functionalized with acetone groups rather than DMF. The exact mechanism of these reactions is unknown, and no intermediate stages have been found.

The $[\text{Bi}_{38}\text{O}_{44}]$ oxo-cluster, apart from being reported to crystallize from BiSal_2 , was even earlier reported to grow from *bismuth subsalicylate*, a structurally ambiguous, colloidal precursor [10]. In this case, acetone was used as the solvent resulting in $[\text{Bi}_{38}\text{O}_{44}(\text{Hsal})_{26}(\text{Me}_2\text{CO})_{16}(\text{H}_2\text{O})_2] \cdot (\text{Me}_2\text{CO})_4$ cluster growth. Similarly to the BiSal_2 case, the compound was found thanks to crystallization, and the growth mechanism remains ambiguous:



However, in the case of subsalicylate, a smaller, $[\text{Bi}_9\text{O}_7(\text{Hsal})_{13}(\text{Me}_2\text{CO})_5]$ molecule was also formed along with the $[\text{Bi}_{38}\text{O}_{44}]$ cluster [10].

To balance the chemical equation resulting in $[\text{Bi}_{38}\text{O}_{44}(\text{Hsal})_{26}(\text{H}_2\text{O})_4(\text{DMF})_{18}]$ formation from BiSal_2 requires a source of oxygen and water:



Because of that, it is possible that the $[\text{Bi}_{38}\text{O}_{44}]$ growth process is hydrolytical in nature. This theory is supported by the hydrolytical growth of other bismuth-oxo clusters [131, 138]. Moreover, due to the crystallization of $[\text{Bi}_9\text{O}_7]$ oxo-cluster from the bismuth subsalicylate precursor, it is interesting whether this or other, intermediate species are present in the BiSal_2 organic solution.

Solvolysis is a reaction in which reactants are a solute and its solvent react with each other, yielding a new compound in the process. It is classified as a nucleophilic substitution or elimination reaction, where the solvent decomposes certain bonds in the solute. *Hydrolysis* is, similarly to solvolysis, a substitution or elimination reaction, where it is a molecule of water that reacts with solute [49].

4.1.1 The main objectives

The aim of this chapter is speciation of the dissolution process of BiSal_2 in two solvents, acetone and dimethylformamide (DMF), aimed towards understanding the growth mechanism of the $[\text{Bi}_{38}\text{O}_{44}]$ oxo-cluster, and finding intermediate species formation. The mechanism of some of the other bismuth-oxo cluster species is linked to hydrolysis [138]. Because of that, a controlled, water environment was implemented in order to analyse the influence of water on the system.

In this chapter, the results of laboratory spectroscopic measurements are reported. Namely, UV–Vis and Raman spectra analysis, and dynamic light scattering (DLS). Additionally, single-crystal diffraction and PXRD were used. Transmission electron microscopy (TEM) was also attempted on deposited DMF and Acetone samples.

4.2 Experimental section

4.2.1 Synthesis and chemicals

For syntheses, crystallization, and other manipulations, the chemicals presented in Chapter 3 (Tab. 3.1) were used. In terms of the solvents, for some experiments "bench" solvents were used, at times referred to as "wet". These solvents were nominally the same purity as "dry" solvents, with the difference of being left in closed, exposed to atmosphere containers, for a period longer than two months. Both acetone and DMF are fully miscible with H_2O .

Precursor mechanochemical synthesis

The bismuth (III) disalicylate (BiSal_2) used in the experiments were synthesized from bismuth (III) oxide (Bi_2O_3) and salicylic acid ($\text{C}_7\text{H}_6\text{O}_3$), as described in Chapter 3.

The samples for UV–Vis and DLS measurements were made from freshly synthesized bismuth (III) disalicylate, PXRD of which was measured after DLS measurement. This procedure ensured the quality of DLS measurement, and then confirm the quality of the used precursor. For the Raman and synchrotron experiments, the precursor was prepared ahead of time, and its quality was monitored through PXRD, ensuring no changes.

4.2.2 BiSal₂ dissolution in DMF and Acetone

Synthesizing [Bi₃₈O₄₄] was performed simply by dissolving bismuth (III) disalicylate in DMF and acetone. This method was based on literature [9] and used throughout the project. Typically 50 mg of bismuth (III) disalicylate (500.21 g/mol) was dissolved in 2.5 ml of a solvent, which from 4.4 is equal to 0.040 M concentration.

$$C_{mol} = n/V = m/(VM) \quad (4.4)$$

Similar concentrations were used in all of the experiments unless stated otherwise.

[Bi₃₈O₄₄] oxo-cluster growth from other precursors

Attempts to synthesize [Bi₃₈O₄₄] with other than BiSal₂ precursors were made. Bismuth (III) trisalicylate (BiSal₃) was used in the same way as BiSal₂. Mechanochemically synthesized BiSal₃ was dissolved in acetone and DMF in concentrations similar to disalicylate.

Bismuth (III) oxide (Bi₂O₃) and a mixture of Bi₂O₃ and salicylic acid (HSal) were also used. However, due to Bi₂O₃ being insoluble in acetone, DMF and other, accessible solvents, the aging approach was taken. Four samples were prepared. 91.5 mg of Bi₂O₃ was placed in four vials (1–4). To vials 1 and 3, 108.5 mg of salicylic acid was added. 3 ml of DMF was added to all of the vials, and additionally, 50 μ l of water was added to vials 3 and 4. The quantities were chosen to reflect the 1:4 (Bi₂O₃:HSal) ratio used in mechanochemical BiSal₂ synthesis. The salicylic acid dissolved fully in the vials, and Bi₂O₃ remained as undissolved powder, with no signs of agglomeration. The vials were placed in a dark place for 14 months.

4.2.3 Controlled water environment protocol

For the UV–Vis and DLS experiments, the samples of bismuth (III) disalicylate in a solvent were created in an isolated, controlled environment. These samples are referred to as *dry solvent* samples (Fig. 4.1).

For them, 99.9% anhydrous DMF was used with pure disalicylate. The ingredients were placed in a glove bag, purged 4 times with argon. The DMF bottle was opened in the glove bag and sealed with a Suba-seal[®] and accessed with a syringe. BiSal₂ was weighed inside of the glove bag, on an analytical balance and placed into vials, keeping the proportion of the powder to solvent as 50 mg/2.5 ml as a default, unless stated otherwise. The vials were sealed with screw rubbed seal lids, and wrapped in parafilm.

4.2.4 UV–Vis spectroscopy

UV–Vis spectra measurements were performed with a Mettler-Toledo Spectrophotometer UV5 Nano and a UV–Vis Shimadzu C412. Quartz cuvettes were used, to avoid the restraining ultraviolet end of the visible spectrum. The standard size of cuvettes were used, with a 10 mm light path. Two types of cuvettes was used, macro able to fit up to 1000 μ l of liquid, and micro with thicker walls, fitting up to 200 μ l. Cuvettes with dry solvent samples were additionally wrapped in parafilm. A cuvette filled with pure solvent was measured before each sample measuring series.

4.2.5 Raman spectroscopy

Raman spectra measurements were obtained with Renishaw inVia spectrometer, using a green (532 nm), red (633 nm) and ultraviolet (785 nm) laser wavelengths. The samples were placed on a metal holder with no background in the range of measurements, up to 3000 cm⁻¹.



Figure 4.1: A photograph of 30 samples assembled and measured under the controlled, dry atmosphere of argon. The number from 0 to 5 represent the percentage (vol.) of water added to the DMF solution. The letters from A to E represent the amount of dissolved bismuth (III) disalicylate per 2.5 ml of DMF, starting from 10, 20... up to 50 mg.

4.2.6 Dynamic light scattering (DLS)

A Malvern Zetasizer DLS machine was used for DLS. The sample solution was prepared in a way that involved synthesizing a good quality BiSal_2 and dissolving it in dry DMF and benches DMF.

Multiple samples were prepared in different ways, however, due to the sensitivity of DLS to foreign particles and agglomeration, only a rigorous protocol resulted in successful measurement. The samples were kept undisturbed for a period of time, in order to allow for sedimentation, and decanted. Then, the solutions were filtered with paper filters ($20\ \mu\text{m}$) into airtight vials, with their lids wrapped in parafilm. The vials were placed in a sonic bath for 5-10 min in order to minimize agglomeration, before being transported to a DLS cuvettes. The cuvettes were sealed for the time of measurement, with their lids wrapped in parafilm. Some samples were left open to the atmosphere for the time of measurement.

Five samples in total were successfully measured. Two samples were prepared a week before measurement, with bench DMF - one of them was sealed, and once opened. Three samples were prepared a day before measurement, with dry DMF - two were kept rigorously dry, and 10% of distillate water was added to the third one. These were measured after 24 h, and one of the rigorously dry samples was kept open. Standard quartz cuvettes were used for the measurement, fitting up to $1000\ \mu\text{l}$ of a liquid.

The machine measured the intensity of light, which fluctuates in time due to Brownian motions of particles suspended in the solution. This fluctuation is then calculated into a correlation function, based on which size distribution is calculated by the program. Each sample was measured 5 times, and from each of the measurements, a mean size distribution was calculated. Measurement times of up to 15 min were chosen, to ensure a reliable result. The viscosity and refractive index of DLS was taken into account for the correlation function calculation.

4.2.7 PXRD

The complementary PXRD measurements were done with two diffractometers, Bruker D2 PHASER XE-T and Bruker D8 DISCOVER. Both use Cu K α radiation, and zero background Si sample holders.

4.2.8 Crystallization and single crystal diffraction

Crystallization attempts were made from saturated solutions of acetone and DMF. An excess of bismuth (III) disalicylate was placed in a vial, which then was shaken for 2–5 min. The undissolved leftover was filtered out, and the clear solution was left for crystallization.

Crystallization of bismuth oxo-clusters from BiSal₂ was performed. Additionally, crystallization from BiSal₃, Bi₂O₃ and a mixture of Bi₂O₃ and salicylic acid was also attempted.

Some of the crystallization samples were left in enclosed vials, and some were covered with sparsely perforated parafilm beakers. All of them were placed under a fume hood for the time of crystallization.

4.2.9 TEM

The TEM measurements were performed with a JEOL JEM 2100 FEG Transmission Electron Microscope (TEM), operating at 200 keV. Carbon-covered copper grate plates were used as a substrate.

A sample of 1-day old bismuth (III) disalicylate was dissolved in 2.0 ml of dry DMF, to prepare two different concentrations (0.12 and 0.24 M) for TEM measurement. Solutions were then spun in a centrifuge for 30 min with 8000 rpm in order to get rid of any residue. Afterwards, the clear solution was transferred into glass vials, closed and put in a sonic cleaner filled with water for 10 min, in order to break down potential agglomerates. Solutions prepared in this way were further transferred on a copper grid using single-use glass pipettes.

Two methods of applying the solution on the substrate were used. The first one was placing a plate on absorbent paper, and placing a couple of drops of the solution on it. The excess solution would be absorbed by the paper ("on paper" method). The second one was placing the plate in tweezers, so its bottom does not touch anything. Then, place one drop onto a plate, and let the solvent evaporate ("suspended" method).

4.3 Results

4.3.1 Crystallization

Bismuth (III) disalicylate yielded vividly red, large (10–50 mm) crystals. The time of crystallization varied from a couple of days to weeks. When bench acetone was used, large crystals appeared the very next day in an enclosed vial. Crystals in dry DMF formed over a week in a beaker. However, this observation was not consistent – the next attempts to form crystals from Acetone failed to produce results in such a short period of time.

One batch of such crystals, synthesized from DMF solution, was confirmed to be [Bi₃₈O₄₄(HSal)₂₆(H₂O)₄(DMF)₁₈] using single-crystal X-ray diffraction. However, the crystals tended to disintegrate in the X-ray beam, therefore a full structure solution was not possible. An initial analysis was done with the help of Yoann Rousselin, showing an unambiguous match to the unit cell of previously reported [Bi₃₈O₄₄(HSal)₂₆(H₂O)₄(DMF)₁₈] cluster [9].

The BiSal₃ solution did not yield any crystals. Neither did pure Bi₂O₃, nor the Bi₂O₃ and salicylic acid mixture. The BiSal₃ dissolved in both DMF and acetone was left for over 12 months in sealed vials and for periods required for evaporation in open beakers. The beakers

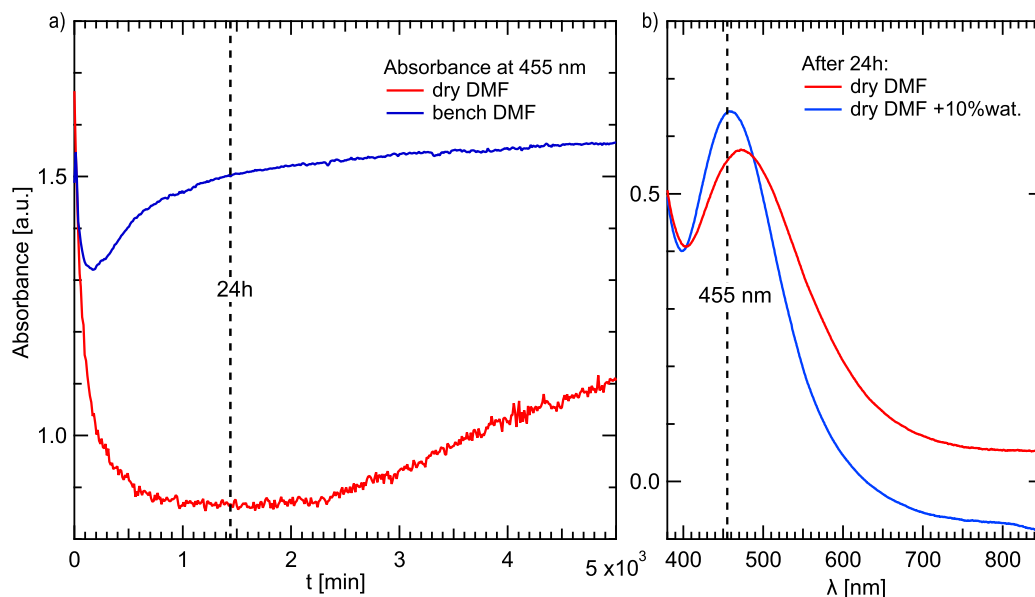


Figure 4.2: **a)**, Time dependence of the UV-Vis absorbance of the 455 nm wavelength, for sealed samples in bench and dry DMF. After an initial sedimentation period (exponential decay), no change is seen in dry DMF, for over 30 h. In contrast, rapid reaction is seen in the bench DMF, slowing down after 24 h. **b)**, A spectrum of two samples prepared in a way corresponding to the previous panel – with dry DMF, and DMF with the addition of 10% of water. Samples were measured 24 hours after mixing. The formation of the larger species in panel **a** causes an increase in intensity and sharpening of the absorption feature at 455 nm, in agreement with the strong pink color of the samples.

were both left open, and partially sealed with perforated parafilm in order to decrease the evaporation rate. None of the tries yielded a crystalline product.

4.3.2 UV-Vis Spectroscopy

BiSal₂ dissolved in DMF creates a vividly pink solution. Its hue shifts towards an orange-pink hue with time. The color can be attributed to a broad peak, with a maximum value ranging from 465 nm to 455 nm (Fig. 4.2, b). The shift from a higher to a lower wavelength peak takes place shortly after the solution is mixed, but it is long enough to be observed in a controlled water environment. The broadness of the peak decreases with time.

For samples with dry solvents, measured right after mixing, the peak is even broader and asymmetric, with a longer tail, extending up to 900 nm. It decreases significantly at the red region and slowly starts to increase back around 620 nm. The overall increase in absorption is caused by undissolved particles scattering the light. However, the asymmetry of the peak cannot be explained this way. It implies either very small, or a mixture of species present in solution [18]. Neither explanation excludes another, but the latter is working well with another observation.

At low bismuth concentration, two peaks at 455 and 540 nm were detected. This can be seen in the Fig. 4.3. In most of the UV-Vis measurements, only the 455 nm peak is visible. However, its broad tail might obscure the 540 nm peak, and therefore it cannot be ruled out that the absorption spectrum of BiSal₂ dissolved in acetone and DMF comes from both these peaks. It is plausible, that the existence of two peaks indicates two, different in size species.

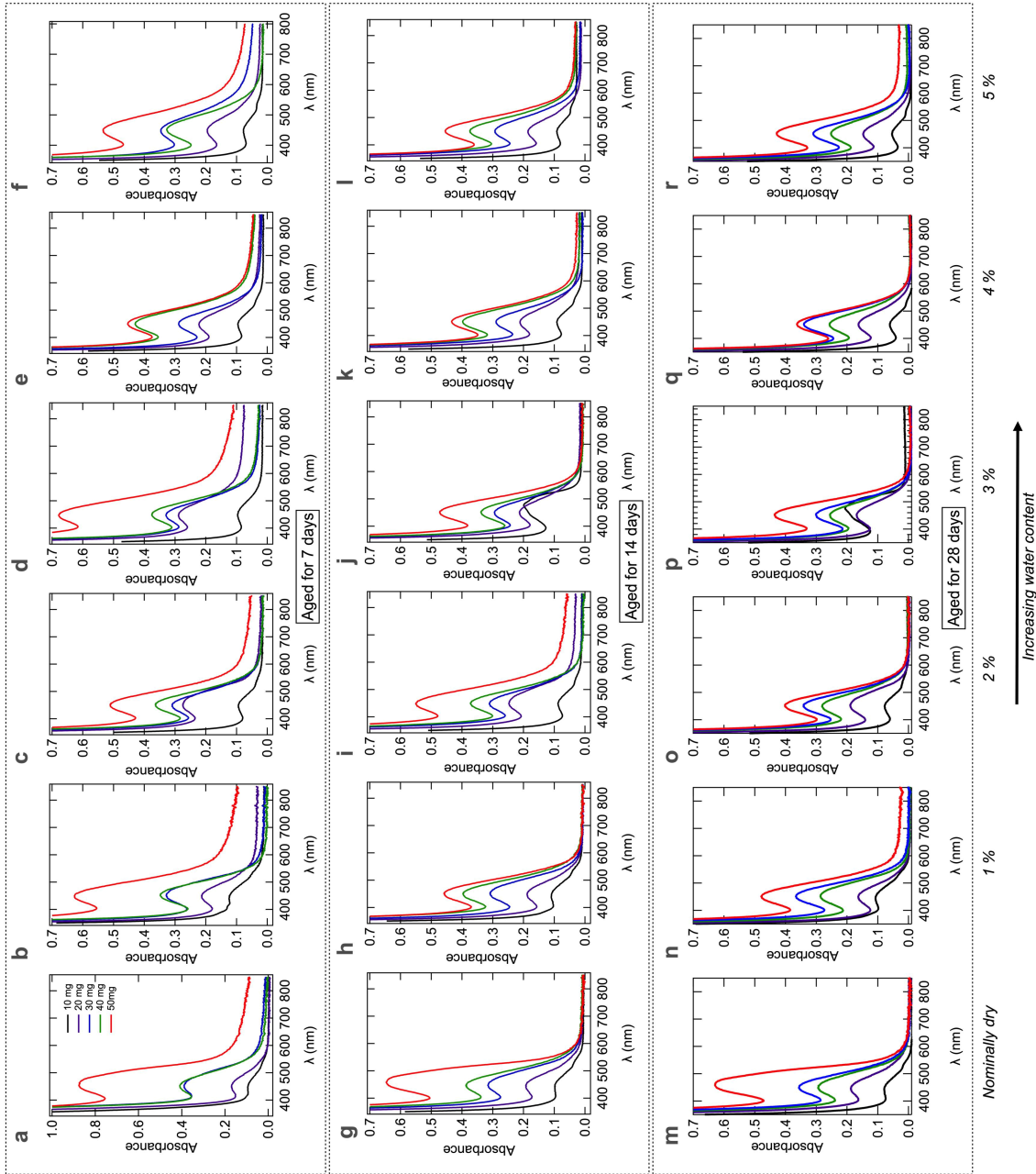


Figure 4.3: Detailed description can be found on the following page.

Figure 4.3: Results of UV–Vis measurements as a function of BiSal₂ concentration, H₂O content and time. The UV–Vis spectrometer, balance, solvents, etc. were placed in a glove bag, under Ar atmosphere. Freshly prepared BiSal₂ was used, and both solvents and samples were handled using Suba-seal[®] caps and syringes. A small amount of solid state BiSal₂ was extracted in a glove bag for a PXRD measurement confirming its purity.

Thirty different samples were prepared, each with unique combination of BiSal₂ concentration (10, 20, 30, 40, 50 mg per 2.5 ml of dry DMF) and volume of added water (0, 1, 2, 3, 4, 5%). Each row (**a-f**, **g-l**, and **m-r**) represents the time of aging – 7, 14 and 28 days. In each row, the addition of H₂O increases from left to right, from 1 to 5%. Each graph shows samples with the same amount of added water and varying BiSal₂ concentration.

The presented spectra show that the addition of water does not change peak position, nor influence the spectrum in any other way, significant ways. The concentration of BiSal₂ on the other hand, influences the observed spectrum. At low concentration two peaks instead of a single one are visible. The most prominent peak is located at 455 nm, and the second one around 540 nm. For higher concentrations only the first peak is visible. The aging of the samples did not result in any visible changes in spectrum. The increased background, most prominent in highest concentration samples (red), is due to scattering occurring on undissolved particles.

Another observation is that the broad absorption feature peaks at 465 nm initially, before shifting to 455 nm. This could be associated with increase in concentration of the main species (455 nm), and simultaneous decrease in the concentration of the other (540 nm).

Bi₂O₃ and salicylic acid – aging

The samples with a mixture of Bi₂O₃ and salicylic acid in DMF (1 and 3), after 3 months visibly gained pink coloration, while pure DMF is colorless. The samples with pure Bi₂O₃ (2 and 4) remained colorless (Fig. 4.4, b). Similar pink coloration is also present in DMF solution with BiSal₂. Samples 3 and 4 were spiked with 50 μ l of H₂O.

After 14 months the coloration of the samples 1 and 3 became intense enough to be measured with UV–Vis. Samples without addition of HSal (2 and 4) remained colorless, and their absorption spectrum resembles that of pure DMF (Fig. 4.5, 2 and 4). The spectrum of sample 3 shows a peak around 520 nm, similar to the less intense peak present in BiSal₂ UV–Vis measurements (Fig. 4.5, 3 and BiSal₂). Sample 1 containing no addition of water only shows a broad absorbance, that is merging with and intense peak near ultraviolet region. Both samples 1 and 3 show the peak near ultraviolet region, which is a result of high concentration of HSal dissolved in DMF.

Bismuth (III) trisalicylate

When BiSal₃ is dissolved in DMF, the solution goes through a color change, similarly to the BiSal₂ samples. However, the color change is much more severe (Fig. 4.6). Initially, BiSal₃ solution can be vividly pink, and at times even purple. In time it becomes salmon, and even vividly yellow. The color change is also reflected in the UV–Vis spectrum (Fig. 4.7). The peak of absorption shifts from 506 to 455 nm in 48 h, which represents the color change from purple to yellow. This change is accompanied by narrowing of the apparent peak width, similarly to the BiSal₂ solution.

The severity of color change varied, depending on the particular sample. Most of the prepared solutions were immediately pink, and only reached salmon hue, even after weeks of

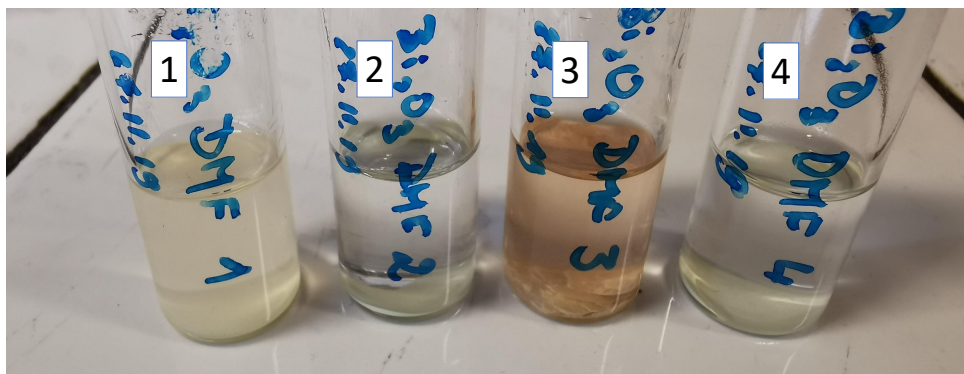


Figure 4.4: Four vials filled with the same amount of Bi_2O_3 and DMF. Salicylic acid was added to the vial 1 and 3, and $50 \mu\text{l}$ of H_2O were added to the vial 3 and 4. Samples were aged for 14 months and visibly changed the color in the case of 1 and 3, of which both contained Bi_2O_3 and salicylic acid. Worth noting is that the majority of Bi_2O_3 remains undissolved.

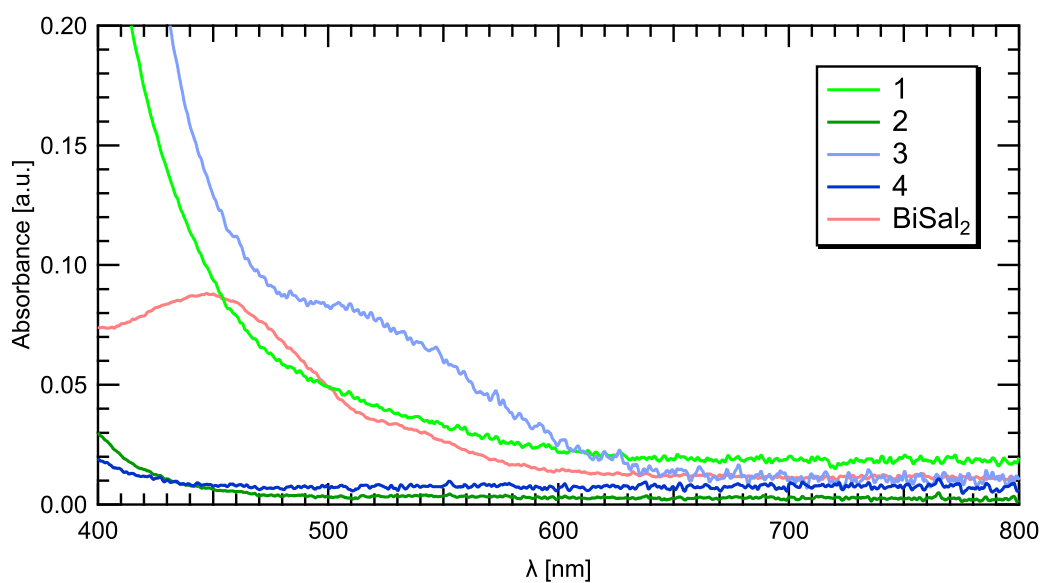


Figure 4.5: A UV-Vis spectrum of the Bi_2O_3 and salicylic acid samples, compared to a sample with low concentration of bismuth (III) disalicylate in DMF solution. The characteristic 455 nm peak, featured in BiSal_2 samples, is not visible here. However, sample 3 shows a peak at 520 nm, which is featured also in the Fig. 4.3. This can be likely be attributed to the smaller species. Moreover, this confirms that bismuth clusters can form even from undissolved Bi_2O_3 in salicylic acid dissolved in organic solvent.

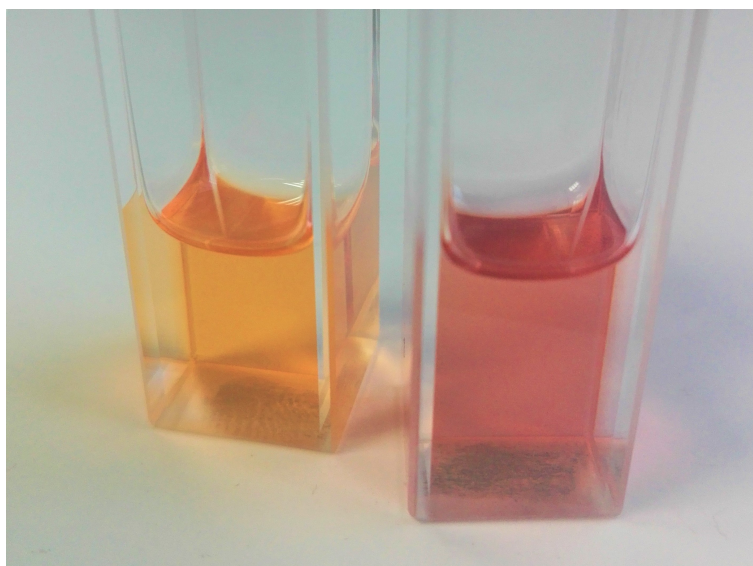


Figure 4.6: A photograph of two samples prepared from a dry solvent. One after 24 hours of being open to the environment (left, yellow) and another sealed in an inert atmosphere (right, pink).

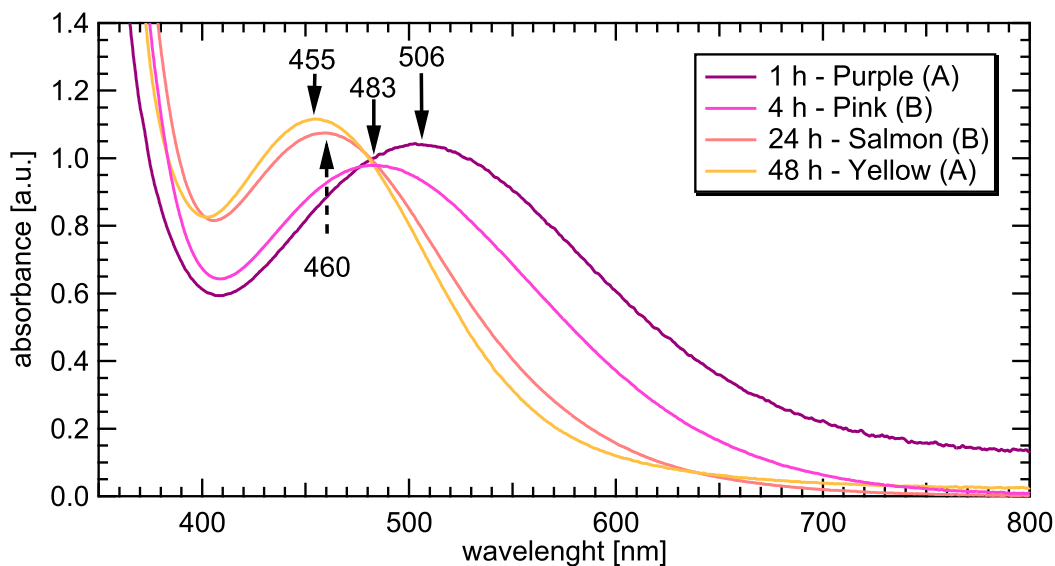


Figure 4.7: Absorption spectra of BiSal₃ dissolved in DMF. The measurements were performed at varying times from the initial mixing, and were performed for two different samples. The samples were prepared with freshly synthesized, pure BiSal₃ and dry DMF. The peak of absorption is at a different position for all four of the measurements, and is linked to a different color – purple (506 nm), pink (485 nm), salmon (460 nm) and yellow (455 nm). The colors of the plots resemble the colors of the solution. The samples were stored in lid-sealed vials, wrapped with parafilm around the lids.

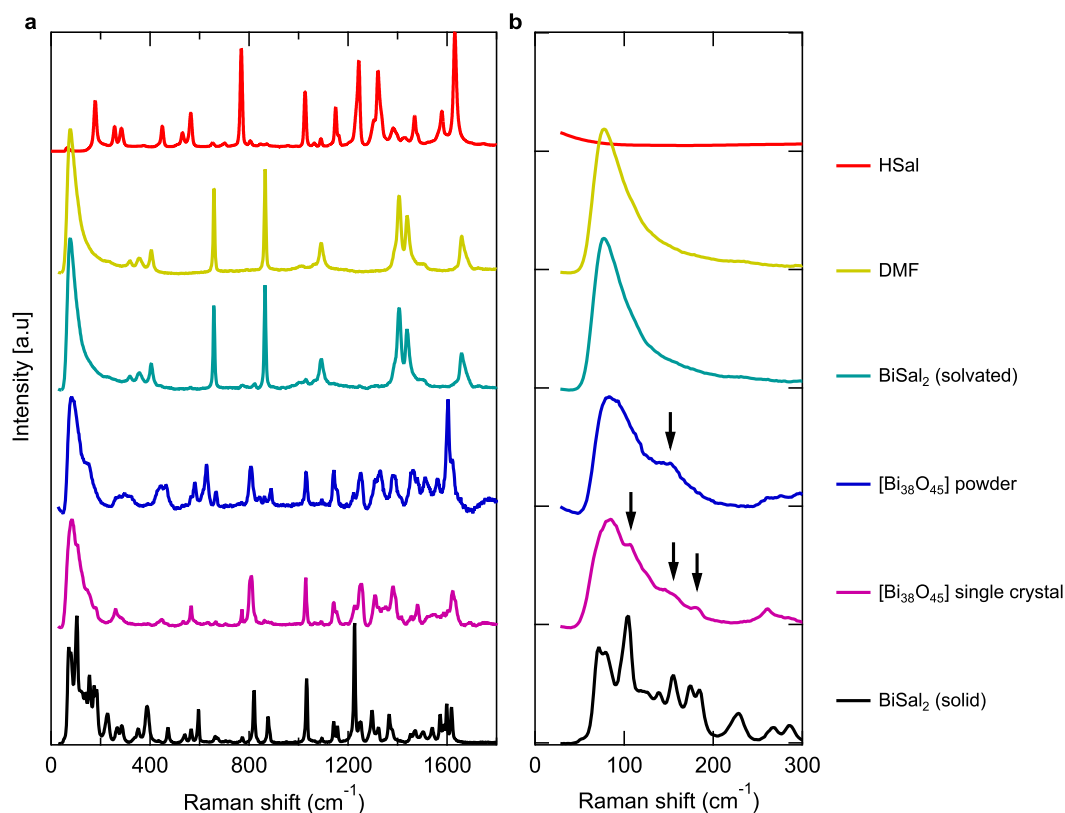


Figure 4.8: A comparison of Raman spectra of different samples. The BiSal_2 in solid state, pure DMF and solid state HSal were compared to spectra of dissolved BiSal_2 . The dissolved BiSal_2 is virtually identical to the pure DMF, which means that the solvent obscures the signal of solvated species. No traces of the solid state species can be seen in the dissolved BiSal_2 . Spectra of crystalline $[\text{Bi}_{38}\text{O}_{44}(\text{HSal})_{26}(\text{H}_2\text{O})_4(\text{DMF})_{18}]$ were also measured. Although this the Raman signal of the cluster is also not visible in solvated BiSal_2 , the $[\text{Bi}_{38}\text{O}_{44}]$ cluster in single crystal shows a strong low energy response ($< 300 \text{ cm}^{-1}$). Grinding the crystal into polycrystalline sample wipes out the majority of the low energy response. A spline background has been subtracted from all the datasets shown here.

aging. The observations suggest, that using fresh BiSal_3 and dry DMF increases a chance of obtaining an initially purple sample. However, some samples prepared from such ingredients were pink. The use of H_2O in synthesis of BiSal_3 was one of the factors that could have influenced this result.

The presence of the 455 nm peak in aged BiSal_3 samples is worth noting due to the same peak being present in dissolved BiSal_2 . This implies that similar, or even the same species form from BiSal_3 in DMF solution, even though no crystallization occurs.

4.3.3 Raman spectroscopy

Raman spectra of BiSal_2 samples dissolved in DMF, the $[\text{Bi}_{38}\text{O}_{44}]$ oxo-cluster single crystal and crystalline powder were gathered. They were compared to the solid state BiSal_2 and HSal, and liquid DMF spectra (Fig. 4.8).

The Raman spectroscopy for BiSal₂ in DMF was implemented as a means of complementary analysis. However, the spectrum of BiSal₂ solution is virtually identical to the one of pure DMF. Samples of DMF with salicylic acid and water were also measured as a comparison, again showing only DMF on the spectrum. The use Raman spectroscopy for distinguishing bismuth species present in BiSal₂ DMF solution was therefore impossible.

Looking at various Raman spectra of [Bi₃₈O₄₄(HSal)₂₆(H₂O)₄(DMF)₁₈], it can be noticed that low energy bismuth-oxo modes are sensitive to the long-range structure. Signal clearly visible below 200 cm⁻¹ in single crystals, become less pronounced after gentle grinding (Fig. 4.8). In solution phase on the other hand, these modes are not visible at all. The mid-range single crystal spectrum of [Bi₃₈O₄₄] shows well defined peaks, that do change their intensities with the change of measurement direction, indicating anisotropic optical properties of [Bi₃₈O₄₄] oxo-cluster crystals. The ground crystals spectrum does not show well defined peaks, however, an interesting, rising background is still present.

Raman spectroscopy did not help to explain the phenomenon of white BiSal₂ becoming pink when exposed to air. Since the crystals of the [Bi₃₈O₄₄] oxo-cluster are red, it naturally comes to mind that the cluster growth on the edges of BiSal₂ grains could cause the pink color. However, the peaks present in mid-range solid state [Bi₃₈O₄₄] oxo-cluster measurement are not reflected in the solid state BiSal₂ data.

4.3.4 DLS

Due to a high polydispersity of most samples, caused by factors such as agglomeration and presence of dust, DLS measurements were challenging to perform and analyse. However, using the weighted arithmetical mean method on the measurements of most stable solutions, it was possible to obtain an insight into the size of particles in various samples of BiSal₂ in DMF.

The DLS measurements point out towards three, main sized of particles, present in solution. Big agglomerates, reaching 0.1 μm sizes, and two particles, the smaller peaking at 1.3–1.7 nm, and bigger at 2.3–3.1 nm diameter.

Samples prepared from bench DMF were measured after a week. The open one presents bigger species, according to the size distribution (Fig. 4.9, b). This can be explained as access to the environment – and in that both H₂O and O₂ from air – enables [Bi₃₈O₄₄] growth. The overall size distribution of these samples is also broader, than for samples based in dry DMF. This can be associated with longer time the solution was kept, before the measurement.

In the case of dry DMF samples, only large aggregates (>200 nm) are seen when sample is sealed (Fig. 4.9, a, sealed). Any other species present in this samples are therefore below the size limit of DLS (~1 nm). Tuning the water content by atmospheric exposure, or adding 10% (Vol.) of H₂O, yields sizes similar to samples based in bench solvent. Open access to moisture from air yields smaller size than adding water (Fig. 4.9, a, open). This again supports that access to water increases contribution of the larger species, [Bi₃₈O₄₄].

Tries to perform DLS for BiSal₃ dissolved in DMF were unsuccessful due to high polydispersity of the samples. This was similar for the samples of aged Bi₂O₃ and HSaI in DMF.

4.3.5 TEM

Attempts of preparation and measurement of a TEM sample, containing clusters at various stages of growth, were made.

The lower concentration (30 mg/2.0 ml – 0.12 M) turned out to be too diluted for the bismuth clusters to be easy to distinguish on the grid. The "on paper" method was used with this concentration.

The second, "suspended" method was attempted next, with the higher concentration (60 mg/2.0 ml – 0.24 M). This revealed, that this concentration with the method was indeed too

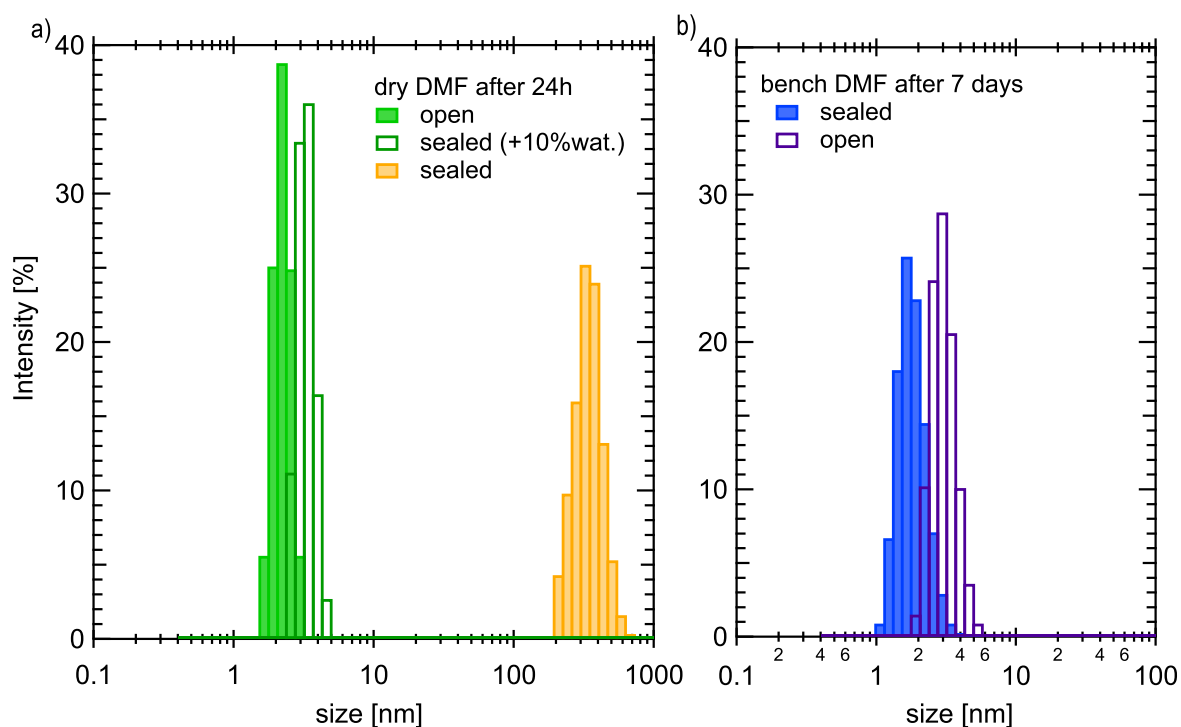


Figure 4.9: The size distribution in samples of BiSal₂ dissolved in DMF, as seen with dynamic light scattering (DLS). **a)** A set of samples was produced with dry DMF. It was measured after 24 hours from the time of mixing. A fully sealed sample shows only large aggregates, with no molecule-sized particles detected. The sample with access to air shows species in the 1.3–1.7 nm range, and one spiked with 10 Vol. % of water, species in 2.3–3.1 nm range. **b)** A set of samples made with bench DMF. It was measured 7 days after mixing, with one sample sealed and the other left open for that time. The size distribution is broader than on the previous graph. The size distribution again shows a smaller species in the 1.3–1.7 nm range for a sealed sample, and a bigger one (2.3–3.1 nm) in the sample open to atmosphere.

high, or perhaps the tendency of clusters to crystallize too dominant, to allow to observe free clusters on the grid. Instead, a crystalline mass appeared.

At the same time, a problem of resolution emerged, due to the small size oxo-clusters, which is 1.3–1.7 nm for the smaller, and 2.3–3.1 nm for the bigger according to DLS. However, salicylate groups that are most likely contributing to the DLS size, cannot be visible on carbon substrate, and the resolution of TEM was too low to show the cores alone, even in a good sample. Next attempt with higher concentration was performed on a grid with formvar (a type of resin) instead of carbon, to possibly increase contrast in between salicylate layer and substrate. The "on paper" method of the drop application was used. Although the concentration seemed to work well, the clusters proved to be too small to distinguish with the utilized microscope. Worth noting is that a big problem proved to be low stability of clusters in electron beam, where they moved around. This made the observations and manipulation with resolution impossible in the particular setup.

4.4 Discussion of the results

4.4.1 Growth mechanism

The process of oxo-cluster growth from BiSal₂ has an unknown, growth mechanism. A helpful step before the data analysis in regard to the reaction mechanism, is forming theoretical, chemical equations. It was done with the accessible precursor species and the [Bi₃₈O₄₄] oxo-cluster product in mind.

Balancing chemical equations

Balancing the stoichiometry of the [Bi₃₈O₄₄] oxo-cluster growth from BiSal in organic solvent can be achieved in two ways. With and without the use of ions. For the simplicity, only DMF is used as a solvent in the equations. Changing the solvent results in change of non-salicylate ligands surrounding the core, and does not influence the core structure [9, 10]. Because of that, solvents other than DMF are presumed to exhibit the same reaction mechanism. However, they are likely to have different reaction rates.

The non-ionic way involves the following reaction scheme:



Which, after adding exact formulas, results in the following chemical equation:



What is very notable about this equation (4.6), is the need of adding oxygen source. This is a very interesting finding, given the possible significance of allowing the sample for open access to the atmospheric oxygen. The additional source of oxygen could be omitted if the reaction was given enough H₂O molecules. However, it would then require removing hydrogen as a product, for example as H₂ molecule. Both of these options are unlikely to be the actual reaction mechanisms, due to the unfulfilled redox reaction requirements. Reduction of O₂ molecule to a product, or bound hydrogen to H₂, cannot take place without oxidizing other atoms in exchange. And no apparent reducers that could fulfil that requirement are present in the solution.

Another important note is the part that H₂O takes in the reaction. Removing it from the equation would make the reaction impossible, unless DMF molecules were used as a source of

oxygen. That, however, would have to result in an unidentified produce. It would also increase the importance of the solvent over the nominal quality and becoming a ligand – which taken into account how many solvents produce the $[\text{Bi}_{38}\text{O}_{44}]$ core, is unlikely.

The ionic reaction scheme, on the other hand, allows to omit the addition of an oxygen source, by using dissociated water:



In this reaction, 4 more moles of H_2O are used as a substrate, to compensate for the lack of oxygen molecule. At the same time, 8 hydrogen cations are released.

Although the growth of $[\text{Bi}_{38}\text{O}_{44}]$ involving only BiSal_2 , water and solvent as a ligand is a more likely scheme, than one involving oxygen molecule, it has to be noted, that this reaction (4.7) is not correctly written, simply to the fact that the charges are not balanced. It can be easily imagined, that the charges are balanced with dissociated BiSal_2 . Although it could be fixed in the reaction scheme, if correct charges were placed onto other molecules, it does deflect from the real goal of this theoretical exercise. Which is looking into what species are most likely to be chemically involved in the process of $[\text{Bi}_{38}\text{O}_{44}]$ cluster formation, and in what proportions.

The most important find of the stoichiometric chemical equations, is without a doubt the small amount of H_2O required. In compare to 38 moles of BiSal_2 (19007.98 g, with 500.21 g/mol) in both examples, the 6 to 10 moles of water (108.12-180.20 g, with 18.02 g/mol) are a very small amount. It means that for 200 mg of BiSal_2 , an amount typically synthesized mechanochemically in one batch, just 1.138–1.897 μl of H_2O (with density assumed as 1 g/cm³) is required for a full conversion to the $[\text{Bi}_{38}\text{O}_{44}]$ cluster. To synthesize such batch, up to 100 μl of H_2O is used. Mechanochemically synthesized BiSal_2 contains therefore enough water to fully react into the $[\text{Bi}_{38}\text{O}_{44}]$ cluster.

Water taking part in the reaction

Because water takes part in the synthesis of BiSal_2 precursor, it is also present in the water-controlled environment used in UV–Vis measurement. At the same time, there is still a tendency of samples with excess of water to form larger species more quickly, or at all in the case of time-independent results. Because of that, it is clear that water is a factor that influences the reaction rate of the $[\text{Bi}_{38}\text{O}_{44}]$ in its growth mechanism.

The most obvious and simple explanation could be that the excess of water is acting in the $[\text{Bi}_{38}\text{O}_{44}]$ growth mechanism according to the Le Chatelier's principle (Equilibrium Law). The excess of water simply pushed the equilibrium of the reaction in the direction of the products. In a reaction, where no equilibrium is reached, it would in analogous way increase the reaction speed. This theory of how excess of water influences the reaction, is in line with the DMF, UV–Vis and synchrotron observation, where bench solvents tend to feature larger species, presumably $[\text{Bi}_{38}\text{O}_{44}]$, more prominently, than the smaller one.

4.4.2 Spectroscopic discussion

BiSal_2 dissolution in acetone and DMF

Kinetics measurements enabled an analysis of changes in the UV–Vis absorption spectrum in a function of time. The spectrum changes faster and more significantly with access to atmosphere (Fig. 4.2, a), and with it to the air and water it contains. Moreover, the shape of the absorption peak changes over time, along with its intensity. The peak tends to get sharper and more defined, with the maximum intensity increasing at 455 nm (Fig. 4.2, a and b). These changes

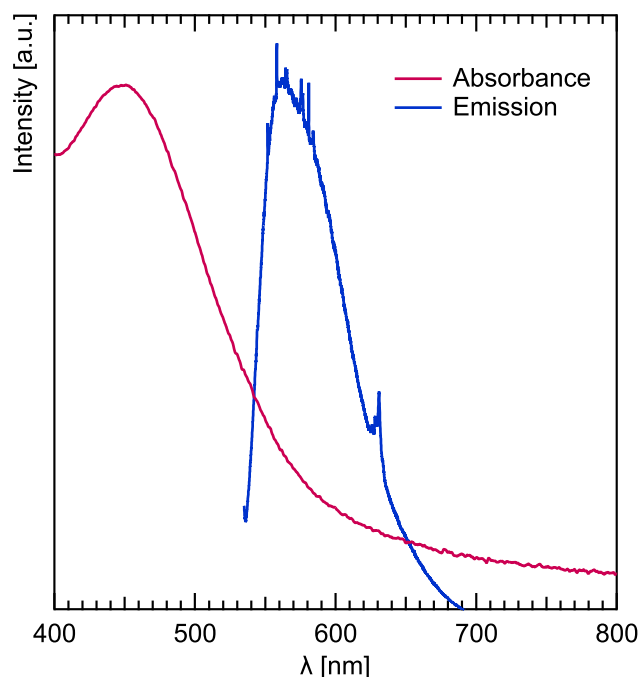


Figure 4.10: An interesting, luminescence effect was observed when measuring Raman spectra of bismuth (III) disalicylate in DMF solution. When excited with a 532 nm laser, a characteristic spectrum was emitted. When aligned with UV–Vis spectrum, it becomes clear that the $[\text{Bi}_{38}\text{O}_{44}]$ cluster exhibits photo luminescence. The peaks present in the emission spectrum come from DMF, and the measurement was collected with the Raman spectrometer.

in the spectrum could be caused by formation of the $[\text{Bi}_{38}\text{O}_{44}]$ oxo-cluster from the smaller species, and thus decrease the contribution of broad 540 nm peak associated with said smaller species (Fig. 4.3) – this causes the sharpening of the broad feature. The 540 nm peak associated with smaller species is most likely obscured by the overall, broad intensity the absorbance feature, in most of measurements, and is only revealed with a small bismuth (III) disalicylate concentration.

The larger species, presumably the solvated $[\text{Bi}_{38}\text{O}_{44}]$ cluster, was also discovered to be photoluminescent (Fig. 4.10). This was observed using the Raman spectroscopy setup. The rise of background present in the solid $[\text{Bi}_{38}\text{O}_{44}]$ cluster samples was also present in BiSal_2 dissolved in DMF. The background was more intense for samples that presented more intense UV–Vis absorption, and measuring Raman spectrum for them in a larger range of energy revealed a luminescence effect. The shift in wavelength from absorption to emission does fit fluorescence effect. Moreover, the effect of the increasing background was only visible for a laser that was in the absorption region of the disalicylate solution (green), and disappeared with a different laser (red).

The luminescence effect can be seen with a naked eye, as the samples are vividly colored. Moreover, bismuth oxide quantum dots, which have structure similar to the $[\text{Bi}_{38}\text{O}_{44}]$ oxo-cluster core, absorb light in a similar way to the samples prepared from bismuth (III) disalicylate [245].

Oxo-cluster growth from other precursors

The UV–Vis measurements of Bi_2O_3 in DMF (Fig. 4.5) show that although it does not dissolve in DMF, it definitely reacts with salicylic acid dissolved in it. This reaction is very slow in comparison to dissolution of BiSal_2 in DMF. The 520 nm peak present in a sample spiked with water, is interesting due to its close match with the peak indicative of a smaller species in BiSal_2 samples. It can be seen only in samples that contain water, which should not be overlooked. This points towards the $[\text{Bi}_{38}\text{O}_{44}]$ formation, or at least the formation of its precursor, being a water-dependent process. It is, however, just as important to note, that both samples, with and without addition of water, show pink coloration. Water could therefore act as a catalyst, rather than a reactant, and simply increase the reaction rate.

The UV–Vis measurements of BiSal_3 dissolved in DMF show even closer similarity to the BiSal_2 , than aged Bi_2O_3 . Peaks present in the BiSal_3 solution are broad in shape, and after aging the highest absorbance matches the one of BiSal_2 samples. However, their range is wider than those of BiSal_2 and spreads from 500 to 455 nm (Fig. 4.7). The variety of solution colors is also wider, spanning from purple and pink to orange and yellow, rather than from pink to orange-pink (salmon). The change in color happens in time from the dissolution, and is seemingly linked to the access to atmosphere. Nominally dry samples tend to be more purple initially.

The main difference in between BiSal_2 and BiSal_3 samples lies in the crystallization attempts. BiSal_3 yielded no crystals, neither from DMF nor acetone solutions. Moreover, DLS measurements of BiSal_3 yielded no result, due to high polydispersity of the samples.

4.4.3 DLS

Turning now to the DLS measurements of the solvated BiSal_2 (Fig. 4.9), it becomes clear that adding water (or access of atmosphere) to the system, either by introducing it manually or allowing the air moisture to be absorbed over a longer period of time, results in an increased quantity of larger species in solution (Fig. 4.9, a – sealed + 10% water, b – open). Restricted access to H_2O and O_2 results in smaller species dominating the size distribution.

These results match the UV–Vis observation of two, smaller and larger species in solution. The size ranges of these species (1.3–1.7 and 2.3–3.1 nm). The larger species matches the $[\text{Bi}_{38}\text{O}_{44}]$ clusters, which has ~ 2.3 nm in diameter. DLS cannot confirm the exact species, but will be taken into consideration in the following chapter.

The larger species is present in solution with access to atmosphere and addition of water. This supports the water-dependent reaction mechanism. Because only a small amount of water is enough for the formation of the $[\text{Bi}_{38}\text{O}_{44}]$ oxo-cluster, according to the stoichiometry of this reaction, this dependence is most likely associated with more than H_2O being a reaction ingredient.

4.5 Conclusions

Bismuth (III) disalicylate dissolution in DMF and acetone

Based on the DLS evidence, it can be concluded that BiSal_2 dissolved in DMF produces at least two, different in size species. The species are estimated to be 1.3–1.7 and 2.3–3.1 nm in diameter. This is supported by UV–Vis absorption experiments, which show wide peaks with two, distinctive maxima at 450 and 540 nm. The size of the larger species matches this of the $[\text{Bi}_{38}\text{O}_{44}]$ clusters.

The reaction occurring in solution is sensitive to atmosphere access, water content of the solvent, and concentration of BiSal_2 . The smaller species is more stable in anhydrous, sealed solution, with lower concentration of BiSal_2 . The stoichiometry of the $[\text{Bi}_{38}\text{O}_{44}]$ cluster growth

confirms further that H₂O most likely takes part in the reaction. The reaction mechanism not only contains H₂O as one of the ingredients, but also requires its excess for increasing reaction rate of the [Bi₃₈O₄₄] cluster formation.

It was confirmed with single crystal diffraction, that [Bi₃₈O₄₄] metal-oxo cluster is crystallized from the DMF solution.

Other precursors

The process of aging Bi₂O₃ in DMF for 14 months shows a reaction occurring, provided that salicylic acid is present in the solution. Analysing the UV–Vis absorption of the obtained solution shows similarity to one of the BiSal₂ dissolution product. This indicates that the oxo-cluster product can form even from a more stable, solid-state Bi₂O₃ precursor, provided that an extensive aging with presence of salicylic acid is implemented. Moreover, this reaction occurs faster with addition of water, further emphasizing the influence of H₂O on the system, further adding to the hydrolysis argument.

The dissolution of BiSal₃ in DMF likely produces some bismuth-oxo cluster species, given the similarity of its UV–Vis spectra to the solvated BiSal₂. The UV–Vis shows change in peak position with time, paired with a change in color of the solution. This suggests a variety of species can be present in the BiSal₃ solution, as it reacts over time. However, no crystallization product and lack of DLS evidence restrains more precise conclusions.

Questions to be answered

The UV–Vis and DLS point towards two, varying in size molecules present in the solvated BiSal₂. The most important question is whether these two species can be identified with total X-ray scattering method. This question is explored in Chapter 5.

4.5.1 Remaining questions

The aging of Bi₂O₃ and HSal in DMF showed that the presence of acid in DMF solution enables a chemical reaction. It is interesting to see a reaction occurring with such stable form of bismuth. It would be interesting to investigate the influence of other acids, as well as the possibility of synthesizing [Bi₃₈O₄₄] from other bismuth compounds, such as bismuth (III) gallate and bismuth citrate. The attempts of that were unsuccessful in this project, due to low solubility in chosen solvents, but could potentially work with aging of a compound in solution.

The color change of BiSal₃ dissolved in DMF is a fascinating observation, that is even more interesting when looking at the gradual change in UV–Vis peak position. Because other speciation methods were unsuccessful for this system, and due to difficulties in obtaining a fresh sample of BiSal₃ at the time of the synchrotron experiment, this system is not explored in the following chapter. However, it would be interesting to see future works on the BiSal₃ dissolved in organic solvents, focused on its speciation.

The unsuccessful TEM observation of the species present in DMF leaves room for additional research in that direction. Using Cryo TEM would possibly allow the observation of the clusters, despite their relatively small size and large oxygen share in the overall composition.

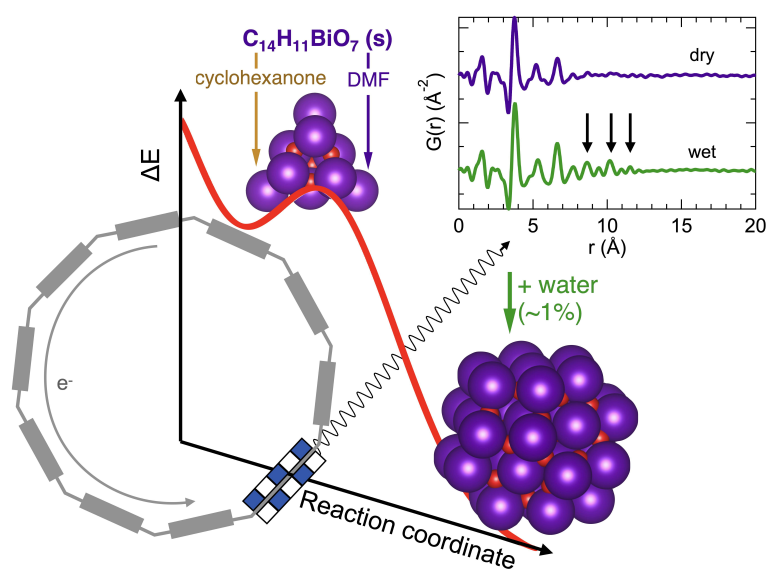
4.5.2 Author contribution

Laboratory experiments, including bismuth (III) disalicylate synthesis, and UV–Vis, DLS and PXRD measurements were performed by the thesis author. The protocol allowing for maintaining the anhydrous environment for UV–Vis measurements was developed and executed by the thesis author.

Raman spectra measurements and their analysis was done by the thesis author with the help of Prof. María del Carmen Marco de Lucas. The TEM measurements were performed by Prof. Valérie Potin and analyzed with the thesis author.

Chapter 5

Growth and stability of bismuth-oxo clusters – total scattering



5.1 Introduction

In Chapter 4 UV–Vis and DLS evidence showed two different species in bismuth (III) disalicylate (BiSal_2) solution. The difference in between the species was their size, with the larger species appearing when more H_2O was present in the system. The larger species is presumably the $[\text{Bi}_{38}\text{O}_{44}]$ cluster, which crystallizes from the solution.

The Pair Distribution Function (PDF) of total scattering data is used in this chapter. This technique can help in identifying both species synthesized from dissolved BiSal_2 . Monitoring of the oxo-cluster growth from BiSal_2 will hopefully also eliminate ambiguity, regarding the water-dependence of the process. As stated in Chapter 2, PDF technique allows to monitor structural changes directly in solution phase.

Because the literature contains a vast library of varying in size bismuth oxo-clusters (Fig. 5.1), the $[\text{Bi}_{38}\text{O}_{44}]$ cluster system is ideal for PDF analysis. Calculating PDF signal of solid-state oxo-cluster models, allows to create fingerprinting tools, which can be utilized in initial PDF analysis (Fig. 5.2).

Some of the work presented in this chapter was published in the Journal of the American Chemical Society [199].

Bismuth oxo-cluster species and their use

Clusters containing bismuth and oxygen come in various shapes and sizes [131, 137]. Bismuth siloxides and sulphonates, bismuth-oxide based thin films, bismuth clusters, and heterometallic complexes are only some of the groups of bismuth compounds, studied in regard of their structure, growth mechanisms and potential applications [139]. Their properties have advantages in a variety applications [7]. As mentioned in Chapter 3, medical and pharmaceutical uses are often found for bismuth compounds. Some are used as catalysts [122, 123] and materials transporting oxygen [90, 220]. Electrical properties enable some to be used as ferroelectric materials [195, 230], but also in photovoltaic systems [121, 234] and LEDs [187].

The potential of advanced, nano-scaled compounds is high, but their current use limited. This is because of factors such as challenging application and high cost, but also poor understanding of their synthesis and growth process. This is in part, because of the synthesis of nanomaterials such as metal-oxo clusters, is typically held in solution. Without fully understanding the molecular structure growth in solutions, from the precursor to product, designing an advanced and efficient application process can be difficult, or even impossible. Developing growth mechanisms, rooted in the theoretical models, and further proved with experimental data, would improve on that applicability, facilitating complex oxo-clusters use among other nano-scaled materials [181, 206, 217].

Pair distribution function (PDF) method of analysing total scattering data helps in understanding difficult systems. Because it offers a way of analysing solution-based system, it is ideal for oxo-clusters [96, 97] and other types of materials [45]. The most valuable trait of the PDF method, is that it enables to take a direct look at structural information of a material. Spectroscopy, electrochemical methods, dynamic light scattering (DLS) or even nuclear magnetic resonance (NMR) are some of the most popular methods used for analysis of solvated species, and yet none of them offers direct, structural information. Calculating a PDF pattern from total scattering data, results in an atom-atom distance distribution graph, described in direct space. This representation offers a straight-forward size analysis, and access to performing model fits for speciation purposes.

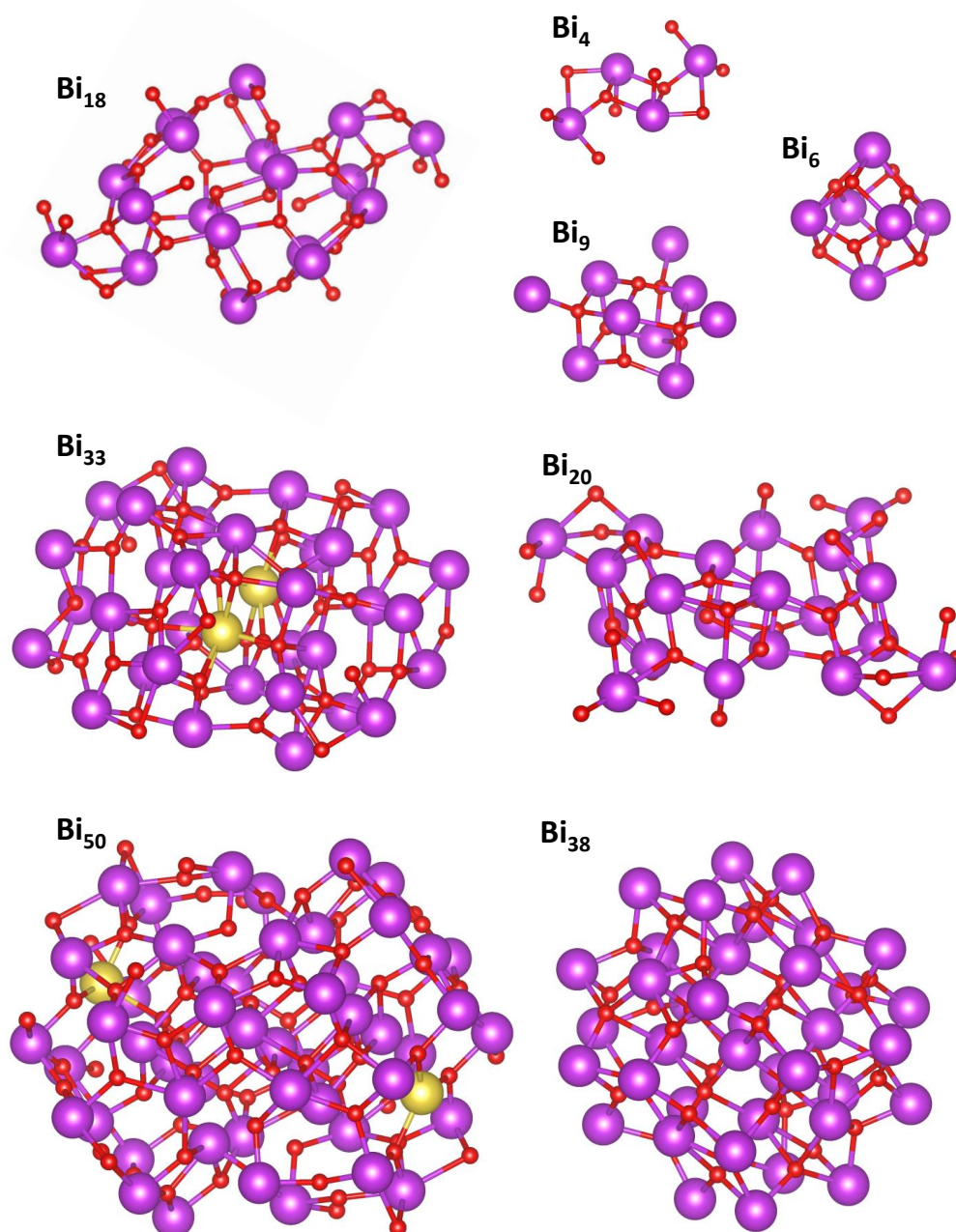


Figure 5.1: Models of various bismuth-oxo cluster cores. The presented frameworks consist mainly of bismuth (purple) and oxygen (red) atoms, with Bi₅₀ and Bi₃₃ containing additional sodium sites (yellow). All of these cores are in a center of bismuth-oxo clusters, crystallized with various ligands. Bi₅₀, Bi₃₃, Bi₂₀, Bi₁₈ and Bi₄ cores are functionalized in literature with bis(trimethylsilyl)acetamide and its derivatives [137]. The Bi₃₈ core is functionalized with salicylic acid and solvent – DMF or acetone [9, 10], similarly to the Bi₉ core [10]. And finally, the Bi₆ core is surrounded with NO₃ and H₂O ligands [138]. The presentation of the cores without ligands, serves clarity, and highlights the structure to which X-ray scattering is most sensitive. Moreover, the ligands come from the choice of precursor and synthesis method, and if the same structure is found to form in another way, the ligands would likely be different.

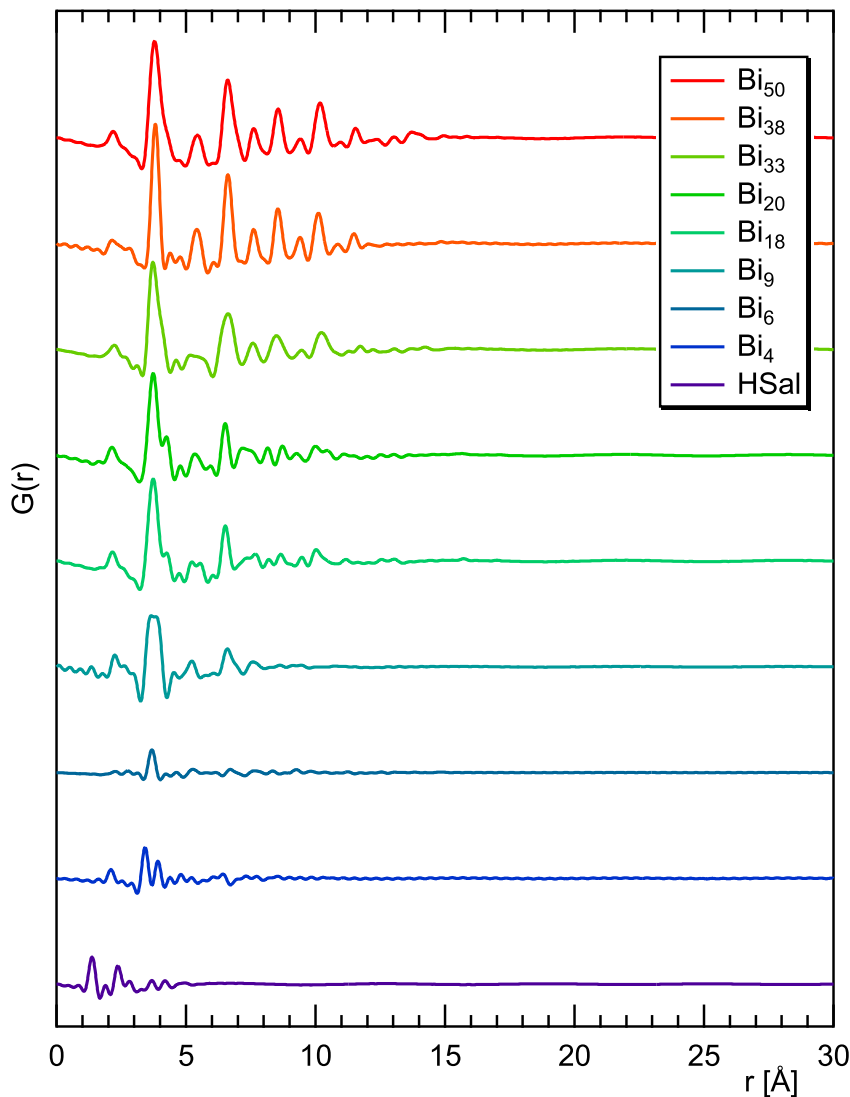


Figure 5.2: Simulations of PDF patterns of various bismuth-based oxo-clusters. Bismuth oxo-clusters of different origins and sizes can be found in the literature. From giants containing 50 bismuth atoms, such as $[\text{Bi}_{50}\text{Na}_2\text{O}_{64}(\text{OH})_2(\text{OSiMe}_3)_{22}] \cdot 2\text{C}_7\text{H}_8 \cdot 2\text{H}_2\text{O}$ [137], through still impressive $[\text{Bi}_{38}\text{O}_{44}(\text{HSal})_{26}(\text{H}_2\text{O})_4(\text{DMF})_{18}]$ [9], $[\text{Bi}_{33}\text{NaO}_{38}(\text{OSiMe}_3)_{24}] \cdot 3\text{C}_7\text{H}_8$ [137], $[\text{Bi}_{20}\text{O}_{18}(\text{OSiMe}_3)_{24}] \cdot 3\text{C}_7\text{H}_8$ [137], $[\text{Bi}_{18}\text{Na}_4\text{O}_{20}(\text{OSiMe}_3)_{18}]$ [137], to smaller species, such as $[\text{Bi}_9\text{O}_7(\text{HSal})_{13}(\text{Me}_2\text{CO})_5]$ [10], $[\text{Bi}_6\text{O}_4(\text{OH})_4](\text{NO}_3)_6 \cdot \text{H}_2\text{O}$ [138], $[\text{Bi}_4\text{O}_2(\text{OSiEt}_3)_8]$ [137]. Presented here are simulations [102] of their PDF patterns. The PDF patterns of the bismuth-oxo clusters are juxtaposed with salicylic acid [198]. A chart composed in this way enables fingerprinting of unknown species present in a sample.

5.1.1 The main objectives

The aim of this chapter is analysis of the dissolution of BiSal₂ in organic solvents, with emphasis on dimethylformamide (DMF) and acetone. The means of analysis are total scattering measurements and PDF method. Speciation is focused on confirming the larger species as [Bi₃₈O₄₄] cluster, and identifying the smaller species present in sparse water environment. This goal is directly following Chapter 4, where two different in size species were detected in DMF and acetone solution of BiSal₂.

Apart from the identification of species present in solution, this chapter also aims to further analyse the influence of H₂O on the solvated BiSal₂ system. For that, synchrotron measurements were performed in various solvents, and with various amount of water added to the solvent.

The additional goal is determination whether the change in color of BiSal₂ after mechanochemical synthesis, is related to bismuth-oxo cluster formation in solid state BiSal₂.

5.2 Experimental section

5.2.1 Synthesis and chemicals

Similarly to bismuth (III) disalicylate in Chapter 4, the chemicals presented in Chapter 3 (Tab. 3.1) were used in this chapter. Additionally, some chemicals provided by beamline labs and scientists were used. Caution was taken to use chemicals with purity not lower than in other experiments. 50 mg of bismuth (III) disalicylate (500.21 g/mol) was dissolved in 2.5 ml of a solvent, resulting in 0.040 M concentration, analogically to the one used in Chapter 4.

Well-characterized, mechanochemically synthesized samples of bismuth (III) disalicylate (BiSal₂) were used in each experiment. The BiSal₂ was dissolved in five, different solvents. Dimethylformamide (DMF), acetone, methyl ethyl ketone (MEK), pentanone and cyclohexanone (CH). Both anhydrous (dry), and bench (aged minimum for 1 month and more from the time of opening) were used.

5.2.2 Synchrotron experiments

Facilities

The data analyzed in this chapter was gathered in two facilities, European Synchrotron Radiation Facility (ESFR) in Grenoble, and PETRA III – Deutsches Elektronen-Synchrotron DESY in Hamburg.

The experiment in ESRF was done using the ID15-B beamline. It was equipped with a Perkin Elmer XRD detector. Measurements were done using a beam energy of 87 keV ($\lambda = 0.01425$ nm).

The experiment at PETRA-III storage ring at DESY (Hamburg, Germany) was done using the high energy Swedish Materials Science Beamline (P21.1), equipped with Perkin Elmer XRD 1621 (PE1621) detector. A series of measurements was done with the beam energy of 102.057 keV ($\lambda = 0.01215$ nm). Two, different detector positions were used in order to capture a large scattering range, and also capture small angle signal. This proved to be especially useful for the solid state BiSal₂ samples.

Liquid samples preparation and measurements

The experiments were performed by dissolving fresh BiSal₂ in the array of solvents (Acetone, DMF, Pentanone, Cyclohexanone and MEK), and syringing samples into quartz capillaries.

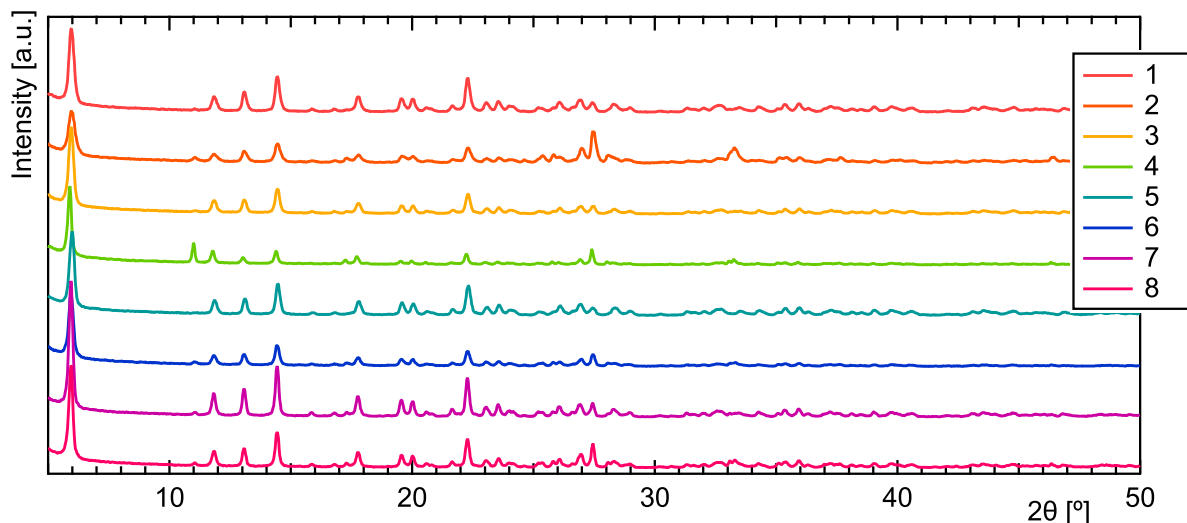


Figure 5.3: A set of PXRD patterns of bismuth (III) disalicylate batches synthesized for PETRA-III experiment. The sample no. 5 was exclusively used in the solution part of the experiment, whereas all samples were measured as dry powders.

The capillaries were provided by the beamlines. High purity BiSal_2 was synthesized in four of batches (Fig. 5.3), 14 days before the experiment.

Time-dependent measurements of capillaries filled with samples were performed, by filling the capillaries with a mixture of BiSal_2 and solvent, made with either anhydrous (dry) or bench (wet) solvents. The bench solvents, similarly to these used in Chapter 4, were anhydrous solvents left in enclosed, unsealed containers for a period longer than two months.

BiSal_2 solid state measurements

Four batches of bismuth (III) disalicylate in a powder form were measured at PETRA-III. This process was meant to explain the phenomenon of BiSal_2 powder becoming pink.

Four batches out of eight synthesized were chosen for a synchrotron experiment. The samples number 1 and 5 were almost white, whereas samples 7 and 8 vividly pink. The PXRD patterns indicate sample number 5 as the purest, free of Bi_2O_3 residue. This can be observed as a least intense 27.5° peak (Fig. 5.3). Because of that, only this sample was used in preparation of the liquid samples for the PETRA-III experiment.

Quartz capillaries with solid disalicylate were filled on the site and a couple of measurements were done for each capillary. A measurement of empty quartz capillary was also added, similarly to capillary with pure solvent, to be used as a background for calculations. Each measurement was again adjusted for the powder samples, which required far less time of exposition due to the crystalline structure.

Since the bismuth (III) disalicylate has a characteristic, intense low angle peak (6°), the most important measurements were done on the last day, with the detector adjusted so that the beam stop did not obscure that peak.

5.2.3 Data integration and PDF extraction

All the data from the experiment was integrated using the pyFAI suite [13]. Due to the use of 2D detectors (Fig. 5.4), the integration required converting 2D image into a function of

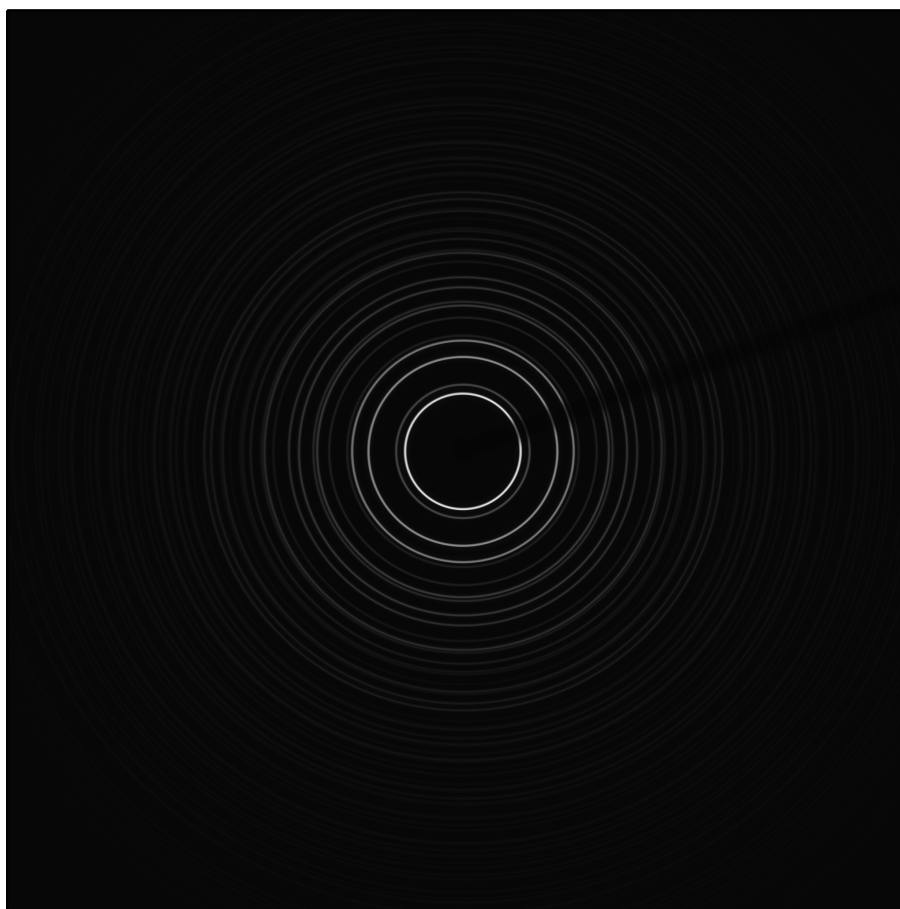


Figure 5.4: A detector image of CeO₂ calibrant rod. The image was measured in PETRA-III, at a Swedish Materials Science Beamline (P21.1). The diffraction cones and shadow of a beamstop are clearly visible. The calibration process transforms the 2D image into a 2D plot.

intensity, using a calibrant with well-defined diffraction pattern. Rods of CeO₂ were used for that purpose.

Conversion of total scattering data to PDF was calculated using PDFgetX3 software [101], starting with CeO₂. The calibration was confirmed as correct by refining obtained CeO₂ data with PDFgui, and achieving a good results (Fig. 5.5).

Typical values of Q_{max} were 13-16 Å⁻¹, when calculating PDF of datasets for liquid samples. For the solid-state BiSal₂ Q_{max} of 19 and above was used. The background was measured as a capillary filled with solvent, and subtracted from the PDF of each sample. Exclusively quartz capillaries were used.

PDF fitting

PDF data was fitted, using least square refinement method. Scale factor, atomic coordinates and thermal factors of oxo-cluster models were refined to fit the data. The atomic coordinates of solid state structures were constrained by their symmetry. The solution-based species were constrained to only refine in set boundaries. Both atomic coordinates and thermal factors of atoms other than bismuth, in that oxygen and carbon, were for the majority of fits constrained,

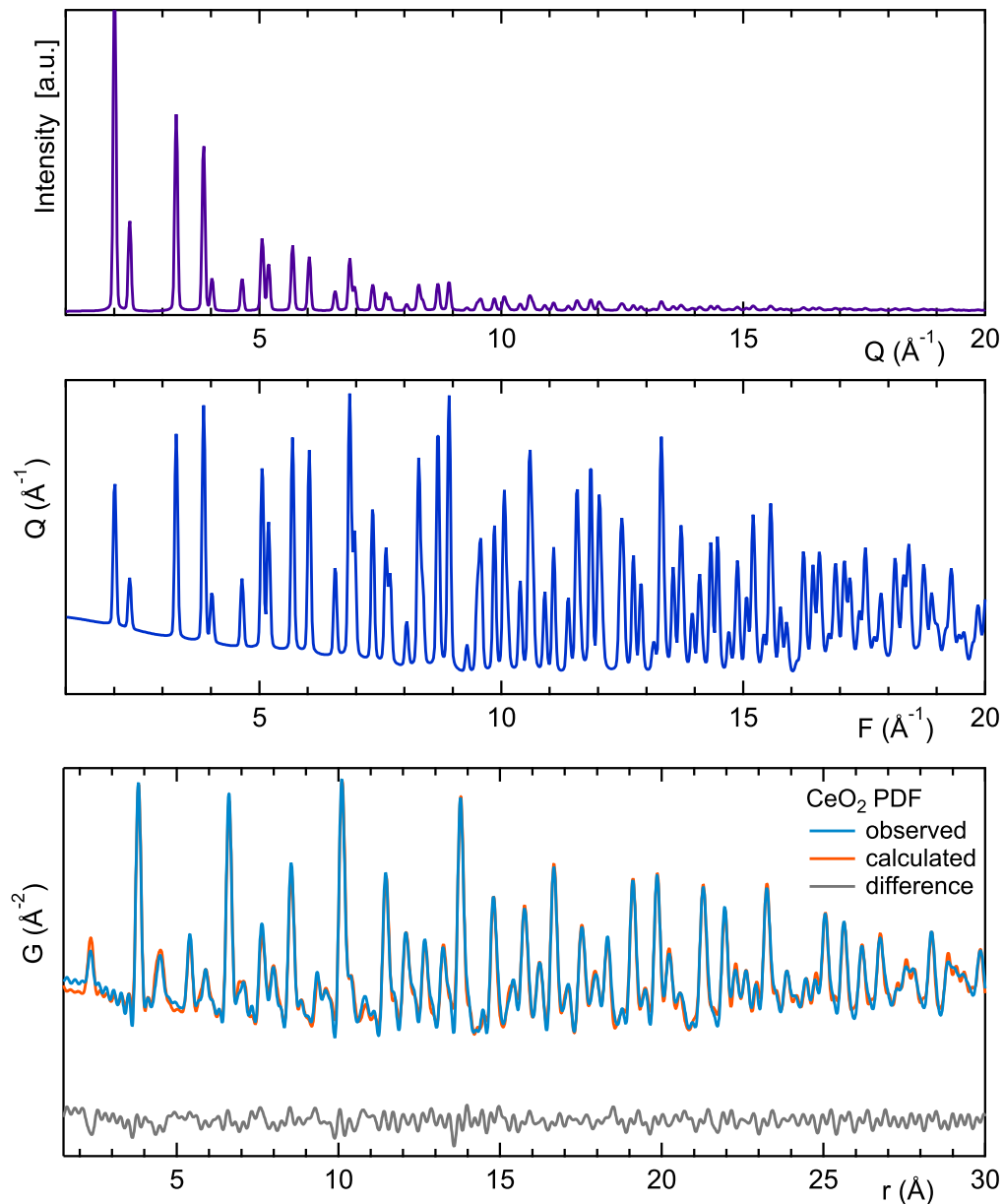


Figure 5.5: Set of graphs associated with the same measurement. A total scattering signal of CeO₂ at the top, followed by its structure factor $F(Q)$, followed again by PDF derived from the structure factor. The PDF fit was calculated using PDFgui software. This process confirms a correct integration of the detector image, into 2D waves. As the CeO₂ is used initially to integrate the 2D detector image into 2D waves, it can be useful to use the integrated data of the calibrant further. Fitting a model to the integrated calibrant data is one such way, of ensuring a correct integration. This also enables finding a correct Q_{damp} parameter, required for fitting of the experimental data.

in order to decrease the amount of parameters and reduce refinement time. Peak widths were adjusted using delta1 and delta2 coefficients.

The Q_{damp} parameters for PETRA experiments were 0.0538 and 0.0298 for the closer detector position, and 0.0602 for ESRF experiments. This parameter derives from the limited Q-resolution of the total scattering measurement, and can also be called damping factor.

For the fitting of calculated PDFs, two programs based on the use of DiffPy CMI software were used. The first allowed to fit crystalline CeO_2 callibrant with pyFAI, using small box approximation model, appropriate for solid-state structures. The second program, DiffPy, can be used for crystalline solids, as well as molecules in solution. For the latter it utilizes Debye function method. DiffPy was used in fitting models to both solid-state and dissolved BiSal_2 samples.

5.3 Results

5.3.1 PDF fingerprints

In order to identify species that could be present in solution, we calculated the PDF of a variety of bismuth oxo-clusters, available in CCDC database (Fig. 5.2). Distinguishing PDF patterns can be done using a fingerprinting method, which is based in comparing the experimental data to simulations generated for expected structures. Although clusters composed from the same type of atoms in a similar structure might form peaks in the same positions, the overall size of a cluster and difference in intensities of said peaks can be a distinction criteria.

5.3.2 Bismuth (III) disalicylate – solid state

Although the previous, PXRD data shows no additional phase in the bismuth (III) disalicylate (Chapter 4), amorphous or otherwise, the direct space look into the BiSal_2 structure could bring new information. Synchrotron solid state experiments were performed at PETRA-III.

The first peak of the BiSal_2 structure could be captured only with a close detector position. This conformation of a beamline resulted in a good quality, small-angle measurement. However, such close to the sample position significantly reduces the range of a measurement, a quality vital for a good quality PDF. Because of that, measurements with further detector distance were also done, capturing large-angle data. A procedure of stitching both typed of measurements together was then performed, in order to maximize accuracy of the Fourier transform (Fig. 5.6). This was done for all four of the measured, solid state samples.

The solid state samples were compared with each other. Sample 1 and 5 were nearly white, with a pale pink hue, whereas the 7 and 8 were vividly pink. The difference in color is relevant to the hypothesis of some bismuth-oxo cluster formation taking place on the surface of BiSal_2 grains, causing the pink coloration of otherwise white substance.

The PDFs of all four samples are virtually identical, with only minor differences in intensities (Fig. 5.7, a). The fact that no new peaks can be detected, could point towards all four samples having the same qualitative composition. The differences in peak intensities are small enough, that factors other than quantitative differences in between samples could be responsible for that. Non-identical quartz capillary background subtraction are one such example.

To complete the analysis, fitting of a BiSal_2 model available in literature [9] was performed (Fig. 5.7, b and c). Although most of the PDF patterns is well approximated with the model, at lower r values (below 10 Å). This is especially prominent for the 2.5, 3.9 and 5.0 Å peaks. The initial explanation was that this is related to a small, ~ 5 Å structure, present in the solid state BiSal_2 . However, if such species was present in the samples, and was related to the color change, its concentration would vary in between the samples. The fits, however, are do not differ for the measured samples, and the leftover intensities are the same. Another clue is

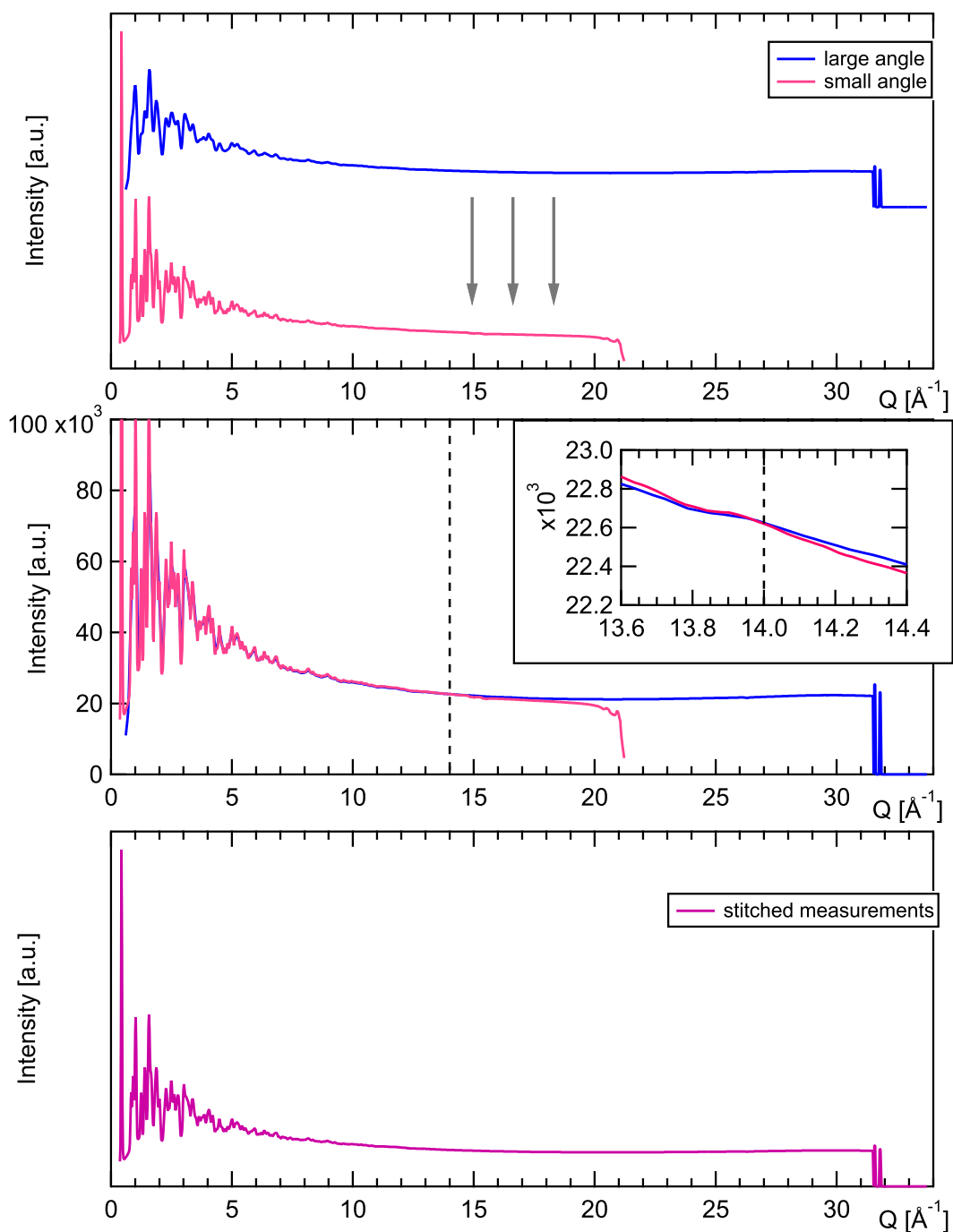


Figure 5.6: Graphs illustrating process of stitching together small and large angle measurements. The first step was normalization of both measurements at a chosen Q (upper graph). Multiplication of one of the measurements was used to achieve the that. Then, a point of slicing the data was chosen, at 14 \AA^{-1} for the example (middle graph). At that point the data was cut, and small angle measurement up to 14 \AA^{-1} was joined with the large angle data after 14 \AA^{-1} . Then, the resulting wave was interpolated, in order for the point to be spread in equally throughout. This results in a hybrid dataset, containing good quality low and large angle information (lower graph).

that the peaks in question are significantly more narrow, than other peaks in the PDF patterns. Because of the peak width calculation being universal for the entirety of the fit, the more narrow peaks might be left unfit. The presence of such peaks on the other hand, could be related to correlated-motion phenomenon. The BiSal₂ exhibits a harmonic-like structure in solid-state, which one could easily imagine to be anisotropically flexible and rigid. This could result in a well-defined atom-atom distances in a small range, and a more flexible atom-atom distance in a large range. That could explain the anisotropic peak width present in the calculated PDF patterns.

5.3.3 Bismuth (III) disalicylate – solution

The initial measurements were performed with five, different solvents (Fig. 5.8). The two, distinctive species seen previously in DLS UV-Vis were found to be just as distinct in their PDF signal. The smaller one has characteristic peaks at 3.8, 5.4, 6.5, and 7.5 Å. The larger one at 3.8, 5.4, 6.5, 7.5, 8.5, 10.2, and a small one at 11.5 Å.

Important to note is that the very last peaks of each species, at 7.5 Å for the smaller one, and 11.5 Å for the larger one, have rather small intensity. Therefore, the 8.5 and 10.2 Å peaks of the larger cluster are most often taken as a differentiating tool.

Identification of the species

The first step was identification of the smaller and larger species. After comparing the data to the PDF patterns calculated based on models, fitting was performed.

The size of both structure cores can be read from the PDF data, with the [Bi₉O₇] cluster core reaching ca. 7.5 Å (Fig. 5.9, a) and the [Bi₃₈O₄₄] cluster core 12 Å (Fig. 5.9, b).

Because of the high scattering power of bismuth, its signal is the most prominent in the PDF pattern of bismuth-oxo clusters. The loss in ligand signal is further amplified by the elastic, single-bond connection to the core. This enables rotation and bending in a reference to the bismuth-oxo core, which broadens the already weak signal. Because of that, in the PDF measurements, only the structure of the core can be reliable.

As suspected, the larger species does fit with PDF of the [Bi₃₈O₄₄] cluster (Fig. 5.10, c). Looking at the measurements showing the smaller species, shows a clear match with the [Bi₉O₇] (Fig. 5.10, a and b). The solid-structure models of each cluster were fitted to the data with bismuth positions constrained to a 0.2 Å radius. This ensures that the fitted model does not deviate unrealistically from the initial structure.

Although the ligands have small contribution to the overall PDF signal, in comparison to the bismuth core, the high concentration of salicylic acid in the system (2 molecules per 1 bismuth atom), can be seen as increased peak intensity at 1.2 and 2.1 Å (Fig. 5.10, b, red arrows). This contribution can be fit with two-phase fit.

Water, solvent and time-dependence

Initially, over night measurements of samples were performed, resulting in detailed, time-resolved plots (Fig. 5.11). These samples were prepared from dry solvents (unless stated otherwise), and sealed for the time of measurements.

No significant changes were observed in that time period for all of the samples, apart from the wet DMF. In wet DMF a clear increase in signal at 8.5 and 10.2 Å can be seen in the initial 50 minutes. Even a small signal at 11.5 Å can be distinguished, although its intensity is comparable to the noise. Nevertheless, this particular measurements captures the transformation from [Bi₉O₇] to [Bi₃₈O₄₄] oxo-cluster in wet solvent. The difference in between dry and wet DMF is even clearer, when looking at a profile line set to one of the characteristic peaks in Fig. 5.12.

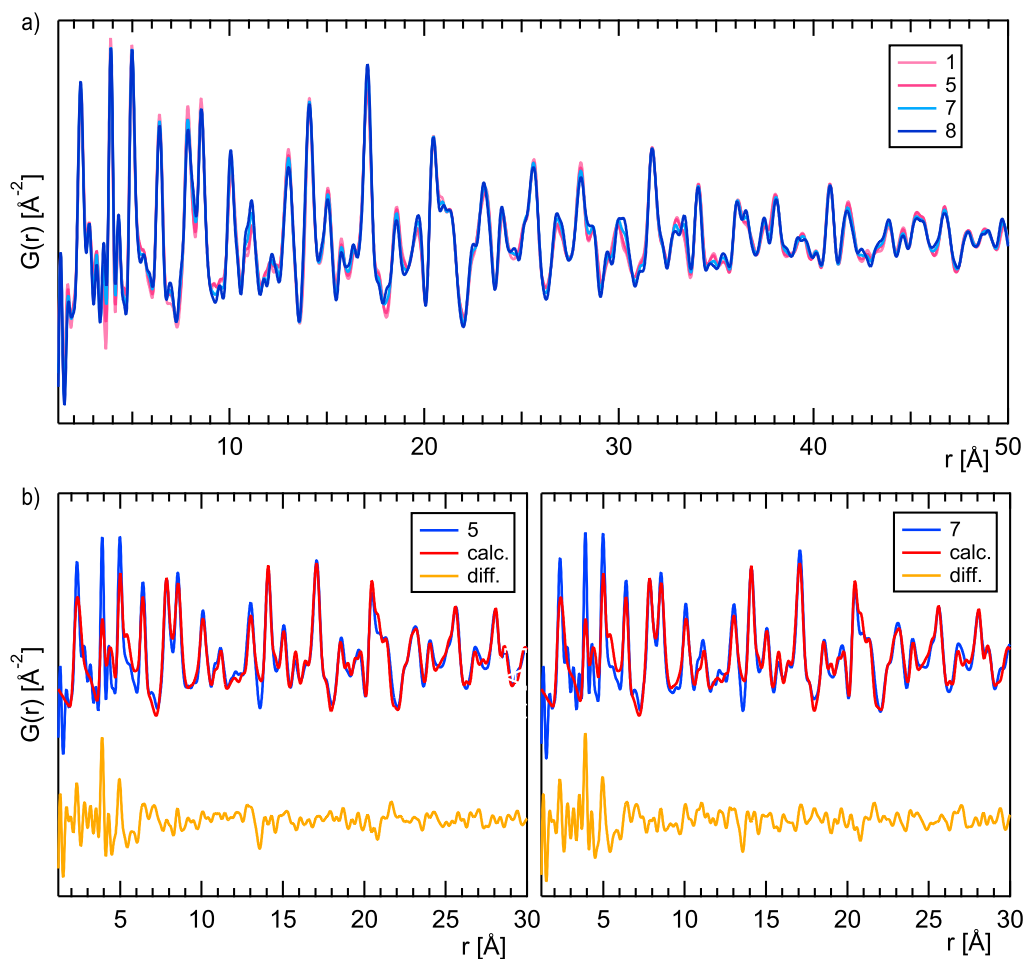


Figure 5.7: PDF patterns of bismuth (III) disalicylate samples. Of four samples used for the synchrotron experiment, number 1 and 5 were pale pink in color. Number 7 and 8 were significantly more vivid, and close to fuchsia in hue. **a**, PDF of all four samples, number 1, 5, 7 and 8. All of the measurements are overlaid, showing how similar the pattern is. No significant differences were found based on the comparison, despite the clear difference in samples color. **b**, A DiffPY fit of a BiSal_2 model [9] to the PDF data of a pale sample (5). **c**, A DiffPY fit of a BiSal_2 model [9] to the PDF data of a vivid sample (7). Both fits suit the respective data well, apart from peaks at 2.5, 5.0 and especially 3.9 Å. There is, however, no correlation of the fit to the color of a BiSal_2 sample.

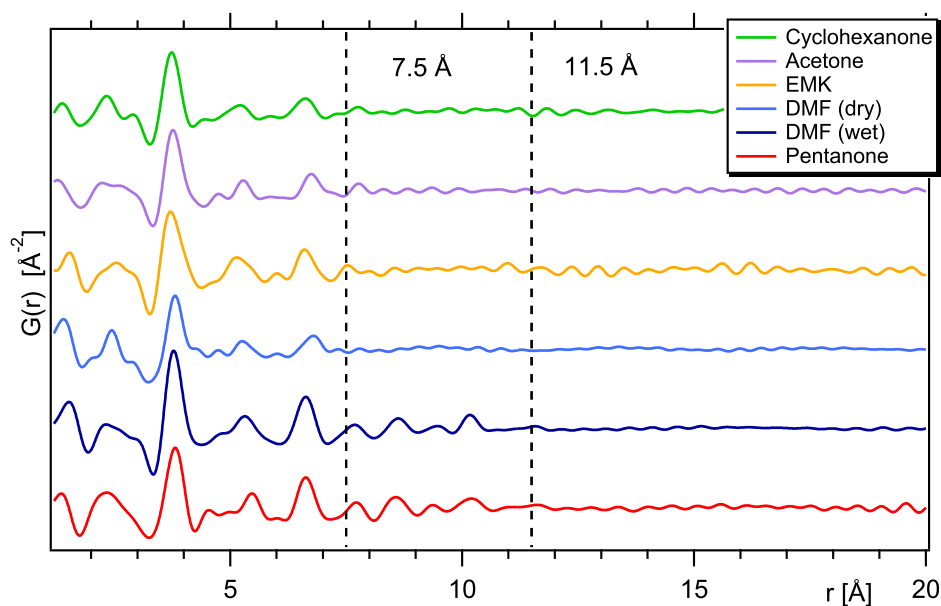


Figure 5.8: PDF measurements of bismuth (III) disalicylate in various solvents. The resulting can be divided into two groups. In acetone, cyclohexanone, pentanone, dry DMF and MEK (methyl ethyl ketone), a small species can be found, with the size not reaching beyond 7.5 Å. In pentanone and wet DMF, a larger species is present, with the size around 11.5 Å, if a last, small peak is taken into consideration. The former fits well with the $[\text{Bi}_9\text{O}_7]$ cluster core, whereas the latter shows peaks characteristic for the $[\text{Bi}_{38}\text{O}_{44}]$ cluster.

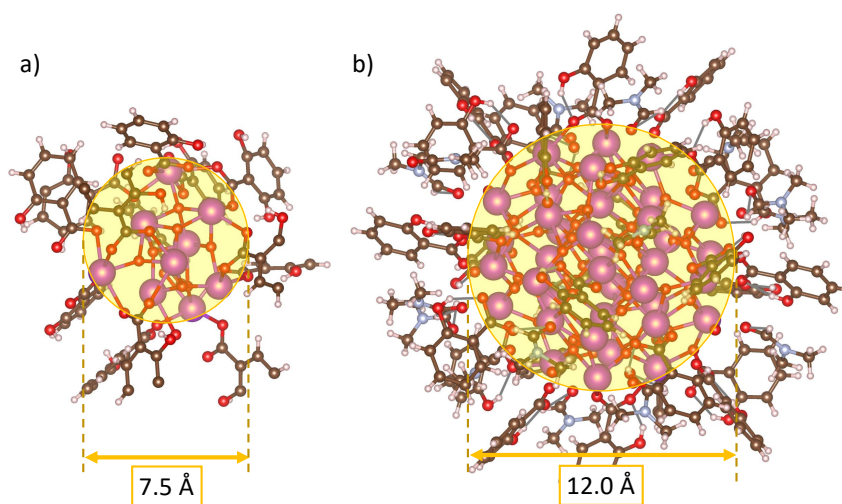


Figure 5.9: Solid-state structures of relevant oxo-clusters with their ligands, composed of bismuth (purple), oxygen (red), carbon (brown) and hydrogen (white). The bismuth-oxo cores are contained in yellow circles, representing the corresponding core diameter. a), $[\text{Bi}_9\text{O}_7]$ core with salicylate and solvent (acetone) ligands [10]. b), $[\text{Bi}_{38}\text{O}_{44}]$ surrounded by salicylate and solvent (DMF) ligands [9].

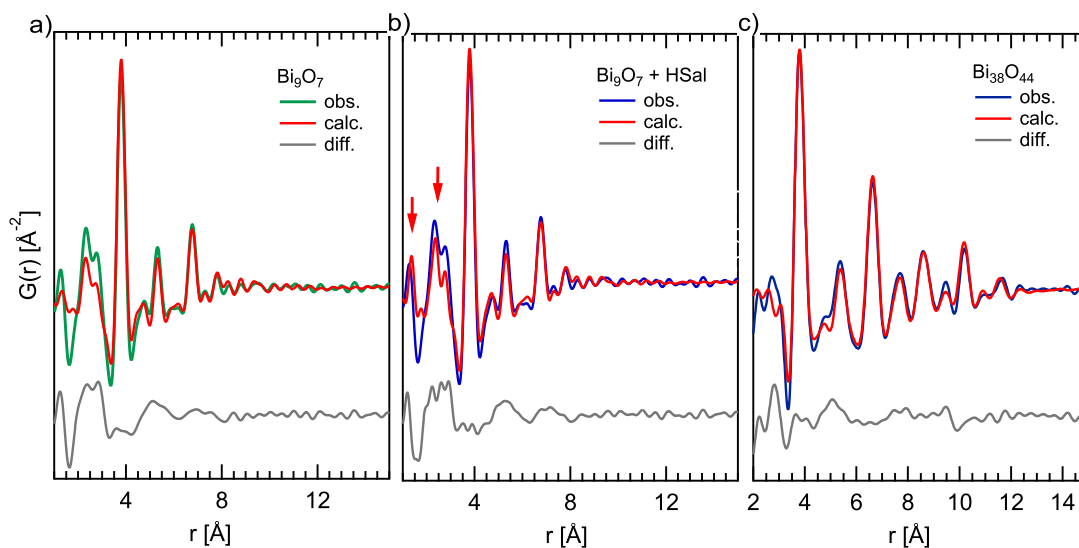


Figure 5.10: Solid-structure models fits to the PDF data in DMF. a, $[\text{Bi}_9\text{O}_7]$ with salicylate ligands model fit to dry DMF sample, resulting in $R_w = 0.325$. b, Two-phase, $[\text{Bi}_9\text{O}_7]$ with salicylate ligands and free salicylic acid (HSal) model fit to dry DMF sample, resulting in $R_w = 0.299$. The red arrows point out towards the intensity filled with the HSal phase. c, $[\text{Bi}_{38}\text{O}_{44}]$ model with salicylate ligands fit to wet DMF sample, resulting in $R_w = 0.190$. The positions of bismuth for all models were restrained to move in 0.2 \AA radius around their original, solid-state position.

In cyclohexanone initially bismuth (III) disalicylate signal was captured from undissolved particles, to then reveal the smaller, $[\text{Bi}_9\text{O}_7]$ cluster. The co-existence of the BiSal_2 and the $[\text{Bi}_9\text{O}_7]$ can be seen in the earlier datasets, up until 40 min, when only the smaller cluster is visible. DMF, Acetone and MEK showed the same, $[\text{Bi}_9\text{O}_7]$ signal from the very beginning. Pentanone, however, from the very first measurements showed $[\text{Bi}_{38}\text{O}_{44}]$ cluster, with the mentioned, characteristic 8.5 and 10.2 \AA peaks. The peak distribution and intensity in these measurements did not change over time.

A comparison of PDF patterns of wet DMF and cyclohexanone can be seen in Fig. 5.13. This shows, how the BiSal_2 slowly dissolves, leaving only the smaller cluster at 17 hours from the start of measurement. The wet DMF on the other hand, allows to observe slow rise in the larger cluster peaks, from the initial pattern, showing exclusively the $[\text{Bi}_9\text{O}_7]$ cluster.

Influence of water

As an alternative to the dry and bench solvents, dry solvents spiked with water were used in some of the measurements, in order to analyse the influence of water on the development of the solvated BiSal_2 system. Two solvents were chosen for that, acetone and DMF. After mixing the solvents with BiSal_2 , 1 and 10% of water were added to each solvent, resulting in four samples.

At first sight, all of the measurements feature prominently the 10.2 \AA peak, specific to the $[\text{Bi}_{38}\text{O}_{44}]$ cluster (Fig. 5.14, dashed lines). The signal of this cluster is so strong in fact, that the 11.5 \AA peak to be clearly distinguishable from the background. This is especially visible at 24 and 54 h measurements, and is in part a result of long (4 s) exposure time for each measurement, and summation of up to 100 measurements for each, individual result. This procedure reduces the background noise, while amplifying the scattering signal.

Additional analysis based on subtracting measurements, reveals a complete $[\text{Bi}_9\text{O}_7]$ signal. It is found exclusively in the 10% of H_2O samples (Fig. 5.14, lower row). The signal in 1%

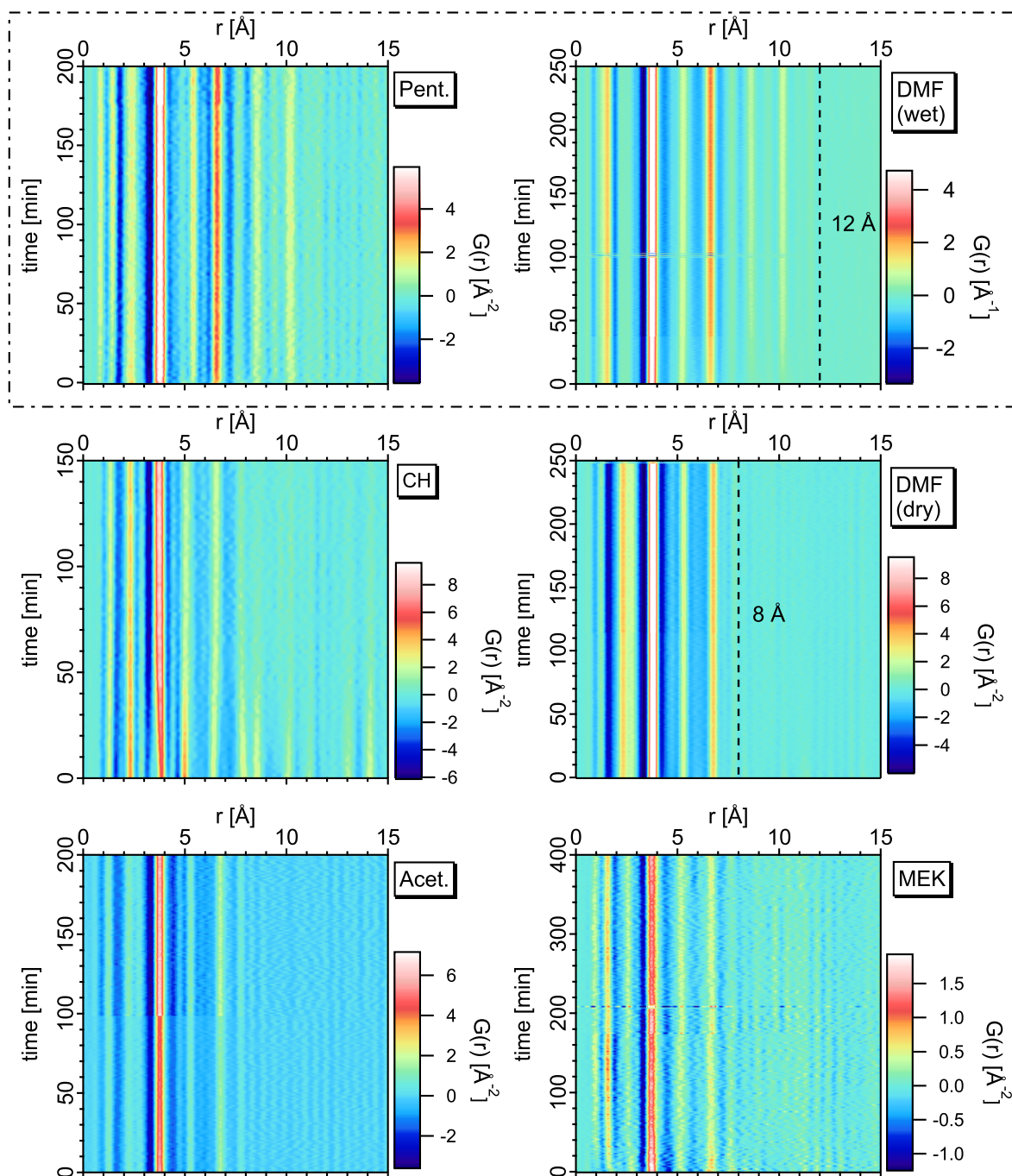


Figure 5.11: A color plots of stacked PDF measurements, of BiSal_2 dissolved in various solvents. The top two solvents (broken-line square) are dry pentanone and wet DMF. They show explicit peaks at around 8.5 and 10.2 Å, and to the smaller extent at 11.5 Å. These are indicative of the $[\text{Bi}_{38}\text{O}_{44}]$ cluster presence in solution. In the case of pentanone, peaks are visible from the first measurement, whereas wet DMF shows increase in their intensity as a function of time. All other solvents, cyclohexanone (CH), dry DMF, acetone (Acet.) and MEK contain only the smaller cluster.

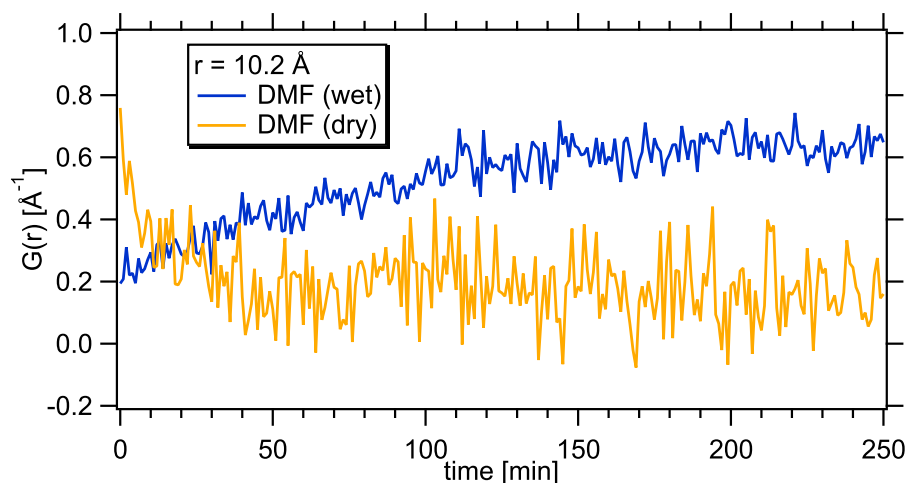


Figure 5.12: The profile lines at 10.2 Å, for both dry and wet DMF samples. Corresponding color plots can be seen in Fig. 5.11. The profiles show how the intensity in dry DMF stays at the same level, after a brief period of decreasing – this is most likely due to undergoing dissolution of BiSal₂ in the initial 50 min. The wet sample shows a steady increase in the intensity, corresponding to the rise of one of the characteristic for [Bi₃₈O₄₄] cluster peaks.

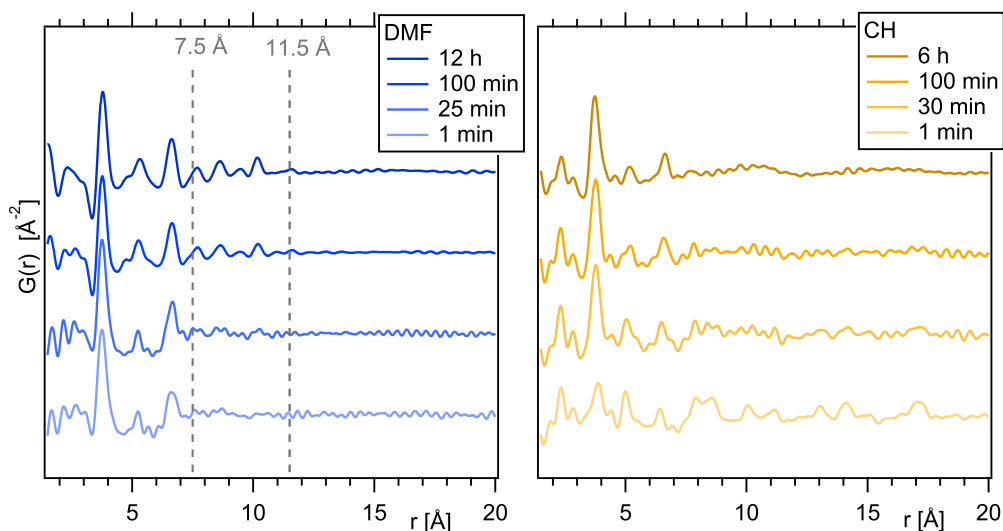


Figure 5.13: Time-resolved PDF data for bismuth (III) disalicylate in two solvents. In wet DMF (left), the reaction immediately produces [Bi₉O₇(HSal)₁₃], converting it to [Bi₃₈O₄₄(HSal)₂₆(H₂O)₄(DMF)₁₈] over the course of couple dozen minutes. Dry cyclohexanone (right) produces only [Bi₉O₇(HSal)₁₃]. In the initial phase, BiSal₂ signal is visible due to not full dissolution. At 6 hours the [Bi₉O₇] can be seen.

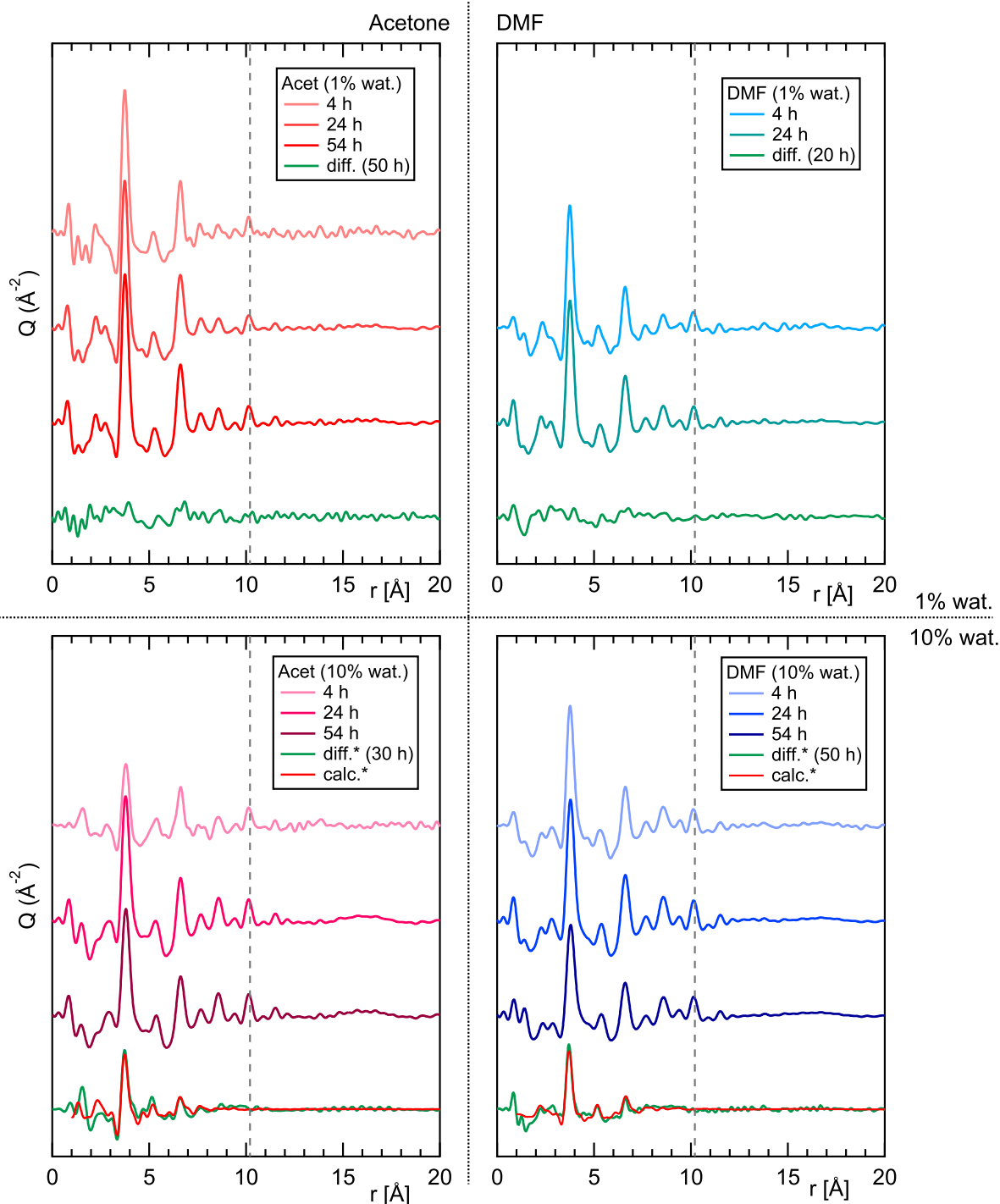


Figure 5.14: An overview of time-resolved PDF data for four, different samples. The presented samples are based in two liquids, acetone (left) and DMF (right). To anhydrous solvents, 1 (upper row) and 10% (lower row) of H_2O were added. On each graph, multiple graphs are presented, gathered at specific time (4, 24 and 54 h). The time is counted from mixing the BiSal_2 with solvent and adding water. Additionally, difference curves are presented on each graph, in green. The differences were calculated by subtracting the measurements, and represent a change in time presented in the brackets. The 10% measurements show a change in between the 54 and 4 h measurements (diff.), which matches well with the $[\text{Bi}_9\text{O}_7]$ cluster. A fit to the $[\text{Bi}_9\text{O}_7]$ model was calculated for the differences of the 10% measurements (calc.). *, tagged plots are multiplied by 3.

samples does not change (Fig. 5.14, upper row). Because it is the later measurement (54 h) that is subtracted from the earlier one (4 h), the concentration of the $[\text{Bi}_9\text{O}_7]$ cluster decrease in time for the 10% samples. This highlights, that in the 1% samples, the concentrations of neither of the clusters change.

Plots were normalized before subtracting by multiplying the values of $G(r)$, so that the 10.2 Å peak is at the same level. This procedure ensures that the difference plots show all of the changes in PDF signal, excluding the $[\text{Bi}_{38}\text{O}_{44}]$ concentration. These adjustments were minor, and did not exceed 0.01 of the original values. Therefore, the analysis of $[\text{Bi}_{38}\text{O}_{44}]$ concentration change was omitted, as the 10.2 Å peak height is at similar level in all of the samples.

A similar, subtraction-based comparison of 1 and 10% DMF samples reveals additionally, that there is a higher concentration of the $[\text{Bi}_9\text{O}_7]$ cluster in the 1% sample (Fig. 5.15, a). This directly implies that the higher addition of water increases the production of the larger, $[\text{Bi}_{38}\text{O}_{44}]$ cluster.

The samples with lower water content were fit with the $[\text{Bi}_9\text{O}_7]$ + salicylic acid model (Fig. 5.15, b and c). This was done in order to compare it to fit of the same model to the higher water concentration sample (Fig. 5.15, d). Although the most intense peak fits fully in the 1% samples, it is almost filled also in the 10% sample, even though it is known to contain predominantly the larger, $[\text{Bi}_{38}\text{O}_{44}]$ cluster. This is to be expected, due to all of the $[\text{Bi}_9\text{O}_7]$ peaks being also present in the $[\text{Bi}_{38}\text{O}_{44}]$ cluster signal. Because of that, it is unreliable to use two-phase fit in this system, in order to establish the respective $[\text{Bi}_9\text{O}_7]$ and $[\text{Bi}_{38}\text{O}_{44}]$ concentrations for each sample.

Worth highlighting is that the $[\text{Bi}_{38}\text{O}_{44}]$ cluster signal was detected in acetone after addition of water, in the described above measurements (Fig. 5.14). This stands in contrast to the dry acetone in-situ measurements presented as color plots in Fig. 5.11, and is consistent with the DMF solvent.

5.4 Discussion of the results

5.4.1 Bismuth (III) disalicylate – solid state color change

Although unambiguous traces of $[\text{Bi}_{38}\text{O}_{44}]$ cluster were not found in the solid-state BiSal_2 , it does not disprove the theory that a bismuth-oxo cluster formation is responsible for the change in color. The change from white to pink is apparent after mechanothesized BiSal_2 is exposed to the environment. Even a minor amount of a cluster species could cause a visible change in the white powder appearance. At the same time, the color change could also appear due to a structural change in the BiSal_2 crystalline structure, rather than chemical change.

The acquired evidence shows that no, quantitatively significant amount of an additional phase is present in mechanochemically synthesized BiSal_2 . The same observation is made based on synchrotron, as well as laboratory PXRD and Raman spectroscopy evidence (Chapter 3).

Looking at the solid BiSal_2 PDF signal (Fig. 5.7, a) it is clear that no difference can be seen in between samples varying in intensity of the pink hue. Both pale, almost white pink samples 1 and 5 have virtually the same signal as vividly pink samples 7 and 8. This observation is then repeated, when looking at the fit to the data (Fig. 5.7, b and c). Different in color samples 5 and 7 exhibit virtually identical fit of a model their respective datasets.

The intensity of three peaks in the low- r range (5 Å and below) is not properly fit, leaving signal that could be of a small metal-oxo cluster. A more likely explanation, however, is that the narrow widths of these peaks are responsible for the poor quality of fit in that region. Supporting this claim is the fact, that no fully unfit peaks can be found in the data. Moreover, the particular structure of BiSal_2 can enable anisotropic and local rigidity, causing low- r range peaks to be better defined, just as they are in the data.

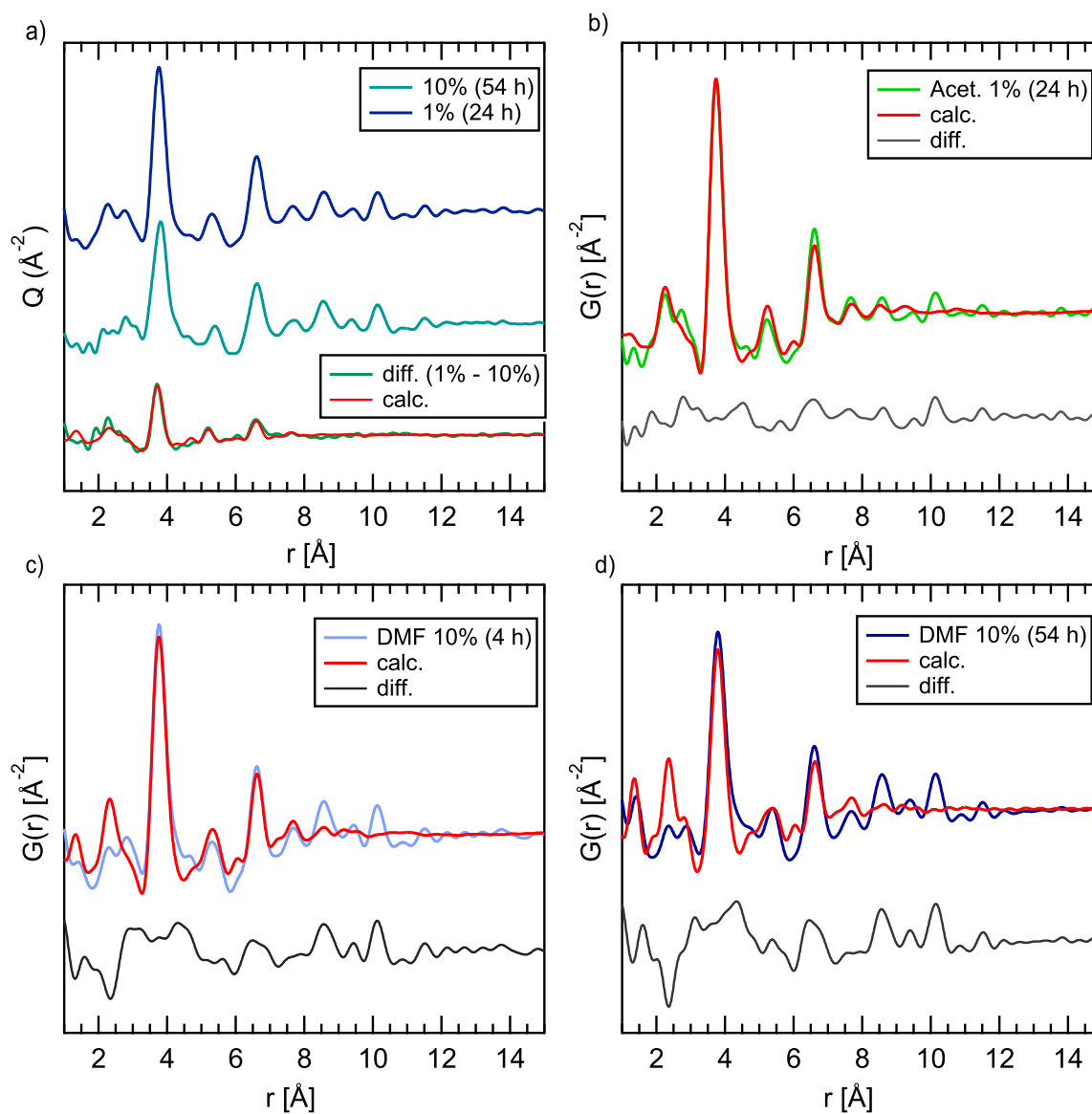


Figure 5.15: An overview of time-resolved PDF data for four, different samples. The presented samples are based in two liquids, acetone (left) and DMF (right). 1 (upper row) and 10% (lower row) of H₂O were added to anhydrous solvents.

The solid-state BiSal_2 analysis is significant when looking at the $[\text{Bi}_{38}\text{O}_{44}]$ cluster growth. It is assumed to take place in a solution phase, with the BiSal_2 acting as a precursor when solvated. If the BiSal_2 transforms chemically in some quantity before the dissolution, that could change the outlook on the $[\text{Bi}_{38}\text{O}_{44}]$ formation. However, the evidence supports the solid-state, mechanochemically synthesized BiSal_2 to be a pure, single-phase substance.

5.4.2 $[\text{Bi}_{38}\text{O}_{44}]$ oxo-cluster solution-based growth

The key features allowed the fingerprinting of the smaller structure, and its identification as $[\text{Bi}_9\text{O}_7]$. In particular, the characteristic peaks at 8.5, 10.2 and 11.5 Å, which distinguish this structure from the larger $[\text{Bi}_{38}\text{O}_{44}]$.

There is no evidence of smaller than $[\text{Bi}_9\text{O}_7]$ species, such as monomers or dimers, present in any of the solvents used. Access to water and atmosphere, through use of bench solvents or leaving sample open, promotes formation of the $[\text{Bi}_{38}\text{O}_{44}]$ cluster. This cluster was observed in DMF, acetone and pentanone samples, with pentanone promoting its formation even in dry conditions. At the same time, cyclohexanone promotes stability of the $[\text{Bi}_9\text{O}_7]$ cluster, even when the sample is not sealed (Fig. 5.13, right).

Looking at the samples with addition of 1 and 10% of water (Fig. 5.14), it can be stated that the speed of $[\text{Bi}_{38}\text{O}_{44}]$ growth is increased by excess of water. Only ca. 1.5 μl of water is enough to turn 200 mg of BiSal_2 into the $[\text{Bi}_{38}\text{O}_{44}]$ cluster, according to the stoichiometric calculations performed in Chapter 4, which indicated that even nominally dry samples could produce the $[\text{Bi}_{38}\text{O}_{44}]$ cluster. And it is confirmed experimentally, that traces of $[\text{Bi}_{38}\text{O}_{44}]$ can be found in dry acetone and DMF with only 1% of H_2O , but also in dry pentanone with no added water. Increasing the addition of water in acetone and DMF to 10%, shows decrease in $[\text{Bi}_9\text{O}_7]$ signal contribution to the total PDF signal of a sample. Not only is that true, when a 1 and 10% samples are juxtaposed, but also when the 10% sample measurements taken at different times (50 h difference) are compared. This means, that the addition of a larger amount of water, allows for more $[\text{Bi}_{38}\text{O}_{44}]$ to be formed.

Most importantly for the analysis of growth mechanism, synchrotron evidence shows formation of the $[\text{Bi}_{38}\text{O}_{44}]$ cluster from BiSal_2 , with the $[\text{Bi}_9\text{O}_7]$ cluster as an intermediate step (Fig. 5.13, left), in wet DMF (Fig. 5.11, DMF wet).

$[\text{Bi}_{38}\text{O}_{44}]$ and $[\text{Bi}_9\text{O}_7]$ structural similarity

The $[\text{Bi}_9\text{O}_7]$ cluster, initially formed from bismuth (III) disalicylate, is a direct precursor to the $[\text{Bi}_{38}\text{O}_{44}]$ cluster. This is supported also by the similarities in their structure, with a central octahedron (Fig. 5.16), and with the synchrotron evidence.

The $[\text{Bi}_{38}\text{O}_{44}]$ cluster is interesting structurally, due to its "magic-size", Keplerate shape [42]. It is composed of a central Bi_6 octahedron, encapsulated by a Bi_8 cube, held inside a truncated octahedral Bi_{24} cage. These structures are joined together with oxygen atoms (Fig. 5.16, a). Interestingly enough, the conformation of atoms in the $[\text{Bi}_9\text{O}_7]$ cluster resembles an inner part of a full Keplerate, which can be seen when bismuth atoms are colored accordingly (Fig. 5.16, b).

The structural similarity, together with the PDF evidence confirming presence of the $[\text{Bi}_9\text{O}_7]$ and $[\text{Bi}_{38}\text{O}_{44}]$ clusters in the BiSal_2 solution, points towards a specific growth mechanism. Initial formation of $[\text{Bi}_9\text{O}_7]$ cluster, that is then expanded to the larger, $[\text{Bi}_{38}\text{O}_{44}]$ form.

Solvent-dependence

The tendency of cyclohexanone to form exclusively $[\text{Bi}_9\text{O}_7]$, and for the pentanone to right away form $[\text{Bi}_{38}\text{O}_{44}]$ cluster, point out towards a key input of the utilized solvent on the cluster

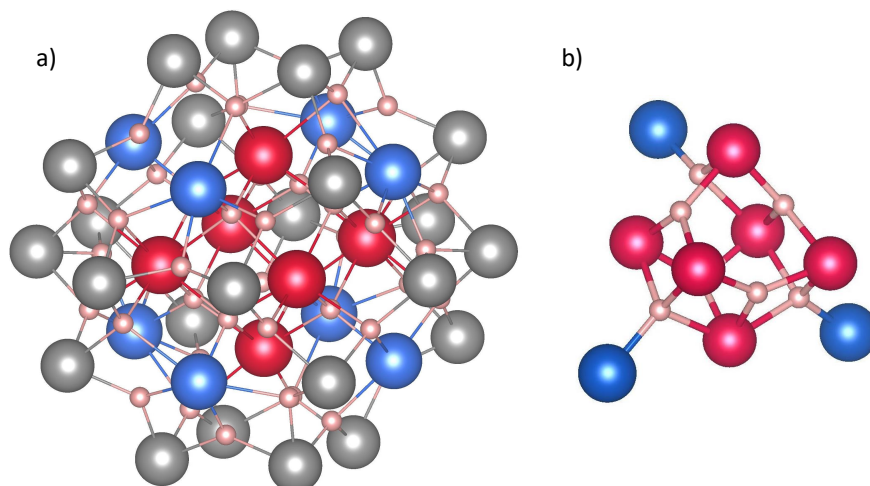


Figure 5.16: Models of solid-state structures of the clusters relevant to this chapter, as reported in literature [9]. a), A model of $[\text{Bi}_{38}\text{O}_{44}]$ cluster core. The oxygen sites are shown in light, pink hue. The central Bi_6 octahedron is in red, surrounded by blue Bi_8 cube. The remaining, grey Bi sites form a truncated octahedron, composed of 24 sites. All of the bismuth positions combined form a Keplerate. b) A model of $[\text{Bi}_9\text{O}_7]$ cluster core. Although the solid-state structure is significantly distorted, the arrangement of Bi sites is analogous to the Bi_6 octahedron of Keplerate, and three of surrounding it Bi_8 cube sites.

growth. One explanation is that the used solvent enables BiSal_2 to dissociate quicker, hence promoting full reaction.

It is also possible, that some solvents promote activation of the $[\text{Bi}_9\text{O}_7]$ cluster, to become the inner octahedron of $[\text{Bi}_{38}\text{O}_{44}]$, after bismuth sites surround it in Keplerate formation. Solvent could also facilitate solvation of BiSal_2 , increasing its concentration, and therefore as a result, increase also the $[\text{Bi}_{38}\text{O}_{44}]$ cluster formation speed. It is also worth noting, that the solvent serves also as a ligand in the crystallized forms of both clusters [9, 10].

Regardless of the exact reason, the $[\text{Bi}_{38}\text{O}_{44}]$ cluster can be obtained in pentanone, as well as acetone and DMF, provided they are sufficiently wet. Cyclohexanone and MEK promote the $[\text{Bi}_9\text{O}_7]$ stability, which can also be achieved in dry acetone and DMF under rigorously anhydrous circumstances.

5.5 Conclusions

Bismuth (III) disalicylate color change

According to all of the performed experiments, no quantitatively significant traces of additional phases can be found in the solid-state BiSal_2 samples. This is supported with Raman spectroscopy, PXRD amorphous content analysis, and PDF analysis of varying in color samples.

$[\text{Bi}_{38}\text{O}_{44}]$ growth mechanism

The results of synchrotron experiments align with the UV-Vis and DLS observations. Two, different species are detected. The smaller one (ca. 0.7 nm) is the $[\text{Bi}_9\text{O}_7]$ oxo-cluster, and the bigger one (ca. 1.2 nm) is the $[\text{Bi}_{38}\text{O}_{44}]$. Thanks to distinctive atom-atom distances in $[\text{Bi}_9\text{O}_7]$

and $[\text{Bi}_{38}\text{O}_{44}]$ clusters (Fig. 5.2), and varying size, the total scattering measurements enabled identification of both oxo-clusters.

The mechanism of $[\text{Bi}_{38}\text{O}_{44}]$ growth uses water as one of the main ingredients, next to the BiSal_2 . Structural similarity of both cluster cores (Fig. 5.16) are in line with the experimental observations, suggesting the larger cluster to be formed from the smaller one. Increase in excess of water promotes formation of the $[\text{Bi}_{38}\text{O}_{44}]$ cluster. The formation of the $[\text{Bi}_9\text{O}_7]$ cluster seems to be an immediate process, whereas the $[\text{Bi}_{38}\text{O}_{44}]$ cluster requires more time – from dozens of minutes for initial signs of formation, to days for the increase of its concentration in water-rich solvent.

5.5.1 Remaining questions

The influence of utilized solvent on the $[\text{Bi}_{38}\text{O}_{44}]$ formation is undeniable. And yet, the exact reason it is occurring is not clear. Performing a study, where the influence of a variety of solvents on the $[\text{Bi}_{38}\text{O}_{44}]$ formation, analysing their solvation properties, could be an interesting project.

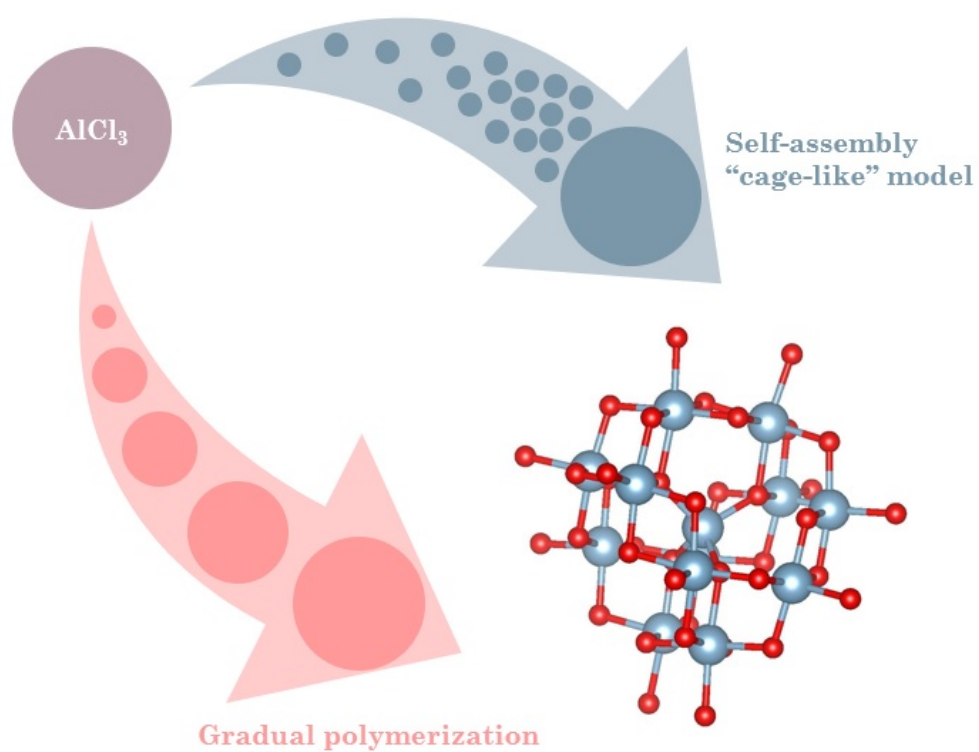
Although no traces of a derivative phase was found in the solid state bismuth (III) disalicylate, it does not disprove the theory that a metal-oxo cluster formation is responsible for the pink coloration. The methods used are quantitatively sensitive, and in order to detect a derivative phase of similar atomic composition, would require a significant amount of it. Reaction occurring on the surface of disalicylate crystallites, could be insufficient for obtaining such amount. That is why bismuth (III) disalicylate could be an interesting object of crystallite surface studies, which was beyond the scope of this work.

5.5.2 Author contribution

Synchrotron data acquisition in ESRF, including synthesis and operating the beamline, was done by Dr. Simon A. J. Kimber and the beamline staff. In PETRA-III, the synthesis preparation was performed by the thesis author, and the operating the beamline by Dr. Simon A. J. Kimber, Siham Mouhtadi and the thesis author, with the aid of beamline scientists. Processing of the synchrotron data and its analysis was done by the thesis author.

Chapter 6

Speciation of the $[Al_{13}]$ oxo-cluster precursor solution



6.1 Introduction

Aluminium is the third most abundant element in the Earth's crust, after oxygen (46%) and silicon (28%). At 8.3% it proceeds even iron (5.6%) [8]. Despite the sheer mass of aluminium on Earth, its chemistry in solution is not yet fully understood.

It is known that aluminium in an acidic solution can form a variety of oxo-cluster species, of which the best understood and the most stable is Keggin-shaped Al_{13} . Aluminium in different forms can also create floccs, undergo glass-phase formation or coagulation in water solution [212]. The mentioned Keggin-shaped $[Al_{13}]$ itself can also transform, either in isomerization process or reaction resulting in $[Al_{30}]$ oxo-cluster formation. Full structural understanding of these processes could improve the reproducibility of reactions used in practical applications of aluminium solutions. It could also enable the use of $[Al_{13}]$ and other forms of aluminium in various processes, like the synthesis of intricate Al-based thin layers and other advanced materials.

6.1.1 The use of aluminium in water solution

Mining and rare element extraction

Aluminium is commonly found in Acid Mine Drainage (AMD), which is a result of mines overflowing with water. AMD, apart from aluminium, can contain significant amounts of Rare Earth Elements (REE), useful in many industries. Purifying AMD is therefore important both for the environment, polluted with abandoned mining activity and for obtaining the previous resources. The reaction of coagulation plays an important role in this purification process.

Aluminium in $[Al_{13}]$ Keggin form takes a part in the coagulation of metallic and heavy atom compounds, present in water. This plays an important role in the effective extraction of REE, which is crucial to sustainable technological progress [147]. The $[Al_{13}]$ oxo-cluster promotes adsorption and entrapment of REE due to a large number of charges it can generate at outer OH groups and is proven to promote 100% effectiveness in REE extraction [147] – hence the chemistry of $[Al_{13}]$ in various pH is important to understand in order to then control these processes.

Water purification and environment

A precursor for the $[Al_{13}]$ cluster formation, polyaluminium chloride solution (PACl), is also used in water purification [27]. The coagulation effect is used in that process [27, 250] [31], enabling water purification for further use. Other processes of polluted water purification, for example involving the use of peatlands, can also use aluminium for enhancing their effectiveness [174].

Medicine and cosmetics

Aluminium compounds are even used in medicine. An example is aluminium hydroxide used for stomach issues, heartburn, and reducing the concentration of phosphates in an organism. Although it is digested in water-insoluble $Al(OH)_3$ form, the solubility in acidic environment increases and Al^{3+} cations are free to react and assemble the oxo-cluster structure. Although the biotoxicity of aluminium is known [192], the reactions it is undergoing in organisms are not.

Aluminium is also popularly used in cosmetics intended as perspiration inhibitors, including deodorants and shower gels [117].

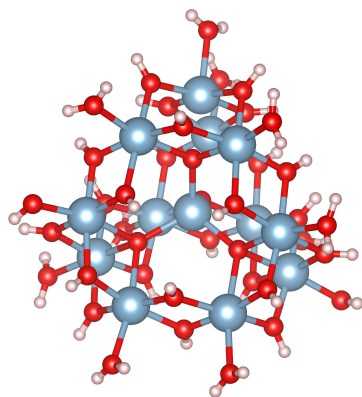


Figure 6.1: The structure of ϵ isomer of the $K\text{-[Al}_{13}\text{O}_{40}]$ cluster [197].

6.1.2 Aluminium oxo-clusters and their structure

It is generally known that AlCl_3 insufficiently acidic water solution dissociates into Al^{3+} ions, which further assemble into various oxo-clusters. In high enough pH aluminium precipitates as $\text{Al}(\text{OH})_3$ or in other, insoluble form. The structures of the most stable of the oxo-clusters formed in this way are well-known and described below.

Keggin- Al_{13}

The best known species is $[\text{Al}_{13}]$ oxo-cluster, where Al atoms form a Keggin-shaped structure [110], characteristic due to its cubic symmetry (Fig. 6.1). The Keggin-shaped structure is also present in many different chemically systems (Fig. 6.2), with the first one described in literature for phosphotungstic acid ($\text{PW}_{12}\text{O}_{40}$) [110].

There are five isomers to the Keggin structure – α , [110, 120, 125] β , γ [1, 188], δ [154] and ϵ [236] (Fig. 6.3), which are described for many other Keggin structures [244] (Fig. 6.3). All of the Keggin isomers are thought to exist for the $[\text{Al}_{13}]$ cluster, with distinguishing between them possible due to a specific NMR signal of the central, tetrahedral aluminium site [154]. But the most common is the ϵ - $[\text{Al}_{13}]$ [99, 147, 154, 169]. The difference between Keggin isomers is a rotation of one or more of the four octahedral triads by 60° . There triads composed in total of 12 sites are surrounding the core atom site. That sums to the total of 13 Al atoms, connected with 40 O sites.

The aluminium sites in $[\text{Al}_{13}]$ are predominately octahedral, with only the central site being tetrahedral. The tetrahedral site of $[\text{Al}_{13}]$ is crucial for its identification in NMR studies. As Keggin-shaped $[\text{Al}_{13}]$ is the most popular subject of research among Al clusters, it will be referred to by default as Al_{13} , $K\text{-[Al}_{13}]$ or tridecamer in this work, unless isomerization is playing a role in the particular discussion.

The synthesis of $K\text{-[Al}_{13}]$ from AlCl_3 solution is sometimes referred to as polymerization, and $K\text{-[Al}_{13}]$ itself as tridecamer. That nomenclature is especially popular when discussing the growth mechanism of aluminium oxo-clusters, and therefore is important when discussing the said subject. There are two main directions in terms of $[\text{Al}_{13}]$ formation. The first is a gradual polymerization, including oligomers in the middle steps, ranging from Al_3 to Al_{12} . The second is an immediate assembly from monomers and dimers [25]. These growth mechanisms are also relevant to the isomerization of different Keggin $[\text{Al}_{13}]$ forms. Some favour partial dissolution by detaching of Al_3 cap, and reassembling it as a new isomer. Other theories involve the full or nearly full dissolution of a $[\text{Al}_{13}]$ unit before reassembly as another isomer.

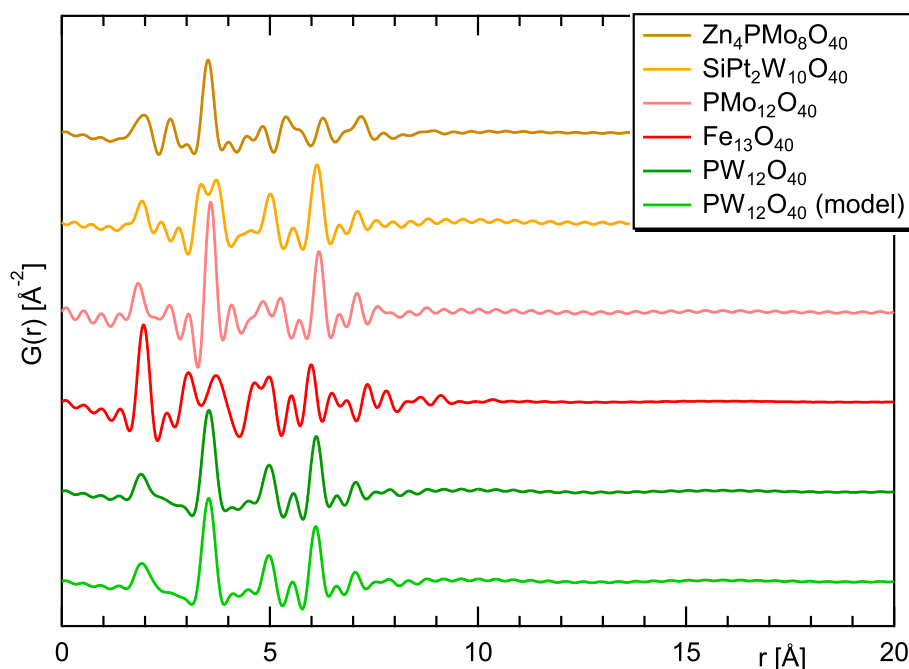


Figure 6.2: PDF simulations for multiple Keggin structures. ϵ -Keggin $Zn_4PMo_8O_{40}$ [236] and α -Keggins $SiPt_2W_{10}O_{40}$ [120], $PMo_{12}O_{40}$ [125], $Fe_{13}O_{40}$ [30], $PW_{12}O_{40}$ [110]. The peak positions for all of the models are similar. However, due to different atomic scattering factors of atoms present in each of the molecule, the intensities vary significantly. Apart from the literature examples, a Keggin structure of $PW_{12}O_{40}$ was modelled based on the internal symmetry of a Keggin cluster (model). This type of modeling allows for generating a structure with fewer variables than models with all atoms generated with separate coordinates. Comparing the model to the literature structure shows high similarity.

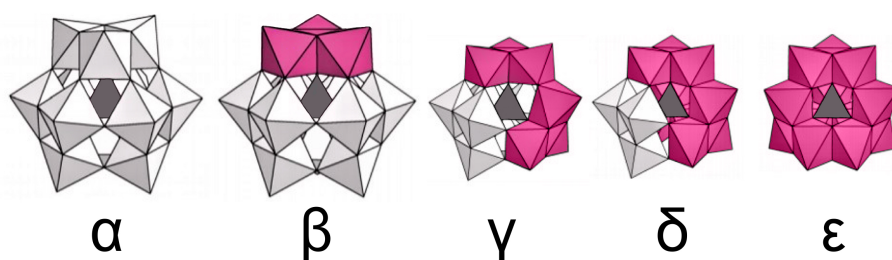


Figure 6.3: Visual representations of Keggin isomers – α , β , γ , δ and ϵ . The difference between isomers is the rotation of a triad of octahedrally coordinated Al atoms, four of which surround a tetrahedrally coordinated center (red/black). The rotating is shown between α and β isomers, with the magenta triad in β being rotated in regard to the white triad in α . γ isomer has two, δ three, and ϵ four rotations in regard to the α isomer.

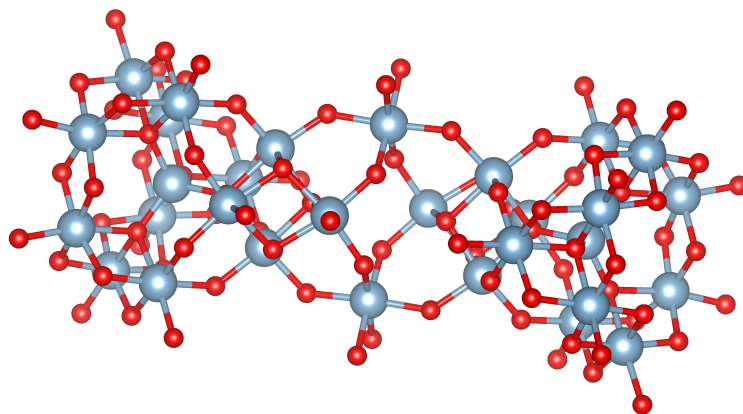


Figure 6.4: The structure of crystallized $[Al_{30}O_{90}]$ in literature [1].

Flat M-[Al₁₃]

The importance of referring to the Keggin [Al₁₃] oxo-cluster in a precise way, for example as K-[Al₁₃] [27], is important due to a species of oxo-cluster bearing identical amount of Al sites. This other [Al₁₃] oxo-cluster, Mögel [Al₁₃] (M-Al₁₃), is not an isomer to K-[Al₁₃] [99, 184]. Its structure varies also significantly from the Keggin. It is a flat, centrosymmetric trigonal disc, composed of 13 Al and 48 O atoms. All of the M-[Al₁₃] aluminium sites are octahedral.

The M-[Al₁₃] cluster was initially found only in solid state [184]. It was discovered later that it is also present in solution next to the K-[Al₁₃], and even transform into it by aging [27, 68]. Due to its structure being formed only from octahedrally coordinated Al, its signal can be hard to distinguish in NMR. However, using ESI-Q-MS, NMR and ferron assay methods combination, it was discovered that through dissolution M-[Al₁₃], K-[Al₁₃] is formed.

M-[Al₁₃] is a good coagulant due to its high charge [27]. At low concentration (0.491 to 0.00463 mol L⁻¹) M-[Al₁₃] transforms to K-Al₁₃. At higher concentrations (1.51 to 2.52 mol L⁻¹) it is thought to dissociate into Al₁-Al₃ species [27].

K-[Al₁₃] cluster is not usually specified in literature as any of the Keggin isomers, so in the case of aluminium oxo-clusters it is safe to assume that it represents generally Keggin-type Al₁₃. Through this work, the Mögel [Al₁₃] cluster will be exclusively referred to as Mögel or simply M-[Al₁₃].

[Al₃₀]

Another important structure is [Al₃₀] oxo-cluster, composed of two ϵ -[Al₁₃], capped and connected with four octahedrally coordinated Al atoms [5, 6]. It consists of 30 Al and 90 O sites (Fig. 6.4). [Al₃₀] cluster forms when heating ϵ -[Al₁₃] [5, 77, 175].

In terms of the [Al₃₀] cluster formation mechanism, a discussion is ongoing — one of proposed mechanism being based on disassembly of K-[Al₁₃] into monomers and dimers, followed by [Al₃₀] assembly. The second is simply reordering existing K-[Al₁₃] molecules and joining them with four octahedrally coordinated aluminium centers, forming the characteristic bridge of a single [Al₃₀] cluster.

In order to form a [Al₃₀] oxo-cluster, the ϵ -[Al₁₃] cluster has to be heated with glycine and Ca²⁺ kations in 90 °. This leads to dimerization, by formation of a 4-Al bridge. Additionally during the synthesis of [Al₃₀], isomerization of some of the ϵ Keggin to γ -[Al₁₃] form takes place [5, 237].

6.1.3 Chemistry of $AlCl_3$ solution

Many studies have been done over the years, focusing on understanding the mechanism of aluminium clusters formation and speciation. Some methods are favored, in that NMR and ESI-MS [210, 211], but also Raman spectroscopy [176] and not spectroscopic ferron assay method are used [55, 158, 185]. And yet, the $K-[Al_{13}]$ formation is still presented in literature with two, possible growth models.

Aluminium dissolved in water – hexaqua-aluminium ion

It is commonly thought that $AlCl_3$ in water solution dissolves into hexaqua-aluminium ion, which without accounting for the ionic structure, would be formulated as $Al(H_2O)_6Cl_3$. Evidence suggest that this molecule is highly stable thermodynamically in varying concentration, even at temperatures reaching 125 °C [38, 176]. Molecular dynamics calculations support the stability argument as well [39, 163]. The stability of hexaqua-aluminium ion reaches so far in fact, that a second hydration sphere of 12 water molecules was detected [176].

Most works on aluminium oxo-clusters growth disregard influence of Cl^- anion on the hexaqua-aluminium ion and $K-[Al_{13}]$ formation. However, it is important to remember this anion exists in the solution next to aluminium species, especially when looking at atom-atom distances with PDF method. Evidence suggest interactions between both Cl and Al associated structures [38] with hydration shells [39], and in some cases even existence of direct Cl-Al bonds [163]. Interestingly enough, an extensive molecular dynamics study of Cl^- anion in water shows how similarly to Al^{3+} it is, when coordinated with water molecules [16]. On average 6.3 water molecules coordinate a single Cl^- anion, which approximates to an octahedrally coordinated Cl site [16]. With this information in mind, a list of atom-atom distances possible to see in total scattering experiment can be formed (Table 6.1).

Table 6.1: List of atom-atom distances present in $AlCl_3$ solution in water, chosen based on potential pair distribution function studies interest.

atom pairs	distance [Å]	method
Cl-O (Cl ion in H_2O)	3.1-3.2	DFT* [16]
Cl-H	2.3	DFT* [16]
Al-Cl (ions)	4.4 and 6.0	CPMD** [39]
Al-Cl (bound)	2.2-2.5	Spectroscopic [88]
Al-O (1st hydration sphere)	1.88-1.9	Raman*** [176]
Al-O (2nd hydration sphere)	3.9-4.1	Raman*** [176]
O-H	1.0	Raman*** [176]
O-O (H_2O molecules)	2.8	X-ray Raman [21]

*DFT – Density Functional Theory

**CPMD – Car-Parrinello-based molecular dynamics

***chloride, perchloride and nitrate water solutions

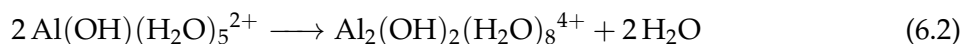
Theories of $K-[Al_{13}]$ formation mechanism

As established, hexaqua-aluminium ion is coordinated hexahedrally by six water molecules. With this coordinated Al site as a starting point, there are two main mechanisms of $K-[Al_{13}]$ polymerization proposed in literature. Both of them are based in oxolation and hydrolysis reactions. The first one is *gradual polymerization*, consisting of many steps with oligomeric intermediate species, gradually growing from the starting monomer. Up until the final tridecamer, $K-[Al_{13}]$. The second is *immediate formation*, where $K-[Al_{13}]$ assembles from monomers and in some cases also dimers, after reaching sufficiently low acidity of the environment [25].

The gradual polymerization is also described as “core-links” model, and the immediate formation as “cage-like” model [25]. Regardless of the mechanism, once K-[Al₁₃] start forming it becomes the dominating species [3]. Also, in both mechanisms the chemical species undergo similar mechanism. Hexaqua-aluminium ion undergoes deprotonation as the OH⁻ concentration in the solution is increased [69]:



which is the hydrolytic step [163]. The next reaction is oxolation:



which is the condensation step of oxo-cluster growth. The rising pH of a solution deriving from addition of OH⁻ is often expressed as a hydrolysis ratio, expressed as $m = [\text{OH}^-]/[\text{Al}]$, where [OH⁻] is concentration of added OH⁻, and [Al] concentration of aluminium in solution [3].

A question whether or not aluminium solutions in pH below 7 are a heterogeneous mixture of multiple aluminium species, or are dominated by a single species, is an important one to answer. This would help to solve the mystery of [Al₁₃] and [Al₃₀] growth mechanisms, and shine a light at K-[Al₁₃] isomerization.

The gradual polymerization mechanism generally agrees with that AlCl₃ solution initially forms hexaqua-aluminium ions [178–180]. It is also worth noting that the described oligomers are composed of octahedrally coordinated Al. There is important NMR [3] and ESI-MS [246, 247] evidence that oligomers form, and their gradually increased charge exist while AlCl₃ solution undergoes hydrolysis (Table 6.2). The premise of gradual polymerization is generally described as growth dependent on the pH of a solution, with starting point at pH = ca. 4, up to nearly neutral pH = 7. As the pH grows, the n in Al _{n} increases, up until precipitation of aluminium hydroxide occurs right after [Al₁₃] and other clusters agglomeration [50, 246]. Some suggest also that the concentration of aluminium in solution plays a role. Smaller concentration favors K-[Al₁₃] formation, whereas higher concentration enables oligomers formation [3].

Table 6.2: Speciation of AlCl₃ hydrolysis as a function of pH – overview of species found in pH ranges with a variety of methods. Overview of species found in varying pH of a solution.

pH	species found	medium	method
3.0 – 5.0	Al ₁ –Al ₂	AlCl ₃	ESI-Q-MS [50]
ca. 4	Al ₁ –Al ₂	diluted AlCl ₃	ESI-MS [246]
ca. 4.8	Al ₃ –Al ₅	diluted AlCl ₃	ESI-MS [246]
ca. 5.0	up to Al ₁₀	diluted AlCl ₃	ESI-MS [246]
ca. 5.0	Al ₁₃ (+ <Al ₅)	AlCl ₃	ESI-Q-MS [50]
> 5.0	Al ₁₁ –Al ₂₁	diluted AlCl ₃	ESI-MS [246]
ca. 6.4	floccs of Al(OH) ₃	diluted AlCl ₃	ESI-MS [246]
ca. 7.0	agglomeration/flocking	AlCl ₃	ESI-Q-MS [50]

ESI-Q-MS – electrospray ionization quadrupole mass spectrometry

At the same time, some ESI-MS studies point out towards AlCl₃ solution containing mainly hexaqua-aluminium ion, up until K-[Al₁₃] formation occurs [210, 211]. In these studies, no evidence of intermediate species can be found, only small oligomers (Al₁–Al₃) and the final oxo-cluster. This is evidence of the immediate formation of K-[Al₁₃] from AlCl₃ solution, and is not without merit.

Tetrahedral AlO_4 center of K- $[Al_{13}]$

Formation of the central, tetrahedral AlO_4 site is an interesting point in the K- $[Al_{13}]$ cluster growth. It was assumed that local, highly alkaline environment forms in solution after injection of base drops into acid $AlCl_3$ solution. This allows formation of AlO_4 center to occur [23]. However, it does not explain the formation of K- $[Al_{13}]$ when its preparation does not involve alkaline solution [159]. Formation of the tetrahedral center is mysterious especially due to the potential precursor and intermediate species being composed exclusively of octahedral Al sites.

K- $[Al_{13}]$ isomerization

Although the isomerization of K- $[Al_{13}]$ oxo-cluster is not analyzed in this work, it is important to mention in regard to the ε - $[Al_{13}]$ oxo-cluster formation. The mechanism of isomerization is most likely connected to the cluster growth.

NMR shows that the isomerization cannot happen via rotation of parts of the $[Al_{13}]$ cluster, due to the energy of such rotation being too large to reasonably achieve in experimental environment. Therefore, the isomerization must take place with partial decomposition and then assembly of isomeric $[Al_{13}]$ from oligomers [154]. Changes in NMR suggest hydrolysis process occurring, which can be attributed either to $[Al_{13}]$ condensation or dissociation into Al^{3+} cations [154]. The data gathered indicated presence of α - $[Al_{13}]$, γ - $[Al_{13}]$ and δ - $[Al_{13}]$ in this process, apart from formed $[Al_{30}]$ and initial ε - $[Al_{13}]$. There is also $Al(H_2O)_6^{3+}$ cation signal increasing while heating is ongoing [154]. This suggestions present in literature, can be connected with the K- $[Al_{13}]$ cluster formation. It would be reasonable to assume that it supports the immediate formation from small species, since the isomerisation is most likely connected to at least partial (if not full) dissociation of K- $[Al_{13}]$ and reassembly or an isomer from small species.

6.1.4 PDF data analysis

Oxo-cluster modeling based on symmetry

Various aluminium oxo-cluster species were simulated, using symmetry operations contained in tables of International Tables for Crystallography, volume A1 [61]. This procedure allowed to simulate oxo-clusters and n-mers, that are alleged to be a part of $[Al_{13}]$ chemistry in literature [2–4, 27, 39, 50], yet were not separated from solution through crystallization nor other means.

Another benefit of this approach is limiting the amount of variables. The regular form of Keggin, for example, allows for creating models consisting of fewer variables than a model based on describing all atom positions (Fig. 6.5). This allows to modify the model easier, and with a symmetric result. The latter property is important for models of clusters in solution, where their average over time shape is bound to be more symmetric than in a crystal. The strains of force present in crystal lattice can distort the structure significantly.

The symmetry-bound modeling allows for easy modification of the model. It also helps to ensure that the model does not get distorted to unreasonable shape when fitting PDF data.

Principal Component Analysis - PCA

Principal Component Analysis (PCA) is a method of reducing a dataset to its components. Usually, a large amount of data is transformed into a set with smaller amount of variables, that still contains all of the information of interest. This method was previously used in literature for total scattering data analysis [44].

The initial step of PCA is standardizing the data, in order to ensure that the length of waves is identical and range uniformly distributed. Then, covariance matrix is formed from the data.

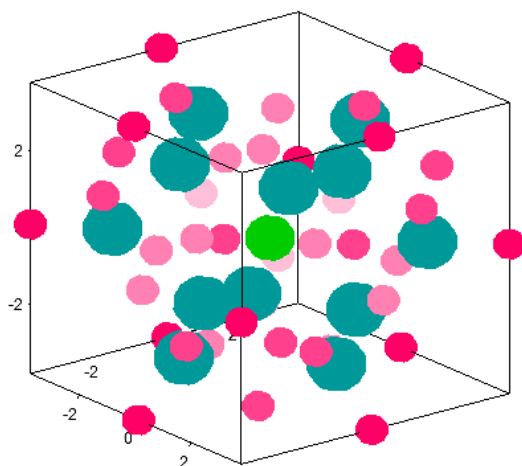


Figure 6.5: A generated 3D model of a Keggin structure. Symmetry operations from International Crystallographic Tables [61] and Igor software operations allow to generate such structures with only 6 sets of one or two variables. Alternative is a set of 3 variables (x, y, z) for each atom, which does not constrain the molecule and can easily overwhelm a refinement.

It is symmetric, with its entries being also symmetrical in regard to the main diagonal direction. Its entries are covariances associated with pairs of the initial variables. This matrix allows to recognize whether information are correlated. A positive sign of a covariance indicates a correlation.

This information is then used to identify the principal components of the dataset. The principal components are the information contained in dataset, divided into mathematically unrelated sequences of information - in the case of PDF data, into new set of peaks, representing atom-atom positions. The most information is placed into the first component, and then the second, and so forth. This could translate into the most prominent chemical component in a dataset becoming the first component, and the last just be the background noise. However, the components themselves have no inherent meaning, and therefore should not be analyzed as they were representing fully separate chemicals [89, 189].

6.1.5 Speciation using NMR and ESI-MS methods – disadvantages

Generally, the ESI-MS method detects a multitude of species present in $[Al_{13}]$ precursor solution, with its size ranging from $n = 1$ to 12 (Al_n). This method, however, requires the liquid sample to be modified. Modifying a sample for the purpose of a method can modify the species present in it, especially when the species are undergoing a reaction with delicate equilibrium — influenced by pH, concentration, and time. In the core of ESI-MS lies that the detection takes place after ionization, and therefore a sample may undergo changes. Not only can it ionise, but also local changes in concentration may occur. The latter causes the measurement to inadequately represent the equilibrium of a system in solution. Moreover, the sample is measured in gaseous phase rather than liquid.

Because of these reasons, the species found with ESI-MS can be seen as possibly present in solution, but not certain to be found there. It is also not surprising that other methods, such

as potentiometry, spectrophotometry or multinuclear magnetic resonance (MR) spectroscopy generally do not indicate presence of species as numerous, as the ESI-MS does [50].

Another point that has to be made when talking about issues with speciation methods is indirect evidence. Both NMR (measuring interactions of nuclear spins in magnetic field) and ESI-MS (measuring molecular weight of species ionized with high voltage) do not provide direct, structural information about the content of the sample. Interpretation of such results provides a variety of possibilities in explaining the mechanism of reaction, difficult to unambiguously assess. This is why scattering methods are an interesting tool, which can provide direct structural information without modifying the sample. It is also yet to be used to analyse the growth of $K-[Al_{13}]$ oxo-cluster.

6.1.6 The main objectives

The aim of the experimentation and data analysis contained in this chapter is determination whether PDF data presented supports “cage-like” self-assembly, or rather “core-link” gradual polymerization mechanism of $\epsilon-[Al_{13}]$ oxo-cluster formation. In that, establishing what species based in literature are the most likely intermediate species of the process.

Using scattering methods provides the advantage of being directly susceptible to structural information. The PDF method allows for implementing the use of scattering on Al oxo-cluster formation in solution, enabling to see atom-atom distance distribution of a sample at a given time. Analyzing the resulting PDF functions with regard to the structures proposed in literature which used spectroscopic, along with creating models, can shine a light on the elusive character of the $\epsilon-[Al_{13}]$ cluster growth.

6.2 Experimental section

The synthesis of $\epsilon-[Al_{13}]$ was performed from acidic $AlCl_3$ water solution, thorough neutralization with NaOH. The process was measured in time intervals, from 1 to 180 min, from the start of hydrolysis. The starting pH value was 4.0, and control measurements on solutions before neutralization were made.

The experiment was performed ESRF synchrotron (Grenoble, France) using the ID15-B beamline. It was equipped with Perkin Elmer XRD detector. Measurements were done using beam energy of 87 keV ($\lambda = 0.01425$ nm).

6.2.1 Data integration and PDF extraction

Similarly to Chapter 5, the data was integrated using pyFAI suite [13]. Conversion of total scattering data to PDF was calculated using DiffPy software [101]. The calibration once again was done with CeO_2 , with PDFgui.

Background was subtracted from each sample, for which a measurement of a capillary filled with water was used. An issue with background subtraction was detected, where a procedurally correct subtraction resulted in a too intense, negative peak in the place of O-O distance in water (2.8 Å). In order to ensure that the background measurement was done correctly, the structure factor was compared to water structure factor available in literature (Fig. 6.6), which shows that they do match each other well. Because of that, some of the datasets contain relatively intense, negative peak at 2.8 Å, which was avoided when possible.

6.2.2 PDF fitting

PDF data was fitted, using least square refinement method. Scale factor, atomic coordinates and thermal factors of oxo-cluster models were refined to fit the data.

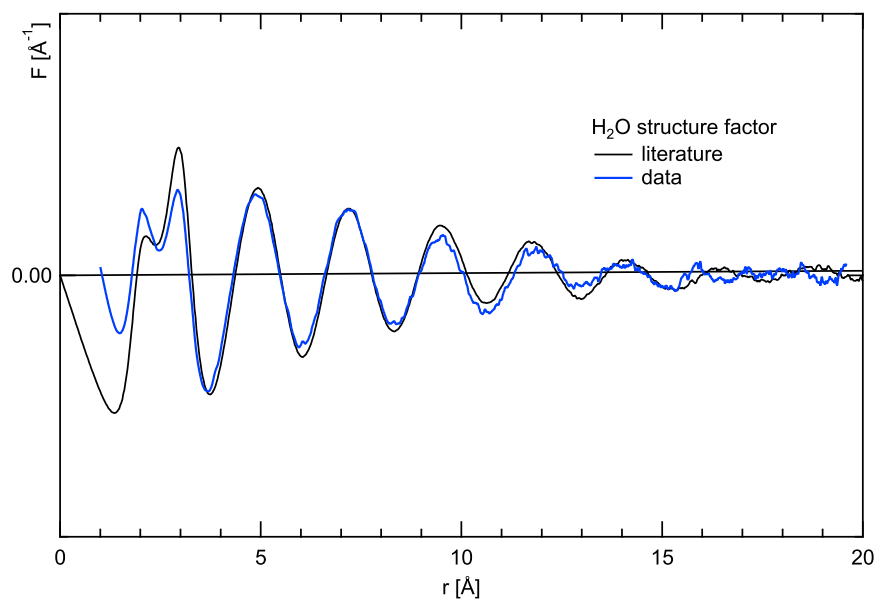


Figure 6.6: A comparison of H₂O structure factor in literature and the data. The comparison was made to determine whether the data for aluminium solution samples was gathered correctly. The agreement between measured and literature data for H₂O is in agreement.

For the fitting of calculated PDFs, two software methods were used. The fitting of calculated PDFs to data was done with DiffPy CMI software.

6.2.3 Oxo-cluster modeling based on symmetry - in Igor PRO

Igor PRO software was used for creating adjustable models, with limited amount of variables. The values were adjusted to the most suitable atom-atom distance in the models. They were then used in PDF generation for fingerprinting, and fitting of PDF data.

The atom coordinates in models of molecules were generated as waves with the least possible amount of variables. For each set of atoms bound by a symmetry operation, three waves were created, representing the x, y and z coordinates. Then, sets were assembled into .XYZ files and opened in Vesta software in order to control the atom-atom distances [146]. Variables were adjusted and the process repeated, until appropriate atom-atom distances were found.

Here is an example of an Igor PRO function generating all 13 Al positions of the ϵ -[Al₁₃] cluster, based solely on two variables:

```
function coordinates(A,B)
variable A,B
wave x, y, z

x[0] = {0,A,B,A,-A,B,-A,-A,-B,A,A,-B,-A}
y[0] = {0,A,A,B,-A,-A,B,A,-A,-B,-A,A,-B}
z[0] = {0,B,A,A,B,-A,-A,-B,A,-A,-B,-A,A}

end
```

Various oxo-clusters and potential precursors were modelled in the described above manner. The ϵ -[Al₁₃] and [Al₃₀] oxo-clusters were modelled with atom-atom distances resembling

Table 6.3: Chemical formulas of modelled aluminium species with n of Al atoms. Codes are representing the structures.

n	formula	name/code
30	$Al_{30}O_{90}$	30-O
13	$Al_{13}O_{40}$	K13-O
	$Al_{13}O_{48}$	M13-O
6	Al_6O_{24}	6-O-circ
3	Al_3O_{14}	3-O
	$Al_3O_{13}Cl$	3-1Cl
	Al_3Cl_{14}	3-Cl
	Al_3O_{13}	3-O-3fold
2	Al_2O_{10}	2-O
	Al_2O_9Cl	2-1Cl
	$Al_2O_8Cl_2$	2-2Cl
	$Al_2O_6Cl_4$	2-4Cl
	Al_2Cl_{10}	2-Cl
	Al_2Cl_7	2-Cl-tet
1	$AlCl_3$	1-Cl-tri
	AlO_6	1-O
	AlO_5Cl	1-1Cl
	AlO_4Cl_2	1-2Cl
	$AlCl_6$	1-Cl
0	ClO_6	-

these of the crystalline structure. Similarly, M- $[Al_{13}]$ model was generated. Based on the symmetry of these clusters, linear monomeric, dimeric and trimeric species were assembled, with octahedral coordination (Al_1-Al_3). Additionally, a trimer with 3-fold and a hexamer ring with 6-fold rotational symmetry were created, also supporting octahedral coordination of Al atoms. Models of $AlCl_3$ with planar, trigonal coordination and Al_2Cl_7 model with tetragonal Al coordination were also created.

The presence of Cl in the solution was considered by using Cl in a place of O in some versions of the models, with separate variables controlling the Cl-Al distance. This allowed for adjusting a separate bond length. Additionally, a model where a central Cl atom is octahedrally coordinated with oxygen was created (ClO_6). Models of $[Al_{13}]$ coordinated with chlorine ions were also simulated. This was done by generating a cloud of Cl atoms rather than fixed positions. The occupancy of Cl sites was set to match the 7+ charge of $\epsilon-[Al_{13}]$.

A full list of modelled structures can be found in Table 6.3.

6.2.4 Principal Component Analysis (PCA)

The PCA was performed using Igor PRO software and build in instructions. Time-resolved series of measurements on a sample in which the $\epsilon-[Al_{13}]$ oxo-cluster was growing, was subjected to PCA in an attempt of splitting signal coming from particular species present in the solution.

The function was set to divide the signal of 7 samples into a set amount of components. Different amounts of components from 4 to 10 were tested. This was done in order to establish the smallest, significant amount of calculated components.

Each extracted set of PDF measurements was calculated with the same Q_{max} , Q_{min} and r_{poly} parameters, limiting differences unrelated to the samples. Datasets were cut to uniform wave size, some for the purpose of reducing amount of background. Only then the datasets were subjected to the PCA.

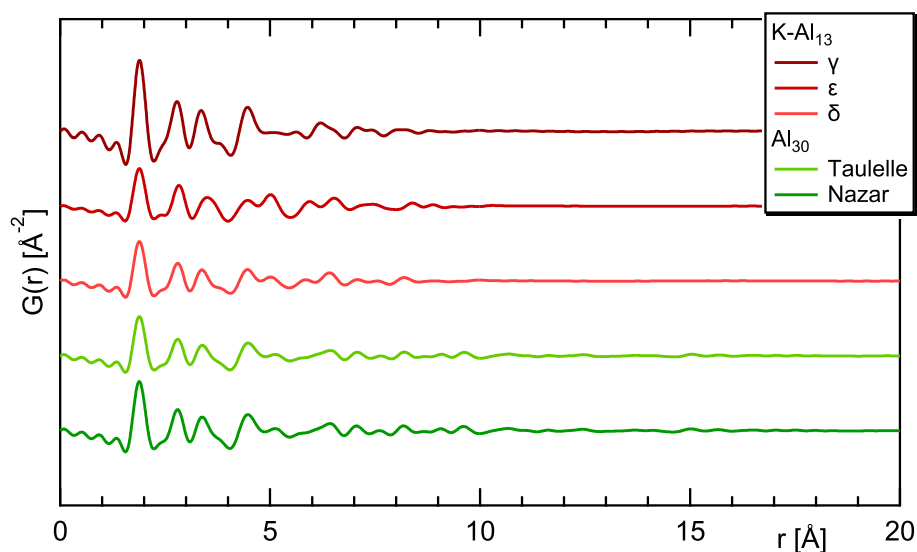


Figure 6.7: PDF models calculated for various types of K-[Al₁₃] [1, 153, 175] and [Al₃₀] [6, 175] oxo-clusters. This comparison shows only subtle differences between the isomers of K-[Al₁₃]. The [Al₃₀] cluster, due to being composed of two K-[Al₁₃] joined by a bridge, has also a similar PDF pattern to the Keggin. However, larger size causes it to have small peaks at larger distances than the K-[Al₁₃] cluster size. These are, however, too subtle to reliably distinguish in an actual measurement.

6.3 Results

PDF patterns of published aluminium structures were calculated and initially compared (Fig. 6.7), allowing for an overview of some of the [Al₁₃] isomers and dimer variants.

The differences between K-[Al₁₃] isomers are not very pronounced, and most noticeable in 4.0-5.5 Å region, as a varying peak intensity. The trend of similar patterns is again repeated with the comparison of K-[Al₁₃] to the [Al₃₀] cluster. Only additional, small peaks surpassing 9.5-10.0 Å differentiate [Al₃₀]. This difference comes from the smaller size of K-[Al₁₃]. These are, however, only small peaks. They do not indicate the longest atom-atom distance in [Al₃₀], stretching over 20 Å.

Because of these differences being rather subtle, it becomes clear that distinguishing between various K-[Al₁₃] and even [Al₃₀] can be difficult in a measured sample. That is due to total scattering background subtraction, truncation error and other factors that can lead to formation of PDF background features and lowering the intensity of atom-atom distance peaks.

6.3.1 Generated models and fingerprinting

Various models were generated and adjusted using Vesta software [146]. It was done according to the bond distances and angles modification with variables adjustments. Large oxo-clusters were modelled based on crystallized species (Fig. 6.8) and smaller structures were based on theoretical models, present in literature (Fig. 6.9).

PDFs of generated models

The generated models of oxo-clusters and oligomers were used to calculate PDFs (Fig. 6.10 and 6.11). These serve as a fingerprinting tool, allowing to compare the model-based PDF to data, and choose the initial matches.

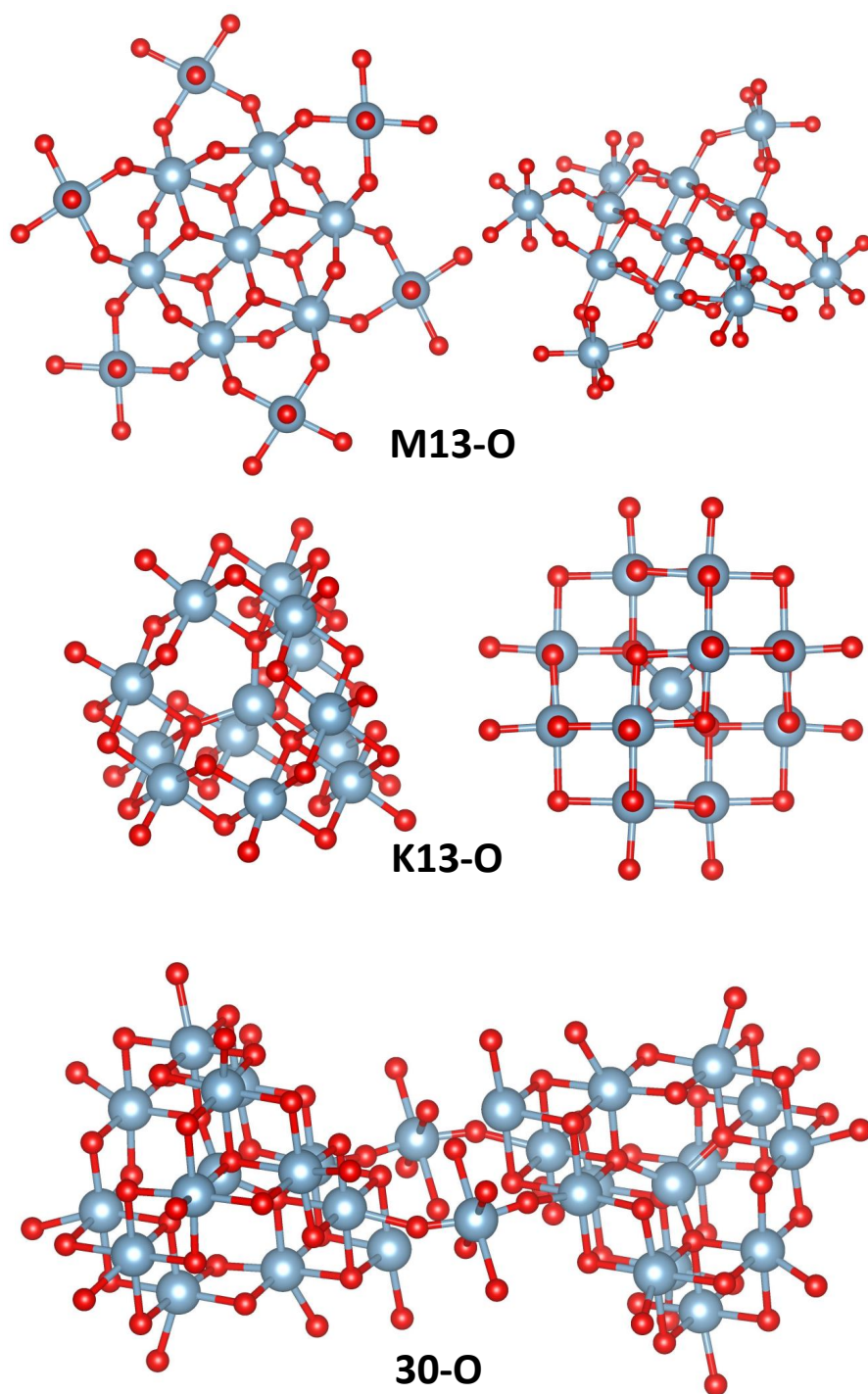


Figure 6.8: Chosen oxo-cluster molecules generated as models in Igor PRO. The models are labeled according to Table 6.3. Blue atoms represent Al, and red O sites. Only large oxo-clusters, Al_{13} - Al_{30} , are presented in this figure.

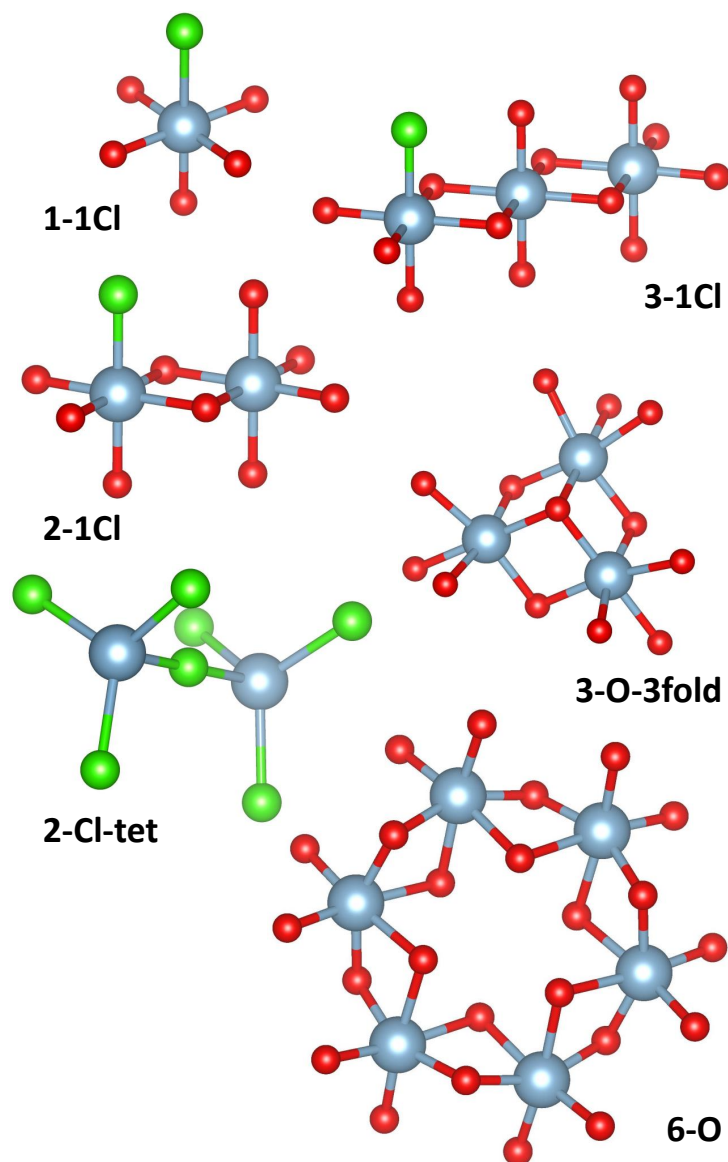


Figure 6.9: Chosen oxo-cluster molecules generated as models in Igor PRO. The models are labeled, according to Table 6.3. Blue atoms represent Al, and red O sites. Only potential precursors to the K-[Al₁₃] oxo-cluster are shown in this figure.

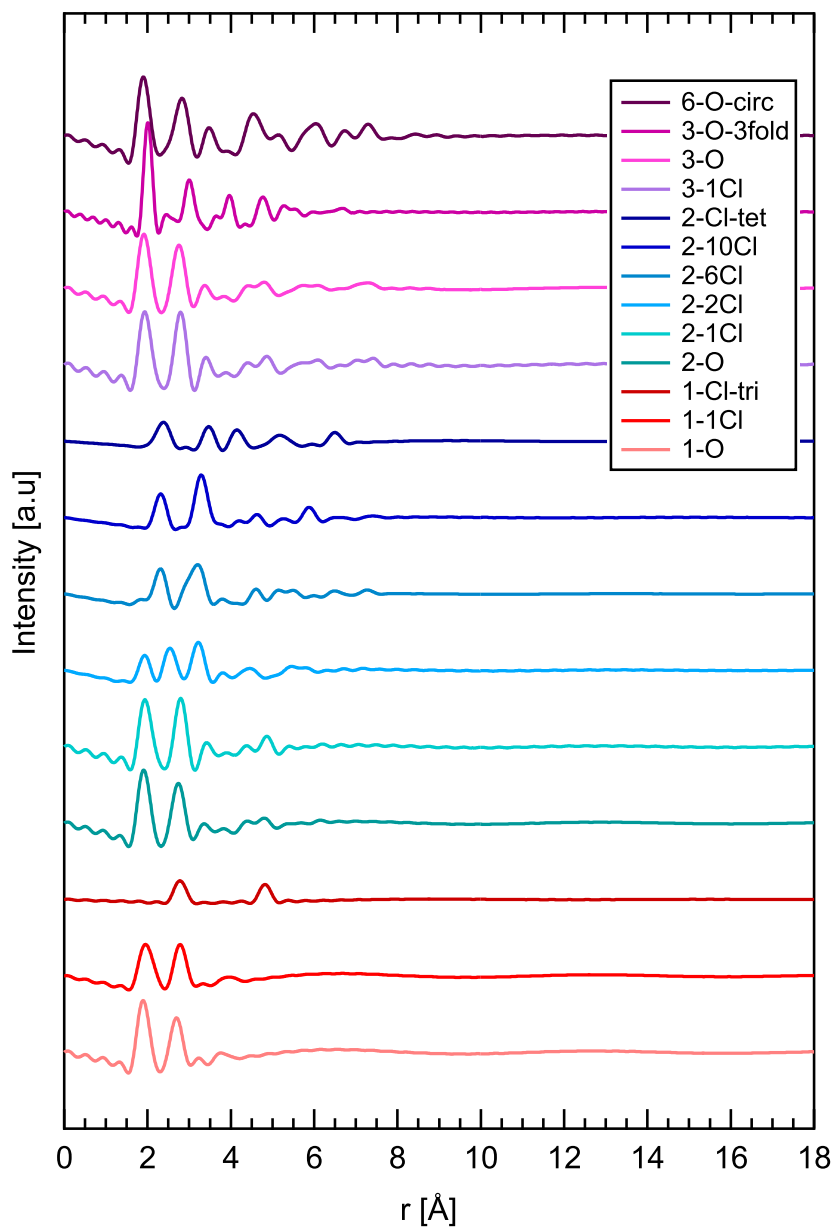


Figure 6.10: PDF patterns calculated based on models of chosen, small oligomers (Al_1 – Al_6). The atom-atom distances, and therefore peak positions, can be adjusted by modifying the variables responsible for bond lengths. The peak distribution and overall intensity ratio depend on the atoms present in the model.

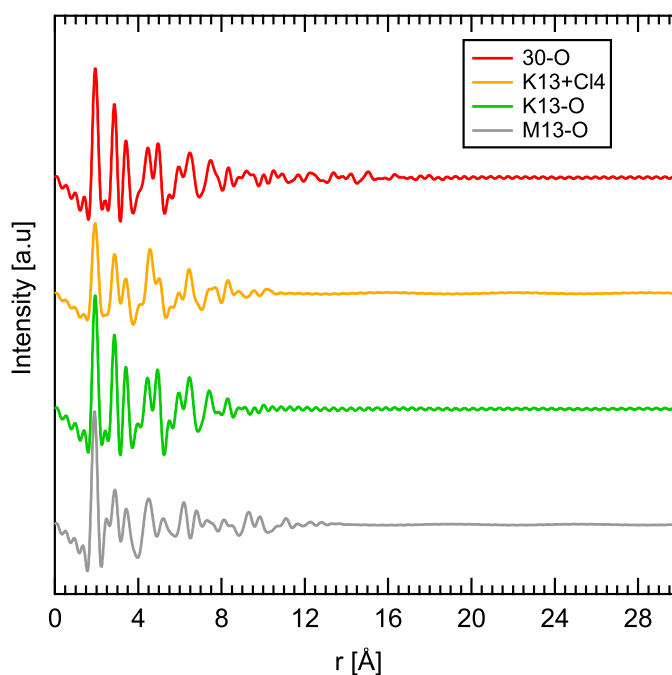


Figure 6.11: PDF patterns calculated based on models of chosen, large oligomers (Al_{13} - Al_{30}), in that the tridecamer, $[\text{Al}_{13}]$ oxo-cluster. The atom-atom distances, and therefore peak positions, can be adjusted by modifying the variables responsible for bond lengths. The peak distribution and overall intensity ratio depend on the atoms present in the model.

6.3.2 Hydrolysis series

The synthesis of ϵ - $[Al_{13}]$ was done by neutralization of acidic $AlCl_3$ water solution, from pH = 4.0 to 7.0. The reaction results in $[Al_{13}]$ oxo-cluster formation, and the sample was measured in a function of time. Extracted PDFs are presented together in Fig. 6.12, with addition of a PDF calculated from ϵ - $[Al_{13}]$ model.

There is an obvious distinction between measurements done at and below 20 min from the start of the reaction and measurements done after that point. The *early hydrolysis* measurements show three, distinct peaks, which are reminiscence of these present in $AlCl_3$ precursor solution. The *late hydrolysis* measurements at 40 min, immediately show a peak distribution, which somewhat matches the $[Al_{13}]$ models.

6.3.3 $AlCl_3$ water solution

The precursor solution, $AlCl_3$ dissolved in water, was measured with the starting pH of 4 (Fig. 6.13, black arrows). The total scattering data of that solution shows peaks that match the atom-atom distances of Al-O (1.9 Å), O-O (intramolecular in octahedrally coordinated Al sites, 2.5 Å) and Cl-O (3.2 Å) (Table 6.1).

A considerably high value of a negative peak at 2.8 Å (Fig. 6.13, red arrow), which persists through some of the extracted PDFs of early reaction stages, comes from the H_2O background subtraction. It is associated with O-O distance between H_2O molecules.

6.3.4 $[Al_{13}]$ synthesis - early time hydrolysis

At 1, 5, 10 and 20 min from the neutralization of pH from 4 to 7, the PDF data resembles the one of acidic $AlCl_3$ solution (Fig. 6.12). No new, significant peaks appear in the initial 20 min.

In order to assess what models match these peaks, their PDF patterns were analyzed. Visual comparison of peak distribution and adjustment of the models in terms of their atom positions were implemented. The peak alignment of $AlCl_3$ data does not sufficiently match any of the patterns shown in Fig. 6.14, apart from the 1-O. This is an Al atom, octahedrally coordinated with O – a monomer ($AlCl_6$). Dimers (2-x) and trimers (3-x) match the peaks almost just as well, with additional, less intense peaks ca. 5, 6 Å and so on (Fig. 6.10, 2-x and 3-x). These further peaks could be lost in the data due to background noise. The peak representing O-O distance of the presented 1-O model PDF is offset to 2.7 Å instead of peaking at 2.5 Å (Fig. 6.14, 1-O, blue arrow). However, this subtle difference can be adjusted at PDF fitting stage.

The circular hexamer (6-O-circ) exhibits too many intense peaks that are distinctively unfit to the early hydrolysis data. They are also noticeably intense up to ca. 7.5 Å, which disqualifies this structure from early hydrolysis stage compatibility.

The 3-O-3fold model resembles one of the four triads capping a Keggin molecule. It is representing a trimer that due to its structure, could be a good fit for the K- $[Al_{13}]$ cluster precursor. However, it shows more intense peaks than the data. Its O-O peak intensity (2.5 Å) in relation to other peaks is too low. Moreover, an intense 3.0 Å peak (Fig. 6.14, 3-O-3fold, red arrow) which is Al-Al distance in the model, could not be fit to match the data correctly without increasing the already too big Al-O distance (2.0 rather than 1.9 Å). Fitting the 3-O-3fold to PDF data results in a R_w value similar to other models (= 0.48, Fig. 6.15, a). However, looking at the displacement in atom positions generated by the fit (Fig. 6.15, b) indicates that it was achieved through unrealistic distortion within the molecule. Al-Al distance in the model after calculation fits perfectly to the 3.2 Å peak of early hydrolysis data. At the same time, the Al-O distances within the Al-O six-atom ring are at a reasonable, 1.9 Å length. The Al-O distance between Al and the central and external O atoms are, however, too big, at above 2.0 Å and reaching even 2.5 Å. This offset appears as a compensation for the 2.5 Å atom-atom distance, which is absent

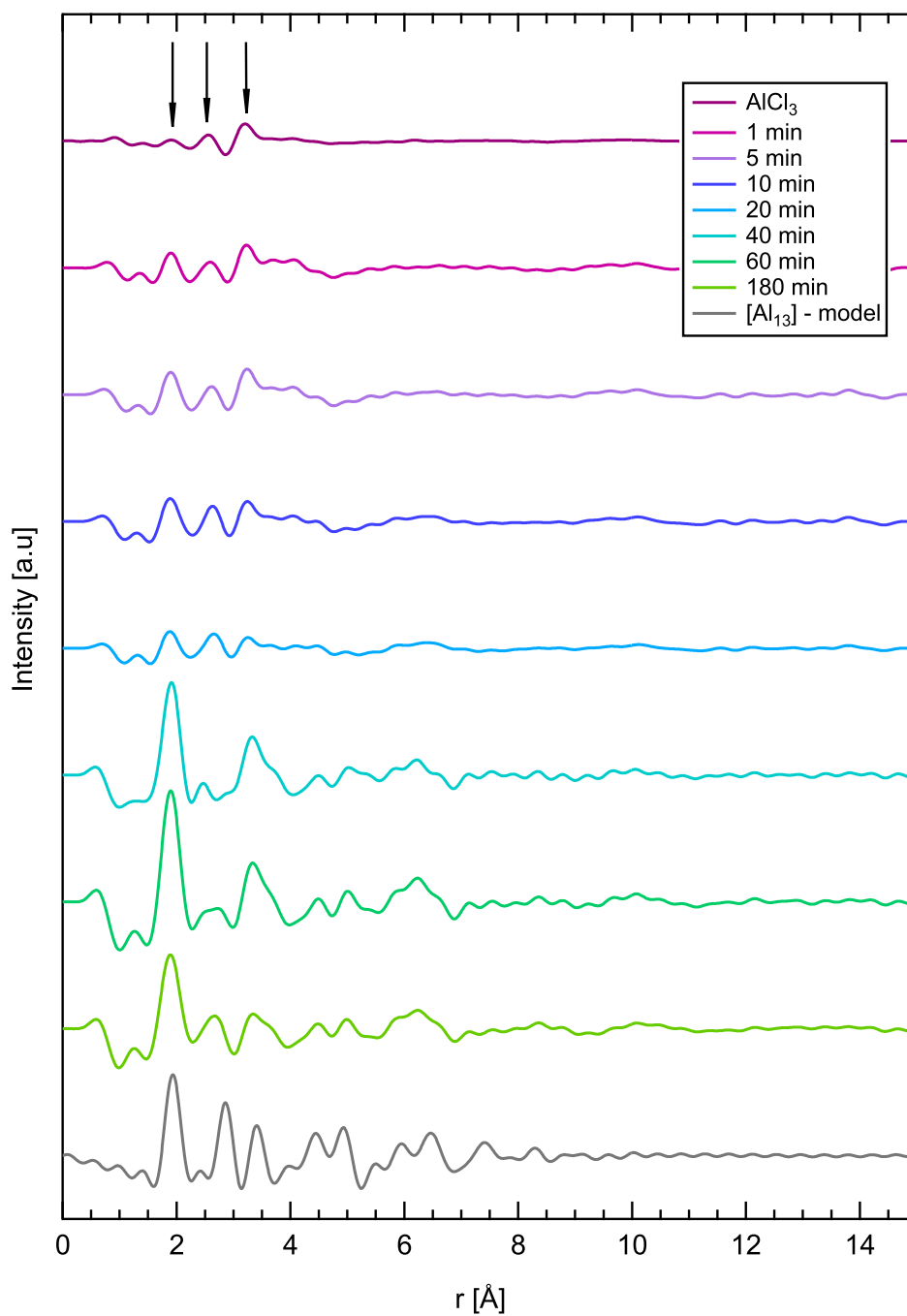


Figure 6.12: Series of PDF measurements, performed as a function of time. The last PDF pattern is calculated from generated ϵ - $[Al_{13}]$ model, and serves as a comparison for the later stages of hydrolysis in which the $[Al_{13}]$ becomes the dominant species.

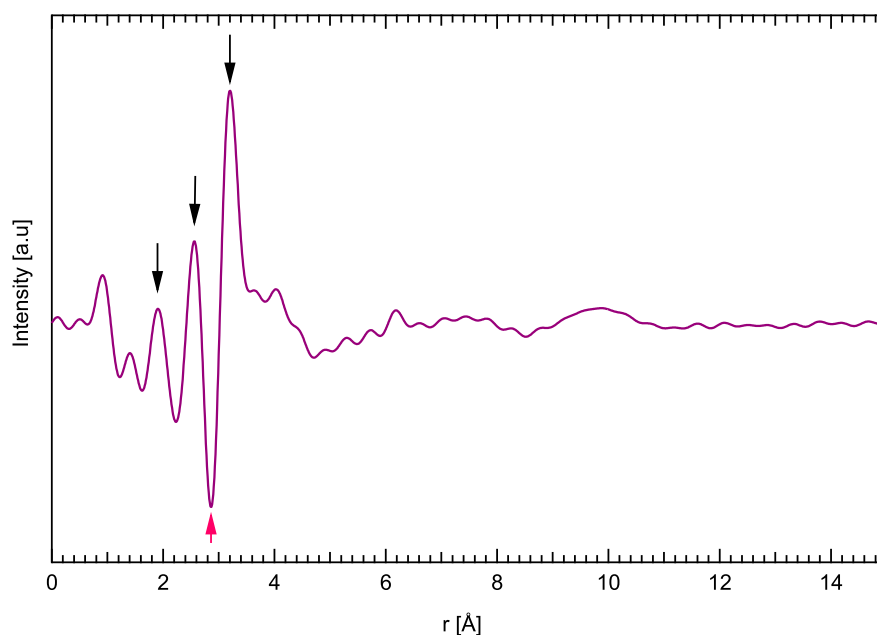


Figure 6.13: PDF pattern of $AlCl_3$ water solution. The pH of the solution is 4.0, and it is a precursor for the ϵ - $[Al_{13}]$ cluster synthesis. Characteristic peaks that are present also in early stages of the synthesis (1-20 min) are marked with black arrows. The red arrow marks a negative peak that comes from H_2O background subtraction.

in the model. It is also necessary to properly fit all three, main peaks of the early hydrolysis data with the 3-O-3fold model.

The dimer with tetragonally coordinated Al atoms (2-Cl-tet) had inherently unfavorable peak distribution, with too many intense peaks. The flat, $AlCl_3$ molecule (1-Cl-tri) on the other hand, results in two peaks that are too far apart to match the data.

In this elimination process, linear oligomers were chosen as the best match for the hydrolysis series, and used in the fits. A monomer was used in the final analysis, due to no improvement in fit with the use di- and trimer models. There was also no distinctive peaks found in the data, that would suggest that di- or trimers are actually present in the solution. It has to be pointed out, however, that the intensity of oligomer-specific peaks in the models is decreasing with the r-value, and could be easily obscured by the PDF background.

Remaining question is whether or not some of the O sites should be exchanged for Cl, in order to fill the 3.2 Å peak. There is a noticeable change in the intensity of the 3.2 Å peak associated with O-Cl distance. It is visibly decreasing in time, towering over the 1.9 Å peak before the reaction, becoming close to its intensity at 5 and 10 min, and then less intense at 20 min (Fig. 6.12). This suggests that the O-Cl distance becomes less "fixed" in place as the reaction is ongoing. Because of that, in order to ensure the comparability of the fits, two-phase fits with AlO_6 (1-O) and ClO_6 species used.

PDF patterns fitting

Q_{min} and Q_{max} parameters were set accordingly to 1.85 and 15.0 respectively. The $r_{min} = 0.0$, and $r_{poly} = 1.2$. In order to improve fit, fixing and refining some of the parameters — coordinates,

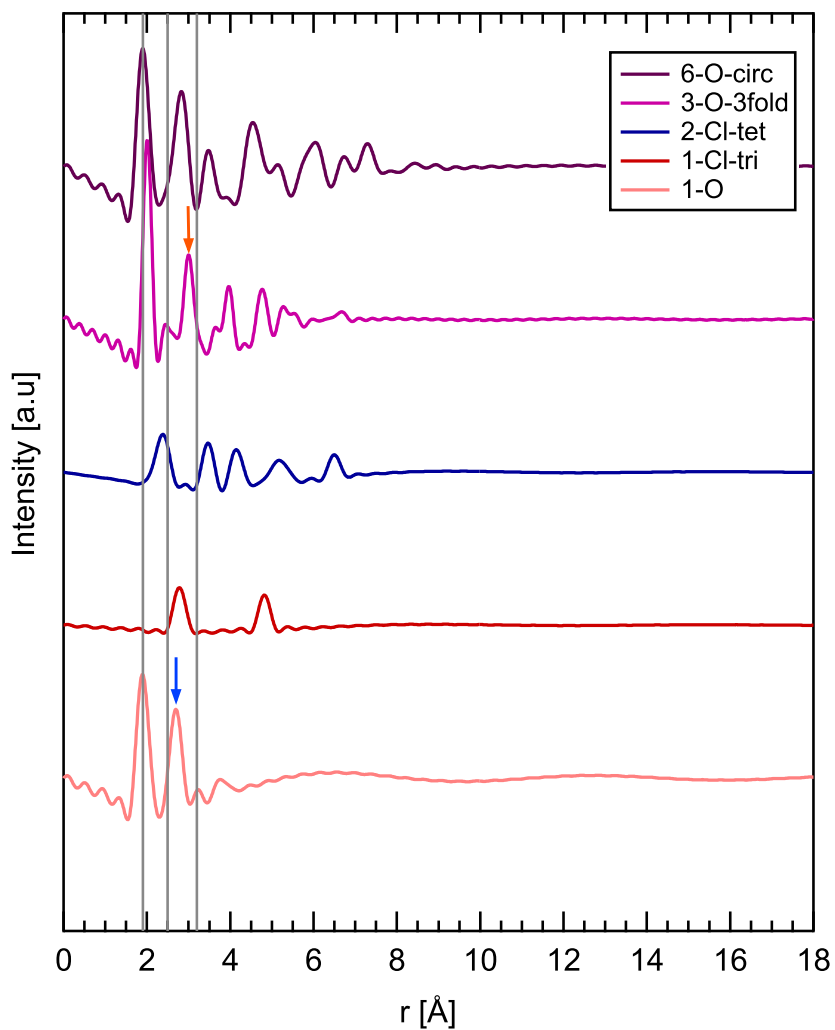


Figure 6.14: A comparison of selected oligomers. Guiding lines are set to 1.9, 2.5 and 3.2 Å, in accordance to the peaks present in early hydrolysis stage of the K-[Al₁₃] cluster formation, and AlCl₃ precursor solution. The red arrow points into Al-Al distance peak, that is offset in the 3-O-3fold model. This offset could be compensated by adjusting the model. The blue arrow points towards O-O distance peak of 1-O monomer model, which could also be adjusted to better fit the early hydrolysis data.

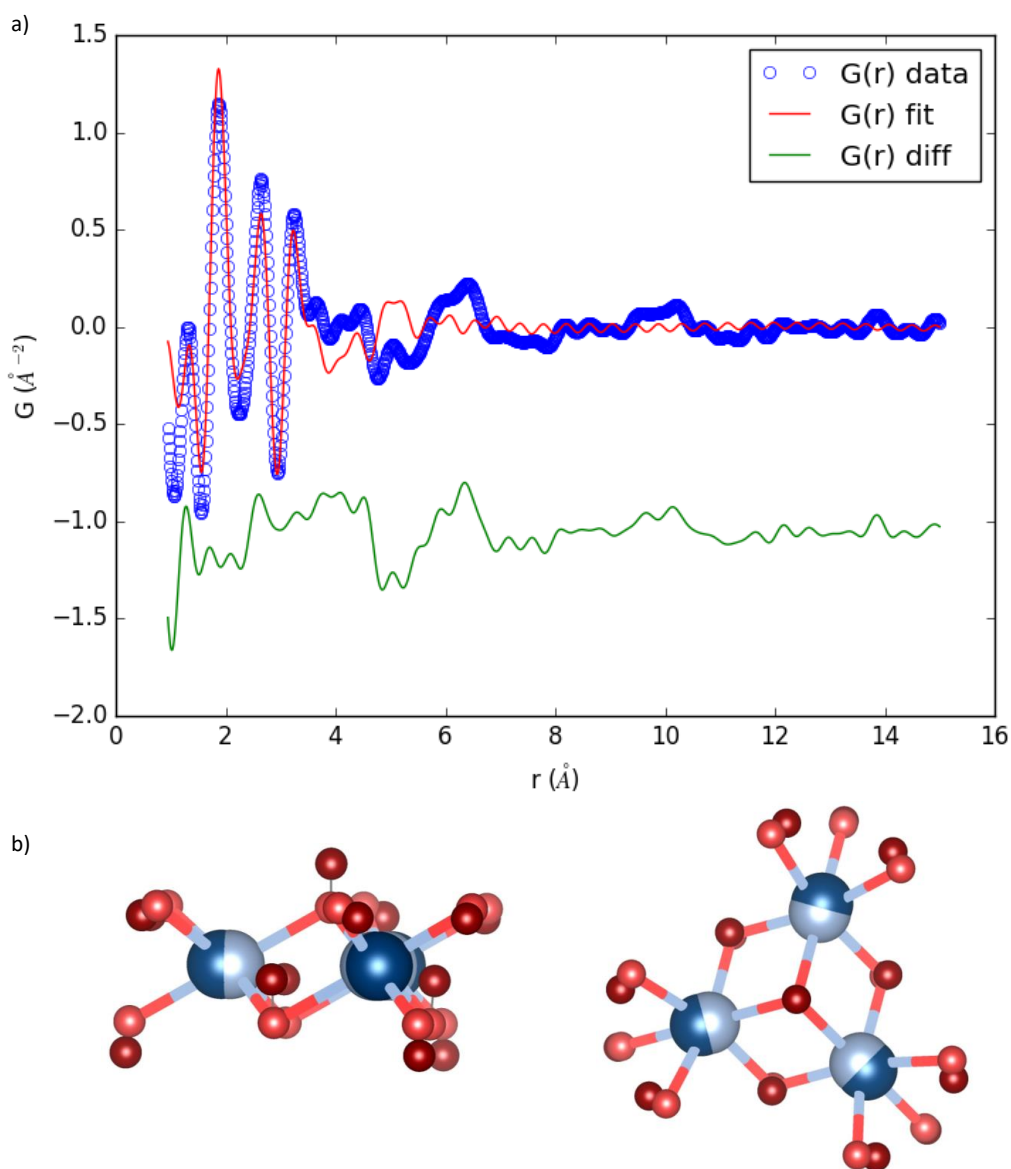


Figure 6.15: a), A PDF fit of Al_3O_{13} trimer model (3-O-3fold) to early hydrolysis, 20 min data. The R_w value of the fit is 0.48 due to the poor fit above 3.5 Å. b), Overlay of two Al_3O_{13} trimer models (3-O-3fold), before and after the fit. The blue and red atoms are Al and O, with the lighter shades being the default positions and darker the positions after the fit. Al atoms spread wider after the fit, and the central ring becomes more flat. However, what is the biggest offset from the default model is the new, floating positions of the central and the external O sites.

scale, displacement parameters – was implemented interchangeably. Another way of modifying the influence of said parameters was changing the initial values, while not dividing from the actual model and distances significantly.

After each measurement the values of coordinates were checked in order to ensure that the resulting model is still physical, and the atom-atom distances remain relatively unchanged. This was done in order to ensure that O-O distances, for example, are not used to fit the background by the calculation. In order to find the best fit for the early hydrolysis data, two different model variants were used, and two different sets of varying in background subtraction PDFs.

First variant (Model 1):

- $\text{AlO}_6 + \text{ClO}_6$
- Multiphase fit
- Measurement name indication: "fixed O"/FO

Second variant (Model 2):

- $\text{AlO}_6 + \text{ClO}_6$ with modified oxygen occupancy
- Multiphase fit
- Measurement name indication: "O occupancy"/OC

The Model 2 was used to achieve 6.3 O atoms per 1 Cl atom. The goal was simulating a Cl-O distance present in the solution, rather than a ClO_6 molecule. ClO_6 molecule as such could produce unwanted O-O distance, and be unrealistic to be present in the solution as such.

More variety was added to the fits by using two background subtraction levels. With the first level being lower than the second.

First subtraction level (Set 1):

- Negative water peak lower than other, negative peaks
- Negative peaks create a V-shape
- Measurement name indication: "normal"/"norm"/NB

Second subtraction level (Set 2):

- Background subtracted less than in previous set, water O-O peak
- Negative peaks create a U-shape
- Measurement name indication: "better background"/"better BG"/BB

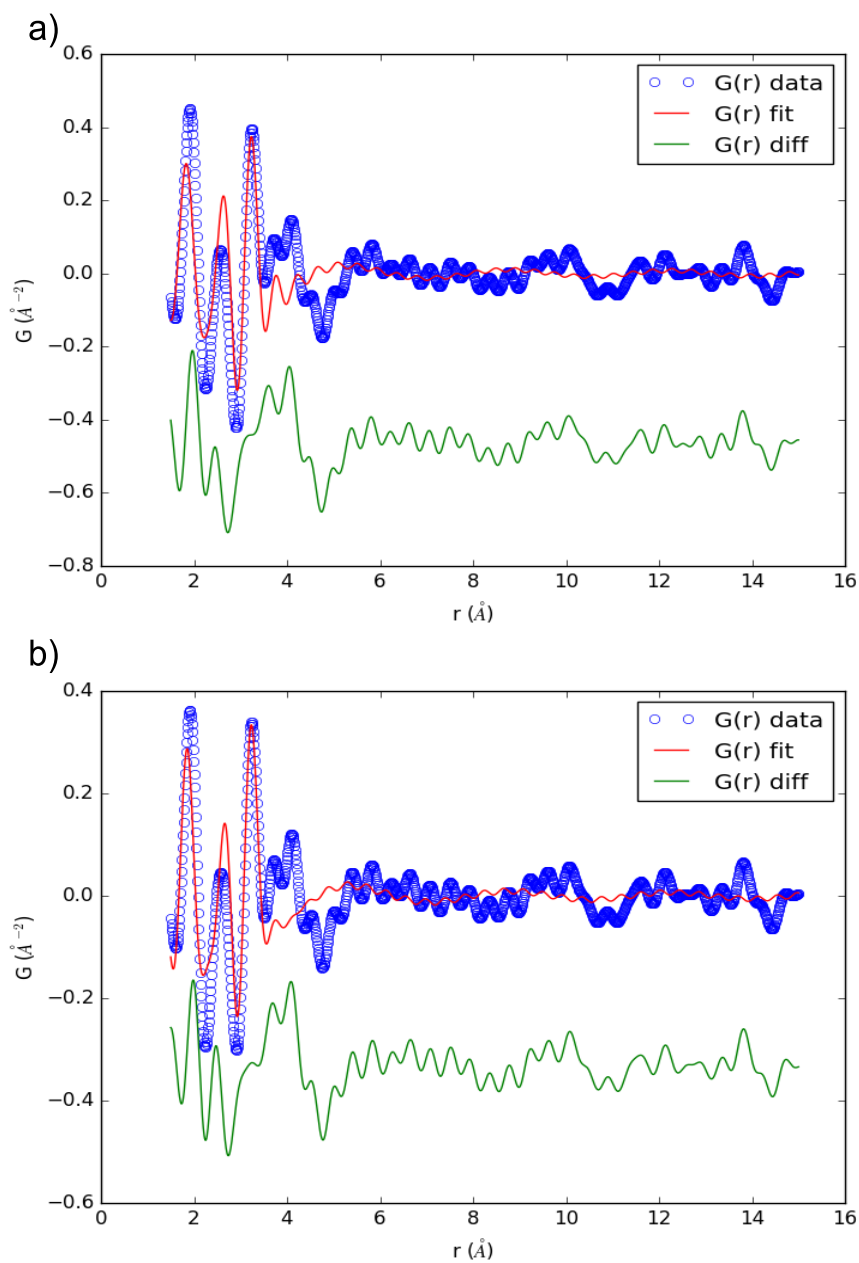


Figure 6.16: PDF fits of 1 min dataset with Model 1, fixed O position in ClO_6 . a), A fit to the set 1 - normal background subtraction. b), A fit to the set 2 - a better background subtraction

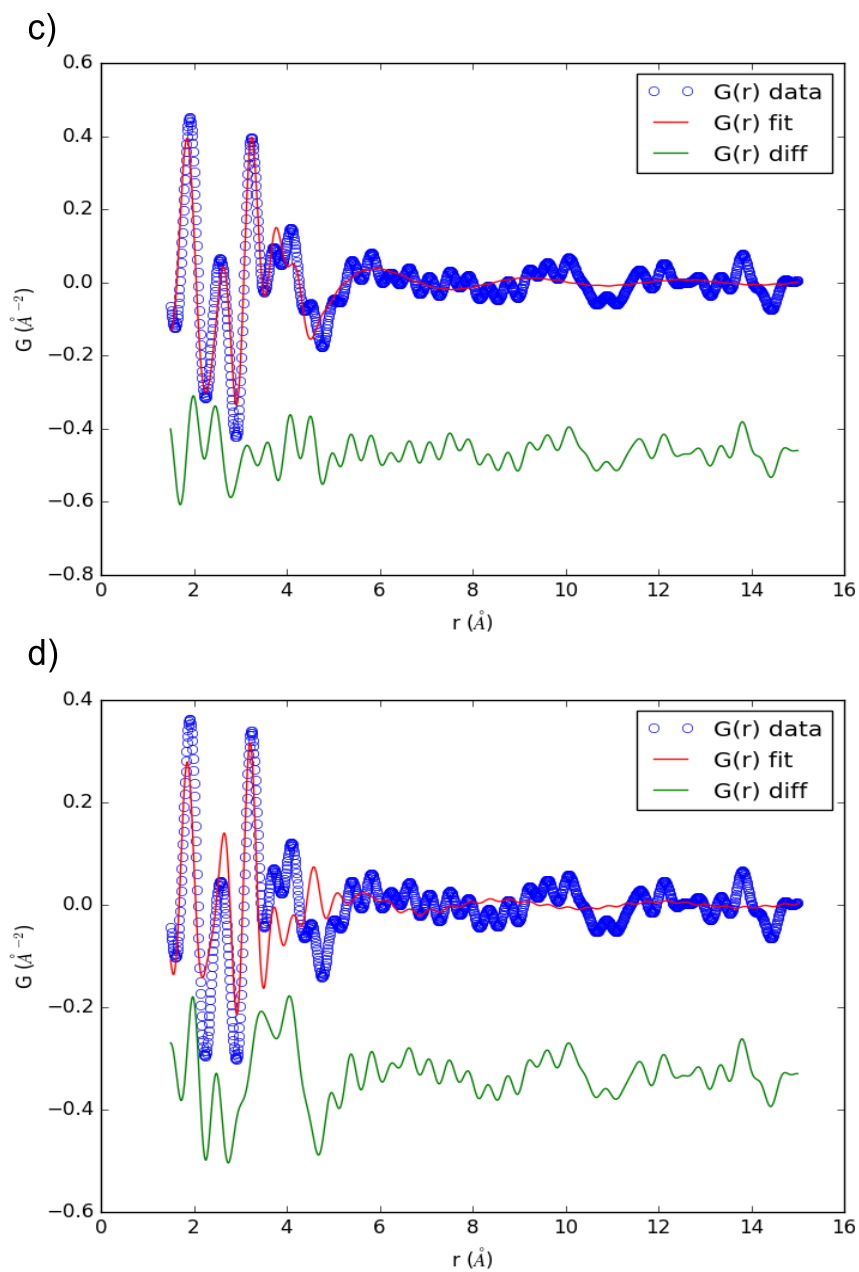


Figure 6.17: PDF fits of 1 min dataset with Model 2, with modified oxygen occupancy around Cl atom. c), A fit to the set 2 - a better background subtraction. d), A fit to the set 1 - normal background subtraction.

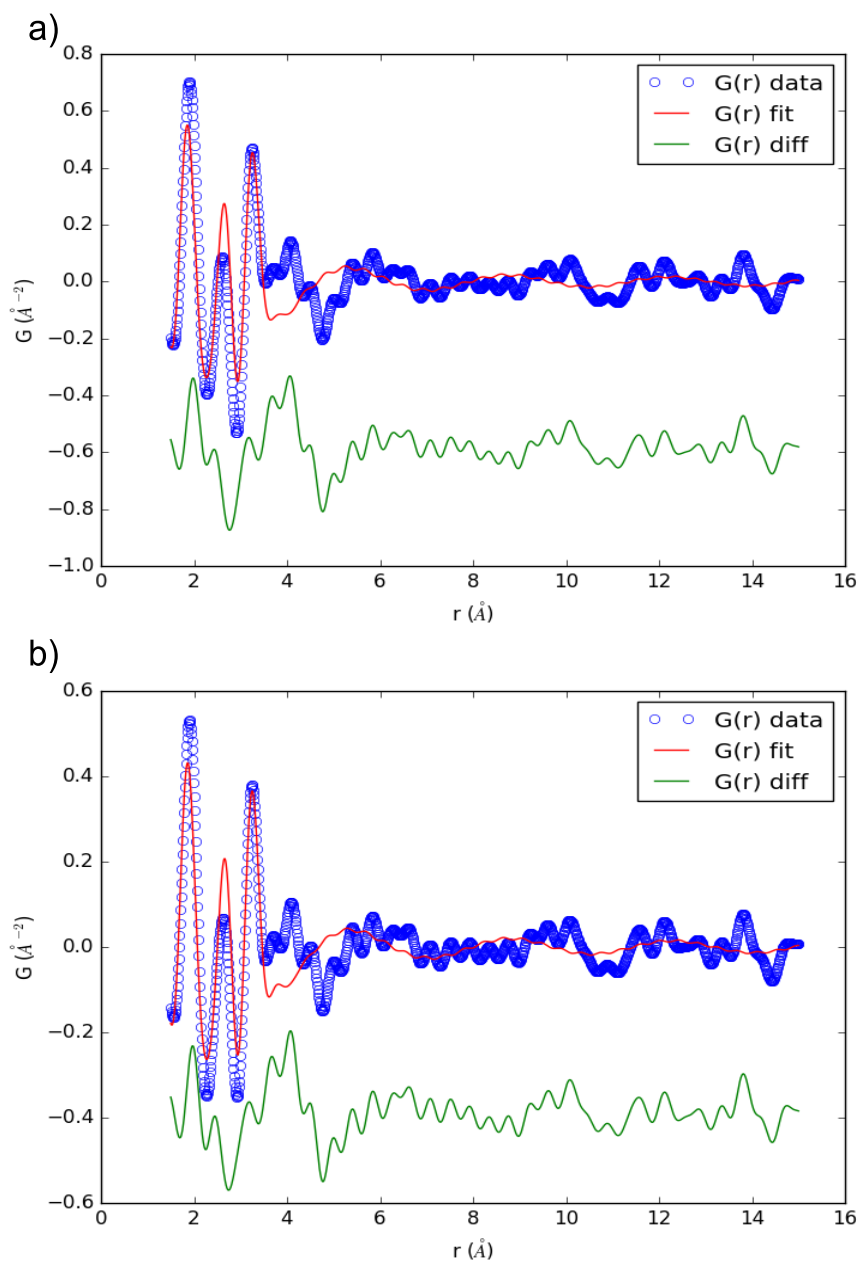


Figure 6.18: PDF fits of 5 min dataset with Model 1, fixed O position in ClO_6 . a), A fit to the set 1 - normal background subtraction. b), A fit to the set 2 - a better background subtraction.

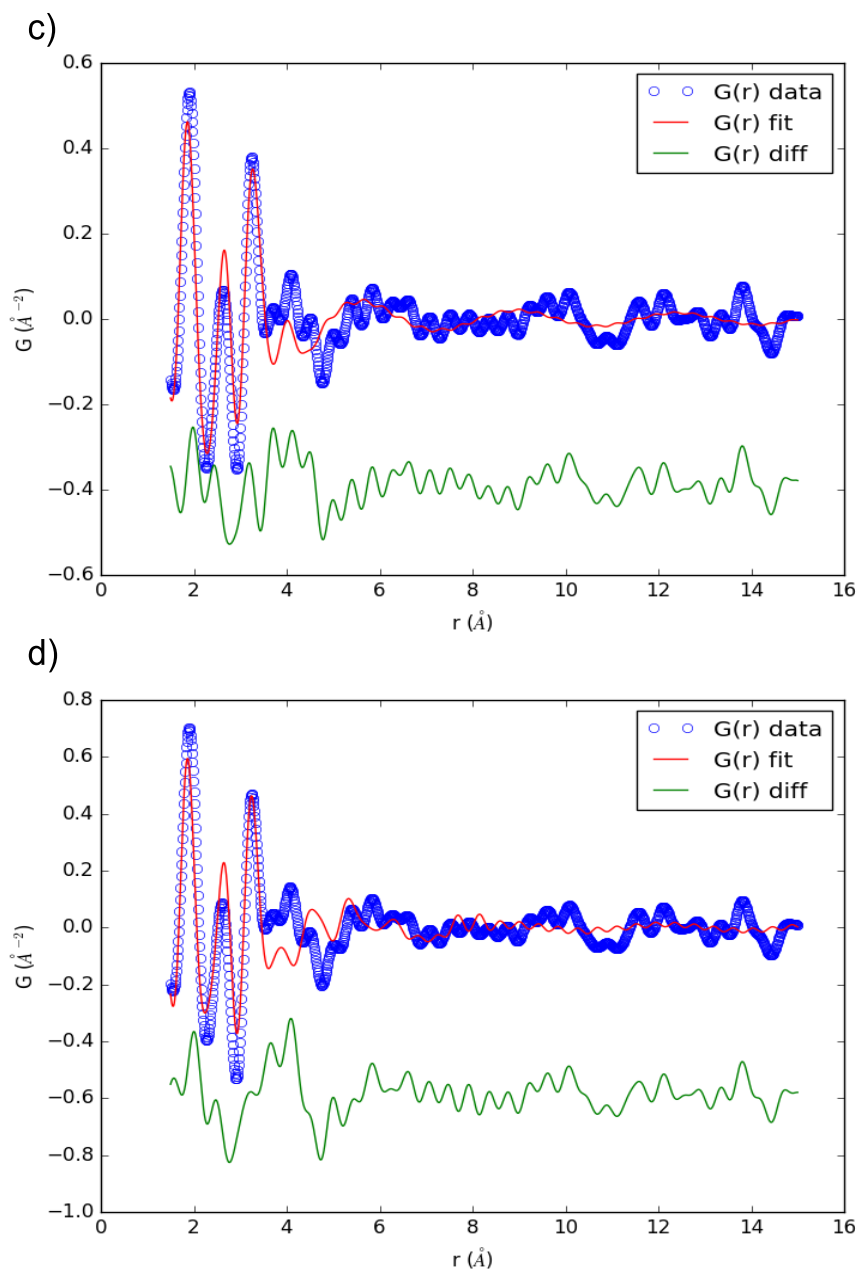


Figure 6.19: PDF fits of 5 min dataset with Model 2, with modified oxygen occupancy around Cl atom. c), A fit to the set 2 - a better background subtraction. d), A fit to the set 1 - normal background subtraction.

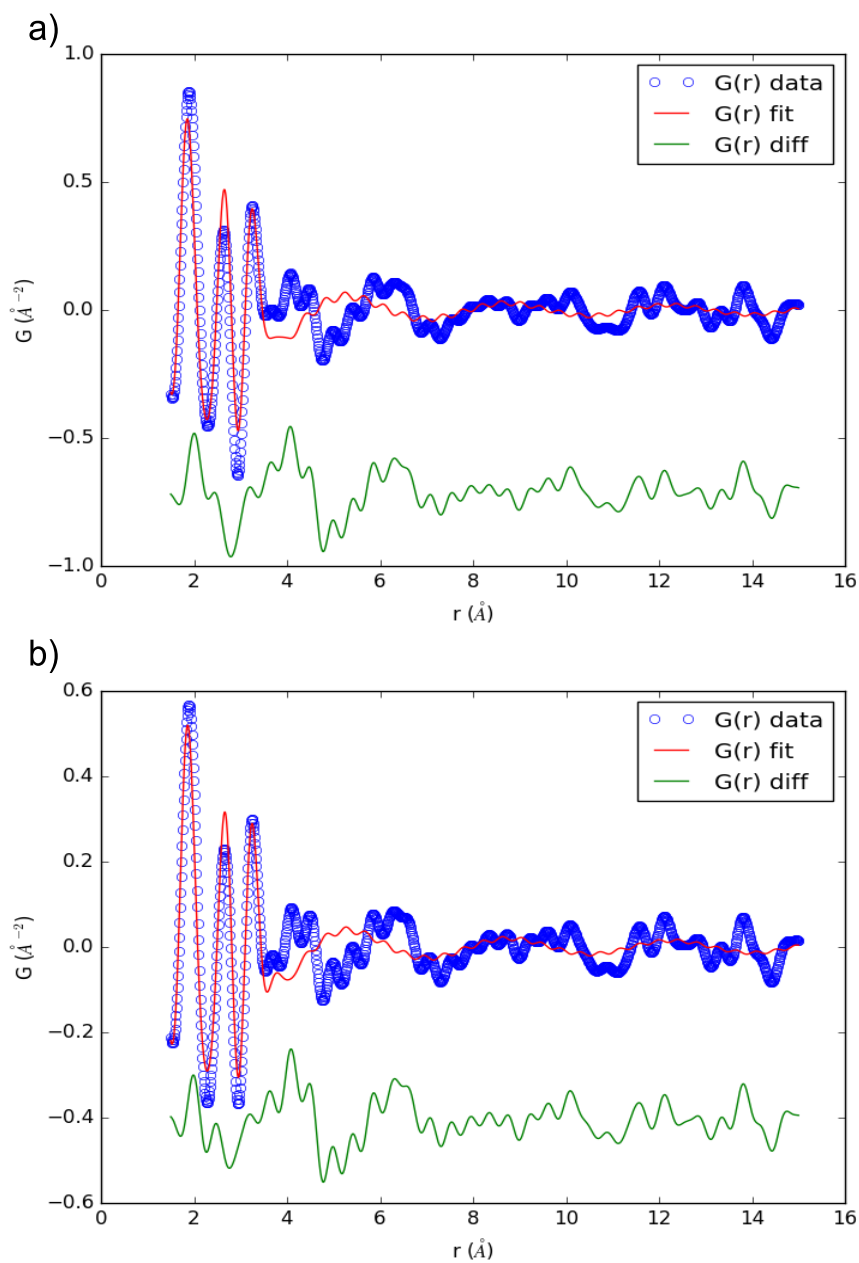


Figure 6.20: PDF fits of 10 min dataset with Model 1, fixed O position in ClO_6 . a), A fit to the set 1 - normal background subtraction. b), A fit to the set 2 - a better background subtraction.

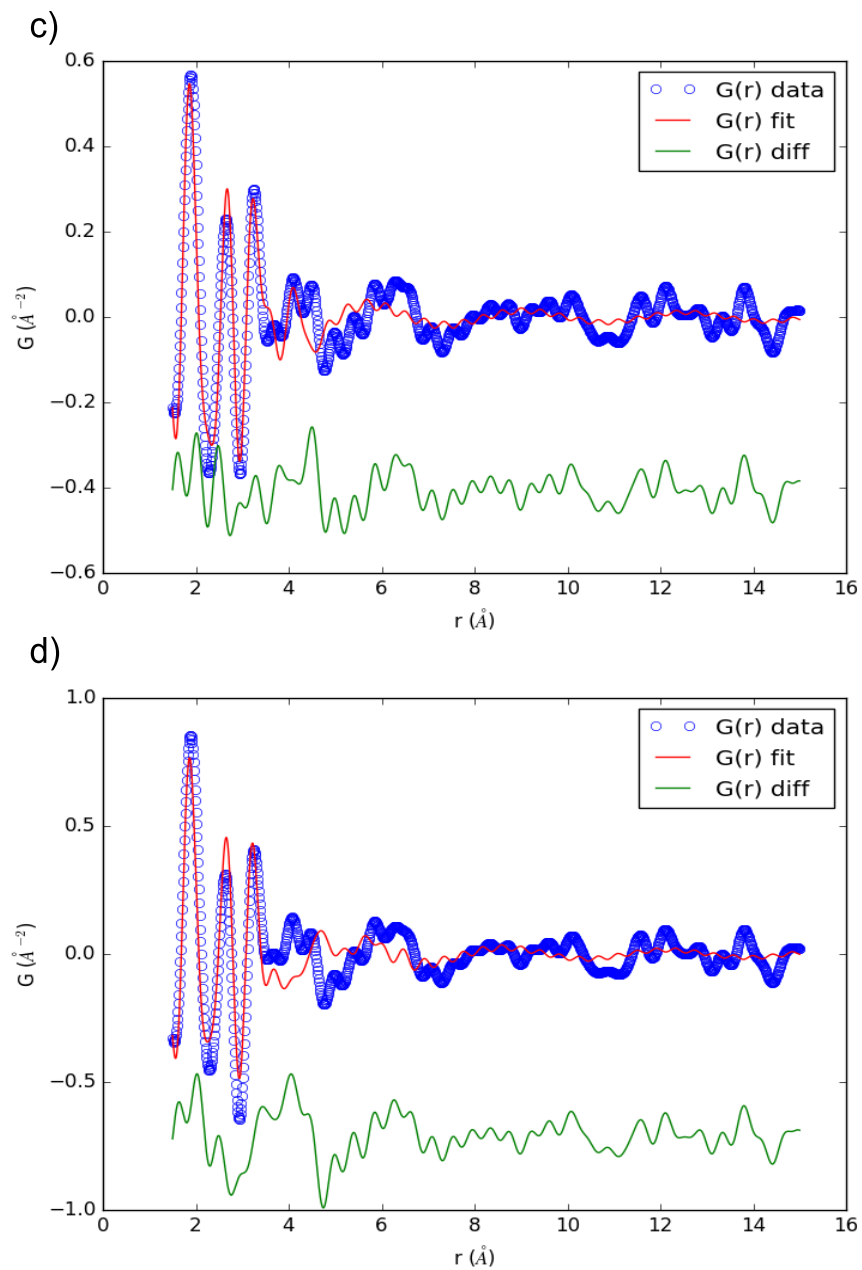


Figure 6.21: PDF fits of 10 min dataset with Model 2, with modified oxygen occupancy around Cl atom. c), A fit to the set 2 - a better background subtraction. d), A fit to the set 1 - normal background subtraction.

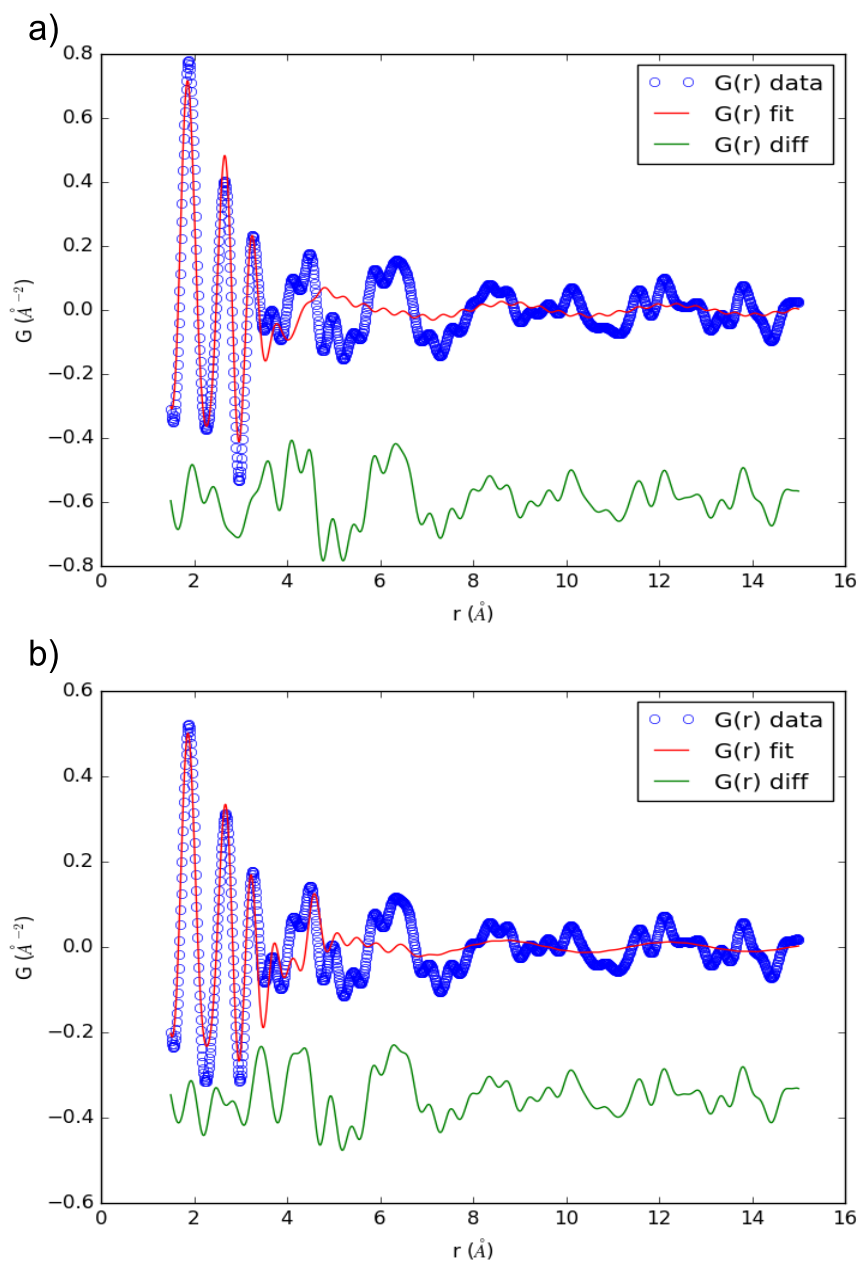


Figure 6.22: PDF fits of 20 min dataset with Model 1, fixed O position in ClO_6 . a), A fit to the set 1 - normal background subtraction. b), A fit to the set 2 - a better background subtraction.

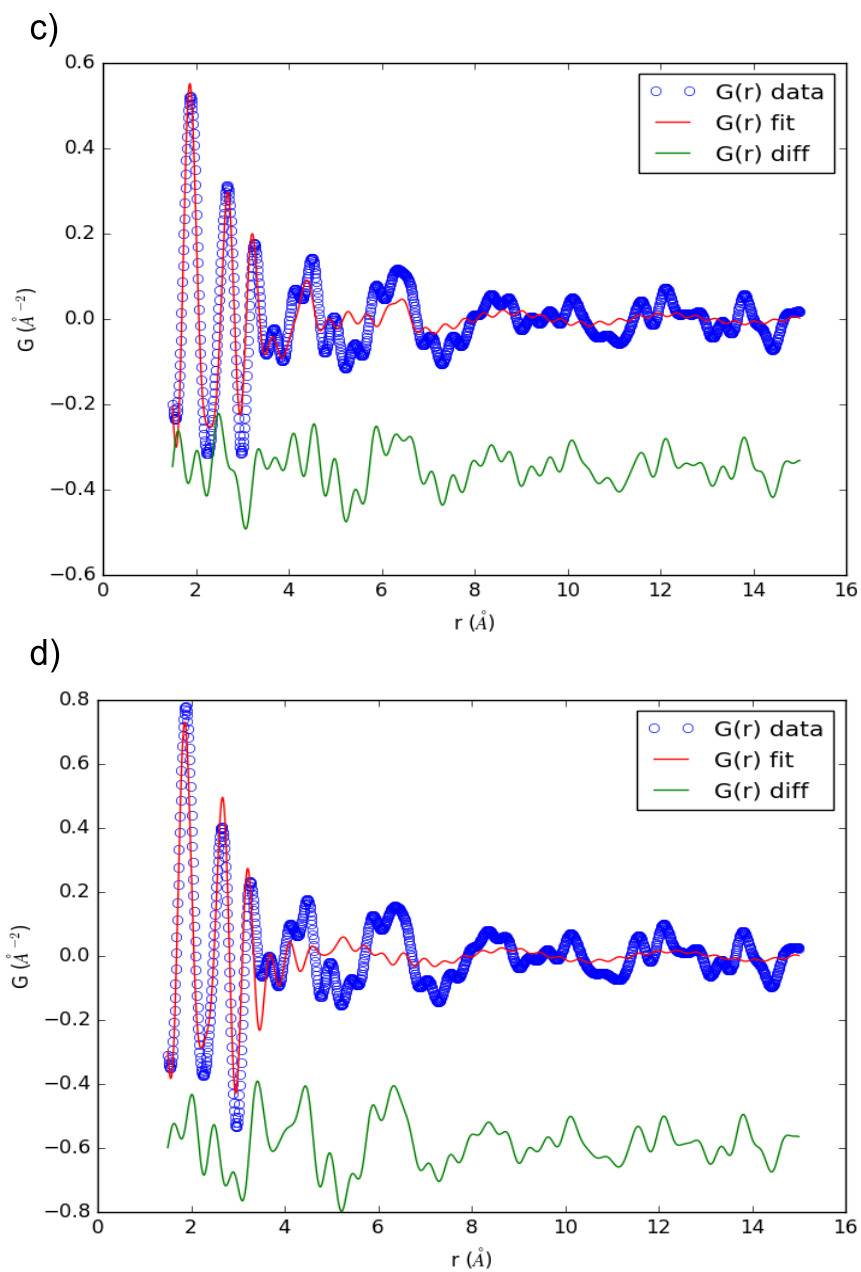


Figure 6.23: PDF fits of 20 min dataset with Model 2, with modified oxygen occupancy around Cl atom. c), A fit to the set 2 - a better background subtraction. d), A fit to the set 1 - normal background subtraction.

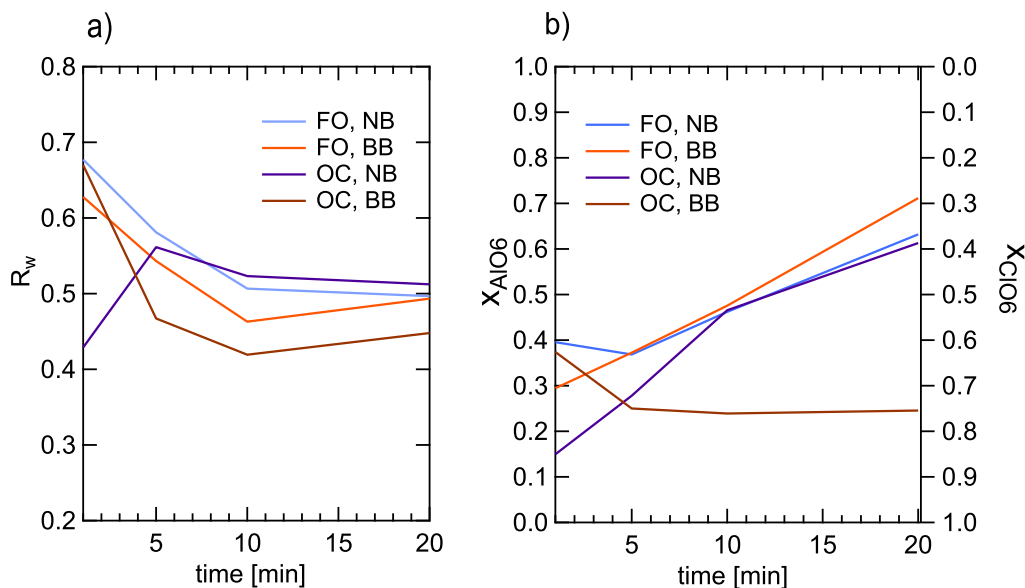


Figure 6.24: Graphs associated with Table 6.4, where variations of Model 1 (Fixed oxygen, FO), Model 2 (Oxygen occupancy, OC), Set 1 ("Normal" background, NB) and Set 2 ("Better background, BB) are presented. a), R_w value distribution across early stage hydrolysis fits. b), The change in molar fraction of AlO_6 and ClO_6 .

Fit analysis

Fits for all four early hydrolysis measurements, with both Model 1 and 2, and Set 1 and 2 of PDFs, are presented in a form of pairs (Fig. 6.16, 6.17, 6.18, 6.19, 6.20, 6.21, 6.22 and 6.23). The a) and b) graphs (Fig. 6.16, 6.18, 6.20, 6.22) are Model 1 (fixed O position), c) and d) (Fig. 6.17, 6.19, 6.21 and 6.23) are Model 2 (O occupancy). Similarly, a) and d) are fits to the Set 2 ("normal"), b) and c) to the Set 2 ("good background").

As indicated by the R_w graph (Fig. 6.24), there is an argument to be made whether or not using ClO_6 model with multiple O positions in low occupancy is better than ClO_6 with distorted fixed O positions. Similarly, increasing the background subtraction seems to be improving the fit slightly. However, the overall improvements in R_w are not immense and due to the overall high value, using R_w alone as an indicator of a good fit is not enough.

The phase fractions presented below in Table 6.4 show that the best of the fits, OC, BB (O occupancy, better background), is going against the established logic. The AlO_6 contributions stagnates, rather than keep increasing. At the same time fit slightly worse in terms of R_w average, OC, NB (oxygen occupancy, "normal" background), does not exhibit such phase fraction anomaly. The AlO_6 fraction is expected to increase, as the Cl-O peak associated with the other phase visibly decreases in intensity with time. The fits with fixed oxygen position of ClO_6 model (FO) generally fall in line with the decrease of ClO_6 contribution. However, the R_w values are consistently lower in these fits. Moreover, the model generates a peak that is O-O distance in ClO_6 molecule (Fig. 6.17, 6.19, 6.21 and 6.23), c, above 4 Å), which artificially lowers down R_w . This peak fits into a feature, that is otherwise a sinusoidal frequency, consistent throughout the datasets. In later datasets, peaks associated with $[Al_{13}]$ arise in the same place, which further confuses the fits with fixed oxygen position of ClO_6 .

Because of that, ultimately the best two-phase fit for the early hydrolysis datasets is the OC (oxygen occupancy) model. Also, the background in GB set was most likely not subtracted sufficiently, and the NB set is a better calculated PDF.

Table 6.4: R_w values of PDF fits to the 1-20 min hydrolysis data, with molar fraction of the fitted phases.

Fixed oxygen, "normal" background			
time [min]	R_w	x_{AlO_6}	x_{ClO_x}
1	0.677	0.395	0.605
5	0.581	0.369	0.631
10	0.507	0.462	0.538
20	0.497	0.632	0.368
average:	0.565		

Fixed oxygen, "better" background			
time [min]	R_w	x_{AlO_6}	x_{ClO_x}
1	0.628	0.295	0.705
5	0.543	0.373	0.627
10	0.463	0.476	0.524
20	0.493	0.711	0.289
average:	0.532		

Oxygen occupancy, "normal" background			
time [min]	R_w	x_{AlO_6}	x_{ClO_x}
1	0.429	0.150	0.850
5	0.562	0.278	0.722
10	0.523	0.466	0.534
20	0.512	0.613	0.387
average:	0.506		

Oxygen occupancy, "better" background			
time [min]	R_w	x_{AlO_6}	x_{ClO_x}
1	0.670	0.374	0.626
5	0.467	0.250	0.750
10	0.419	0.239	0.761
20	0.448	0.245	0.755
average:	0.501		

6.3.5 $[Al_{13}]$ synthesis - late time hydrolysis

Initially, models of $[Al_{13}O_{40}]$ with varying amount of Cl sites surrounding its were tested. The goal behind these models was to simulate a cloud of Cl atom surrounding the core in various positions, that may or may not be fully occupied at the same time depending on the amount of sites. The sites were placed further than a bond distance, around 3.2 Å away from the nearest core atom. The sites were distributed around the core, using the same symmetry operations that were used for creating the Al and O sites in the core. Models with 0, 4, 6, 8, 14, 26, 50 and 74 Cl sites with modifiable occupancy were created and applied to the late hydrolysis measurements.

An improvement of the fit was detected when the Cl sites were allowed to change positions in the restraints of their symmetry operations (Fig. 6.25, green). The fitting improves especially with medium amounts of Cl sites, in particular the 26-site model. However, when Cl positions are fixed and only occupancy and thermal factors of Cl sites are fit, the R_w value does not change significantly, regardless of the amount of Cl sites surrounding the $[Al_{13}O_{40}]$ cluster.

Looking at the R_w values of the fits collectively (Fig. 6.25), it becomes apparent that late hydrolysis data is not free from the challenge of achieving a good R_w value. A single-phase fit with the $[Al_{13}O_{40}]$ model, without Cl cloud, is the most basic and already addresses all of the major peaks (Fig. 6.26, 6.27, and 6.28). Multi-phase fits with 0, 26, and 74 Cl sites were also

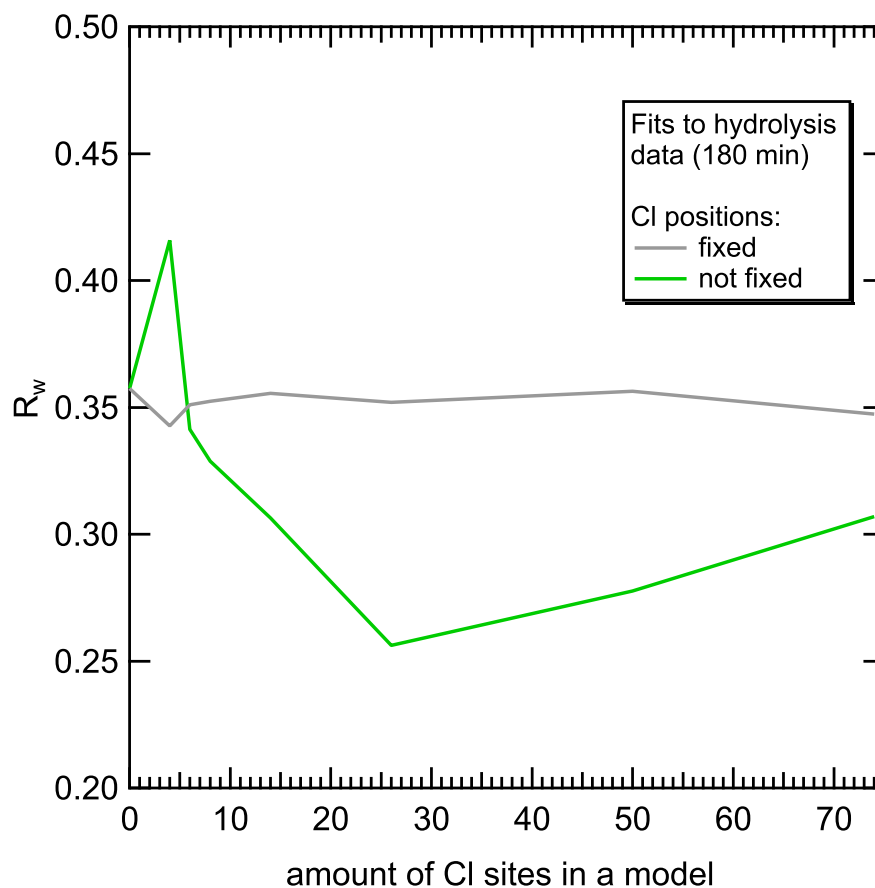


Figure 6.25: A graph representing the change in R_w value as a function of amount of chlorine sites in the fitted model. $[Al_{13}O_{40}]$ models with 0 to 74 Cl sites were used to fit 180 min data hydrolysis data. Two variants of fits are presented, one allowing Cl positions to be changed, and with fixed Cl positions.

compared in order to determine the best, possible fits (Table 6.5).

Table 6.5: R_w values of chosen PDF fits to the 40-180 min, late hydrolysis data. Three, different $[Al_{13}]$ models were used, with 0, 26 and 74 Cl sites surrounding the Keggin. Multiphase fits were done with Al_3 three-fold model (Al_3O_{13}), AlO_6 and ClO_6 molecules.

time [min]	R_w			average:
	40.00	60.00	180.00	
$Al_{13}O_{40}$	0.2856	0.3026	0.3598	0.3160
$Al_{13}O_{40}, AlO_6, ClO_6$	0.2274	0.3182	0.2631	0.2696
$Al_{13}O_{40}, AlO_6$	0.2519	0.3128	0.3352	0.3000
$Al_{13}O_{40}, 3-O-3fold$	0.2391	0.3526	0.2096	0.2671
$Al_{13}O_{40}Cl_{26}, AlO_6$	0.2639	0.2506	0.2716	0.2620
$Al_{13}O_{40}Cl_{26}, 3-O-3fold$	0.1796	0.1938	0.1433	0.1722
$Al_{13}O_{40}Cl_{74}, AlO_6$	0.1580	0.2435	0.2801	0.2272
$Al_{13}O_{40}Cl_{74}, 3-O-3fold$	0.1173	0.2077	0.1730	0.1660

6.3.6 PCA - overview of components

PCA was performed in order to separate potentially overlooked species and provide aid to the fingerprinting of PDF signal. However, after seeing the extracted components (Fig. 6.29) it becomes clear that the PCA did not, in fact, separate particular, chemical species. That is not surprising, given that some the same atom-atom distances can be found in multiple species. Therefore, the intensities of associated with these atom-atom distance peaks do not always change proportionally to the rest of their signal. This forces interpretation of specific peaks in each component, in a search of some patterns.

PCA of all of the hydrolysis series, from 1 to 180 min, was done with Q_{min} of each measurement set to 1.0 and Q_{max} to 20.0. All of the PDF extraction parameters were kept uniform among all of the measurements, to ensure no artifacts. Six different components were extracted, and their overall intensities of components PDFs were not adjusted (Fig. 6.29). The number of components in this PCA are followed by an "a".

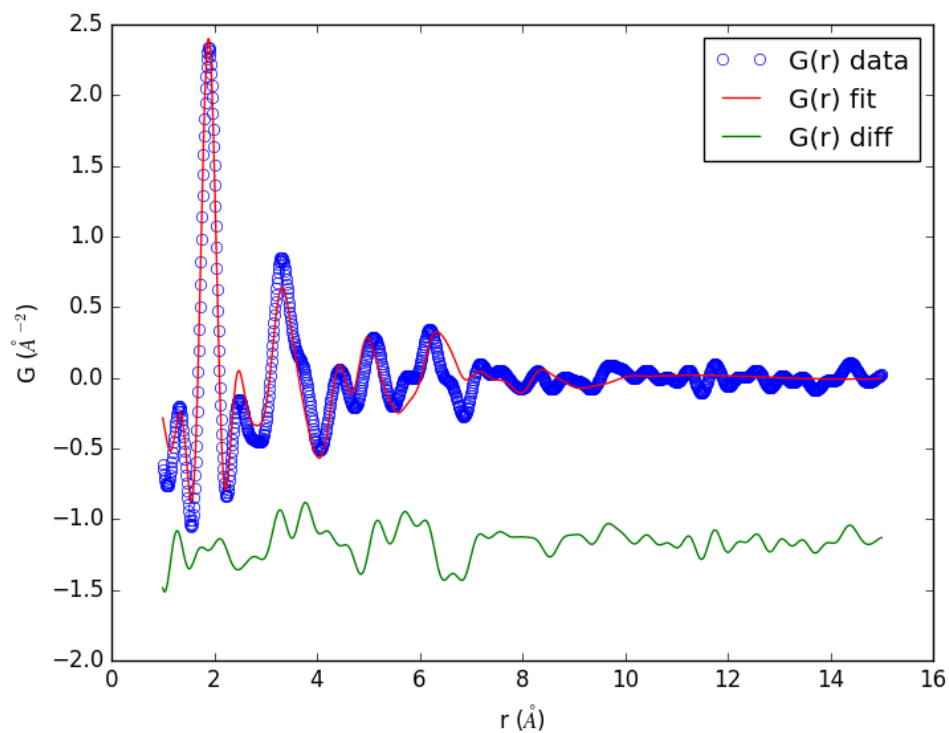
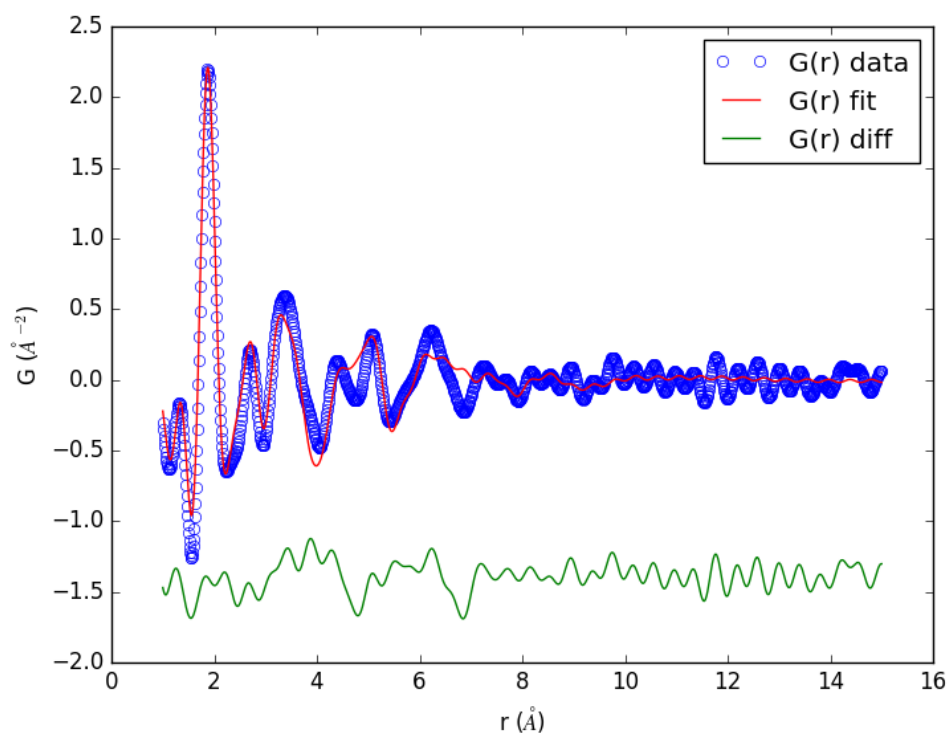
Component 1a exhibits one, predominant feature. It is the characteristic peak of O-O distance in water (2.8 Å). In addition, a decreasing in intensity oscillation can be found in this component.

Component 2a contains peaks which can be associated with K- $[Al_{13}]$. This component contains the entirety of intensity originating from Al-O distance (1.9 Å). This peak is present also in species like AlO_6 . On the top of that, 3.3 Å peak coming from the Cl-O distance in ClO_6 is also present in this particular component.

Component 3a exhibits a negative peak at 2.6 Å. It can be explained as the decreasing amount of AlO_6 due to $[Al_{13}]$ formation, as the Al-O distance in $[Al_{13}]$ is less defined. It can as well be a part of asymmetric 2.8 Å, O-O distance of the water peak, that was separated into Component 1 and now Component 3 with PCA.

Component 4a has two main peaks at 1.3 and 2.3 Å. The first one can be associated with a hydrogen bond. The latter could be Cl bound with Al, but is most likely the O-O distance in AlO_6 grouping.

Components 5a and 6a exhibit low intensity, and are mostly connected to background changes. The highest peaks of the Component 5a are at 2.6 and 4.9-5.0 Å, whereas the 6a component echoes the peaks from Component 2, located at 1.9 (Al-O), 3.3 (Cl-O) and also 2.9 Å.

Figure 6.26: PDF fit of the $[Al_{13}O_{40}]$ model to the 40 min dataset.Figure 6.27: PDF fit of the $[Al_{13}O_{40}]$ model to the 60 min dataset.

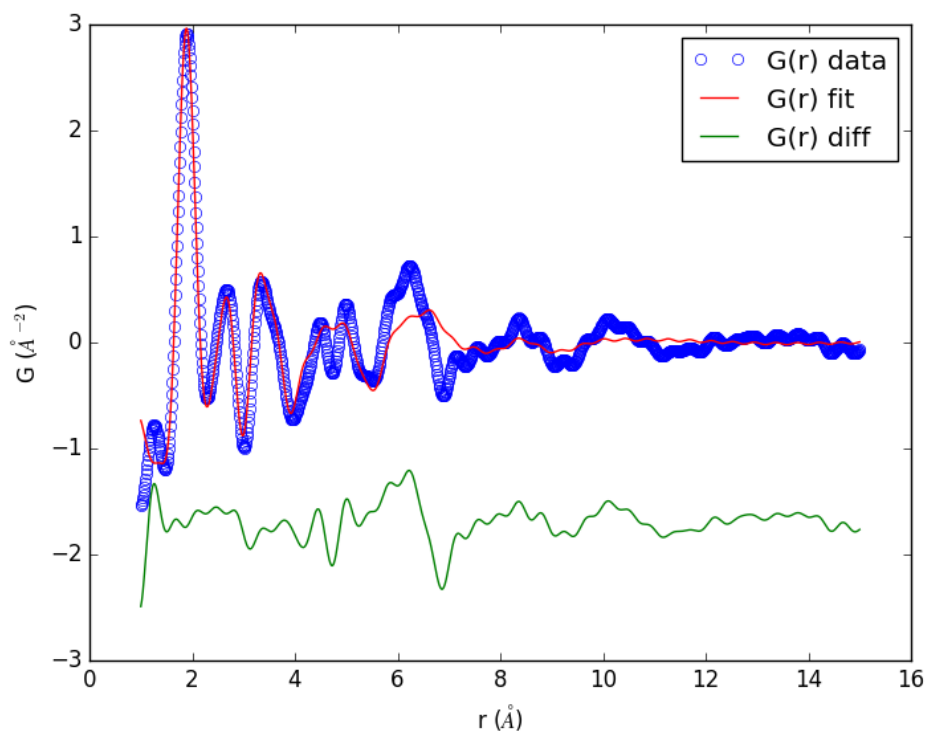


Figure 6.28: PDF fit of the $[Al_{13}O_{40}]$ model to the 180 min dataset.

Early time hydrolysis only

Early hydrolysis datasets, from 1 to 20 min, were in addition subjected to the PCA separately. This was done in addition to the PCA of the entire 1 to 180 min range of measurements. It was performed on dataset with Q_{min} set to 1.0 and Q_{max} to 15.0 when extracting PDF. Four different components were extracted (Fig. 6.30). The number of components in this PCA are followed by an "b".

Component 1b contains some of the signal belonging to both AlO_6 (Al-O, 1.9 Å) and ClO_6 (Cl-O, 3.2 Å). However, the intensity of second peak associated with AlO_6 is missing. This intensity (2.3 Å) is transferred to other components – mainly Component 2b, and Component 4b to a lesser extent. There is also a resemblance of Component 1b to the $[Al_{13}]$ (Fig. 6.31). Although a part of the main peak intensity (1.9 Å, Al-O distance) most certainly fits the $[Al_{13}]$ cluster, the rest of the resemblance is superficial. That is why it likely belongs to AlO_6 . The significant Cl-O peak (3.2 Å), visible in this Component 1b creates a visual artifact, that creates the superficial resemblance to the as if the $[Al_{13}]$ cluster.

The $[Al_{13}]$ cluster PDF fits better to Component 2b, looking at the shape of signal above 4 Å (Fig. 6.32). If the intensity of 1.9 Å peak was transferred from Component 1b, the Component 2b would be fit almost fully with the $[Al_{13}]$ cluster PDF signal. Only two peak of Component 2b do not fit the $[Al_{13}]$ cluster. The first is at 2.8 Å and can be associated with O-O distance in water. The second one is the missing peak of AlO_6 , located at 2.3 Å.

Component 3b contains a diad of peaks, with 1.9 Å as it is center (Fig. 6.30). These are just "feet" of the hill that is the main 1.9 Å peak, which were transferred to this component as the change in peak shape is registered as a separate signal. Apart from that split peak, this component contains mainly background noise.

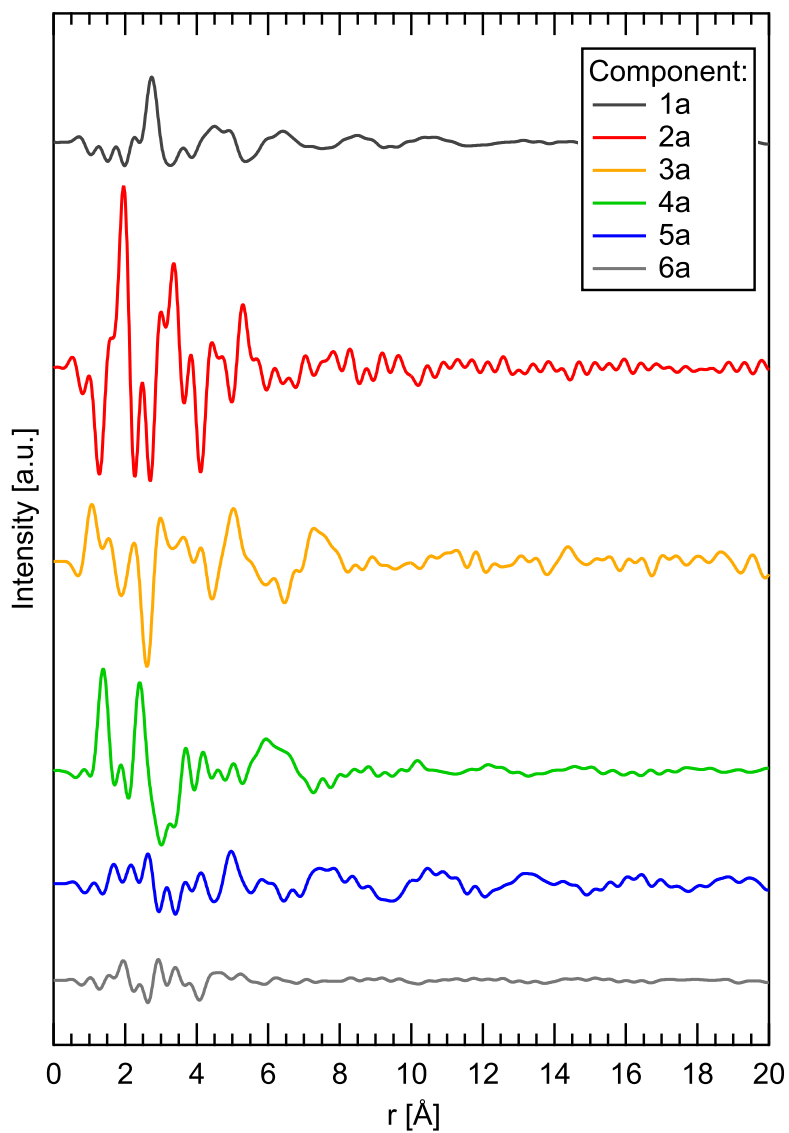


Figure 6.29: PDF components extracted with PCA. Measurements from 1 to 180 min were used to obtain six components. The distribution of peaks among the components does not resemble a complete PDF pattern of any expected compounds, which means that some of the peaks were separated.

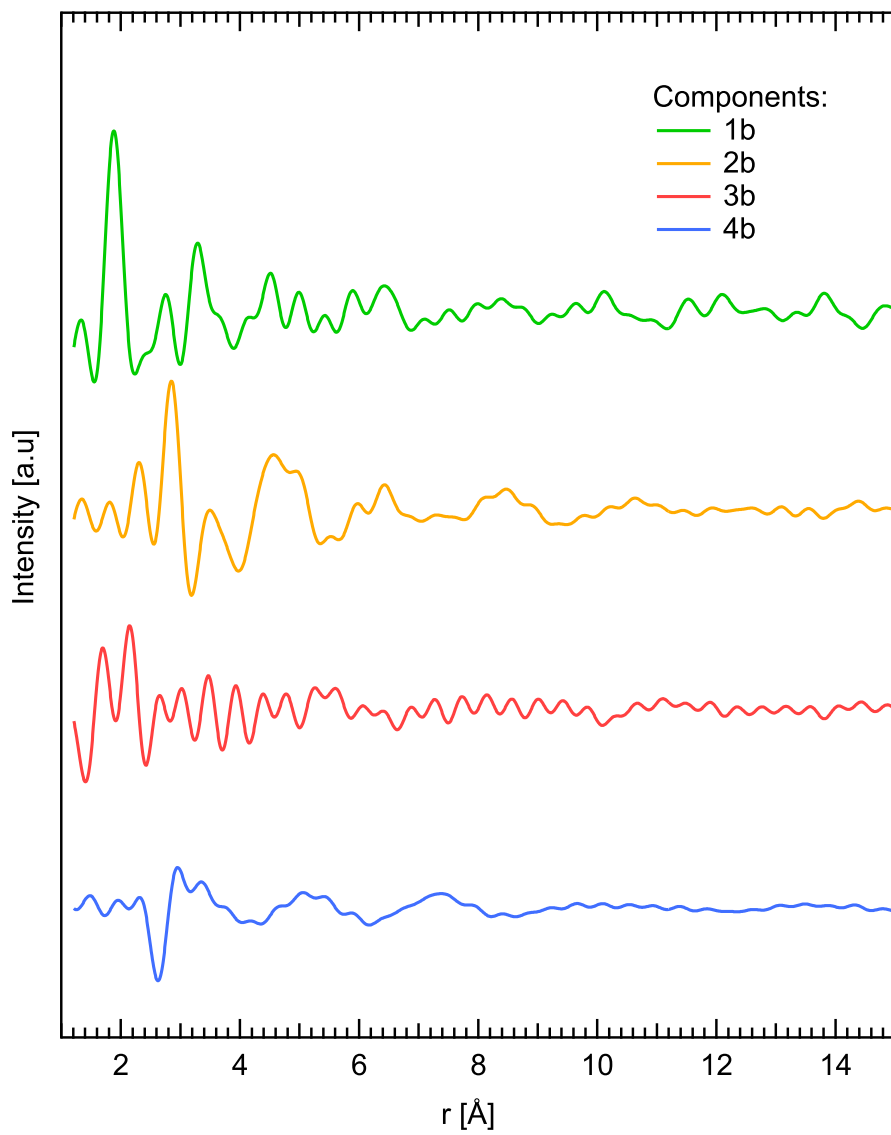


Figure 6.30: PDF components of the early time dataset, extracted with PCA. Measurements from 1 to 20 min were used to obtain four components.

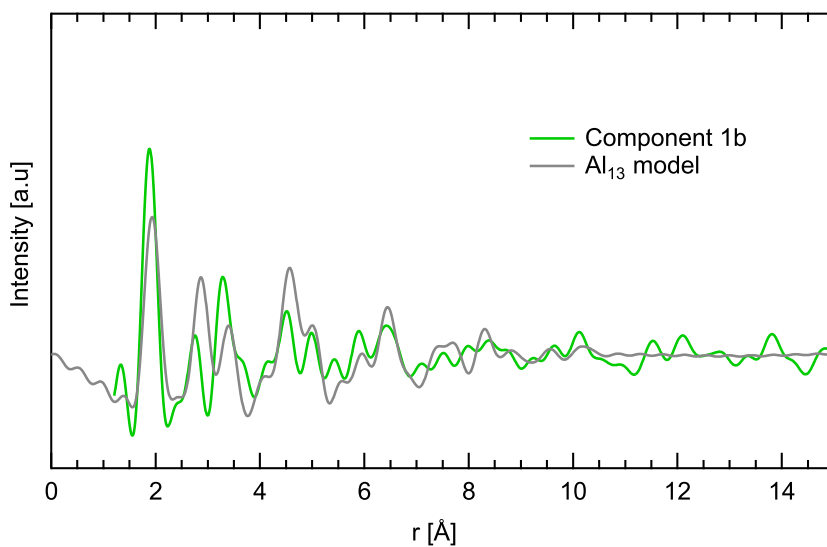


Figure 6.31: Comparison of the Component 1b to PDF signal of $[Al_{13}]$ model. The first peak of both matches. However, the rest of cluster signal does not match quite well to the Component 1b.

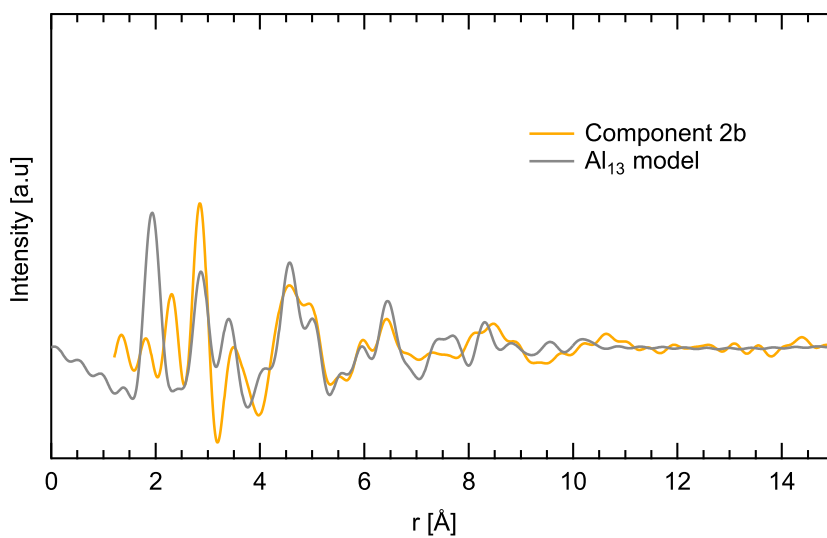


Figure 6.32: Comparison of the Component 2b to PDF signal of $[Al_{13}]$ model. The cluster signal matches well to the entirety of Component 2b. However, the first peak at 1.9 Å is missing, most likely due to being transferred to Component 1b.

The negative peak of Component 4b is analogous to the 2.6 Å peak in Component 3a - it could be AlO_6 amount decreasing at a cost of the $[\text{Al}_{13}]$ cluster formation, as the Al-O distance in $[\text{Al}_{13}]$ is less defined. Alternatively, it could be a part of an asymmetric 2.8 Å peak. Due to the very low overall intensity of Component 4b, any other peaks might be simply oscillations. There is also a larger oscillation with a 1.5 Å wavelength – similar to the one in Component 5a.

In this PCA analysis, the Component 2b resemblance to the $[\text{Al}_{13}]$ oxo-cluster PDF signal is an important observation. It indicates that this cluster is most likely present as synthesis products even before the main conversion moment, observed as an abrupt change in PDF signal at 40 min.

6.4 Discussion of the results

6.4.1 Early stage hydrolysis

Early stages of hydrolysis exhibit predominant signal contribution from small species, fitting to pair distribution function of hexaqua-aluminium ion (AlO_6) and Cl^- coordinated with 6 water molecules.

The case of the Al_3 with three-fold symmetry model distorting to unrealistic Al-O distances in some of the bonds, is not strong enough to diminish the possibility of this species being present in solution. Because of the complex nature of the AlCl_3 solution, alleged in literature by many, it is not without merit to assume that the unrealistic distortions resulted in an attempt to fit all the peaks just with the Al_3 three-fold model (Al_3O_{13}), could be caused by the insufficient amount of phases in the fit. A complex analysis of that, resulting in a definitive answer and a small R_w value (< 0.15), was, however, unsuccessful (Tab. 6.6). Although the AlO_6 model is a simpler molecule and fits the PDF data better because of the lack of distortion of the model, it cannot be ruled out that Al_3O_{13} trimer exists in solution. Looking at its construction, resembling one-fourth of the $[\text{Al}_{13}]$ Keggin, it would be surprising if such molecule never existed in the process of $\text{K}[\text{Al}_{13}\text{O}_{40}]$ growth, especially if the “cage-like” self-assembly model is the more accurate mechanism.

Table 6.6: R_w values of chosen PDF fits to the 1-20 min hydrolysis data, with Al_3 three-fold model (Al_3O_{13}).

time [min]	R_w	
	3-O-3fold	3-O-3fold + AlO_6 + ClO_6
1	0.6841	0.5837
5	0.4898	0.5823
10	0.5163	0.4588
20	0.4814	0.4707

What is clear, based on the PDF studies, is that no intermediate-sized oligomers in Al_4 - Al_{12} range were detected (Fig. 6.33). Linear polymers of this size, apart from the two main peaks, exhibit many smaller features reaching a further distance. More importantly, the intensity of the 2.7 Å peak increases with the size of a linear oligomer, surpassing the 1.9 Å peak intensity present in the PDF data. This rules out the participation of linear polymers larger than Al_3 in the reaction.

Apart from the two main species, the PCA points towards one more species present in the solution, the $\text{K}[\text{Al}_{13}]$ cluster. The PCA analysis does not clearly distinguish between $\text{K}[\text{Al}_{13}]$ and AlO_6 signal, especially in terms 1.9 Å Al-O distance, and therefore it does not help directly in identifying any other precursor species present in early hydrolysis. It was, however, helpful in showing the $\text{K}[\text{Al}_{13}]$ cluster, even though it is not clearly visible in the 0-20 min dataset.

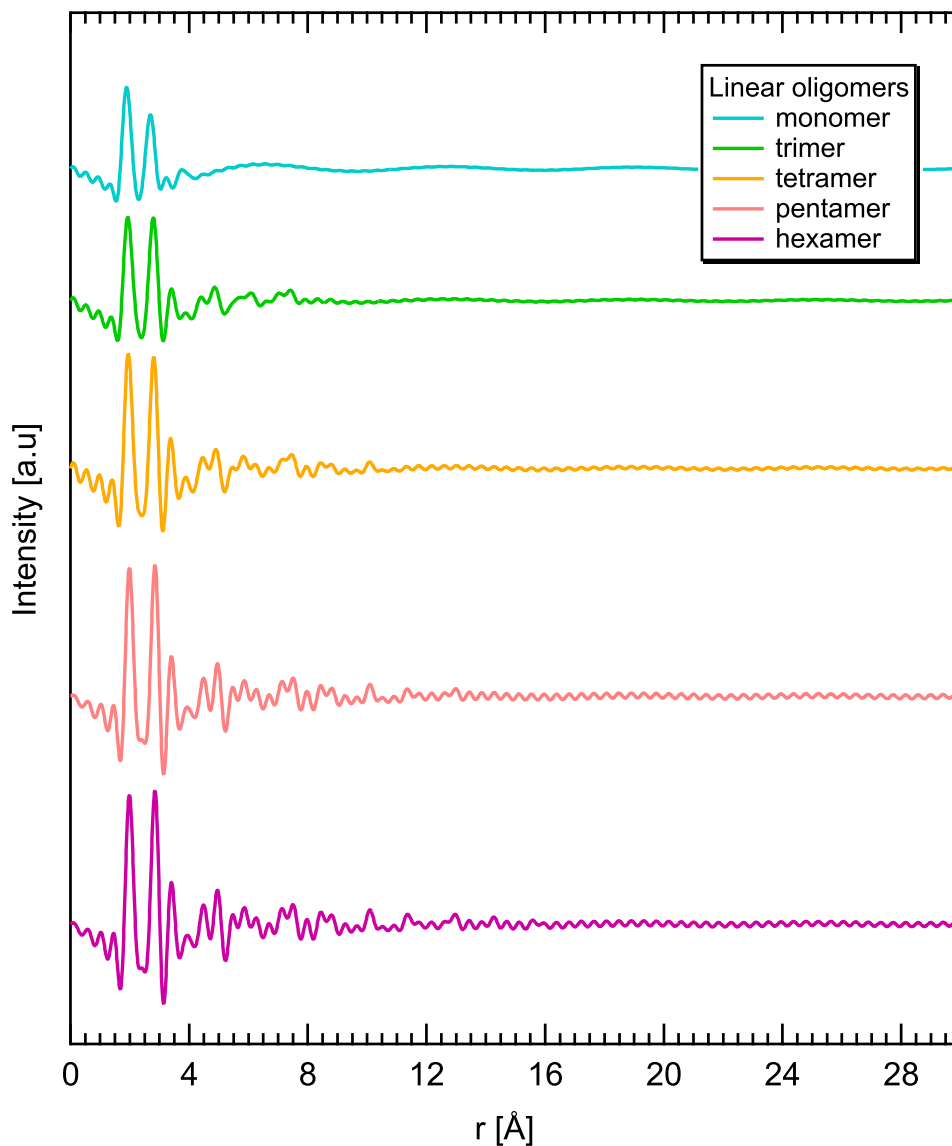


Figure 6.33: A comparison of PDF patterns calculated based on models of linear oligomers (Al_1 – Al_6). The evolution in complexity of the patterns, accompanying the growth of oligomer size, shows how less and less a PDF pattern matches these measured in the early hydrolysis dataset. An especially convincing trait is the proportion between the first and second peaks, which changes towards the latter being more intense. In all of the data, it is the first peak that is more intense.

Table 6.7: The best R_w values of PDF fits to the 1-180 min hydrolysis data, chosen with cautious consideration. For the 1-20 min measurements – AlO_6 with ClO_6 (FO, NB) multi-phase model was used. For the 40-180 min measurements – $[\text{Al}_{13}\text{O}_{40}]$ with Al_3O_{13} (3-O-3fold) multi-phase model was used.

time [min]	R_w
1	0.429
5	0.562
10	0.523
20	0.512
40	0.239
60	0.353
180	0.210

6.4.2 Late stage hydrolysis

After 40, 60 and 180 min into the hydrolysis the PDF patterns start clearly resembling the $[\text{Al}_{13}]$ model. Therefore, the interpretation of the patterns is more clear than in the early time hydrolysis. However, there is still a place for interpretation due to ambiguously high R_w values.

The use of Cl cloud surrounding $[\text{Al}_{13}\text{O}_{40}]$ has to be questioned due to the stagnation of R_w value improvement when Cl positions are fixed. When allowed to move, the Cl atoms seem to position themselves in a way that enables fitting of a broad feature, the present ca. 5.8–6.5 Å (Fig. 6.34). This feature is especially prominent in the late hydrolysis data and is one of the sources of high R_w values. In all of the calculated PDFs for $[\text{Al}_{13}]$ isomers, there are two peaks present at this position. And yet, there is seemingly no possibility to merge these peaks into one, broad feature in order to fit the data better. This leads to believe that some coordination with other molecules might exist in the solution for the K- $[\text{Al}_{13}]$ cluster, causing increased signal at this range.

Due to the background and challenging 5.8–6.5 Å feature, the average R_w of fit using the most basic, single-phase $[\text{Al}_{13}\text{O}_{40}]$ model is equal to 0.316. It is higher than any multi-phase fit (Table 6.5). The most interesting finding is, that by far the best fits are achieved with the use of $[\text{Al}_{13}\text{O}_{40}\text{Cl}_{74}]$ and Al_3O_{13} (3-O-3fold) multi-phase model (Fig. 6.35, 6.36, and 6.37), with the average $R_w = 0.1660$, the lowest among all of the fits. What is even more interesting, is that the improvement is evident even without Cl cloud, with the use of $[\text{Al}_{13}\text{O}_{40}]$ and Al_3O_{13} (3-O-3fold) multi-phase model (average $R_w = 0.2671$).

This brings three observations. The first one is that the Cl cloud surrounding Keggin finds its place when paired with the Al_3O_{13} (3-O-3fold) trimer. The second one is that the Al_3O_{13} (3-O-3fold) trimer used as an additional molecule result in a better fit than using AlO_6 , as long as ClO_6 is not added. The third observation is that the 5.8–6.5 Å feature is the main problem in fitting the late hydrolysis data. The broad feature is seemingly best fitted when Al_3O_{13} trimer is used.

The potential presence of Al_3O_{13} (3-O-3fold) trimer in the early hydrolysis stage and the improvement of late hydrolysis fits with this trimer, making this molecule seem like a plausible stage of the K- $[\text{Al}_{13}\text{O}_{40}]$ growth. Even more so due to the similarity of the trimer to a quarter or Keggin molecule. It also does not exclude the possibility of AlO_6 being a prominent part of the reaction, as a precursor of the Al_3O_{13} (3-O-3fold) trimer. What seems clear looking at the fits is that the K- $[\text{Al}_{13}\text{O}_{40}]$ is coordinated by other molecules, although it cannot be determined unambiguously from the data whether or not these are Cl ions.

The least speculative fit to the early hydrolysis data is the multi-phase model composed of AlO_6 and ClO_6 (FO, NB). To the late hydrolysis, a multi-phase model composed of $[\text{Al}_{13}\text{O}_{40}]$ and Al_3O_{13} (3-O-3fold) fits well, avoiding potentially artificial decrease of R_w values by adjusted chlorine cloud distance from the molecule (Tab. 6.7).

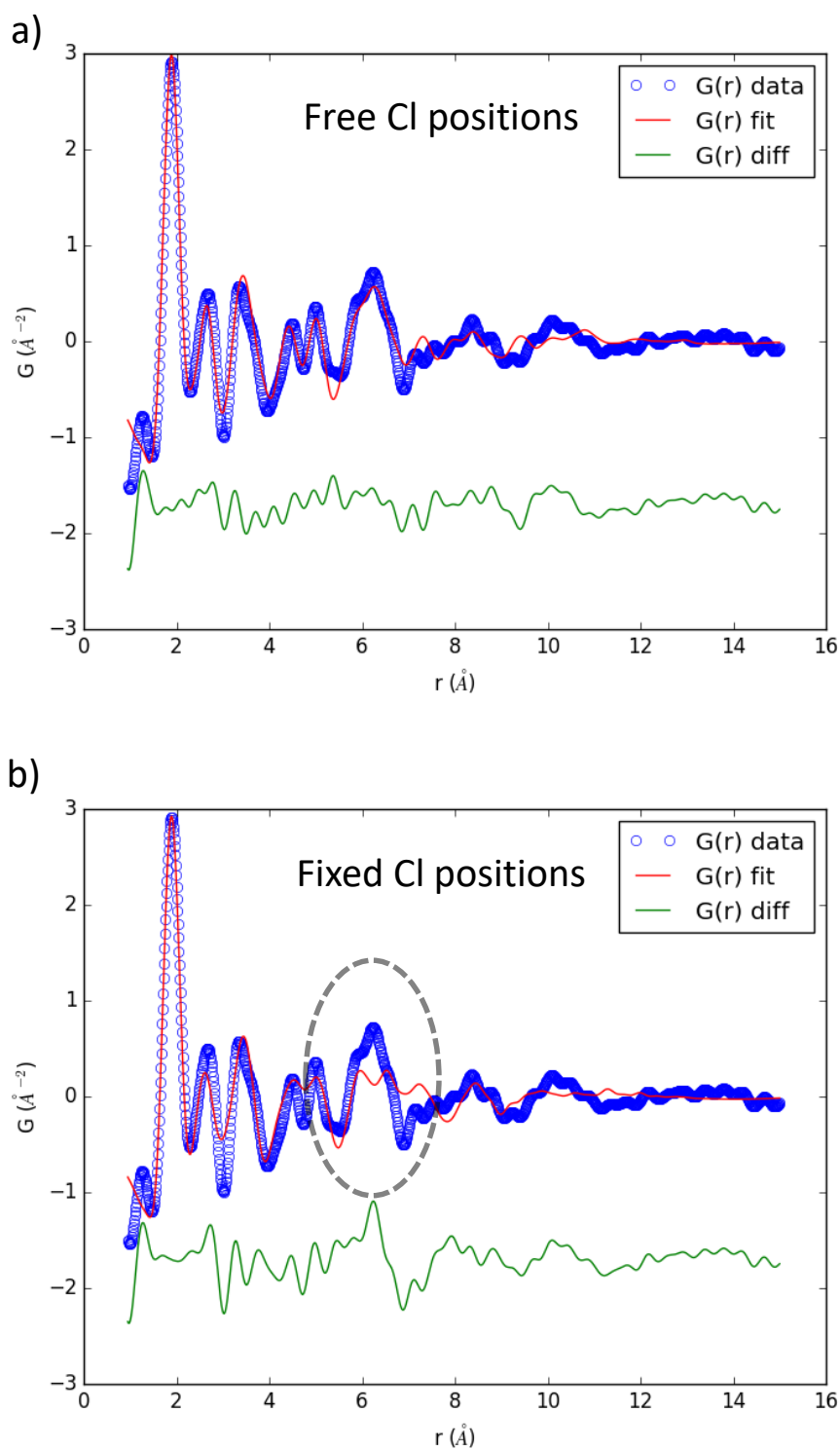


Figure 6.34: PDF fits 180 min hydrolysis data. The $[Al_{13}O_{40}Cl_{26}]$ model was used with a) Cl positions free to adjust, and b) fixed Cl positions. A broad feature located ca. 5.8–6.5 Å is fitted by the Cl atoms, when free to move. However, when their positions are fixed, the fit is missing intensity at that position (bottom graph, grey circle).

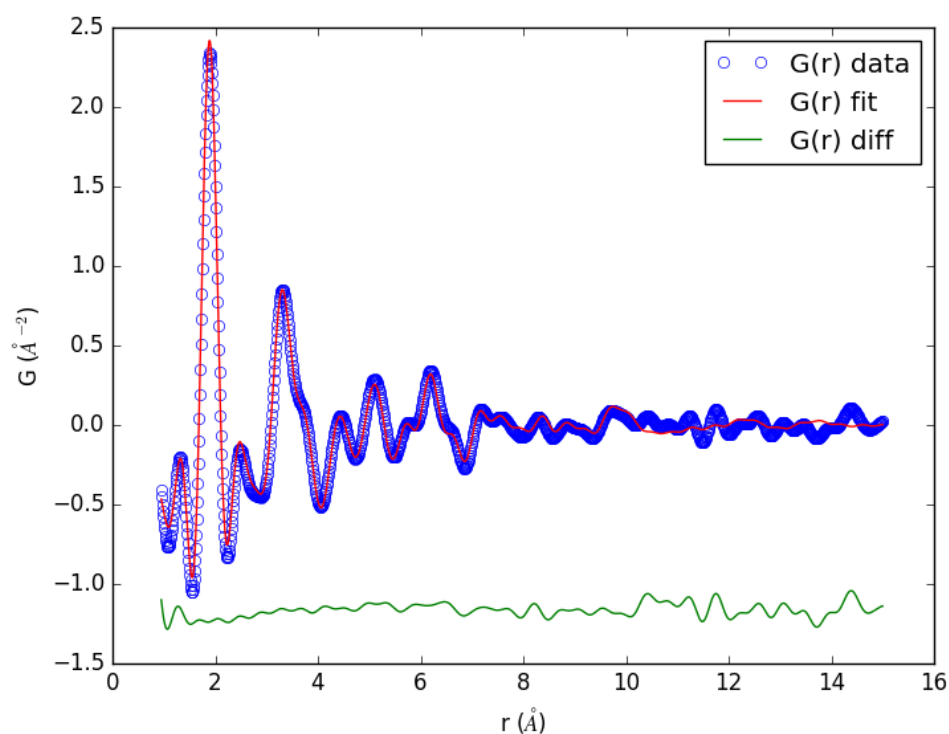


Figure 6.35: PDF fit of $[\text{Al}_{13}\text{O}_{40}\text{Cl}_{74}]$ with Al_3O_{13} (3-O-3fold) multi-phase model to the 40 min dataset.

6.4.3 Criticism of the fits

In the difference curve of some of the PDF fits a sinusoidal background can be seen. It is especially prominent in the early hydrolysis data. No sharp, unambiguous peaks that could not be fit with the peaks present in models were found in this sinusoidal signal. This background is most likely caused by a sharp feature in total scattering data, translating to the PDF. It is also the main source of poor R_w values for the early hydrolysis data. Attempts to eliminate this background at data integration and PDF calculation stages were made but failed to lower it without losing a significant amount of information from the main peaks.

The second source of high R_w values is that model peaks do not fully match the data. The reason for that is most likely connected to the background interfering with the peak intensity fitting. The overall low intensity of early hydrolysis data peaks results in their height being not much intense than this of the background signal. The mentioned, sinusoidal feature in the PDF also contributes to the non-ideal peak height fit. Spikes that are a part of the background further increase the R_w value.

In terms of the late hydrolysis data, the broad 5.8–6.5 Å feature is the main problem in fitting the data. It can be connected to molecules or atoms surrounding the $[\text{Al}_{13}\text{O}_{40}]$ cluster, as the cluster is likely coordinated in solution.

6.5 Conclusions

Early stages of hydrolysis exhibit predominant signal contribution from small species, fitting to pair distribution function of hexaqua-aluminium ion and Cl^- atom coordinated with 6 water molecules. Apart from these two, main species, the PCA (Principal Component Analysis)

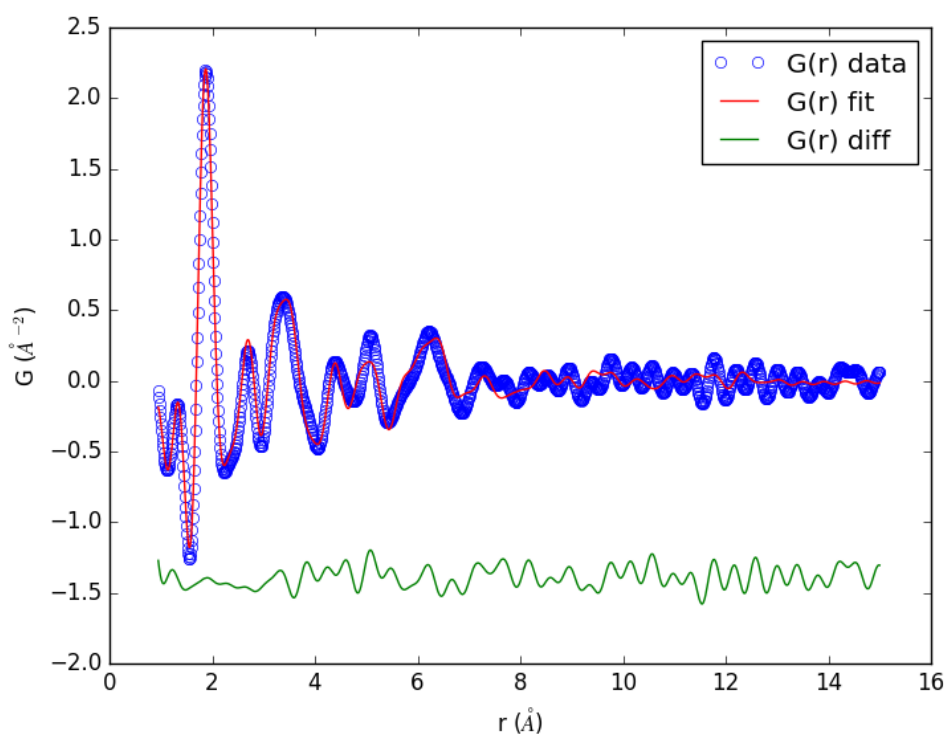


Figure 6.36: PDF fit of $[Al_{13}O_{40}Cl_{74}]$ with Al_3O_{13} (3-O-3fold) multi-phase model to the 60 min dataset.

shows traces of the K- $[Al_{13}]$ cluster signal in the early time hydrolysis datasets. The latter find means that the K- $[Al_{13}]$ cluster must be formed from the small species dominating the early hydrolysis data.

The PCA analysis does not clearly differentiate the K- $[Al_{13}]$ and AlO_6 signals, due to both containing prominent Al-O (1.9 Å) distance. It cannot be ruled out that a small oligomer, such as Al_2 or Al_3 , is present in the solution. That is even more likely due to the similarity in PDF signal of linear Al polymers. It is, however, unlikely that a linear polymer larger than Al_3 is present in the early hydrolysis stage. After 20 min of hydrolysis, the next measurements marked above 40 min already exhibits intense in K- $[Al_{13}]$ signal, indicating that the majority of cluster growth occurred.

A Al_3O_{13} trimer with 3-fold symmetry is another, likely intermediate stage in the K- $[Al_{13}]$ formation. Although its presence in the early hydrolysis stage can be disputed, it does increase the accuracy of late hydrolysis fit significantly. It is also logical that a molecule, which structurally resembles a part of K- $[Al_{13}]$, is involved in its growth.

Taking these points into account, the formation of K- $[Al_{13}]$ oxo-cluster was found to be based on the assembly from small species ($n = 1-3$), which is the “cage-like” mechanism. Despite the ESI-MS evidence found in the literature, no larger oligomers were found in the PDF data. Due to the fact that the PDF method would be sensitive to the presence of larger oligomers, it is indeed unlikely that they are formed as such in the K- $[Al_{13}]$ cluster growth process.

It is also unlikely that an intermediate species were missed during the 20 min break, before the 40 min measurement. That is due to the fact, that the $[Al_{13}O_{40}]$ cluster is already present in small amounts in the early time hydrolysis, according to the PCA analysis.

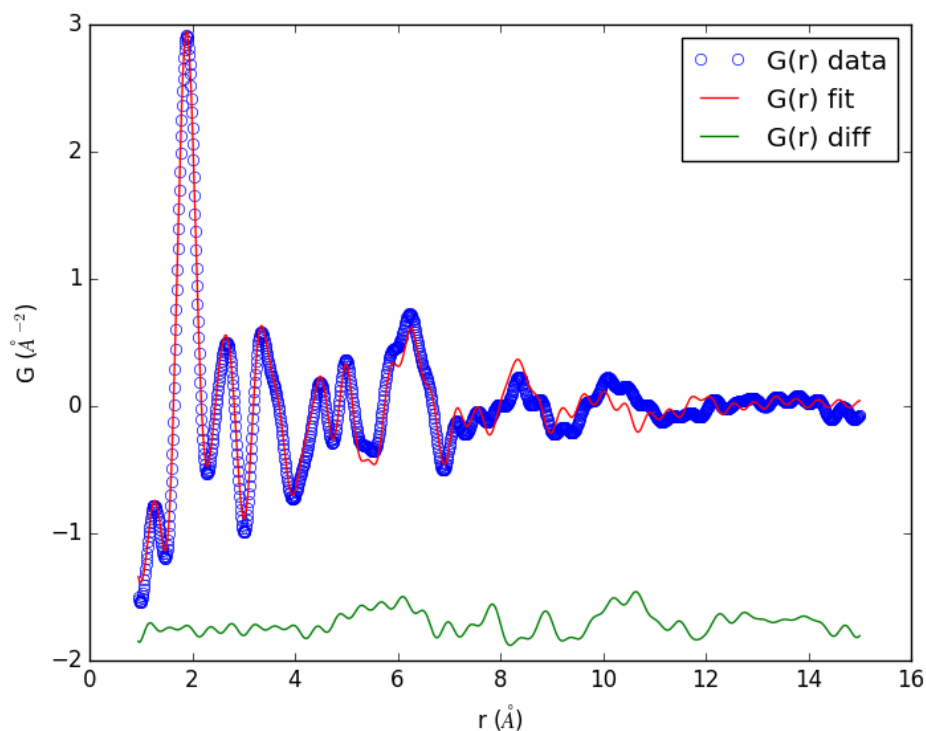


Figure 6.37: PDF fit of $[\text{Al}_{13}\text{O}_{40}\text{Cl}_{74}]$ with Al_3O_{13} (3-O-3fold) multi-phase model to the 180 min dataset.

6.5.1 Remaining questions

Synthesis of ϵ - $[\text{Al}_{13}]$ oxo-cluster from AlCl_3 precursor solution most likely does not include large ($n = 4$ - 12) oligomers in its growth mechanism. This work, however, did not incorporate simultaneous ESI-MS studies, which are in the literature pointing out towards the “core-links” model. It is also not clear, what exact Al_1 – Al_3 species does take an active role in the “cage-like” self-assembly, and what is the importance of Al_3O_{13} with three-fold symmetry. This could be answered with better quality, and early-time focused PDF measurements of this system.

The presented data do not provide information on other than ϵ isomers of $[\text{Al}_{13}]$, and therefore does not directly answer whether or not large oligomers, such as Al_4 - Al_{10} , are involved in isomerization process. Utilising the PDF method to analyse this case could be challenging for two reasons. First of all, the PDF signals of isomers do not differ significantly. Secondly, the isomerization process ongoing, while the precursor isomer is still present in solution insignificant amount, could obscure signal of intermediate species, if their structures are similar to the $[\text{Al}_{13}]$ cluster. However, it would be interesting to analyse this reaction, along with $[\text{Al}_{30}]$ cluster formation.

6.5.2 Author contribution

Processing of the synchrotron data and its analysis, including creating molecule models and the literature review, was done by the thesis author.

Synchrotron data acquirement, including synthesis and operating the beamline, was done by Dr Eric Breynaert, Dr Olivier Deschaume and Dr Simon A. J. Kimber.

Chapter 7

General discussion and final conclusions

7.1 Results of the project

As expected, a long-term project can meet with some difficulties along the way. And so, such difficulties have been met and had to be breached time and time again, whether connected with science or not. It was, however, unexpected that a global pandemic would impede the scientific work, limiting laboratory access and almost entirely banning international and national travel for an extended period of time – aspects crucial for obtaining satisfying and fully realized answers, to the initially posed questions. It was especially difficult for a project so heavily focused on performing synchrotron experiments. And yet, interesting results and discoveries were made in the mechanosynthesis of bismuth APIs and speciation of metal-oxo clusters. Below, the main achievements of the work presented in the dissertation are briefly described in the context of their making and exploration of possible uses.

The entirety of the results presented in this dissertation can be divided into two groups. The first is all contained in Chapter 3, the first topical chapter. These results are concerned with the mechanochemical synthesis of bismuth APIs. The rest of the topical chapters (Chapters 4 to 6) showed results of speciation with the PDF method. This division is applied in this chapter, and the results are examined in two groups in terms of their implications for future projects and potential use.

7.1.1 Mechanochemical synthesis of APIs

Mechanochemical synthesis of bismuth APIs was improved for bismuth (III) disalicylate (BiSal_2) and trisalicylate (BiSal_3), and developed for bismuth (III) gallate (BiGall) and bismuth citrate (BiCit). The initial goal was the improvement of BiSal_2 synthesis, for the purpose of using this compound as a precursor in bismuth-oxo cluster growth. When dozens of samples failed to yield BiSal_2 , it became clear that this reaction was challenging to reproduce based on literature [9]. It resulted in increased personal interest in mechanochemistry, and eventually attempts of performing analogous syntheses by grinding Bi_2O_3 with acids similar to salicylic acid.

The elucidation of all of the failed initial BiSal_2 synthesis attempts was rather surprising – it was the inactive Bi_2O_3 batch, that resulted exclusively in BiSal_3 . After using another identical bottle of Bi_2O_3 , the BiSal_2 started appearing in the product. However, even then the conversion from precursor to product was not satisfactory. After even more adjustments and parameter adjustments, the most favourable were selected. Heating of the reaction mixture before grinding, use of ionic salt, lack of cooling while grinding and the use of 10 mm steel balls turned out to be essential for the reliable synthesis of BiSal_2 . At the same time, some opposite parameters are required for successful BiSal_3 synthesis - no heating of the reaction mixture, cooling while grinding and use of 7 mm steel balls. The precise parameters are listed in Tab. 3.2. Because the structure of BiSal_3 is unknown, it was impossible to perform Rietveld refinements to confirm

the full conversion. However, due to no sign of leftover precursor signal in the PXRD, it is most likely that full conversion was achieved. In the case of BiSal₂ it was confirmed with Rietveld refinement. The best established parameters were tested for a specific mass of a precursor mixture, however, therefore, any tries involving a larger amount may require adjustments. This is important to highlight, the mechanochemical synthesis has a large potential in industrial use. One more vital observation was that the inactive Bi₂O₃ can be activated with heat, although it was not established what is the cause of that. The heating is not paired with a change in mass, and the inactive and active batches of Bi₂O₃ were identical.

Both BiGall and BiCit were easier to synthesize, as Bi₂O₃ "activity" seemed to not play any role in these syntheses. The mechanochemical synthesis of BiGall requires further development for easier application to large scale synthesis, specifically in terms of full conversion. The PXRD measurements consistently showed leftover Bi₂O₃ in the product, and no adjustment of the reaction parameters was successful in eliminating impurity. In the case of bismuth citrate, the full conversion of a synthesis reaction is by far the easiest to achieve with no Bi₂O₃ traces. The only requirement for successful BiCit synthesis is the use of the LAG method since without water the grinding does not result in a pure product. It was even confirmed, that BiCit can form through aging a mixture of citric acid and Bi₂O₃ in a moist environment for up to seven days.

Apart from the four mentioned compounds, one more reaction mixture was attempted – Bi₂O₃ and acetylsalicylic acid. However, seemingly no chemical reaction took place in this attempt. That being said, it is plausible that more bismuth compounds can be synthesized mechanochemically, and this could be easily pursued in future research.

The synthesis of BiGall and BiCit, and improvement of BiSal₂ and BiSal₃ syntheses in laboratory scale, open doors for their large-scale synthesis research – as already hinted. It is valuable to pursue especially with the intention of lowering the environmental impact of industrial-scale syntheses, both for pharmaceutical and chemical use of bismuth APIs. The presented four compounds can be also used as an inspiration for research concerns with synthesizing other bismuth compounds mechanochemically, especially from bismuth (III) oxide and a simple organic acid. The potential use of mechanochemical synthesis of bismuth citrate is especially interesting due to the fact, that it was shown to be useful in a fight against coronaviruses – specifically, the COVID-19 virus [241]. BiCit is also intriguing due to the discovered water-dependent property of its structure.

Bismuth citrate structures

Although the structure of bismuth citrate remains unsolved, a water-dependent change in it was discovered through PXRD measurements of the mechanochemically synthesized sample. It was analyzed with PXRD, Raman spectroscopy and TGA, and conclusively can be attributed to a reversible structural change. This change is physical rather than chemical in nature, due to no changes in Raman spectra and visible changes in PXRD. It is also evident that the "wet" structure (**2b**) is most likely highly symmetric and highly porous, which aligns well with the water-dependent change. The idea is that the dry crystal structure (**2a**) is origami-like. Therefore, when BiCit is dry, it is folded – and then inflates to a highly porous, water-filled framework when exposed to an excess of water (Fig. 7.1). This would explain the changes in the PXRD pattern, that show a multitude of peaks associated with dry powder and only a small amount of regularly distributed peaks for wet paste of BiCit.

Another important observation is that only mechanochemically synthesized BiCit undergoes structural change. Neither BiCit synthesized through aging nor commercial change when exposed to an excess of water. That is until they are mechanochemically ground. After grinding commercial BiCit, it starts exhibiting the same structural change as the mechanochemical one. The possible explanation of that phenomenon tights to the speculated origami-like crystal

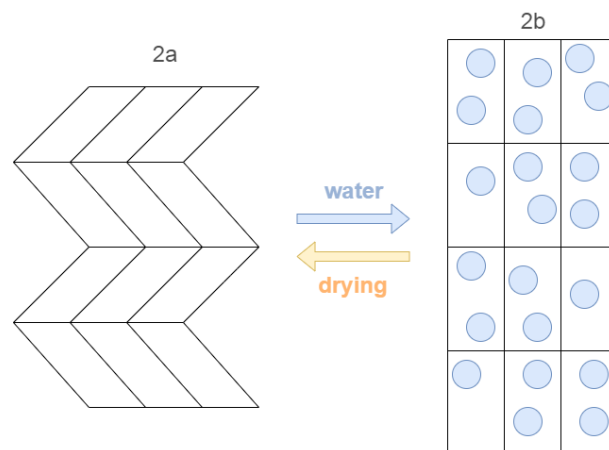


Figure 7.1: A schematic representation of speculative bismuth citrate structure. The harmonic-like, dry **2a** structure expands in the presence of water. This results in a regular **2b** structure of cubic crystal system, with water-filled pores. The change in structure is fully reversible, and can only be performed if bismuth citrate is mechanochemically activated.

structure of BiCit. When crystals of BiCit are large, it is impossible for water to penetrate and inflate the lattice of **2a** structure. Mechanochemical grinding decreases the size of crystallite significantly, more than manual grinding used for mixing commercial BiCit with water. The decreased crystallite size enables water to penetrate the crystal lattice, and inflate it to the **2b** structure. Of course, this explanation will not be fully confirmed until the crystal structure of BiCit is solved. Hopefully, this water-dependent property will be an incentive for elucidation of the BiCit crystal structure.

Industrial scale mechanochemical synthesis

The most important unanswered question in the topic of mechanosynthesis of bismuth APIs is whether or not these reactions could be used on an industrial scale. Without a doubt, restraining the use of bulk solvent and chemical waste should be one of many goals to achieve, on the road towards an ecologically neutral society. Whether mechanochemistry may be one of the tools in achieving that goal, has to be determined [225]. Although on the surface it seems that it would most certainly result in a more green alternative, the in-depth analysis of energetic costs of the mechanochemical versus solvent-based methods would have to be performed. And after that, scaling the reactions to industrial scale and adjusting the parameters would be required [57, 72, 80].

It goes without saying, that such industry-heavy, ecological analysis of the bismuth APIs synthesis was beyond the scope of this project. It is also a very specific subject, the outcome of which can depend on the location of the production site, as well as the type of energy source it is using. That being said, a novel, solvent-deficient way of synthesizing a compound is certain to allow for innovation and advancements to be made. It is therefore an interesting perspective for the potential utility of the mechanochemical synthesis routes described in this dissertation.

7.1.2 PDF method analysis of oxo-cluster growth

The [Bi₃₈O₄₄] oxo-cluster

Thanks to improving the mechanochemical synthesis of BiSal₂, it was used as a precursor to bismuth-oxo cluster growth. The growth of the Keplerate-shaped [Bi₃₈O₄₄] cluster was reported in the literature, where it was shown in acetone and DMF from commercial bismuth subsalicylate [10], as well as from the mechanochemical BiSal₂ [9]. Crystallization was utilized in the literature to find the structure of this cluster. This was repeated in this project, with crystallization of the [Bi₃₈O₄₄] cluster as a confirmation of the literature report. The following experiments were performed in order to establish the growth mechanism of this cluster. For that, spectroscopic laboratory methods were used, as well as synchrotron-based total scattering analysis with the PDF method. Additionally, the growth environment was analyzed in terms of the water content influence, as well as solvent effect. Apart from DMF and acetone, new solvents were used – cyclohexanone, pentanone and MEK.

Water dependence of the growth mechanism was detected in the laboratory experiments. It manifested as a tendency for the larger species to dominate the signal when the utilized solvent contained more water. This was true both for bench solvent, and anhydrous solvent with the addition of water. The difference was noticeable in comparison to anhydrous (dry) solvents. This was extensively analyzed with a water-controlled experiment, where 30 samples with different concentrations of BiSal₂ and different additions of water (0–5%) were prepared from anhydrous solvent. In this experiment, the samples were carefully prepared in an argon-filled glove bag with the use of Suba-seal[®]. Despite that, no water-dependent changes were detected. This is most likely due to a long time from mixing the samples to the measurement, which was 7 days. The samples could not be measured right away, due to the time required for the precipitation of undissolved particles. However, later synchrotron experiments showed that the [Bi₃₈O₄₄] cluster growth is in fact water-dependent, although the growth of the final product usually does not take more time than 24 hours – even with a dry solvent. This water dependence is consistent with DLS measurements, and other UV–Vis observations. It is also important to highlight, that in the mechanochemical synthesis of BiSal₂ precursor water is used in the LAG reaction. Therefore, using freshly synthesized BiSal₂ provides enough water for the growth of a large amount of [Bi₃₈O₄₄]. The excess of water is therefore influencing the equilibrium of the growth reaction, increasing the speed of the [Bi₃₈O₄₄] cluster formation. In the PDF measurements, dry DMF resulted exclusively in smaller cluster signal, and bench DMF showed signal characteristics for the [Bi₃₈O₄₄] oxo-cluster.

In terms of speciation, the laboratory experiments (both UV–Vis spectroscopy and DLS), pointed towards two different in size species being present in BiSal₂ solution. The DLS provided approximate sizes of these species, fitting in 1.3–1.7 and 2.3–3.1 nm diameter ranges. UV–Vis showed two, broad peaks, that were best visible in the water-controlled experiment mentioned before. With the smallest concentration of BiSal₂, it was clearly visible that a broad UV–Vis absorption feature is composed of two, broad peaks. Thanks to the use of PDF method, it was established that the growth of Keplerate-shaped [Bi₃₈O₄₄] cluster is preceded by a smaller, [Bi₉O₇] cluster, and it is these two clusters that were detected with DLS, as their sizes match the diameter ranges detected with DLS.

The choice of solvent rendered important in terms of the final product. It was established that some solvents prevent the larger cluster from forming, whereas others seem to form it immediately. Pentanone always yields the larger [Bi₃₈O₄₄] cluster, right after mixing. Cyclohexanone on the other hand exclusively yields the [Bi₉O₇] cluster, and no traces of the [Bi₃₈O₄₄] cluster can be found even on the next day. This shows that the growth process of the [Bi₃₈O₄₄] cluster depends heavily on the solvent, which can be taken advantage of in further studies of the system, especially in terms of the [Bi₉O₇] cluster. The influence of the solvent can be a result of the solvent taking an active part in the [Bi₃₈O₄₄] cluster growth since the cluster is

functionalized not only with salicylic groups but also with groups deriving from the solvent itself. Another explanation is that the solvent can act as a catalyst, facilitating hydrolysis of precursor molecules and then ololation and oxolation reactions forming the bismuth-oxygen cores. Some solvents, like cyclohexanone, can therefore stabilise the otherwise intermediate molecule by increasing the energetic barrier of the next reaction.

The results obtained with laboratory methods in this part of the project hinted towards interesting answers. However, only after PDF analysis was employed, the answers could be confirmed and elaborated on. The total scattering method was an essential part in speciating and understanding the growth mechanism of the $[\text{Bi}_{38}\text{O}_{44}]$ cluster.

The Keggin-shaped $[\text{Al}_{13}]$ oxo-cluster

The ϵ - $[\text{Al}_{13}]$ cluster was first discovered in 1960 [99], and its growth mechanism from AlCl_3 and other precursor solutions remain a mystery for over 60 years – with the two, mutually exclusive mechanisms that were supported with various laboratory experiments. NMR and ESI-MS were some of the most heavily employed methods, both offering indirect information about the structures present in reaction solution. PDF method was therefore a great, complementary technique to use for adding new information about the growth mechanism of the ϵ - $[\text{Al}_{13}]$ cluster.

The "core-links" gradual polymerization growth model, which is favored by some ESI-MS [246, 247] and NMR users [3], shows a wonderful variety of species taking part in gradual development of the $[\text{Al}_{13}]$ cluster – and yet, the total scattering analysis deemed it incorrect. The PDF studies of measurement series of a water AlCl_3 solution, shows no gradual size development of aluminum species. It does, however, show a "jump" in size occurring in between 20 and 40 min from neutralization of the solution, which is effectively the beginning of $[\text{Al}_{13}]$ growth. This observation is in line with the "cage-like" model, which assumes self-assembly of K- $[\text{Al}_{13}]$ from small (Al_1 – Al_3) aluminum species. Some of the literature using NMR [25] and ESI-MS [210, 211] supports this model. The destructive character of ESI-MS, which involves not only a change of state of the liquid sample, but also ionization, may lead to producing a variety of species that are not present in solution. This could have been the case in the works, that favour the gradual polymerization model. NMR on the other hand, similarly to PDF, allows analysis of a sample without its destruction. However, the NMR signal is not straight forward representation of the structure, and may lead to inaccurate interpretations – which is apparent due to some literature evidence supporting the gradual polymerization model [3]. Ultimately, PDF brought new kind of information, as it was able to clearly show which ϵ - $[\text{Al}_{13}]$ growth mechanism is accurate, the self-assembly from small aluminum species.

Apart from showing that the "cage-like" self-assembly growth mechanism is accurate, it was possible to narrow down the most plausible intermediate species taking part in the ϵ - $[\text{Al}_{13}]$ cluster formation. It is clear that the most suitable are linear polymers, from AlO_6 to Al_3O_{14} , with octahedrally coordinated Al sites. There is an undeniable match of PDF data to the samples AlO_6 . But it is also possible to fit the data with linear oligomers, Al_2 and Al_3 . One more, possible match is a trimer of particular, three-fold symmetry - Al_3O_{13} . The latter is the most interesting structure among possible precursors to the Keggin-shaped $[\text{Al}_{13}]$, due to the similarity of its structure to the four triads of Al sites, that surround the central Al in Keggin. Because of a very similar PDF pattern of linear Al_1 – Al_3 species, it was not possible to distinguish which of them are present in the solution. However, it was clear that the Cl–O distance is visible in the PDF data, as a decreasing in time peak intensity at 3.2 Å. This information is interesting in terms of the role that Cl^- ion most likely in the K- $[\text{Al}_{13}]$ formation process.

The PDF studies of the ϵ - $[\text{Al}_{13}]$ cluster growth compared to the literature understanding of that system, resulted in new developments in the subject. This shows that PDF method can

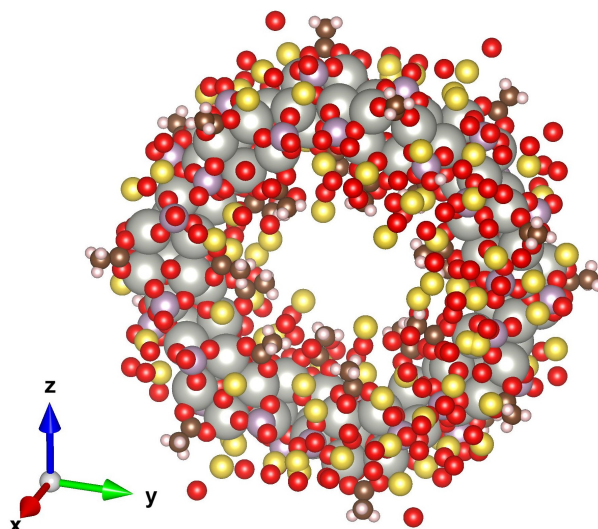


Figure 7.2: A model of $[\text{Pd}_{84}]$ ring-shaped oxo-cluster from a solid-state structure [232]. The light grey spheres represent Pd, Na is in yellow, P in violet, C in dark grey and white are H sites. The simulation is supported by Vesta [146].

be used on its own, with addition of literature information, to extract new information and confirm assumptions about atomic structures based on indirect methods.

Viability of the PDF method for other systems – $[\text{Pd}_{84}]$ oxo-cluster

The two systems analyzed in this work are only examples of oxo-cluster growth reactions suitable for total scattering experiments. There are many other ambiguous systems, in which reaction mechanisms are rather speculated than known. The use of PDF method can be used in many, if not all of these cases, in order to add new information and enable elucidating the intermediate structures. One such system is the Pd_{84} ring-shaped oxo-cluster growth. This system is described below, and presented with a set of laboratory measurements, that provide information analogous to these presented in Chapter 4 for the $[\text{Bi}_{38}\text{O}_{44}]$ cluster growth. This serves a purpose of showing the potential viability of PDF for one more oxo-cluster system.

The Pd_{84} cluster growth can be performed in a relatively simple process. Palladium (II) acetate is dissolved in phosphate buffer of pH ranging from 6.8 to 7.2 over 20 hours, filtered and then left for crystallization for couple of days, after adjusting pH to 4.5, yields $[\text{Pd}_{84}]$ ring-shaped oxo-cluster (Fig. 7.2) in a form of crystals [232]. Similar method of preparation can lead to $[\text{Pd}_{10}]$, $[\text{Pd}_{15}]$ and $[\text{Pd}_{17}]$ clusters crystallization, which suggests that many species are involved in the growth process of the $[\text{Pd}_{84}]$ oxo-cluster [54, 183, 231].

Recreating the literature experiment of $[\text{Pd}_{84}]$ oxo-cluster yielded star-shaped crystals after 3 days, from starting the reaction slurry (Fig. 7.3). The solution was measured using UV-Vis spectrometer, after the mixing and filtration process, and then again after a week of being sealed (Fig. 7.4, a and b). Sealing a sample successfully prevented the crystallization process. The comparison of the initial and aged spectra shows a wide range of peaks in a fresh solution, and fewer of peaks in the aged solution. Such difference could support the theory that initially many species are developed in the solution, and with time the reaction of cluster growth leaves only the most stable species suspended in the solution. Furthermore, DLS measurements of a solution after filtration (Fig. 7.4, d), done over two days period, show clearly a development in size of the species present in the solution. The size after 24 hours matches the size of the $[\text{Pd}_{84}]$ oxo-cluster.



Figure 7.3: A photograph of crystallite formation. The $[\text{Pd}_{84}]$ oxo-cluster crystals started forming after three days from the start of the experiment.

A series of in-situ measurements on the reaction slurry mixed for 20 hours, and then on a filtered solution for another 20 to 40 hours, would most likely provide enough information to analyse and understand the growth mechanism of $[\text{Pd}_{84}]$ oxo-cluster. Obtained data and simulations of PDFs of potential building blocks and precursor clusters for the $[\text{Pd}_{84}]$ ring (Fig. 7.4, c) would enable fingerprinting their presence in a solution while the reaction is ongoing. Therefore, describing the growth process of the $[\text{Pd}_{84}]$ cluster, supported by physical data and interpreted with theoretical models, would be a case analogous to the $[\text{Bi}_{38}\text{O}_{44}]$ cluster growth presented in Chapter 5.

This short presentation shows that the use of PDF method is applicable in a broader subject matter than $[\text{Bi}_{38}\text{O}_{44}]$ and $[\text{Al}_{13}]\text{-}[\text{Al}_{30}]$ oxo-cluster systems. It could be also used for analysis of the $[\text{Pd}_{84}]$ and many other metal-oxo clusters, thought to involve in their growth mechanism a broad array of intermediate species. Moreover, application of the PDF method would require nothing more from the experimental standpoint than performing the synthesis of a metal-oxo cluster with an access to the high energy synchrotron radiation.

7.2 The intended impact

As the last step in this dissertation, it would be meaningful to briefly discuss what the work presented in this dissertation can bring into the future.

It is rarer and rarer in science that a single project brings a groundbreaking discovery. More often, a chain of projects and publications leads towards an important discovery, that can then push scientific advancement forward. This leaves the majority of scientific publications to be pieces of a bigger picture. And this project is no different. The possibility of synthesizing complex materials with mechanochemical grinding, and the use of total scattering data with the PDF method to analyse nanoparticles in solution, are known methods. However, both of these methods can have a wider use than they have at the moment. Because of that, it is important to highlight the utility of known methods by using them to find previously unknown facts and information - and then consider retrospectively how this new information could be applied further, and the methods used analogically for similar purposes.

The mechanochemical syntheses of APIs and other materials is an example of an alternative to the solvent-based processes used in pharmaceutical and chemical industries. As the mechanochemical syntheses may find their way into commercial use in the nearest future, so could

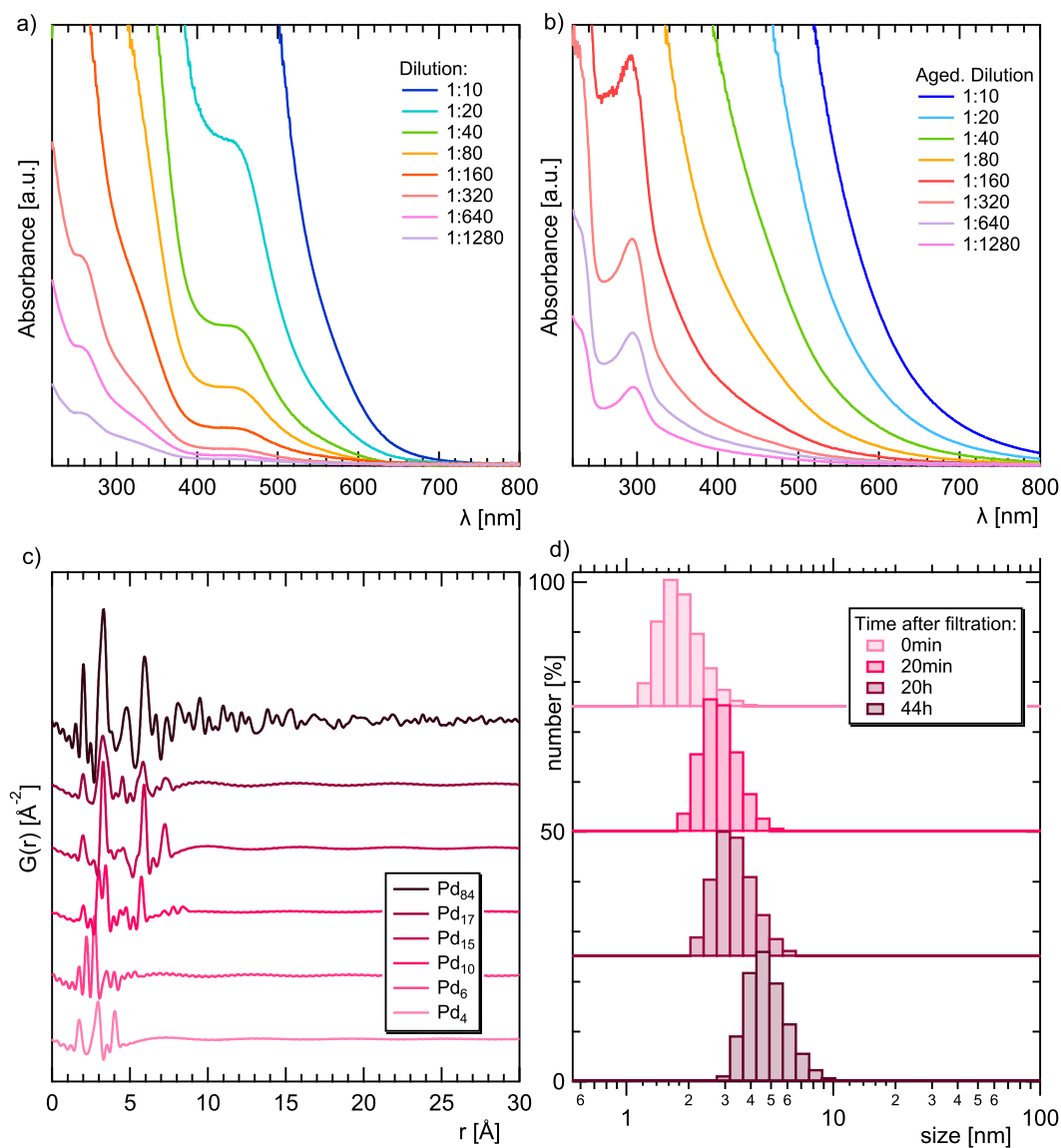


Figure 7.4: **a)** UV-Vis measurements of the solution right after filtration. The measurements were done in different dilutions, allowing to present a variety of peaks present in the solution. **b)** UV-Vis measurements of the solution after being sealed for a week. The measurements were done in different dilutions, allowing to present a variety of peaks present in the solution. **c)** PDF simulations for multiple palladium oxo-clusters, which shows differences in potential precursors of Pd_{84} cluster growth. The structures of $[\text{Pd}_{10}]$, $[\text{Pd}_{15}]$ and $[\text{Pd}_{17}]$ along $[\text{Pd}_{84}]$ from literature were used, whereas Pd_4O_4 and Pd_6O_2 structures are modelled. **d)** Size distribution graphs from a DLS measurement of the solution, started right after the filtration and continued over 44 hours, while the sample was sealed. A size growth of the species present in the solution can be noted.

the described bismuth compounds. This is important as mechanochemical synthesis has the potential to decrease the environmental impact of chemical production.

Total scattering of nanoparticles and oxo-clusters is a subject of growing interest, specifically with the use of the PDF method as a speciation method. The way the PDF complements classical, laboratory experiments can result in increased accuracy of the proposed growth models and a better understanding of the chemistry of a reaction solution. This will happen, provided that the PDF becomes more accessible, and routinely used. The more new results are obtained with the use of total scattering, especially when the classical methods left ambiguous interpretations, the more likely it is to push the PDF forward as a viable tool for nanoparticles and metal-oxo cluster growth analysis. This is how successfully analysing the growth mechanism of $[\text{Bi}_{38}\text{O}_{44}]$ and $[\text{Al}_{13}]$ oxo-clusters contributes in a small part to popularising a viable speciation method. Moreover, as it was demonstrated for $[\text{Pd}_{84}]$ in Chapter 7, the PDF speciation can and should be considered as a tool for any, challenging to interpret growth mechanisms. If given the time and access to equipment and facilities, systems like $[\text{Pd}_{84}]$ could be monitored in-situ with the PDF and additional methods (UV-Vis, DLS, NMR, etc.) in various conditions. The goal would be cataloguing the growth mechanisms in detail, in terms of the intermediate species and structural changes.

When it comes to the use of metal-oxo clusters growth understanding, it is important to extend the knowledge and understanding of the Universe regardless of the economic or even practical prospects. This is true simply because it is impossible to predict where the gained knowledge will lead. And yet, understanding the growth mechanisms of nanoparticles and oxo-clusters, as well as speciating the compounds forming as precursors to the final product, are not without a practical prospect. Understanding the chemistry of a process to the meticulous detail, allows for full control over the process. This could then lead towards the application of such process in the manufacturing of advanced chemical material, through its intentional manipulation into the desired outcome. The PDF method brings the possibility of monitoring the structures present in a reaction solution, and by extending understanding of the structural development of nanoparticles and metal-oxo clusters.

A routine use of the PDF method on solution-based samples is difficult to access. This is due to the necessity of utilising synchrotron radiation. However, facilitating access to synchrotron radiation is a goal of most of the synchrotron sources. The increase of hands-off and mail-in experiments for example, although impossible to make use of with perishable and time-dependent samples, opens up the doors for scientists who for various reasons cannot travel. This, joined with the development of new and better synchrotrons, leaves a hopeful look at the future of accessible synchrotron X-ray radiation, and its use for the PDF method in materials science.

7.3 Acknowledgements

This work has been supported by the EIPHI Graduate School (contract ANR-17-EURE-0002) and the "Investissements d'Avenir" program with ISITE-BFC project (contract ANR-15-IDEX-0003). I acknowledge the European Synchrotron Radiation Facility (Grenoble, France) for the provision of synchrotron beam time on ID15B. I also acknowledge DESY (Hamburg, Germany), a member of the Helmholtz Association HGF, for the provision of experimental facilities. Parts of this research were carried out at P21.1.

The assistance of beam-line scientists was an essential part of this project. Thanks to Jessica M. Hudspeth, Petra Spoerk-Erdely, Valérie Schwanen, and Agnieszka Poulain, who with Simon A. J. Kimber gathered data in ESRF. Thanks to Ann-Christin Dippel, Oleh Ivashko, Olof Gutowski and Philipp Glaevecke, who enabled me, Siham Mouhtadi and Simon A. J. Kimber to gather data at P21.1 at Desy, and assisted in the process. I am grateful to the staff of ID15

at the ESRF and the staff of XFEL in Hamburg for assistance with consumables. I am grateful for the kind help of Sakura Pascarelli and Vasilli Bazhenov in laboratory access in the XFEL, Hamburg, which enabled performing the planned experiment in PETRA-III.

The work on [Al₁₃] was possible thanks to Eric Breynaert and Olivier Deschaume. I appreciate their laboratory work and handling of self-prepared samples, as well as their NMR expertise in analysing the total scattering data.

All of the laboratory work would not be possible, without the help of UBFC scientists and staff. I would like to give thanks to all of them. María del Carmen Marco de Lucas for her expertise on Raman spectroscopy, and access to the equipment. Denis Chaumont for access to the DLS machine. Valérie Potin for the help in TEM analysis. Julien Boudon, for laying down the TGA analysis process, and access to both TGA and UV-Vis equipment. Nicolas Geoffroy, for his help in PXRD measurements, and extended access to the equipment. Jean-Marc Dachicourt, for help in accessing the other PXRD equipment, at times when I couldn't use the first one. Yoann Rousselin for the single crystal diffraction analysis. Michel Meyer, for his help in understanding the nuance of UV-Vis experiments. And at last, David, Camille and Karen I thank you for the aid I could have counted for any time in the lab.

My appreciation goes also to the Friščić group from Montréal's McGill University, and its alumni. Davin Tan, Hatem M. Titi, Patrick J. Julien and Tomislav Friščić for their help in understanding and performing the mechanosynthesis process. Jean-Louis Do, for not only that but also for his friendship and sparking the idea of synthesizing other than salicylate, bismuth APIs. Athina Fidelli, Cristina Mottillo and Ghada Ayoub, for the wonderful atmosphere, and their interest in science, which I found aspirational. Mihails Arhangel'skis, for taking the time to attempt DFT modeling of complex oxo-cluster systems. The hospitality of this hardworking team was an immense help and an inspiration for the entire project.

Thanks to Ivan Halasz from Ruđer Bošković Institute (Zagreb, Croatia), for the help in mechanosynthesis and attempts of bismuth citrate structure solving.

I am grateful to the members of the *comité de thèse*, Nadine Millot and Paul Henry. Their investment was an immense help in forming the scope of this project and delivering on the established goals.

Without my fellow students, the laboratory work would feel tedious and simply not as much fun. To Aya, Housseem, Lina, Margoux - thank you for the moments we shared at work and the interesting conversations. And especially to Siham Mouhtadi, not only a wonderful colleague but also a great friend.

Speaking of friends, I would not be able to complete this dissertation and survive moving to a foreign country without the people closest to me. Thanks to Filip, for brightening up even the darkest moments. Thanks to Ula, for staying connected and caring. Thanks to Hania, for reminding me what really matters and that I can always use a "*wypyo*". Thanks to Shaquille, for supporting me in everything and keeping me level-headed. And thanks to my family, for annoying me even from far away – I would not smile as much without that, and this project helped me realise how much they matter to me.

This project benefited tremendously from the hard work of Agnès Birot, who was able to solve even the most complicated, administrative issue. I will be forever grateful for the warm welcome I owe her, and all of the help she offered to me throughout the years. I am also grateful for the help my *directeur de thèse*, Bruno Domenichini, provided throughout the project.

In the end, I would like to acknowledge the, undeniably, biggest contributor of this work. Thanks to my supervisor and mentor, Simon A. J. Kimber, for ensuring I have enough resources and understanding of scientific topics to take part in this project. For prioritizing my development as a scientist, and remaining helpful and cheerful even in the toughest moments. It will not be hyperbole to say, that without him this project could not be completed. I appreciate all of the work he put into my education, my development, and the help he provided me as a newcomer to a foreign country.

Bibliography

- [1] Samangi Abeysinghe, Daniel K. Unruh, and Tori Z. Forbes. "Crystallization of Keggin-Type Polyaluminum Species by Supramolecular Interactions with Disulfonate Anions". In: *Crystal Growth & Design* 12.4 (Apr. 2012), pp. 2044–2051.
- [2] J. W. Akitt and Julie M. Elders. "Aluminium-27 nuclear magnetic resonance studies of the hydrolysis of aluminium (III). Part 7. – Spectroscopic evidence for the cation $[\text{AlOH}]^{2+}$ from line-broadening studies at high dilution". In: *Journal of the Chemical Society, Faraday Transactions 1: Physical Chemistry in Condensed Phases* 81.8 (Jan. 1985), pp. 1923–1930.
- [3] J W Akitt and Julie M Elders. "Multinuclear Magnetic Resonance Studies of the Hydrolysis of Aluminium (III). Part 8. – Base Hydrolysis monitored at Very High Magnetic Field". In: *Journal of the Chemical Society* (1988), p. 9.
- [4] J. W. Akitt et al. "27 Al nuclear magnetic resonance studies of the hydrolysis and polymerisation of the hexa-aquo-aluminium (III) cation". In: *Journal of the Chemical Society, Dalton Transactions* 5 (Jan. 1972), pp. 604–610.
- [5] Lionel Allouche and Francis Taulelle. "Conversion of Al_{13} Keggin ϵ into Al_{30} : a reaction controlled by aluminum monomers". In: *Inorganic Chemistry Communications* 6.9 (Sept. 2003), pp. 1167–1170.
- [6] Lionel Allouche et al. " Al_{30} : A Giant Aluminum Polycation". In: *Angewandte Chemie International Edition* 39.3 (2000), pp. 511–514.
- [7] Mehran Amiri et al. "Bismuth for Controlled Assembly/Disassembly of Transition-Metal Oxo Clusters, Defining Reaction Pathways in Inorganic Synthesis and Nature". In: *Inorganic Chemistry* 59.6 (Mar. 2020), pp. 3471–3481.
- [8] Don L. Anderson. "Chemical composition of the mantle". In: *Journal of Geophysical Research: Solid Earth* 88.S01 (1983), B41–B52.
- [9] Vânia André et al. "Mechanosynthesis of the Metallodrug Bismuth Subsalicylate from Bi_2O_3 and Structure of Bismuth Salicylate without Auxiliary Organic Ligands". In: *Angewandte Chemie International Edition* 50.34 (2011), pp. 7858–7861.
- [10] Philip C. Andrews et al. "Towards a Structural Understanding of the Anti-Ulcer and Anti-Gastritis Drug Bismuth Subsalicylate". In: *Angewandte Chemie International Edition* 45.34 (2006), pp. 5638–5642.
- [11] Elizabeth J. Anthony et al. "Metallodrugs are unique: opportunities and challenges of discovery and development". In: *Chemical Science* 11.48 (Dec. 2020), pp. 12888–12917.
- [12] Karen J. Ardila-Fierro and José G. Hernández. "Sustainability Assessment of Mechanochemistry by Using the Twelve Principles of Green Chemistry". In: *ChemSusChem* 14.10 (2021), pp. 2145–2162.
- [13] G. Ashiotis et al. "The fast azimuthal integration Python library: pyFAI". In: *Journal of Applied Crystallography* 48.2 (Apr. 2015), pp. 510–519.
- [14] Manuel Aureliano et al. "Characterization of decavanadate and decaniobate solutions by Raman spectroscopy". In: *Dalton Transactions* 45.17 (Apr. 2016), pp. 7391–7399.

- [15] P. Baláž et al. "Hallmarks of Mechanochemistry: From Nanoparticles to Technology". In: *Chemical Society Reviews* 42 (2013), p. 7571.
- [16] Arindam Bankura et al. "A systematic study of chloride ion solvation in water using van der Waals inclusive hybrid density functional theory". In: *Molecular Physics* 113.17-18 (Sept. 2015), pp. 2842–2854.
- [17] R. Becker and W. Döring. "Kinetische Behandlung der Keimbildung in übersättigten Dämpfen". In: *Annalen der Physik* 416.8 (1935), pp. 719–752.
- [18] Alexander N. Beecher et al. "Atomic Structures and Gram Scale Synthesis of Three Tetrahedral Quantum Dots". In: *Journal of the American Chemical Society* 136.30 (July 2014), pp. 10645–10653.
- [19] Patrick J. Beldon et al. "Rapid Room-Temperature Synthesis of Zeolitic Imidazolate Frameworks by Using Mechanochemistry". In: *Angewandte Chemie* 122.50 (2010), pp. 9834–9837.
- [20] Svend Berger et al. "27Al NMR Study of the pH Dependent Hydrolysis Products of Al₂(SO₄)₃ in Different Physiological Media". In: *Molecules : A Journal of Synthetic Chemistry and Natural Product Chemistry* 23.4 (Apr. 2018), p. 808.
- [21] Uwe Bergmann et al. "Nearest-neighbor oxygen distances in liquid water and ice observed by X-ray Raman based extended X-ray absorption fine structure". In: *The Journal of Chemical Physics* 127.17 (Nov. 2007), p. 174504.
- [22] Federica Bertolotti et al. "A total scattering Debye function analysis study of faulted Pt nanocrystals embedded in a porous matrix". In: *Acta Crystallographica Section A Foundations and Advances* 72 (2016), pp. 632–644.
- [23] Paul M. Bertsch. "Conditions for Al₁₃ Polymer Formation in Partially Neutralized Aluminum Solutions". In: *Soil Science Society of America Journal* 51.3 (1987), pp. 825–828.
- [24] Sourav Bhattacharjee. "DLS and zeta potential – What they are and what they are not?" In: *Journal of Controlled Release* 235 (Aug. 2016), pp. 337–351.
- [25] S Bi. "Studies on the mechanism of hydrolysis and polymerization of aluminum salts in aqueous solution: correlations between the "Core-links" model and "Cage-like" Keggin-Al₁₃ model". In: *Coordination Chemistry Reviews* 248.5-6 (Mar. 2004), pp. 441–455.
- [26] Zhe Bi et al. "Transformation of planar Mögel Al₁₃ coagulant during the dilution and aging process". In: *Colloids and Surfaces A: Physicochemical and Engineering Aspects* 416 (Jan. 2013), pp. 73–79.
- [27] Zhe Bi et al. "Transformation of planar Mögel Al₁₃ to epsilon Keggin Al₁₃ in dissolution process". In: *Colloids and Surfaces A: Physicochemical and Engineering Aspects* 407 (Aug. 2012), pp. 91–98.
- [28] S. J. L. Billinge et al. "Deviations from planarity of copper-oxygen sheets in Ca_{0.85}Sr_{0.15}-CuO₂". In: *Physical Review B* 43.13 (May 1991), pp. 10340–10352.
- [29] Simon J. L. Billinge and M. G. Kanatzidis. "Beyond crystallography: the study of disorder, nanocrystallinity and crystallographically challenged materials with pair distribution functions". In: *Chemical Communications* 7 (Mar. 2004), pp. 749–760.
- [30] Avi Bino et al. "Synthesis and Structure of [Fe₁₃O₄F₂₄(OMe)₁₂]⁵⁻: The First Open-Shell Keggin Ion". In: *Journal of the American Chemical Society* 124.17 (May 2002), pp. 4578–4579.
- [31] Xiaowen Bo et al. "Coagulation performance and floc properties of compound bioflocculant-aluminum sulfate dual-coagulant in treating kaolin-humic acid solution". In: *Chemical Engineering Journal* 173.2 (Sept. 2011), pp. 400–406.

- [32] Zbigniew Bojarski. *Krystalografia: podręcznik wspomagany komputerowo*. Wydawnictwo Naukowe PWN, 1996.
- [33] Benjamín C. Bostick et al. "Tungsten Speciation and Solubility in Munitions-Impacted Soils". In: *Environmental Science & Technology* 52.3 (Feb. 2018), pp. 1045–1053.
- [34] Graham A. Bowmaker et al. "Solvent-assisted mechanochemical synthesis of metal complexes". In: *Dalton Transactions* 22 (May 2008), pp. 2926–2928.
- [35] Glen G. Briand and Neil Burford. "Bismuth Compounds and Preparations with Biological or Medicinal Relevance". In: *Chemical Reviews* 99.9 (Sept. 1999), pp. 2601–2658.
- [36] G. Brown et al. "Wiggler and undulator magnets — A review". In: *Nuclear Instruments and Methods in Physics Research* 208.1 (1983), pp. 65–77.
- [37] John W. Cahn and John E. Hilliard. "Free Energy of a Nonuniform System. I. Interfacial Free Energy". In: *The Journal of Chemical Physics* 28.2 (Feb. 1958), pp. 258–267.
- [38] R. Caminiti et al. "Order phenomena in aqueous AlCl_3 solutions". In: *The Journal of Chemical Physics* 71.6 (July 2008), p. 2473.
- [39] Emilie Cauët et al. "Ion Association in AlCl_3 Aqueous Solutions from Constrained First-Principles Molecular Dynamics". In: *Inorganic Chemistry* 51.20 (Oct. 2012), pp. 10856–10869.
- [40] Zbyněk Černý et al. " ^{27}Al NMR studies of the hydrolysis of aluminium (III) chloride in non-aqueous media". In: *Inorganica Chimica Acta* 300-302 (Apr. 2000), pp. 556–564.
- [41] Vadapalli Chandrasekhar, Ramesh K. Metre, and Dipankar Sahoo. " Bi_{38} Oxocarboxylate Cages are Keplerates - Synthesis and Structural Characterization of Two Bi_{38} Oxocarboxylate Cages: Synthesis and Structure of Two Bi_{38} Oxocarboxylate Cages". In: *European Journal of Inorganic Chemistry* 2014.1 (Jan. 2014), pp. 164–171.
- [42] Vadapalli Chandrasekhar, Ramesh K. Metre, and Dipankar Sahoo. " Bi_{38} Oxocarboxylate Cages are Keplerates – Synthesis and Structural Characterization of Two Bi_{38} Oxocarboxylate Cages". In: *European Journal of Inorganic Chemistry* 2014.1 (2014), pp. 164–171.
- [43] Hogeun Chang et al. "To inorganic nanoparticles via nanoclusters: Nonclassical nucleation and growth pathway". In: *Bulletin of the Korean Chemical Society* 42.11 (2021), pp. 1386–1399.
- [44] K. W. Chapman, S. H. Lapidus, and P. J. Chupas. "Applications of principal component analysis to pair distribution function data". In: *Journal of Applied Crystallography* 48.6 (Dec. 2015), pp. 1619–1626.
- [45] Karena W. Chapman. "Emerging operando and X-ray pair distribution function methods for energy materials development". In: *MRS Bulletin* 41.3 (Mar. 2016), pp. 231–240.
- [46] Anthony K. Cheetham and Andrew L. Goodwin. "Crystallography with powders". In: *Nature Materials* 13.8 (Aug. 2014), pp. 760–762.
- [47] Troels Lindahl Christiansen, Susan R. Cooper, and Kirsten M. Ø Jensen. "There's no place like real-space: elucidating size-dependent atomic structure of nanomaterials using pair distribution function analysis". In: *Nanoscale Advances* 2.6 (June 2020), pp. 2234–2254.
- [48] Peter J. Chupas et al. "Application of high-energy X-rays and Pair-Distribution-Function analysis to nano-scale structural studies in catalysis". In: *Catalysis Today*. Time-resolved and in-situ study of heterogeneous catalysts and catalytic processes using X-rays: current possibilities and future prospects, European Synchrotron Radiation Facility, Grenoble, France, 5-7 February, 2008 145.3 (July 2009), pp. 213–219.

- [49] compiled by Alan D. McNaught and Andrew Wilkinson. *Compendium of chemical terminology : IUPAC recommendations*. Second edition. Oxford [Oxfordshire] ; Malden, MA : Blackwell Science, 1997., 1997.
- [50] Mirjana Cvijović et al. "ESI-MS study of speciation in hydrolyzed aluminum chloride solutions". In: *Journal of the Brazilian Chemical Society* (2012).
- [51] Gandrath Dayaker et al. "Catalytic Room-Temperature C-N Coupling of Amides and Isocyanates by Using Mechanochemistry". In: *ChemSusChem* 13.11 (2020), pp. 2966–2972.
- [52] P. Debye. "Zerstreuung von Röntgenstrahlen". In: *Annalen der Physik* 351.6 (1915), pp. 809–823.
- [53] P. Debye and H. Menke. "The determination of the inner structure of liquids by X-ray means". In: 31 (1930), p. 797.
- [54] Massimiliano Delferro et al. "Self-assembly of polyoxoselenitopalladate nanostars [Pd₁₅(μ₃-SeO₃)₁₀(μ₃-O)₁₀Na]⁹⁻ and their supramolecular pairing in the solid state". In: *Dalton Transactions* 39.19 (May 2010), pp. 4479–4481.
- [55] Olivier Deschaume et al. "Impact of Amino Acids on the Isomerization of the Aluminum Tridecamer Al₁₃". In: *Inorganic Chemistry* 56.20 (Oct. 2017), pp. 12401–12409.
- [56] A.-C. Dippel et al. "Beamline P02.1 at PETRA III for high-resolution and high-energy powder diffraction". In: *Journal of Synchrotron Radiation* 22.3 (May 2015), pp. 675–687.
- [57] Jean-Louis Do and Tomislav Friščić. "Mechanochemistry: A Force of Synthesis". In: *ACS Central Science* 3.1 (Jan. 2017), pp. 13–19.
- [58] W. Drube et al. "The PETRA III extension". In: *AIP Conference Proceedings* 1741.1 (July 2016), p. 020035.
- [59] Zygmunt Trzaska Durski. *Podstawy krystalografii rentgenowskiej i analizy strukturalnej kryształów*. Wydaw. Politechniki Warszawskiej, 1973.
- [60] edited by E. Prince. *International tables for crystallography. Volume C, Mathematical, physical and chemical tables*. Springer, Dordrecht, 2004.
- [61] edited by H. Wondratschek and U. Müller. *International Tables for Crystallography Volume A1: Symmetry relations between space groups*. Springer, Dordrecht, 2004.
- [62] Takeshi Egami and Simon J. L. Billinge. *Underneath the Bragg Peaks: Structural Analysis of Complex Materials*. Elsevier, Oct. 2003.
- [63] Michael Ertl et al. "Oxygen Evolution Catalysis with Mössbauerite—A Trivalent Iron-Only Layered Double Hydroxide". In: *Chemistry – A European Journal* 24.36 (June 2018), pp. 9004–9008.
- [64] Clément Falaise et al. "From aqueous speciation to supramolecular assembly in alkaline earth-uranyl polyoxometalates". In: *Chemical Communications* 53.69 (Aug. 2017), pp. 9550–9553.
- [65] C L Farrow et al. "PDFfit2 and PDFgui: computer programs for studying nanostructure in crystals". In: *Journal of Physics: Condensed Matter* 19.33 (Aug. 2007), p. 335219.
- [66] Christopher L. Farrow and Simon J. L. Billinge. "Relationship between the atomic pair distribution function and small-angle scattering: implications for modeling of nanoparticles". In: *Acta Crystallographica Section A Foundations of Crystallography* 65.3 (May 2009), pp. 232–239.
- [67] M. A. Fedotov and R. I. Maksimovskaya. "NMR structural aspects of the chemistry of V, Mo, W polyoxometalates". In: *Journal of Structural Chemistry* 47.5 (Sept. 2006), pp. 952–978.

- [68] Chenghong Feng et al. "Effect of aging condition on species transformation in polymeric Al salt coagulants". In: *Colloids and Surfaces A: Physicochemical and Engineering Aspects*. 6th International Conference on Interfaces Against Pollution 379.1 (Apr. 2011), pp. 62–69.
- [69] John J. Fitzgerald and Allan H. Rosenberg. "Chemistry of Aluminum Chlorohydrate and Activated Aluminum Chlorohydrates". In: *Antiperspirants and Deodorants*. 2nd ed. CRC Press, 1999.
- [70] R. E. Franklin. "The interpretation of diffuse X-ray diagrams of carbon". In: *Acta Crystallographica* 3.2 (Mar. 1950), pp. 107–121.
- [71] J. Frenkel. "A General Theory of Heterophase Fluctuations and Pretransition Phenomena". In: *The Journal of Chemical Physics* 7.7 (1939), pp. 538–547.
- [72] Tomislav Friščić, Cristina Mottillo, and Hatem M. Titi. "Mechanochemistry for Synthesis". In: *Angewandte Chemie* 132.3 (Jan. 2020), pp. 1030–1041.
- [73] Tomislav Friščić et al. "Ion- and Liquid-Assisted Grinding: Improved Mechanochemical Synthesis of Metal–Organic Frameworks Reveals Salt Inclusion and Anion Templating". In: *Angewandte Chemie International Edition* 49.4 (2010), pp. 712–715.
- [74] Tomislav Friščić et al. "Real-time and in situ monitoring of mechanochemical milling reactions". In: *Nature Chemistry* 5.1 (Jan. 2013), pp. 66–73.
- [75] Tomislav Friščić et al. "Screening for Inclusion Compounds and Systematic Construction of Three-Component Solids by Liquid-Assisted Grinding". In: *Angewandte Chemie International Edition* 45.45 (2006), pp. 7546–7550.
- [76] Tomislav Friščić et al. "The role of solvent in mechanochemical and sonochemical cocrystal formation: a solubility-based approach for predicting cocrystallisation outcome". In: *CrystEngComm* 11.3 (Feb. 2009), pp. 418–426.
- [77] G Fu, L F Nazar, and A D Bain. "Aging processes of alumina sol-gels: characterization of new aluminum polyoxycations by aluminum-27 NMR spectroscopy". In: 3.4 (1991), pp. 602–610.
- [78] J. A. Garden and S. D. Pike. "Hydrolysis of organometallic and metal–amide precursors: synthesis routes to oxo-bridged heterometallic complexes, metal-oxo clusters and metal oxide nanoparticles". In: *Dalton Transactions* 47.11 (Mar. 2018), pp. 3638–3662.
- [79] Dylan C. Gary et al. "Two-Step Nucleation and Growth of InP Quantum Dots via Magic-Sized Cluster Intermediates". In: *Chemistry of Materials* 27.4 (Feb. 2015), pp. 1432–1441.
- [80] Agota A. Gečiąuskaitė and Felipe García. "Main group mechanochemistry". In: *Beilstein Journal of Organic Chemistry* 13.1 (Oct. 2017), pp. 2068–2077.
- [81] Luca Gelisio and P. Scardi. "100 years of Debye's scattering equation". In: *Acta Crystallographica Section A Foundations and Advances* 72 (2016), pp. 608–620.
- [82] Carmelo Giacobuzzo et al. *Fundamentals of Crystallography*. OUP Oxford, Feb. 2011.
- [83] W. I. Goldberg. "Dynamic light scattering". In: *American Journal of Physics* 67.12 (Nov. 1999), pp. 1152–1160.
- [84] Davor Gracin et al. "Laboratory Real-Time and In Situ Monitoring of Mechanochemical Milling Reactions by Raman Spectroscopy". In: *Angewandte Chemie International Edition* 53.24 (2014), pp. 6193–6197.
- [85] Zijian Guo and Peter J. Sadler. "Medicinal Inorganic Chemistry". In: *Advances in Inorganic Chemistry*. Ed. by A. G. Sykes. Vol. 49. Academic Press, Jan. 1999, pp. 183–306.

- [86] Marc Henry, Jean Pierre Jolivet, and Jacques Livage. "Aqueous chemistry of metal cations: Hydrolysis, condensation and complexation". In: *Chemistry, Spectroscopy and Applications of Sol-Gel Glasses*. Ed. by Renata Reisfeld and C. K. Jørgensen. Structure and Bonding. Berlin, Heidelberg: Springer, 1992, pp. 153–206.
- [87] José G. Hernández and Carsten Bolm. "Altering Product Selectivity by Mechanochemistry". In: *The Journal of Organic Chemistry* 82.8 (Apr. 2017), pp. 4007–4019.
- [88] Hans-Jörg Himmel. "Characterization of Oligomers of AlCl: Al–Cl versus Al–Al Bonding". In: *European Journal of Inorganic Chemistry* 2005 (2005), pp. 1886–1894.
- [89] Steven M Ho. *Principle Component Analysis (PCA)*. May 2019.
- [90] Jungang Hou et al. "Simultaneously efficient light absorption and charge transport of phosphate and oxygen-vacancy confined in bismuth tungstate atomic layers triggering robust solar CO₂ reduction". In: *Nano Energy* C.32 (2017), pp. 359–366.
- [91] Steven L. Hulbert and Jill M. Weber. "Flux and brightness calculations for various synchrotron radiation sources". In: *Nuclear Instruments and Methods in Physics Research Section A: Accelerators, Spectrometers, Detectors and Associated Equipment* 319.1 (Aug. 1992), pp. 25–31.
- [92] P. Häufe. "Raman-spectrophotometric determination of the tungstate anion and its isopolyanions in aqueous systems". In: *Fresenius' Zeitschrift für analytische Chemie* 310.5 (Jan. 1982), pp. 388–391.
- [93] Nadiia I. Gumerova and Annette Rompel. "Polyoxometalates in solution: speciation under spotlight". In: *Chemical Society Reviews* 49.21 (2020), pp. 7568–7601.
- [94] Milton N. Jackson et al. "An overview of selected current approaches to the characterization of aqueous inorganic clusters". In: *Dalton Transactions* 44.39 (Sept. 2015), pp. 16982–17006.
- [95] Stuart L. James et al. "Mechanochemistry: opportunities for new and cleaner synthesis". In: *Chem. Soc. Rev.* 41.1 (2012), pp. 413–447.
- [96] Kirsten M. Ø Jensen et al. "Polymorphism in magic-sized Au₁₄₄(SR)₆₀ clusters". In: *Nature Communications* 7.1 (June 2016), p. 11859.
- [97] Kirsten M. Ø. Jensen. "Characterization of Nanomaterials with Total Scattering and Pair Distribution Function Analysis: Examples from Metal Oxide Nanochemistry". In: *CHIMIA International Journal for Chemistry* 75.5 (May 2021), pp. 368–375.
- [98] Saihua Jiang et al. "Bismuth subcarbonate nanoplates for thermal stability, fire retardancy and smoke suppression applications in polymers: A new strategy". In: *Polymer Degradation and Stability* 107 (Sept. 2014), pp. 1–9.
- [99] Georg Johansson. "On the crystal structures of some basic aluminium salts". In: *Acta Chemica Scandinavica* 14.3 (1960), pp. 771–773.
- [100] Charles S. Johnson and Don A. Gabriel. *Laser Light Scattering*. Dover Publications, Jan. 1994.
- [101] P. Juhás et al. "PDFgetX3 : a rapid and highly automatable program for processing powder diffraction data into total scattering pair distribution functions". In: *Journal of Applied Crystallography* 46.2 (Apr. 2013), pp. 560–566.
- [102] Pavol Juhás et al. "Complex modeling: a strategy and software program for combining multiple information sources to solve ill posed structure and nanostructure inverse problems". In: *Acta Crystallographica Section A Foundations and Advances* 71.6 (Nov. 2015), pp. 562–568.

- [103] Pavol Juhás et al. "PDFgetN3 : atomic pair distribution functions from neutron powder diffraction data using *ad hoc* corrections". In: *Journal of Applied Crystallography* 51.5 (Oct. 2018), pp. 1492–1497.
- [104] Patrick A Julien, Ivani Malvestiti, and Tomislav Friščić. "The effect of milling frequency on a mechanochemical organic reaction monitored by in situ Raman spectroscopy". In: *Beilstein Journal of Organic Chemistry* 13 (Oct. 2017), pp. 2160–2168.
- [105] Patrick A. Julien, Cristina Mottillo, and Tomislav Friščić. "Metal–organic frameworks meet scalable and sustainable synthesis". In: *Green Chemistry* 19.12 (June 2017), pp. 2729–2747.
- [106] Patrick A. Julien et al. "In Situ Monitoring and Mechanism of the Mechanochemical Formation of a Microporous MOF-74 Framework". In: *Journal of the American Chemical Society* 138.9 (Mar. 2016), pp. 2929–2932.
- [107] Young-Shin Jun, Doyoon Kim, and Chelsea W. Neil. "Heterogeneous Nucleation and Growth of Nanoparticles at Environmental Interfaces". In: *Accounts of Chemical Research* 49.9 (Sept. 2016), pp. 1681–1690.
- [108] S. Karthika, T. K. Radhakrishnan, and P. Kalaichelvi. "A Review of Classical and Non-classical Nucleation Theories". In: *Crystal Growth & Design* 16.11 (Nov. 2016), pp. 6663–6681.
- [109] Michael Kaszuba et al. "Measuring sub nanometre sizes using dynamic light scattering". In: *Journal of Nanoparticle Research* 10.5 (May 2008), pp. 823–829.
- [110] J. F. Keggin. "Structure of the Molecule of 12-Phosphotungstic Acid". In: *Nature* 131.3321 (June 1933), pp. 908–909.
- [111] Robert W Kelsall et al. *Nanotechnologie*. Warszawa: Wydawnictwo Naukowe PWN, 2008.
- [112] Didem Ketenoglu. "Distinctive applications of synchrotron radiation based X-ray Raman scattering spectroscopy: a minireview". In: *Instrumentation Science & Technology* 49.4 (July 2021), pp. 376–394.
- [113] Guido Kickelbick et al. "Hybrid Inorganic–Organic Core–Shell Nanoparticles from Surface-Functionalized Titanium, Zirconium, and Vanadium Oxo Clusters". In: *Chemistry of Materials* 14.10 (Oct. 2002), pp. 4382–4389.
- [114] W. G. Klemperer and W. Shum. "Synthesis and interconversion of the isomeric α - and β -molybdate ($\text{Mo}_8\text{O}_{26}^{4-}$) ions". In: *Journal of the American Chemical Society* 98.25 (Dec. 1976), pp. 8291–8293.
- [115] Robert J. Koch. "Pushing the boundaries of total scattering methods". In: *IUCrJ* 6.Pt 2 (Mar. 2019), pp. 154–155.
- [116] S. V. Krivovichev. "Polyoxometalate clusters in minerals: review and complexity analysis". In: *Acta Crystallographica Section B: Structural Science, Crystal Engineering and Materials* 76.4 (Aug. 2020), pp. 618–629.
- [117] Karl Laden. *Antiperspirants and deodorants*. New York: Marcel Dekker, 1999.
- [118] J. R. Lambert and P. Midolo. "The actions of bismuth in the treatment of *Helicobacter pylori* infection". In: *Alimentary Pharmacology & Therapeutics* 11 Suppl 1 (Apr. 1997), pp. 27–33.
- [119] Jisoo Lee et al. "Nonclassical nucleation and growth of inorganic nanoparticles". In: *Nature Reviews Materials* 1.8 (June 2016), pp. 1–16.
- [120] U. Lee et al. "Synchrotron structure determination of an α -Keggin doubly PtIV-substituted silicotungstate, $(\text{CH}_6\text{N}_3)_8[\alpha\text{-SiPt}_2\text{W}_{10}\text{O}_{40}]\cdot 6\text{H}_2\text{O}$ ". In: *Acta Crystallographica Section C: Crystal Structure Communications* 59.4 (Apr. 2003), pp. m152–m155.

- [121] Meiyong Leng et al. "Lead-Free, Blue Emitting Bismuth Halide Perovskite Quantum Dots". In: *Angewandte Chemie (International Ed. in English)* 55.48 (Nov. 2016), pp. 15012–15016.
- [122] Hao Li et al. "Oxygen Vacancy-Mediated Photocatalysis of BiOCl: Reactivity, Selectivity, and Perspectives". In: *Angewandte Chemie International Edition* 57.1 (2018), pp. 122–138.
- [123] Hao Li et al. "Oxygen Vacancy Structure Associated Photocatalytic Water Oxidation of BiOCl". In: *ACS Catalysis* 6.12 (Dec. 2016), pp. 8276–8285.
- [124] Bernard Lorber et al. "Protein analysis by dynamic light scattering: methods and techniques for students". In: *Biochemistry and Molecular Biology Education: A Bimonthly Publication of the International Union of Biochemistry and Molecular Biology* 40.6 (Dec. 2012), pp. 372–382.
- [125] Ying Lu et al. "Hydrothermal synthesis and crystal structure of a hybrid material based on $[\text{Cu}_4(\text{bpy})_4(\text{H}_2\text{O})_2(\text{PO}_4)_2]^{2+}$ and an α -Keggin polyoxoanion". In: *Journal of Molecular Structure* 2-3.737 (2005), pp. 183–187.
- [126] Chaoran Luan et al. "Four Types of CdTe Magic-Size Clusters from One Prenucleation Stage Sample at Room Temperature". In: *The Journal of Physical Chemistry Letters* 10.15 (Aug. 2019), pp. 4345–4353.
- [127] Peter Luger. *Röntgenografie strukturalna monokryształów*. Państwowe Wydawnictwo Naukowe, 1988.
- [128] Zihao Ma et al. "Immobilization of monodisperse metal-oxo-cluster on graphene for aerobic oxidative desulfurization of fuel". In: *Process Safety and Environmental Protection* 140 (Aug. 2020), pp. 26–33.
- [129] P. Malfertheiner, M. Nilius, and U. Kreusel. "Bismuth and *Helicobacter pylori*". In: *Basic and Clinical Aspects of Helicobacter pylori Infection*. Ed. by G. Gasbarrini and S. Pretolani. Berlin, Heidelberg: Springer Berlin Heidelberg, 1994, pp. 266–279.
- [130] Alessandro Mancini and Lorenzo Malavasi. "Recent advances in the application of total scattering methods to functional materials". In: *Chemical Communications* 51.93 (Nov. 2015), pp. 16592–16604.
- [131] Dirk Mansfeld et al. "From $\{\text{Bi}_{22}\text{O}_{26}\}$ to Chiral Ligand-Protected $\{\text{Bi}_{38}\text{O}_{45}\}$ -Based Bismuth Oxido Clusters". In: *Chemistry - A European Journal* 17.52 (Dec. 2011), pp. 14805–14810.
- [132] V. A Maroni and T. G. Spiro. "The Vibrational Spectrum of the Hydrolytic Hexamer of Bismuth (III)". In: *Journal of the American Chemical Society* 88 (1966), pp. 1410–1412.
- [133] M. Paula M. Marques et al. "An EXAFS Approach to the Study of Polyoxometalate–Protein Interactions: The Case of Decavanadate–Actin". In: *Inorganic Chemistry* 56.18 (Sept. 2017), pp. 10893–10903.
- [134] B. J. Marshall et al. "Antibacterial action of bismuth in relation to *Campylobacter pyloridis* colonization and gastritis". In: *Digestion* 37 Suppl 2 (1987), pp. 16–30.
- [135] L. B. McCusker et al. "Rietveld refinement guidelines". In: *Journal of Applied Crystallography* 32.1 (Feb. 1999), pp. 36–50.
- [136] Michael Mehring. "From molecules to bismuth oxide-based materials: Potential homo- and heterometallic precursors and model compounds". In: *Coordination Chemistry Reviews* 251.7-8 (Apr. 2007), pp. 974–1006.
- [137] Michael Mehring et al. "Polynuclear bismuth-oxo clusters: insight into the formation process of a metal oxide". In: *Chemistry (Weinheim an Der Bergstrasse, Germany)* 12.6 (Feb. 2006), pp. 1767–1781.

- [138] Linda Miersch et al. "Hydrolysis of a Basic Bismuth Nitrate – Formation and Stability of Novel Bismuth Oxido Clusters". In: *Chemistry – A European Journal* 17.25 (2011), pp. 6985–6990.
- [139] Linda Miersch et al. "Synthesis and Characterization of Polynuclear Oxidobismuth Sulfonates". In: *European Journal of Inorganic Chemistry* 2013.9 (2013), pp. 1427–1433.
- [140] Takuo Minato et al. "Robotic Stepwise Synthesis of Hetero-Multinuclear Metal Oxo Clusters as Single-Molecule Magnets". In: *Journal of the American Chemical Society* 143.32 (Aug. 2021), pp. 12809–12816.
- [141] Haralampos N. Miras, Elizabeth F. Wilson, and Leroy Cronin. "Unravelling the complexities of inorganic and supramolecular self-assembly in solution with electrospray and cryospray mass spectrometry". In: *Chemical Communications* 11 (Mar. 2009), pp. 1297–1311.
- [142] Archismita Misra et al. "Beyond Charge Balance: Counter-Cations in Polyoxometalate Chemistry". In: *Angewandte Chemie International Edition* 59.2 (2020), pp. 596–612.
- [143] Katja Dralle Mjos and Chris Orvig. "Metallo drugs in medicinal inorganic chemistry". In: *Chemical Reviews* 114.8 (Apr. 2014), pp. 4540–4563.
- [144] John B. Moffat. *Metal-Oxygen Clusters: The Surface and Catalytic Properties of Heteropoly Oxometalates*. Springer Science & Business Media, Apr. 2006.
- [145] Pedro I. Molina et al. "Aqueous Bismuth Titanium–Oxo Sulfate Cluster Speciation and Crystallization". In: *Angewandte Chemie* 129.51 (2017), pp. 16495–16499.
- [146] K. Momma and F. Izumi. "VESTA 3 for three-dimensional visualization of crystal, volumetric and morphology data". In: *Journal of Applied Crystallography* 44.6 (Dec. 2011), pp. 1272–1276.
- [147] M. L. B. Moraes et al. "The role of Al₁₃-polymers in the recovery of rare earth elements from acid mine drainage through pH neutralization". In: *Applied Geochemistry* 113 (Feb. 2020), p. 104466.
- [148] Achim Müller et al. "Archimedean Synthesis and Magic Numbers: "Sizing" Giant Molybdenum-Oxide-Based Molecular Spheres of the Keplerate Type". In: *Angewandte Chemie International Edition* 38.21 (1999), pp. 3238–3241.
- [149] May Nyman. "Polyoxometalates and Other Metal-Oxo Clusters in Nature". In: *Encyclopedia of Geochemistry: A Comprehensive Reference Source on the Chemistry of the Earth*. Ed. by William M. White. Cham: Springer International Publishing, 2016, pp. 1–5.
- [150] May Nyman. "Small-angle X-ray scattering to determine solution speciation of metal-oxo clusters". In: *Coordination Chemistry Reviews* 352 (Dec. 2017), pp. 461–472.
- [151] C. André Ohlin. "Reaction Dynamics and Solution Chemistry of Polyoxometalates by Electrospray Ionization Mass Spectrometry". In: *Chemistry – An Asian Journal* 7.2 (2012), pp. 262–270.
- [152] Richard P. Oleksak et al. "Evaluation of Thermal and Radiation Induced Chemistries of Metal Oxo–Hydroxo Clusters for Next-Generation Nanoscale Inorganic Resists". In: *ACS Applied Nano Materials* 1.9 (Sept. 2018), pp. 4548–4556.
- [153] Anna F. Oliveri et al. "Isomerization of Keggin Al₁₃ Ions Followed by Diffusion Rates". In: *Chemistry – A European Journal* 22.52 (Dec. 2016), pp. 18682–18685.
- [154] Anna F. Oliveri et al. "Isomerization of Keggin Al₁₃ Ions Followed by Diffusion Rates." In: *Chemistry (Weinheim an der Bergstrasse, Germany)* 22.52 (Dec. 2016), pp. 18682–18685.

- [155] "On the Crystal Structures of FeOHSO_4 and InOHSO_4 , volume = 16, journal = *Acta Chemica Scandinavica* author = Johansson, Georg, year = 1962, pages = 1234–1244," in: ().
- [156] Hideo Onuki and Pascal Elleaume. *Undulators, Wigglers and Their Applications*. CRC Press, Oct. 2002.
- [157] Jose Luis Ortiz-Quinonez et al. "Transformation of Bismuth and $\beta\text{-Bi}_2\text{O}_3$ Nanoparticles into $(\text{BiO})_2\text{CO}_3$ and $(\text{BiO})_4(\text{OH})_2\text{CO}_3$ by Capturing CO_2 : The Role of Halloysite Nanotubes and "Sunlight" on the Crystal Shape and Size". In: *Crystal Growth & Design* 18.8 (Aug. 2018), pp. 4334–4346.
- [158] D. R. Parker, L. W. Zelazny, and T. B. Kinraide. "Comparison of Three Spectrophotometric Methods for Differentiating Mono- and Polynuclear Hydroxy-Aluminum Complexes". In: *Soil Science Society of America Journal* 52.1 (1988), pp. 67–75.
- [159] David R. Parker and Paul M. Bertsch. "Formation of the " Al_{13} " tridecameric aluminum polycation under diverse synthesis conditions". In: *Environmental Science & Technology* 26.5 (May 1992), pp. 914–921.
- [160] R. Pecora, ed. *Dynamic Light Scattering: Applications of Photon Correlation Spectroscopy*. Springer US, 1985.
- [161] Enric Petrus, Mireia Segado, and Carles Bo. "Nucleation mechanisms and speciation of metal oxide clusters". In: *Chemical Science* 11.32 (Aug. 2020), pp. 8448–8456.
- [162] Jörg Polte. "Fundamental growth principles of colloidal metal nanoparticles – a new perspective". In: *CrystEngComm* 17.36 (2015), pp. 6809–6830.
- [163] Vojislava Pophristic, Michael L. Klein, and Marian N. Holerca. "Modeling Small Aluminum Chlorohydrate Polymers". In: *The Journal of Physical Chemistry A* 108.1 (Jan. 2004), pp. 113–120.
- [164] Th Proffen and S. J. L. Billinge. "PDFFIT, a program for full profile structural refinement of the atomic pair distribution function". In: *Journal of Applied Crystallography* 32.3 (June 1999), pp. 572–575.
- [165] Thomas Proffen and Hyunjeong Kim. "Advances in total scattering analysis". In: *Journal of Materials Chemistry - J MATER CHEM* 19 (2009).
- [166] Thomas Proffen et al. "Atomic pair distribution function analysis of materials containing crystalline and amorphous phases". In: *Zeitschrift für Kristallographie - Crystalline Materials* 220.12 (2009), pp. 1002–1008.
- [167] Raul Quesada Cabrera et al. "Spectroscopic studies of sulfite-based polyoxometalates at high temperature and high pressure". In: *Journal of Solid State Chemistry* 186 (Feb. 2012), pp. 171–176.
- [168] Pantaleo Raimondi. "ESRF-EBS: The Extremely Brilliant Source Project". In: *Synchrotron Radiation News* 29.6 (2016), pp. 8–15.
- [169] William V. Rausch and Harold D. Bale. "Small-Angle X-Ray Scattering from Hydrolyzed Aluminum Nitrate Solutions". In: *The Journal of Chemical Physics* 40.11 (1964), pp. 3391–3394.
- [170] Alexander F. Redkin and Galina V. Bondarenko. "Raman Spectra of Tungsten-Bearing Solutions". In: *Journal of Solution Chemistry* 39.10 (Oct. 2010), pp. 1549–1561.
- [171] Paul Reynolds et al. "Bismuth Toxicity: A Rare Cause of Neurologic Dysfunction". In: *International Journal of Clinical Medicine* 3 (2012), pp. 46–48.

- [172] F. Ribot and C. Sanchez. "Organically Functionalized Metallic Oxo-Clusters: Structurally Well-Defined Nanobuilding Blocks for the Design of Hybrid Organic-Inorganic Materials". In: *Comments on Inorganic Chemistry* 20.4-6 (Jan. 1999), pp. 327–371.
- [173] Nicholas R. Rightmire and Timothy P. Hanusa. "Advances in organometallic synthesis with mechanochemical methods". In: *Dalton Transactions* 45.6 (Feb. 2016), pp. 2352–2362.
- [174] Anna-Kaisa Ronkanen et al. "The role of aluminium and iron in phosphorus removal by treatment peatlands". In: *Ecological Engineering* 86 (Jan. 2016), pp. 190–201.
- [175] J. Rowsell and L. F. Nazar. "Speciation and Thermal Transformation in Alumina Sols: Structures of the Polyhydroxyoxoaluminum Cluster $[Al_{30}O_8(OH)_{56}(H_2O)_{26}]^{18+}$ and Its δ -Keggin Moiety". In: *Journal of the American Chemical Society* 122.15 (Apr. 2000), pp. 3777–3778.
- [176] Wolfram W. Rudolph, Roger Mason, and Cory C. Pye. "Aluminium (III) hydration in aqueous solution. A Raman spectroscopic investigation and an ab initio molecular orbital study of aluminium (III) water clusters". In: *Physical Chemistry Chemical Physics* 2.22 (Jan. 2000), pp. 5030–5040.
- [177] Baranov Sa. "Comparison of Classical Nucleation Theory and Modern Theory of Phase Transition". In: *Journal of Advanced Chemical Engineering* 07.01 (2017).
- [178] Arja Sarpola et al. "Hydrolysis products of water treatment chemical aluminium sulfate octadecahydrate by electrospray ionization mass spectrometry". In: *Polyhedron* 26.12 (July 2007), pp. 2851–2858.
- [179] Arja Sarpola et al. "Identification and fragmentation of hydrolyzed aluminum species by electrospray ionization tandem mass spectrometry". In: *Journal of Mass Spectrometry* 39.10 (2004), pp. 1209–1218.
- [180] Arja Sarpola et al. "Identification of the hydrolysis products of $AlCl_3 \cdot 6H_2O$ by electrospray ionization mass spectrometry". In: *Journal of Mass Spectrometry* 39.4 (2004), pp. 423–430.
- [181] Maik Schlesinger et al. "Nanoscaled Bismuth Oxido Clusters: Probing Factors of Structure Formation and Photocatalytic Activity: Nanoscaled Bismuth Oxido Clusters". In: *European Journal of Inorganic Chemistry* 2014.2 (Jan. 2014), pp. 302–309.
- [182] Maik Schlesinger et al. "Two novel nanoscaled bismuth oxido clusters, $[Bi_{38}O_{45}(OMc)_{22}(C_8H_7SO_3)_2(DMSO)_6(H_2O)_{1.5}] \cdot 25H_2O$ and $[Bi_{38}O_{45}(HSal)_{22}(OMc)_2(DMSO)_{15}(H_2O)] \cdot DMSO \cdot 2H_2O$ ". In: *Main Group Metal Chemistry* 36.1-2 (Mar. 2013), pp. 11–19.
- [183] Rachel A. Scullion et al. "Exploring the Symmetry, Structure, and Self-Assembly Mechanism of a Gigantic Seven-Fold Symmetric Pd_{84} Wheel". In: *Angewandte Chemie International Edition* 53.38 (2014), pp. 10032–10037.
- [184] Wilhelm Seichter et al. "Crystal Structure and Formation of the Aluminium Hydroxide Chloride $[Al_{13}(OH)_{24}(H_2O)_{24}]Cl_{15} \cdot 13H_2O$ ". In: *European Journal of Inorganic Chemistry* 1998.6 (1998), pp. 795–797.
- [185] Kirill L. Shafran, Olivier Deschaume, and Carole C. Perry. "The static anion exchange method for generation of high purity aluminium polyoxocations and monodisperse aluminium hydroxide nanoparticles". In: *Journal of Materials Chemistry* 15.33 (Aug. 2005), pp. 3415–3423.
- [186] N. T. Silva et al. "Kinetics of cordierite crystallization from diphasic gels". In: *Journal of Sol-Gel Science and Technology* 47.2 (Aug. 2008), pp. 140–147.
- [187] Adam H. Slavney et al. "A Bismuth-Halide Double Perovskite with Long Carrier Recombination Lifetime for Photovoltaic Applications". In: *Journal of the American Chemical Society* 138.7 (Feb. 2016), pp. 2138–2141.

- [188] Scott E. Smart et al. "Controlled step-wise isomerization of the Keggin-type Al_{13} and determination of the $\gamma\text{-Al}_{13}$ structure". In: *Chemical Communications* 49.97 (Nov. 2013), pp. 11352–11354.
- [189] Lindsay I. Smith. "A tutorial on Principal Components Analysis". In: (2002).
- [190] Hyunsoo So and Michael T. Pope. "Origin of some charge-transfer spectra. Oxo compounds of vanadium, molybdenum, tungsten, and niobium including heteropoly anions and heteropoly blues". In: *Inorganic Chemistry* 11.6 (June 1972), pp. 1441–1443.
- [191] L. Soderholm et al. "The Structure of the Plutonium Oxide Nanocluster $[\text{Pu}_{38}\text{O}_{56}\text{Cl}_{54}(\text{H}_2\text{O})_8]^{14-}$ ". In: *Angewandte Chemie International Edition* 47.2 (2008), pp. 298–302.
- [192] Garrison Sposito. *The Environmental Chemistry of Aluminum, Second Edition*. CRC Press, Nov. 1995.
- [193] Peter W. Stephens. "Phenomenological model of anisotropic peak broadening in powder diffraction". In: *Journal of Applied Crystallography* 32.2 (1999), pp. 281–289.
- [194] Vjekoslav Štrukil et al. "Towards an environmentally-friendly laboratory: dimensionality and reactivity in the mechanosynthesis of metal–organic compounds". In: *Chemical Communications* 46.48 (2010), pp. 9191–9193.
- [195] E. C. Subbarao. "Systematics of bismuth layer compounds". In: *Integrated Ferroelectrics* 12.1 (June 1996), pp. 33–41.
- [196] Hongzhe Sun, Hougyan Li, and Peter J. Sadler. "The Biological and Medicinal Chemistry of Bismuth". In: *Chemische Berichte* 130.6 (1997), pp. 669–681.
- [197] Zhong Sun et al. "A Giant Polyaluminum Species S-Al_{32} and Two Aluminum Polyoocations Involving Coordination by Sulfate Ions S-Al_{32} and S-K-Al_{13} ". In: *Inorganic Chemistry* 50.2 (Jan. 2011), pp. 559–564.
- [198] M. Sundaralingam and L. H. Jensen. "Refinement of the structure of salicylic acid". In: *Acta Crystallographica* 18.6 (1965), pp. 1053–1058.
- [199] Daniel Szczerba et al. "Real-Time Observation of "Soft" Magic-Size Clusters during Hydrolysis of the Model Metallodrug Bismuth Disalicylate". In: *Journal of the American Chemical Society* (Sept. 2021).
- [200] Davin Tan, Leigh Loots, and Tomislav Friščić. "Towards medicinal mechanochemistry: evolution of milling from pharmaceutical solid form screening to the synthesis of active pharmaceutical ingredients (APIs)". In: *Chemical Communications* 52.50 (2016), pp. 7760–7781.
- [201] Seema Thakral et al. "Recent advances in the characterization of amorphous pharmaceuticals by X-ray diffractometry". In: *Advanced Drug Delivery Reviews*. Amorphous pharmaceutical solids 100 (May 2016), pp. 183–193.
- [202] Nguyen T. K. Thanh, N. Maclean, and S. Mahiddine. "Mechanisms of Nucleation and Growth of Nanoparticles in Solution". In: *Chemical Reviews* 114.15 (Aug. 2014), pp. 7610–7630.
- [203] Sabrina L. J. Thomä et al. "Atomic insight into hydration shells around faceted nanoparticles". In: *Nature Communications* 10.1 (Dec. 2019), p. 995.
- [204] Sabrina L. J. Thomä et al. "Pushing data quality for laboratory pair distribution function experiments". In: *Review of Scientific Instruments* 90.4 (Apr. 2019), p. 043905.
- [205] E. V. Timakova, Yu. M. Yukhin, and T. A. Udalova. "Synthesis of Bismuth (III) Oxide Salicylate from Nitrate Solutions for Medical Purposes". In: *Chemistry for Sustainable Development* 17 (2009), pp. 305–313.

- [206] Evgeniya Timakova et al. "Synthesis of basic bismuth (III) oxalate by precipitation from nitrate solutions". In: *Russian Journal of Applied Chemistry* 90 (July 2017), pp. 1040–1046.
- [207] Brian H. Toby and Robert B. Von Dreele. "GSAS-II : the genesis of a modern open-source all purpose crystallography software package". In: *Journal of Applied Crystallography* 46.2 (Apr. 2013), pp. 544–549.
- [208] Julia Torres et al. "Interaction of Molybdenum (VI) Oxyanions with +2 Metal Cations". In: *Journal of Solution Chemistry* 43.9 (Oct. 2014), pp. 1687–1700.
- [209] Craig S. Truebenbach, Marwan Houalla, and David M. Hercules. "Characterization of isopoly metal oxyanions using electrospray time-of-flight mass spectrometry". In: *Journal of Mass Spectrometry* 35.9 (2000), pp. 1121–1127.
- [210] Tatsuya Urabe, Takahisa Tsugoshi, and Miho Tanaka. "Electrospray ionization mass spectrometry investigation of the blocking effect of sulfate on the formation of aluminum tridecamer". In: *Journal of Molecular Liquids. Solution Chemistry (ICSC30 - 2007)* 143.1 (Sept. 2008), pp. 70–74.
- [211] Tatsuya Urabe et al. "Study on chemical speciation in aluminum chloride solution by ESI-Q-MS". In: *Journal of Mass Spectrometry* 42.5 (2007), pp. 591–597.
- [212] John E. Van Benschoten and James K. Edzwald. "Chemical aspects of coagulation using aluminum salts – I. Hydrolytic reactions of alum and polyaluminum chloride". In: *Water Research* 24.12 (Dec. 1990), pp. 1519–1526.
- [213] G. B. M. Vaughan et al. "ID15A at the ESRF – a beamline for high speed operando X-ray diffraction, diffraction tomography and total scattering". In: *Journal of Synchrotron Radiation* 27.2 (Mar. 2020), pp. 515–528.
- [214] M. Volmer and A. Z. Weber. "Nucleus Formation in Supersaturated Systems". In: *Zeitschrift für Physikalische Chemie* 119 (1926), pp. 277–301.
- [215] Oleksandr Voznyy et al. "Computational Study of Magic-Size CdSe Clusters with Complementary Passivation by Carboxylic and Amine Ligands". In: *The Journal of Physical Chemistry C* 120.18 (May 2016), pp. 10015–10019.
- [216] Anna T. Wagner and Peter W. Roesky. "Rare-Earth Metal Oxo/Hydroxo Clusters – Synthesis, Structures, and Applications". In: *European Journal of Inorganic Chemistry* 2016.6 (2016), pp. 782–791.
- [217] M. Walther and D. Zahn. "From bismuth oxide/hydroxide precursor clusters towards stable oxides: Proton transfer reactions and structural reorganization govern the stability of $[\text{Bi}_{18}\text{O}_{13}(\text{OH})_{10}]$ -nitrate clusters". In: *Chemical Physics Letters* 691 (Jan. 2018), pp. 87–90.
- [218] Guan-Wu Wang. "Mechanochemical organic synthesis". In: *Chemical Society Reviews* 42.18 (Aug. 2013), pp. 7668–7700.
- [219] Wei Wang et al. "Crystallizing Elusive Chromium Polycations". In: *Chem* 1.6 (Dec. 2016), pp. 887–901.
- [220] Xizheng Wang et al. "Doped δ -bismuth oxides to investigate oxygen ion transport as a metric for condensed phase thermite ignition". In: *Physical Chemistry Chemical Physics* 19.20 (May 2017), pp. 12749–12758.
- [221] Yunchen Wang et al. "Elucidation of the elusive structure and formula of the active pharmaceutical ingredient bismuth subgallate by continuous rotation electron diffraction". In: *Chemical Communications* 53.52 (2017), pp. 7018–7021.
- [222] Mark Weller et al. *Inorganic Chemistry*. OUP Oxford, 2014.

- [223] Simon White et al. "Commissioning and Restart of ESRF-EBS". In: *Proceedings of the 12th International Particle Accelerator Conference IPAC2021* (2021), 6 pages, 1.452 MB.
- [224] Egon Wiberg, A. F. Holleman, and Nils Wiberg. *Inorganic Chemistry*. Academic Press, 2001.
- [225] Krystyna Wieczorek-Ciurowa and K. Gamrat. "Mechanochemical syntheses as an example of green processes". In: *Journal of Thermal Analysis and Calorimetry* 88.1 (Apr. 2007), pp. 213–217.
- [226] K. Wille. "Introduction to insertion devices". In: *CAS - CERN Accelerator School : Synchrotron Radiation and Free Electron Lasers* (1998), pp. 61–75.
- [227] David B. Williams and C. Barry Carter. "Scattering and Diffraction". In: *Transmission Electron Microscopy: A Textbook for Materials Science*. Ed. by David B. Williams and C. Barry Carter. Boston, MA: Springer US, 1996, pp. 19–33.
- [228] David B. Williams and C. Barry Carter. "The Transmission Electron Microscope". In: *Transmission Electron Microscopy: A Textbook for Materials Science*. Ed. by David B. Williams and C. Barry Carter. Boston, MA: Springer US, 1996, pp. 3–17.
- [229] Curtis B. Williamson et al. "Chemically reversible isomerization of inorganic clusters". In: *Science* 363.6428 (Feb. 2019), pp. 731–735.
- [230] Jiagang Wu et al. "Multiferroic bismuth ferrite-based materials for multifunctional applications: Ceramic bulks, thin films and nanostructures". In: *Progress in Materials Science* C.84 (2016), pp. 335–402.
- [231] Feng Xu et al. "A Supramolecular Heteropolyoxopalladate {Pd₁₅} Cluster Host Encapsulating a {Pd₂} Dinuclear Guest: [Pd₂^{II}⊂{H₇Pd₁₅^{II}O₁₀(PO₄)₁₀}]⁹⁻". In: 133 (Apr. 2011), pp. 4684–4686.
- [232] Feng Xu et al. "Correlating the magic numbers of inorganic nanomolecular assemblies with a {Pd₈₄} molecular-ring Rosetta Stone". In: *Proceedings of the National Academy of Sciences* 109.29 (July 2012), pp. 11609–11612.
- [233] Toshihiro Yamase. "Photo- and Electrochromism of Polyoxometalates and Related Materials". In: *Chemical Reviews* 98.1 (Feb. 1998), pp. 307–326.
- [234] Bin Yang et al. "Lead-Free, Air-Stable All-Inorganic Cesium Bismuth Halide Perovskite Nanocrystals". In: *Angewandte Chemie International Edition* 56.41 (2017), pp. 12471–12475.
- [235] Nan Yang et al. "Bismuth Complexes Inhibit the SARS Coronavirus". In: *Angewandte Chemie International Edition* 46.34 (2007), pp. 6464–6468.
- [236] Xiao-Jian Yang et al. "Hybrid Coordination Networks Constructed from ϵ -Keggin-Type Polyoxometalates and Rigid Imidazole-Based Bridging Ligands as New Carriers for Noble-Metal Catalysts". In: *Chemistry – An Asian Journal* 11.6 (2016), pp. 858–867.
- [237] Changqing Ye, Zhe Bi, and Dongsheng Wang. "Formation of Al₃₀ from aqueous polyaluminum chloride under high temperature: Role of Al₁₃ aggregates". In: *Colloids and Surfaces A: Physicochemical and Engineering Aspects* 436 (Sept. 2013), pp. 782–786.
- [238] Xiaofeng Yi et al. "Structural Chemistry of Metal-Oxo Clusters". In: *Advanced Structural Chemistry*. John Wiley & Sons, Ltd, 2021, pp. 111–161.
- [239] Callum A. Young and Andrew L. Goodwin. "Applications of pair distribution function methods to contemporary problems in materials chemistry". In: *Journal of Materials Chemistry* 21.18 (Apr. 2011), pp. 6464–6476.
- [240] R. A. Young and Robert Alan Young. *The Rietveld Method*. Oxford University Press, 1995.

- [241] Shuofeng Yuan et al. "Metallo drug ranitidine bismuth citrate suppresses SARS-CoV-2 replication and relieves virus-associated pneumonia in Syrian hamsters". In: *Nature Microbiology* 5.11 (Nov. 2020), pp. 1439–1448.
- [242] Yu. M. Yukhin et al. "Bismuth (III) subgallate trihydrate synthesis". In: *Theoretical Foundations of Chemical Engineering* 44.5 (Oct. 2010), pp. 749–754.
- [243] Yury M Yukhin et al. "Synthesis of Bismuths (III) Compounds for Medical Applications". In: *Chemistry for Sustainable Development* 12 (2004), pp. 395–401.
- [244] Fu-Qiang Zhang et al. "On the Origin of the Inverted Stability Order of the Reverse-Keggin $[(\text{MnO}_4)(\text{CH}_3)_{12}\text{Sb}_{12}\text{O}_{24}]^{6-}$: A DFT Study of α , β , γ , δ , and ϵ Isomers". In: *Inorganic Chemistry* 49.12 (June 2010), pp. 5472–5481.
- [245] Hua Zhang et al. "Preparation of Bismuth Oxide Quantum Dots and their Photocatalytic Activity in a Homogeneous System". In: *ChemCatChem* 2.9 (Sept. 2010), pp. 1115–1121.
- [246] He Zhao, Huijuan Liu, and Jiuhui Qu. "Effect of pH on the aluminum salts hydrolysis during coagulation process: Formation and decomposition of polymeric aluminum species". In: *Journal of Colloid and Interface Science* 330.1 (Feb. 2009), pp. 105–112.
- [247] He Zhao et al. "Effect of aluminum speciation and structure characterization on preferential removal of disinfection byproduct precursors by aluminum hydroxide coagulation". In: *Environmental Science & Technology* 43.13 (July 2009), pp. 5067–5072.
- [248] M. Zobel, R. B. Neder, and S. A. J. Kimber. "Universal solvent restructuring induced by colloidal nanoparticles". In: *Science* 347.6219 (Jan. 2015), pp. 292–294.
- [249] Mirijam Zobel et al. "The evolution of crystalline ordering for ligand-ornamented zinc oxide nanoparticles". In: *CrystEngComm* 18.12 (Mar. 2016), pp. 2163–2172.
- [250] A. Zouboulis, G. Traskas, and P. Samaras. "Comparison of Efficiency between Poly-aluminium Chloride and Aluminium Sulphate Coagulants during Full-scale Experiments in a Drinking Water Treatment Plant". In: *Separation Science and Technology* 43.6 (Apr. 2008), pp. 1507–1519.